Bainite formation in the presence of martensite

dos Santos Avila, D.

DOI
10.4233/uuid:434a7a7e-2136-4f0b-a932-66c0db5bb1fa

Publication date
2025

Document Version
Final published version

Citation (APA)
dos Santos Avila, D. (2025). *Bainite formation in the presence of martensite*. [Dissertation (TU Delft), Delft University of Technology]. https://doi.org/10.4233/uuid:434a7a7e-2136-4f0b-a932-66c0db5bb1fa

Bainite formation in the presence of martensite

Bainite formation in the presence of martensite

Dissertation

for the purpose of obtaining the degree of doctor
at Delft University of Technology
by the authority of the Rector Magnificus Prof.dr.ir. T.H.J.J. van der Hagen,
chair of the Board for Doctorates
to be defended publicly on Monday 3, February 2025 at 12:30 o'clock

by

Daniel DOS SANTOS AVILA

This dissertation has been approved by the promotors.

Composition of the doctoral committee:

Rector Magnificus,	chairperson
Prof. dr. M.J. Santofimia	Delft University of Technology, promotor
Dr. ir. S.E. Offerman	Delft University of Technology, promotor

Independent members:

Prof. dr. ir. L.A.I. Kestens	Delft University of Technology
Prof. dr. A. Borgenstam	KTH Royal Institute of Technology, Sweden
Prof. dr. G. Miyamoto	Tohoku University, Japan
Dr. D. Ponge	Max Planck Institute for Sustainable Materials, Germany
Prof. dr. ir. J.M.C. Mol	Delft University of Technology, reserve member

Other members:

Dr. ir. S.M.C. van Bohemen	Tata Steel, Netherlands

This project has received funding from the Research Fund for Coal and Steel under grant agreement No 899521.

Keywords: bainite, martensite, phase transformation, steel

Printed by: Ridderprint | https://www.ridderprint.nl/

Cover by: Daniel dos Santos Avila

ISBN 978-94-6506-909-8

An electronic version of this dissertation is available at https://repository.tudelft.nl/.

Quando eu te encarei frente a frente não vi o meu rosto
Chamei de mau gosto o que vi, de mau gosto, mau gosto
É que Narciso acha feio o que não é espelho

Caetano Veloso

Contents

Summary

Advancing our understanding of the mechanisms of phase transformations is an efficient pathway to designing new steels with enhanced, tailor-made mechanical properties at minimal experimental cost. This dissertation investigates the bainitic transformation in steels. The mechanism of bainite formation is still not well understood, as there is no consensus on the role of carbon diffusion during the growth of bainite. Thus, it is difficult to understand and predict chemical and microstructural effects on the kinetics of bainite formation, such as the effect of prior austenite grain size and the presence of prior martensite. A better understanding of such effects may allow the design of new high performance bainitic steels with lean chemical composition and energy efficient heat treatments. In this dissertation, a new analytical model of the kinetics of bainite formation based on the displacive-diffusionless theory is proposed. This new model can reproduce and offer insights into the effect of prior austenite grain size and prior martensite on the kinetics of bainite formation. Following the understanding achieved with the model, the accelerating effect that martensite has on bainite formation kinetics is used to develop novel advanced high strength steels for the automotive industry that can be manufactured in existing continuous annealing lines thanks to fast bainite formation. Finally, to better understand the nucleation and growth of bainite, a real time observation of bainite formation using *in situ* transmission electron microscopy (TEM) is shown and discussed.

Chapter 2 of this dissertation presents the first part of the newly developed analytical model of the kinetics of bainite formation. The model calculates the rate of bainite formation at austenite grain boundaries (AGB) and at bainite/austenite (B/A) interfaces separately and keeps track of the bainite fraction formed at each type of nucleation site. A maximum fraction of bainite that can be formed at each type of nucleation site is introduced, and this fraction depends on the austenite grain size and the size of bainite sub-units. The model predicts that when the austenite grain size increases, a larger fraction of bainite will nucleate at B/A interfaces. By separating the fraction of bainite nucleated at AGBs and B/A interfaces, the model could correctly capture the effect of prior austenite grain size on bainite formation kinetics. This effect might vary depending on the chemical composition of the steel and on the transformation temperature. In some cases, refining the austenite grain size accelerates bainite formation, while in others, it slows down bainite formation. A theoretical analysis of the model and comparison against published experimental data shows that slower kinetics for smaller austenite grains is favored as the difference between the activation energy for AGB and B/A nucleation of bainite increases, and as the austenite grain refinement results in finer bainite sub-units.

Chapter 3 expands the model to the case in which prior martensite is present. The effect of prior martensite can be fully captured by considering that new nucleation sites are created at or near the martensite/austenite (M/A) interfaces. Even at low volume fractions of martensite (≈ 0.1), the model indicates that most of the bainite nucleation events took place at the M/A interfaces. This outcome of the model is confirmed by experimentally verifying that when a 0.2 volume fraction of prior martensite is present, changes to the austenite grain boundaries – either by changing the austenite grain size or adding boron, which segregates to austenite grain boundaries – do not affect the kinetics of bainite formation. It is also shown that the accelerating effect of prior martensite is more pronounced at higher temperatures; and that the thermal gradient present in dilatometry samples masks the initial rate of bainite formation in the presence of martensite because at the beginning of the programmed isothermal holding the colder part of the samples are still cooling down and forming martensite.

In Chapter 4, the accelerating effect of martensite, extensively discussed in Chapter 3, is explored to design novel third generation advanced high strength steels that can be manufactured in existing continuous annealing lines. By forming bainite at around $20\,^{\circ}\mathrm{C}$ below the martensite start temperature (M_{S}), a volume fraction of 0.2 of prior martensite is formed, and the bainitic transformation is finalized within $300\,\mathrm{s}$, which is the time available for bainite formation in the overaging section of continuous annealing lines. Additionally, by forming bainite at temperatures lower than usual (bainite is usually formed above M_{S}), bainite laths are finer, increasing the ultimate tensile strength of the steels, while the fraction of retained austenite is lower, improving the local formability of the steels. However, because of the lower austenite fraction, the global formability of the steels is reduced. Different compositions were tested to study the effect of carbon, silicon, manganese, chromium, niobium, and molybdenum on the microstructure and mechanical properties of the steels. Carbon and silicon had the strongest effects, as they most strongly influence the fraction and stability of retained austenite. Five of the designed steels, including the reference composition of Fe-0.24C-1.5Si-2.3Mn ($\mathrm{wt.\%}$), showed tensile strengths higher than $1370\,\mathrm{MPa}$, total tensile elongations higher than $8\,\%$, and hole expansion capacities higher than $30\,\%$, and thus meet the requirements for the strongest commercially available grades of complex phase steels with improved formability.

Chapter 5 presents a preliminary analysis of an *in situ* observation of bainite formation by hot stage transmission electron microscopy. To avoid austenitization inside the TEM, as high temperatures lead to foil thickening and evaporation of alloying elements, a martensitic steel with low M_{S} (Fe-1.24C $\mathrm{wt.\%}$, $M_{\mathrm{S}} = 125\,^{\circ}\mathrm{C}$) was used as the starting material, as it retains a volume fraction of 0.2 to 0.4 of retained austenite at room temperature. The specimen was heated to $280\,^{\circ}\mathrm{C}$ inside the TEM, a temperature at which the retained austenite decomposes into lower bainite. The formation and growth of bainite were captured in enough resolution to observe individual laths, and the growth rate was consistent with the diffusional theory of bainite formation. The chapter discusses and proposes new analyses and experiments that can be carried out with the goal of further

improving our understanding of the growth rate of bainite laths and testing the validity of the diffusional and diffusionless theories of bainite formation.

The dissertation is finalized in Chapter 6 by discussing the main technological and scientific contributions of this work and by providing suggestions for future works. In summary, this dissertation introduces a new model that offers important insights into the effect of prior austenite grain size and prior martensite on the kinetics of bainite formation. The model presented here can be further expanded to cases in which other nucleation sites are present (such as ferrite/austenite or carbide/austenite interfaces) and to other transformations other than the bainitic one. The combination of the new model and experiments showed that boron can enhance the hardenability of steels without slowing down the kinetics of bainite formation, opening the way to leaner alloyed steels with more energy efficient heat treatments, which might significantly reduce CO_2 emissions during steel manufacturing. In terms of steel design, the accelerating effect of martensite on bainite formation was used to create new third generation advanced high strength steels that undergo a heat treatment that can be implemented in existing industrial annealing lines, which facilitates the industrial application of such steels. In terms of understanding the mechanism of bainite growth, *in situ* bainite formation in the TEM showed important evidence of carbon diffusion during the growth of bainite laths. The contribution of this dissertation to the field of physical metallurgy of steels extends from the fundamental theories of phase transformations to the industrial application of novel high performance steels.

Samenvatting

Het bevorderen van ons begrip van de mechanismen van fasetransformaties is een efficiënte weg naar het ontwerpen van nieuwe staalsoorten met verbeterde, op maat gemaakte mechanische eigenschappen tegen minimale experimentele kosten. Dit proefschrift onderzoekt de bainitische transformatie in staal. Het mechanisme van bainietvorming wordt nog steeds niet goed begrepen, omdat er geen consensus is over de rol van koolstofdiffusie tijdens de groei van bainiet. Het is dus moeilijk om chemische en microstructurele effecten op de kinetiek van bainietvorming te begrijpen en te voorspellen, zoals het effect van de voorafgaande austenietkorrelgrootte en de aanwezigheid van voorafgaand martensiet. Een beter begrip van zulke effecten kan het ontwerp mogelijk maken van nieuwe bainitische staalsoorten met hoge prestaties, een karige chemische samenstelling en energiezuinige warmtebehandelingen. In dit proefschrift wordt een nieuw model voorgesteld dat is gebaseerd op de verplaatsings- en diffusieloze theorie van bainietvorming, en dit nieuwe model kan het effect van voorafgaande austenietkorrelgrootte en voorafgaand martensiet op de kinetiek van bainietvorming reproduceren en inzichtelijk maken. Vervolgens worden, op basis van het versnellende effect van martensiet op bainietvorming, nieuwe bainitische geavanceerde hogesterktestalen voor de automobielindustrie ontwikkeld die geproduceerd kunnen worden in bestaande continu-gloeilijnen. Tot slot wordt een realtime waarneming van bainietvorming met in situ transmissie-elektronenmicroscopie (TEM) getoond en besproken.

Hoofdstuk 2 van dit proefschrift presenteert het eerste deel van het nieuwe analytische model van de kinetiek van bainietvorming. Het model berekent de snelheid van bainietvorming bij austenietkorrelgrenzen (AGB) en bij bainiet/austeniet (B/A) interfaces afzonderlijk en houdt de bainietfractie bij die gevormd wordt op elk type nucleatieplaats. Er wordt een maximale bainietfractie ingevoerd die kan worden gevormd op elk type locatie, en deze fractie hangt af van de austenietkorrelgrootte en de grootte van bainietsubeenheden. Het model voorspelt dat wanneer de austeniet korrelgrootte toeneemt, een grotere fractie bainiet zal kiemen bij B/A grensvlakken. Door de fractie bainiet die bij AGB's en B/A grensvlakken wordt gekiemd te scheiden, kan het model het effect van de voorafgaande austenietkorrelgrootte op de kinetiek van de bainietvorming correct weergeven. Dit effect kan variëren afhankelijk van de chemische samenstelling van het staal en van de transformatie temperatuur. In sommige gevallen versnelt het verfijnen van de austenietkorrelgrootte de bainietvorming, terwijl het in andere gevallen de bainietvorming vertraagt. Een theoretische analyse van het model en een vergelijking met gepubliceerde experimentele gegevens toonden aan dat een langzamere kinetiek voor kleinere korrels wordt

begunstigd naarmate het verschil tussen de activeringsenergie voor AGB- en B/A-kiemvorming van bainiet toeneemt en naarmate de austenietkorrelverfijning resulteert in fijnere bainietsubeenheden.

Hoofdstuk 3 breidt het model uit naar het geval waarin voorafgaand martensiet aanwezig is. Het effect van voorafgaand martensiet kan volledig worden gevangen door aan te nemen dat nieuwe kiemen worden gevormd op of nabij de martensiet/austeniet (M/A) grensvlakken. Zelfs bij lage volumefracties van martensiet (≈0,1), geeft het model aan dat het grootste deel van het gevormde bainiet kiemt bij de M/A grensvlakken. Deze uitkomst van het model wordt bevestigd door experimenteel te verifiëren dat wanneer een 0,2 volumefractie van martensiet aanwezig is, veranderingen aan de austenietkorrelgrenzen - hetzij door het veranderen van de austenietkorrelgrootte of door het toevoegen van boor, dat segregeert naar austenietkorrelgrenzen - de kinetiek van bainietvorming niet beïnvloeden. Er wordt ook aangetoond dat het versnellende effect van voorafgaand martensiet meer uitgesproken is bij hogere temperaturen en dat de thermische gradiënt die aanwezig is in dilatometerpreparaten de initiële snelheid van bainietvorming maskeert in aanwezigheid van martensiet, omdat aan het begin van het geprogrammeerde isotherm gloeien het koudere deel van de preparaten nog aan het afkoelen is en martensiet aan het vormen is.

In hoofdstuk 4 wordt het versnellende effect van martensiet, uitvoerig besproken in hoofdstuk 3, onderzocht om nieuwe derde generatie geavanceerde hogesterktestalen te ontwerpen die kunnen worden geproduceerd in bestaande continu-gloeilijnen. Door bainiet te vormen bij ongeveer $20\,^{\circ}\mathrm{C}$ onder de martensiet starttemperatuur (M_{S}), wordt een volumefractie van 0,2 van het voorafgaande martensiet gevormd en de bainitische transformatie is voltooid binnen $300\,\mathrm{s}$, wat de tijd is die beschikbaar is voor bainietvorming in de oververhittingssectie van continu-gloeilijnen. Bovendien, door het vormen van bainiet bij lagere temperaturen dan gebruikelijk (bainiet wordt gewoonlijk gevormd boven M_{S}), zijn de bainietlamellen fijner, waardoor de uiteindelijke treksterkte van de staalsoorten toeneemt, en is de fractie behouden austeniet lager, waardoor de lokale vervormbaarheid van de staalsoorten verbetert. Door de lagere austenietfractie is de globale vervormbaarheid van de stalen echter verminderd. Verschillende samenstellingen werden getest om het effect van koolstof, silicium, mangaan, chroom, niobium en molybdeen op de microstructuur en mechanische eigenschappen van de stalen te bestuderen. Koolstof en silicium hadden de sterkste effecten, omdat zij de fractie en stabiliteit van behouden austeniet het sterkst beïnvloeden. Vijf van de ontworpen staalsoorten, inclusief de referentiesamenstelling van Fe-0,24C-1,5Si-2,3Mn ($\mathrm{wt.\%}$), vertoonden een treksterkte van meer dan $1370\,\mathrm{MPa}$, een totale trekrek van meer dan $8\,\%$ en een gatuitzettingsvermogen van meer dan $30\,\%$, en voldoen dus aan de vereisten voor de sterkste commerciële kwaliteiten van complexe fasestalen met verbeterde vervormbaarheid.

Hoofdstuk 5 presenteert een voorlopige analyse van een in situ waarneming van bainietvorming met behulp van transmissie-elektronenmicroscopie. Om austenitisatie binnen de TEM te voorkomen, omdat hoge temperaturen leiden tot fo-

lieverdikking en verdamping van legeringselementen, werd een afgeschrikt laag MS-staal (Fe-1,24C wt.%, $M_S = 125\,^{\circ}\mathrm{C}$) gebruikt als uitgangsmateriaal, omdat het een volumefractie van 0,2 tot 0,4 austeniet behoudt bij kamertemperatuur. Het proefstuk werd in de TEM verhit tot $280\,^{\circ}\mathrm{C}$, een temperatuur waarbij het behouden austeniet uiteenvalt in lager bainiet. De vorming en groei van bainiet werden vastgelegd met voldoende resolutie om individuele latten te observeren en de groeisnelheid was consistent met de diffusietheorie van bainietvorming. Het hoofdstuk bespreekt en stelt nieuwe analyses en experimenten voor die uitgevoerd kunnen worden met als doel ons begrip van de groeisnelheid van bainietlagen verder te verbeteren en de geldigheid van de diffusie- en diffusieloze theorieën van bainietvorming te testen.

Het proefschrift wordt afgesloten in hoofdstuk 6 met het bespreken van de belangrijkste technologische en wetenschappelijke bijdragen van dit werk. In termen van kinetische modellering introduceerde dit proefschrift een nieuw model dat belangrijke inzichten bood in het effect van voorafgaande austenietkorrelgrootte en voorafgaande martensiet op de kinetiek van bainietvorming. Het hier gepresenteerde model kan verder worden uitgebreid naar gevallen waarin andere nucleatieplaatsen aanwezig zijn (zoals ferriet/austeniet of carbide/austeniet interfaces) en naar andere transformaties dan de bainitische. De combinatie van het nieuwe model en experimenten toonde aan dat boor de hardbaarheid van staal kan verbeteren zonder de kinetiek van de bainietvorming te vertragen, wat de weg opent naar lager gelegeerde staalsoorten met energie-efficiëntere warmtebehandelingen, wat de CO_2-uitstoot tijdens de staalproductie aanzienlijk zou kunnen verminderen. Op het gebied van staalontwerp werd het versnellende effect van martensiet op bainietvorming gebruikt om nieuwe derde generatie geavanceerde hogesterktestalen te creëren die een warmtebehandeling ondergaan die kan worden geïmplementeerd in bestaande industriële gloeilijnen, wat de industriële toepassing van dergelijke staalsoorten vergemakkelijkt. In termen van begrip van het mechanisme van bainietgroei, toonde in situ bainietvorming in de TEM belangrijk bewijs dat er koolstofdiffusie is tijdens de groei van bainietlatten. Daarom strekt de bijdrage van dit proefschrift aan de fysische metallurgie van staal zich uit van de fundamentele theorieën van fasetransformaties tot de industriële toepassing van nieuwe hoogwaardige staalsoorten.

List of Symbols

Symbol	Description
b	Magnitude of Burgers vector
C_1	Proportionality constant between T_h and carbon enrichment of the austenite
C_2	Proportionality constant between T_0 and carbon enrichment of the austenite
$C_{\mathrm{A,AGB}}$	Number of bainite sub-units that can be formed by autocatalysis from the first bainite sub-unit nucleated at the austenite grain boundary
$C_{\mathrm{A,MA}}$	Number of bainite sub-units that can be formed by autocatalysis from the first bainite sub-unit nucleated at the martensite/austenite interface
d_γ	Prior austenite grain size
$\mathrm{d}N/\mathrm{d}t$	Nucleation rate of bainite
$\mathrm{d}N_{\mathrm{AGB}}/\mathrm{d}t$	Nucleation rate of bainite at austenite grain boundaries
$\mathrm{d}N_{\mathrm{BA}}/\mathrm{d}t$	Nucleation rate of bainite at bainite/austenite interfaces
$\mathrm{d}N_{\mathrm{MA}}/\mathrm{d}t$	Nucleation rate of bainite at martensite/austenite interfaces
E_{str}	Strain energy
f	Fraction of bainite
$f_\mathrm{b}^{\mathrm{stasis}}$	Fraction of bainite at stasis
f_{BA}	Fraction of bainite formed by autocatalysis
$f_{\mathrm{BA}}^{\mathrm{max}}$	Maximum fraction of bainite that can be formed by autocatalysis at time t
f_{AGB}	Fraction of bainite formed by nucleation at austenite grain boundaries
$f_{\mathrm{AGB}}^{\mathrm{max}}$	Maximum fraction of bainite that can be formed by nucleation at austenite grain boundaries
f_{MA}	Fraction of bainite formed by nucleation at martensite/austenite interfaces
$f_{\mathrm{MA}}^{\mathrm{max}}$	Maximum fraction of bainite that can be formed by nucleation at martensite/austenite interfaces
f_γ	Fraction of austenite available for transformation
f_m	Fraction of martensite
G_N	Universal nucleation function for bainite and Widmanstätten ferrite
G_{SB}	Stored energy of bainite

Continued on next page

Continued from previous page

Symbol	Description
h	Planck constant
k	Boltzmann constant
K_1	Empirical constant from G_N
K_2	Empirical constant from G_N
M_S	Martensite start temperature
n_P	Number of atomic planes in the martensite or bainite embryo
N_m	Number of martensite plates
$n_\mathrm{S,BA}$	Density of potential bainite nucleation sites per bainite/austenite interface area
$n_\mathrm{S,AGB}$	Density of potential bainite nucleation sites per austenite grain boundary interface area
$n_\mathrm{S,MA}$	Density of potential bainite nucleation sites per martensite/austenite interface area
n_BA	Density of potential bainite nucleation sites for at bainite/austenite interfaces at time t
n_AGB	Density of potential bainite nucleation sites for grain boundary nucleation at time t
n_MA	Density of potential bainite nucleation sites at martensite/austenite interfaces at time t
Q^*	Activation energy for the dissociation of dislocations during nucleation of martensite or bainite
Q_0^*	Activation energy for overcoming the short-range barriers to dislocation movement
Q_AGB	Activation energy for bainite nucleation at austenite grain boundaries at time t
$Q_{\mathrm{AGB}\overline{X}}$	Activation energy for bainite nucleation at austenite grain boundaries for the nominal carbon content of the steel
Q_BA	Activation energy for bainite nucleation at bainite/austenite interfaces at time t
$Q_{\mathrm{BA}\overline{X}}$	Activation energy for bainite nucleation at bainite/austenite interfaces for the nominal carbon content of the steel
Q_D	Activation energy for a carbon atom to jump from a bainite embryo to the austenite matrix
Q_MA	Activation energy for bainite nucleation at martensite/austenite interfaces at time t
$Q_{\mathrm{MA}\overline{X}}$	Activation energy for bainite nucleation at martensite/austenite interfaces for the nominal carbon content of the steel
R	Universal gas constant
S_AGB	Area of austenite grain boundaries per unit volume
S_BA	Area of bainite/austenite interfaces per unit volume
S_MA	Area martensite/austenite interfaces per unit volume
T	Temperature
T_0	Temperature at which $\Delta G^{\gamma\rightarrow\alpha}$ is zero

Continued on next page

Continued from previous page

Symbol	Description
T'_0	Temperature at which $\Delta G^{\gamma\rightarrow\alpha}$ is equal to G_{SB} for the composition of austenite at time t
$T'_{0\overline{\mathrm{X}}}$	T'_0 at the nominal carbon content of the steel
T_{h}	Temperature at which ΔG_{m} is equal to G_{N} for the composition of austenite at time t
$T_{\mathrm{h}\overline{X}}$	T_{h} at the nominal carbon content of the steel
t	Time
t_{m}	Thickness of the martensite laths or plates
u_{L}	Length of the bainite sub-unit
u_{T}	Thickness of the bainite sub-unit
u_{W}	Width of the bainite sub-unit
V_{b}	Volume of the bainite sub-unit
V_{m}	Volume of the martensite plate
V^*	Activation volume for martensite or bainite nucleation
v_{L}	Lengthening rate of the bainite sheaf
$\overline{X}$	Nominal carbon content of the steel
X_{b}	Carbon content trapped in bainite, either in solid solution, defects, or carbides
X_{m}	Carbon content trapped in martensite, either in solid solution, defects, or carbides
X_{bm}	Carbon content trapped in bainite and martensite, either in solid solution, defects, or carbides
X_{part}	Carbon partitioned from bainite and martensite to austenite
Z	Shape factor of the austenite grain
α_{m}	Exponent constant of the Koistinen-Marburger equation
ΔG_{m}	Maximum change in Gibbs free energy for ferrite nucleation under paraequilibrium
$\Delta G^{\gamma\rightarrow\alpha}$	Difference in Gibbs free energy between austenite and ferrite with the same chemical composition
ΔQ	Difference between Q_{AGB} and Q_{BA}
δ	Effective thickness of the austenite grain boundaries
λ	Autocatalytic factor
ρ_{A}	Number of atoms per unit area of the closed packed plane
σ	Interfacial energy
τ_{μ}	Athermal resistance to dislocation movement
Ω	Atomic volume of Fe
φ	Proportionality constant relating undercooling and number density of martensite plates nucleated
φ_{i}	Proportionality constant relating undercooling and number density of martensite plates nucleated from initially present sites

Continued on next page

Continued from previous page

Symbol	Description
φ_{A}	Proportionality constant relating undercooling and number density of martensite plates nucleated from sites created at martensite/austenite interfaces

1

Introduction

1

Steel is intimately connected to the modern world. It is used in buildings, infrastructure, automotive, domestic appliances, machinery, and much more. Its consumption has been growing nonstop: In 1950, the world's average steel consumption was $75\,\mathrm{kg\,per\,capita}$; In 2023, consumption was almost three times higher, at $219\,\mathrm{kg\,per\,capita}$ [1]. From 1950 to 2023, not only did the volume of steel consumption change, but steel itself changed. A showcase example of such a change lies in the automotive industry.

Up to the 1970s, steel sheets used in passenger cars were made from mild steel with a tensile strength of up to $330\,\mathrm{MPa}$. Nowadays, there are commercially available steel sheets for the automotive industry with a tensile strength of around $1200\,\mathrm{MPa}$. Such development was pushed by the pressure to reduce the weight of passenger cars while increasing passenger safety. By using stronger grades of steel, the sheets can be made thinner – which reduces the total car weight – and the car body can absorb more impact and better protect the passengers in the event of a crash. The goal of weight reduction is to improve fuel efficiency and reduce material consumption, thus emitting less CO_2 [2].

Most of the drastic improvement in mechanical properties is being achieved by microstructure control. Microstructures containing soft ferritic grains are gradually being substituted by microstructures containing fine mixtures of bainitic ferrite, martensite, and retained austenite in the so-called advanced high strength steels. Further development relies on in-depth knowledge of the underlying mechanisms of phase transformations in steels. This knowledge helps to design lean chemical compositions and energy-efficient heat treatments that create microstructures that yield the desired mechanical properties at a lower environmental and economic cost.

Bainite is arguably the microstructure constituent being used in modern steels that is the least understood in terms of mechanisms of formation. The role of carbon diffusion in the growth of bainitic ferrite is still under debate in the steel community, with two different theories trying to explain the role of carbon during transformation. One theory, called the diffusionless theory, claims bainitic ferrite grows without carbon diffusion and inherits the carbon content of the parent austenite [3]. Another theory, called the diffusional theory, claims carbon diffusion takes place during the growth of bainitic ferrite, which grows either in paraequilibrium with austenite or with only a partial supersaturation [4, 5].

Both theories have been used in kinetic models of bainite formation. While diffusional-theory–based models have focused more on the lengthening rate of bainite sheaves [4–6], diffusionless-theory–based models have focused more on the overall kinetics of bainite formation [7–9]. Despite some success, such models cannot explain the effect of prior austenite grain size and prior martensite on bainite formation kinetics. The inability to account for these effects indicates that the models are incorrectly accounting for the relative contribution of the different nucleation sites – since it is expected that changing the prior austenite grain size and introducing prior martensite alters the density of nucleation sites for bainite.

In this dissertation, the role of nucleation sites on bainite formation kinetics is investigated by developing a new model for bainite formation based on the diffu-

sionless theory. Chapter 2 proposes a new treatment for the potential nucleation sites, in which site saturation is calculated separately for nucleation of bainite plates at austenite grain boundaries and at bainite/austenite interfaces. The proposed model can reproduce and explain the effect of prior austenite grain size based on the difference between the activation energy for bainite nucleation at austenite grain boundaries and at bainite/austenite interfaces.

In Chapter 3, the model is extended to the case in which prior martensite is present, again calculating site saturation separately for the different nucleation sites – austenite grain boundaries, bainite/austenite interfaces, and martensite/austenite interfaces. The model successfully represents the accelerating effect of prior martensite on bainite formation kinetics. The combined modeling and experimental results indicate that once a certain fraction of prior martensite is present (around 0.1 to 0.2 in volume fraction), bainite majorly nucleates at or near the martensite/austenite interfaces, which opens the opportunity to design new steels based on the selective segregation of alloying elements to austenite grain boundaries.

In Chapter 4, new bainitic steels for the automotive industry are designed using the accelerating effect of prior martensite investigated in Chapter 3. Bainite formation is realized in $300\,\mathrm{s}$, and hence the heat treatment can be implemented in existing modern continuous annealing lines for the production of cold rolled bare steel sheets. With a microstructure consisting of tempered martensite, bainitic ferrite, and retained austenite, the steels meet the mechanical properties required for the strongest grades of cold rolled third generation advanced high strength steels.

Chapter 5 presents preliminary results on the *in situ* observation of bainite formation by transmission electron microscopy (TEM). This observation is facilitated by using a steel with a low martensite start temperature that has a high fraction of retained austenite at room temperature. Bainite is formed by the decomposition of retained austenite when heating the sample inside the TEM to $280\,^{\circ}\mathrm{C}$. This setup, in which bainite is formed from retained austenite, avoids problems related to high temperature austenitization inside the TEM, such as the evaporation of alloying elements and thickening of the specimen [10]. High resolution *in situ* observations, such as the one preliminarily presented in Chapter 5, might enhance the understanding of the underlying mechanisms of bainite nucleation and growth and help improve the models developed in Chapters 2 and 3.

The thesis is concluded in Chapter 6 by discussing the contributions of this work to science and technology and providing recommendations for future works.

References

[1] *World Steel in Figures 2024*. worldsteel.org. 2024. url: https://worldsteel.org/data/world-steel-in-figures-2024/ (visited on 09/15/2024).

[2] N. Fonstein. *Advanced High Strength Sheet Steels: Physical Metallurgy, Design, Processing, and Properties*. Springer International Publishing, 2015. doi: 10.1007/978-3-319-19165-2.

[3] L. C. D. Fielding. "The Bainite Controversy". In: *Materials Science and Technology* 29.4 (Apr. 1, 2013), pp. 383–399. doi: 10.1179/1743284712Y.0000000157.

[4] I.-E. Benrabah, Y. Brechet, C. Hutchinson, and H. Zurob. "On the origin of carbon supersaturation in bainitic ferrite". In: *Scripta Materialia* 250 (Sept. 1, 2024), p. 116182. doi: 10.1016/j.scriptamat.2024.116182.

[5] Z. Dai, H. Chen, J. Sun, S. van der Zwaag, and J. Sun. "Carbon solute drag effect on the growth of carbon supersaturated bainitic ferrite: Modeling and experimental validations". In: *Acta Materialia* 268 (Apr. 15, 2024), p. 119791. doi: 10.1016/j.actamat.2024.119791.

[6] L. Leach, J. Ågren, L. Höglund, and A. Borgenstam. "Diffusion-Controlled Lengthening Rates of Bainitic Ferrite a Part of the Steel Genome". In: *Metallurgical and Materials Transactions A* 50.6 (June 1, 2019), pp. 2613–2618. doi: 10.1007/s11661-019-05208-x.

[7] A. Ravi, J. Sietsma, and M. Santofimia. "Exploring bainite formation kinetics distinguishing grain-boundary and autocatalytic nucleation in high and low-Si steels". In: *Acta Materialia* 105 (2016), pp. 155–164. doi: 10.1016/j.actamat.2015.11.044.

[8] S. van Bohemen and J. Sietsma. "Modeling of isothermal bainite formation based on the nucleation kinetics." In: *International Journal of Materials Research* 99 (2008), pp. 739–747. doi: 10.3139/146.101695.

[9] H. Matsuda and H. K. D. H. Bhadeshia. "Kinetics of the Bainite Transformation". In: *Proceedings: Mathematical, Physical and Engineering Sciences* 460.2046 (2004). Publisher: The Royal Society, pp. 1707–1722. doi: 10.1098/rspa.2003.1225.

[10] J. Nutter, J. Qi, H. Farahani, W. M. Rainforth, and S. van der Zwaag. "In situ TEM observations of the growth of bainitic ferrite in an Fe-0.3C-3Mn-1.5Si-0.15Mo steel". In: *Acta Materialia* 252.118924 (2023). doi: 10.1016/j.actamat.2023.118924.

2

Modeling the effect of prior austenite grain size on bainite formation kinetics

While experiments show that refining the prior austenite grain size can either accelerate or decelerate bainite formation in steels, kinetic models based on the successive nucleation of bainitic ferrite subunits can only predict an acceleration. This Chapter presents a new physically-based model for bainite kinetics assuming a displacive and diffusionless growth mechanism which is able to reproduce both faster and slower bainite formation kinetics induced by austenite grain refinement. A theoretical analysis of the model and comparison against published experimental data show that slower kinetics for smaller grains is favored as the difference between the activation energy for grain boundary and autocatalytic nucleation of bainite increases, and as the austenite grain refinement results in finer bainite sub-units. This chapter also theoretically analyzes the density of initially present potential nucleation sites for bainite and shows that the values of density used in other published bainite nucleation models are mostly an underestimation. After using physically consistent values for the density of potential nucleation sites, the apparent lengthening rate of bainite sheaves calculated using the new model is in line with experimentally measured lengthening rates.

Parts of this chapter have been published in Acta Materialia **226**, 119656 (2024) [1].

2.1. Introduction

Understanding bainite formation is of great scientific and industrial interest. Bainitic steels, especially those in which cementite formation is inhibited, combine high strength with high toughness [2]. Despite having mechanical properties that are suited for several applications, such as automotive and pipelines for gas transport, their widespread use is sometimes hindered by processing difficulties such as long transformation times. Refining the prior austenite grain size has been proposed as a strategy to shorten the heat-treatments owing to faster bainite kinetics [3], but refinement of the prior austenite grain size sometimes slows down bainite formation [4]. Even though the literature has shown these opposing effects for decades, the underlying reasons behind these contradictory observations are not yet understood. It is, however, important to understand the effect of prior austenite grain size on bainite formation kinetics to design adequate strategies to accelerate phase transformations based on microstructure control, as well as to increase the strength and toughness of steels through microstructure refinement.

These contradictory results were already shown in early reports reflecting the effect of the prior austenite grain size on bainite formation kinetics. Davenport *et al.* [5] reported that the prior austenite grain size does not have any effect on the kinetics of bainite formation. Barford *et al.* [6], however, found that smaller grains lead to faster bainite formation, and, within the limits of their study, the reaction rate was inversely proportional to the grain size. Umemoto *et al.* [7] also reported faster kinetics for smaller austenite grains and stated that the influence of the grain size on the kinetics is generally less pronounced for bainite than it is for pearlite. Graham *et al.* [8] and Chráska *et al.* [9], on the other hand, found the opposite relationship. According to their results, grain refinement led to slower bainite formation. Chráska *et al.* [9] suggested that the contradictory results in literature were caused by the different measuring techniques being used by different researchers.

These apparent discrepancies were clarified in a study by Matsuzaki and Bhadeshia [10], in which two steels with different chemical compositions exhibited opposite behaviors. Their work demonstrated that the contradictions were not due to differences in experimental setup, but that different steels are affected differently by changes in the prior austenite grain size. Later works, most of them using high resolution dilatometry, confirmed that both acceleration of bainite kinetics by grain refinement [3, 11–13] and by grain coarsening [4, 14–18] are possible.

Several mechanisms explaining the influence of the prior austenite grain size were proposed. For the acceleration of bainite kinetics by grain refinement, Barford *et al.* [6] argued that it occurs because bainite nucleates at the grain boundaries. For the acceleration of bainite kinetics with increasing grain size, Graham *et al.* [8] argued that the softer matrix of coarse-grained steels offers less resistance to the displacement caused by bainite formation.

In a unified explanation, Matsuzaki and Bhadeshia [10] linked the bainite morphology to the effect of prior austenite grain size on bainite kinetics. The re-

searchers assumed that bainite is formed by the successive nucleation of parallel plates that organize themselves in sheaves. A sheaf is created by the nucleation of a plate of bainitic ferrite at the austenite grain boundary and grows by the successive nucleation of new plates of bainitic ferrite. These sheaves, which contain several individual plates of bainitic ferrite, were treated as the basic unit for understanding the transformation kinetics. They hypothesized that when the growth of the bainitic sheaves is faster than their nucleation at the prior austenite grain boundary, larger prior austenite grain sizes show faster bainite formation. Inversely, when nucleation at grain boundaries is faster than the sheaf growth, a smaller grain size leads to faster kinetics. Their hypothesis was supported by metallographic evidence and a model based on the Johnson-Mehl-Avrami-Kolmogorov (JMAK) equation.

Later works that measured the kinetics of bainite formation at different prior austenite grain sizes [11–13] explained their results using the hypothesis from Matsuzaki and Bhadeshia [10]. In these works, it is argued that the observed acceleration of bainite formation by the refinement of the austenite grain size was because the reaction was nucleation-dominated. However, there is no evidence from microstructural characterization supporting these claims. It is thus not clear if Matsuzaki and Bhadeshia's hypothesis and observations can be extended to all steels.

Another challenge is incorporating the effect of the prior austenite grain size in models for bainite formation kinetics. Models such as the JMAK-type used by Matsuzaki and Bhadeshia [10] are versatile and valuable. However, since these models use many parameters with no explicit physical meaning, there is a strong limitation to how much they can be interpreted in terms of the fundamental theories and mechanisms of bainite formation. For that, a comprehensive, physically-based model for bainite formation is needed.

Ravi *et al.* [19] developed a model based on the diffusionless theory of bainite formation that contains only physically-based parameters and distinguishes the activation energies for grain boundary and autocatalytic nucleation. The rate of bainite formation is assumed to be controlled by the nucleation kinetics, as commonly assumed in models that adopt the diffusionless theory [2, 20, 21]. Another commonly shared assumption among diffusionless-theory–based models is that the density of initially present potential nucleation sites is inversely proportional to the austenite grain size [19]. This leads to the conclusion that the rate of bainite formation is also inversely proportional to the grain size – provided that all other parameters stay the same –, thus contradicting the experimental observations discussed above. Also, Ravi *et al.*'s [19] model does not capture the effect of prior austenite grain size on the relative contribution of autocatalysis to the overall kinetics of bainite formation, as will be shown in Section 2.3.1.

In this Chapter, Ravi *et al.*'s [19] model is modified in order to explicitly assume that the relative contributions of grain-boundary nucleation and autocatalysis are a function of the prior austenite grain size. With the proposed modifications, the new model can reproduce and explain both behaviors: the acceleration and the deceleration of bainite formation by grain refinement. The model also shows

good agreement with experimental data extracted from the literature. Also, this chapter re-analyzes and discusses important parameters of the model such as the density of potential nucleation sites and the effect of the size of the bainite sub-unit.

2.2. Model

There are two disputing theories for the mechanism of bainite formation. Although both theories agree that bainite forms by a displacive mechanism that involves carbon diffusion during nucleation, they disagree on the role of carbon diffusion during growth [2, 22, 23]. The model used in the present work adopts the theory of diffusionless growth. According to this theory, bainite plates – also called sub-units – grow without diffusion of carbon, similarly to martensite plates, until their growth is hindered by the plastic deformation of the austenitic matrix. Such plastic deformation is induced by the stresses associated with a displacive transformation. The first sub-units are assumed to nucleate at the austenite grain boundaries, and their formation is followed by successive nucleation of new sub-units at the tips of previously formed ones – a phenomenon hereafter called autocatalysis –, thus creating the characteristic sheaf morphology. The displacive character of the transformation prevents the sheaves from growing past austenite grain boundaries.

The assumption of nucleation with carbon redistribution results in a thermodynamical requirement given by [2]:

$$\Delta G_{\mathrm{m}} \leq G_{\mathrm{N}}. \tag{2.1}$$

The requirement from Equation (2.1) states that the maximum change in Gibbs free energy for ferrite nucleation under paraequilibrium, ΔG_{m}, should be less than the universal nucleation function, G_{N}. The function G_{N} is an empirical function that represents the minimum driving force necessary for bainite nucleation. It is considered to be dependent only on temperature and is calculated as

$$G_{\mathrm{N}} = K_1 \left(T - 273.18\right) - K_2, \tag{2.2}$$

where K_1 and K_2 are empirical constants equal to $3.637\,\mathrm{J\,mol^{-1}\,K^{-1}}$ and $2540\,\mathrm{J\,mol^{-1}}$, respectively, and T is the temperature in Kelvin [2]. The temperature in which ΔG_{m} and G_{N} are equal for a certain composition is called T_{h}. In addition to the nucleation, diffusionless growth also needs to be possible for bainite formation, which gives rise to the condition expressed by Equation (2.3):

$$\Delta G^{\gamma\rightarrow\alpha} \leq G_{\mathrm{SB}}, \tag{2.3}$$

in which $\Delta G^{\gamma\rightarrow\alpha}$ is the difference in Gibbs free energy between austenite and ferrite with same chemical composition, and G_{SB} is the stored energy of bainite, assumed to be $400\,\mathrm{J\,mol^{-1}}$.

The temperature in which $\Delta G^{\gamma\rightarrow\alpha}$ is equal to $-G_{\mathrm{SB}}$ is called T_0'. Also, the temperature in which $\Delta G^{\gamma\rightarrow\alpha}$ is zero is called T_0 [2]. According to this theory, bainite nucleation and growth can only happen in temperatures below both T_0' and T_{h}.

2.2.1. Overview of Ravi et al.'s model

The model developed by Ravi *et al.* [19] is based on the kinetics of bainite nucleation, which is split into two components: grain boundary nucleation and autocatalysis. Grain boundary nucleation is the one that takes place at the prior austenite grain boundaries (AGB). Autocatalysis, or autocatalytic nucleation, is the one that takes place at the interface between the bainitic ferrite and the austenite (B/A interface). In this manuscript, a brief overview of this model is provided for better understanding of the contributions proposed.

The overall bainite nucleation rate, $\mathrm{d}N/\mathrm{d}t$, is given by the sum of the nucleation rates of these two components, respectively $\mathrm{d}N_{\mathrm{AGB}}/\mathrm{d}t$ and $\mathrm{d}N_{\mathrm{BA}}/\mathrm{d}t$, according to Equation (2.4)

$$\frac{\mathrm{d}N}{\mathrm{d}t} = \frac{\mathrm{d}N_{\mathrm{AGB}}}{\mathrm{d}t} + \frac{\mathrm{d}N_{\mathrm{BA}}}{\mathrm{d}t}. \tag{2.4}$$

The nucleation rate at the prior austenite grain boundaries is calculated using Equation (2.5)

$$\frac{\mathrm{d}N_{\mathrm{AGB}}}{\mathrm{d}t} = \frac{kT}{h} n_{\mathrm{AGB}} \exp\left(-\frac{Q_{\mathrm{AGB}}}{RT}\right), \tag{2.5}$$

where k is Boltzmann's constant, T is the temperature in Kelvin, h is Planck's constant, n_{AGB} is the density of potential nucleation sites for nucleation at prior austenite grain boundaries at time t, Q_{AGB} is the activation energy for nucleation at prior austenite grain boundaries, and R is the universal gas constant. The density of potential nucleation sites was derived by van Bohemen *et al.* [21] based on Magee's analysis of the nucleation of martensite [24], and is calculated as

$$n_{\mathrm{AGB}} = \frac{6\delta}{d_\gamma} \frac{\alpha_{\mathrm{m}}}{V_{\mathrm{b}}} \left(T_{\mathrm{h}} - T\right) f_\gamma, \tag{2.6}$$

where δ is the effective grain size thickness, taken as $1\,\mathrm{nm}$, α_{m} is the exponent from the Koistinen-Marburger equation for the given chemical composition, d_γ is the prior austenite grain size, V_{b} is the volume of the bainite sub-unit, and f_γ is the fraction of austenite available for transformation.

Similarly, the nucleation rate for autocatalysis is calculated as

$$\frac{\mathrm{d}N_{\mathrm{BA}}}{\mathrm{d}t} = \frac{kT}{h} n_{\mathrm{BA}} \exp\left(-\frac{Q_{\mathrm{BA}}}{RT}\right), \tag{2.7}$$

where

$$n_{\mathrm{BA}} = \frac{6\delta}{d_\gamma} \frac{\alpha_{\mathrm{m}}}{V_{\mathrm{b}}} \left(T_{\mathrm{h}} - T\right) f_\gamma f, \tag{2.8}$$

where n_{BA} is the density of potential nucleation sites for autocatalytic bainite formation, Q_{BA} is the activation energy for autocatalytic nucleation of bainite, and f is the total fraction of bainite.

Immediately after its nucleation and diffusionless growth, a bainite sub-unit is supersaturated in carbon. The excess carbon can induce the precipitation of

carbides and/or partition to the austenite. As the carbon content of austenite increases as a result of said partitioning, the composition-dependent limiting temperatures for bainite formation, T_h and T'_0, decrease, and are calculated as

$$T_h = T_{h\overline{X}} - C_1 f\left(\frac{\overline{X} - X_b}{1-f}\right), \tag{2.9}$$

$$T'_0 = T'_{0\overline{X}} - C_1 f\left(\frac{\overline{X} - X_b}{1-f}\right), \tag{2.10}$$

where $T_{h\overline{X}}$ and $T'_{0\overline{X}}$ are respectively T_h and T'_0 for the nominal carbon content, C_1 and C_2 are proportionality constants, f is the volume fraction of bainite, $\overline{X}$ is the nominal carbon atomic fraction, and X_b is the atomic fraction of carbon that stays in the bainite, whether in solid solution, trapped at defects, or in the form of carbides.

A lower T_h implies a smaller undercooling for bainite nucleation, which results in a higher activation energy. The activation energies are then calculated as

$$Q_{AGB} = Q_{AGB\overline{X}} - K_\Gamma C_1 f\left(\frac{\overline{X} - X_b}{1-f}\right), \tag{2.11}$$

$$Q_{BA} = Q_{BA\overline{X}} - K_\Gamma C_1 f\left(\frac{\overline{X} - X_b}{1-f}\right), \tag{2.12}$$

where $Q_{AGB\overline{X}}$ and $Q_{BA\overline{X}}$ are the respectively initial activation energies for grain boundary and autocatalytic nucleation when the carbon content in the austenite is the nominal carbon content of the steel, Q_{AGB} and Q_{BA} are respectively the instantaneous activation energy for grain boundary and autocatalytic nucleation, considering carbon enrichment of the austenite, and K_Γ is a proportionality constant [25].

The fraction of available austenite decreases both because it decomposes during bainite formation, and because carbon enrichment will decrease T'_0, thus hindering the activation of some potential nucleation sites. At any given time, the fraction of austenite available for transformation is the given by

$$f_\gamma = (1-f)\left(\frac{T'_0 - T}{T'_{0\overline{X}} - T}\right). \tag{2.13}$$

Finally, the nucleation rate is multiplied by the volume of the bainite sub-unit in order to calculate the rate of bainite formation, $\mathrm{d}f/\mathrm{d}t$:

$$\frac{\mathrm{d}f}{\mathrm{d}t} = \frac{\mathrm{d}N}{\mathrm{d}t} V_b. \tag{2.14}$$

2.2.2. Proposed modification of Ravi et al.'s model

In the model developed by Ravi *et al.*, the fraction of bainite nucleated at grain boundaries and by autocatalysis are distinguished. At any given stage of the transformation, the relative contribution of the two nucleation sites to the overall rate of bainite formation is determined solely by the difference in their activation energies. However, it is reasonable to expect that microstructural features, such as the prior austenite grain size and the size of the bainite sub-unit, would also influence the relative contribution of grain boundary nucleation and autocatalysis to the overall kinetics. Also, the austenite grain size and the size of the bainite sub-unit should limit the total fraction of bainite that can nucleate at each site. In order to tackle both aspects, the geometrical assumption illustrated in Figure 2.1 is proposed.

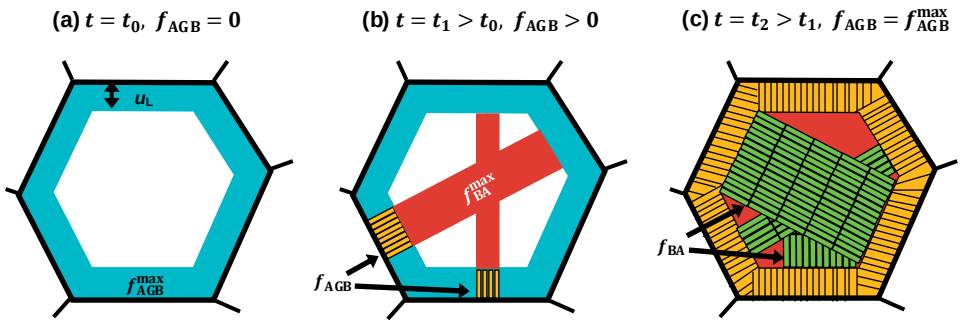

Figure 2.1. Illustration representing the proposed geometrical assumption for bainite formation. A single austenite grain, at different times t, is shown. **a.** The maximum fraction of bainite that can nucleate the austenite grain boundary, f_{AGB}^{max}, is given by the blue-shaded area, and is defined by the length of the bainite sub-unit, u_L, and the grain size. **b.** After some fraction of bainite is formed by grain boundary nucleation, marked as f_{AGB}, new plates of bainite can nucleate by autocatalysis and occupy the red-shaded area indicated by f_{BA}^{max}. **c.** When $f_{AGB} = f_{BA}^{max}$, all the grain interior is available for transformation, such that $f_{AGB}^{max} + f_{BA}^{max} = 1$. The green plates indicated by the arrows and marked as f_{BA} represent the fraction of bainite nucleated by autocatalysis at time t_2.

Figure 2.1a shows that at the start of bainite formation only grain boundary nucleation sites are present. The maximum fraction of bainite that can be formed from these nucleation sites, f_{AGB}^{max}, depends on the prior austenite grain size, d_γ, and on the length of the bainite sub-unit, u_L. This maximum fraction is given by Equation (2.15):

$$f_{AGB}^{max} = Z\frac{u_L}{d_\gamma}, \tag{2.15}$$

where Z is a shape factor equal to 3.35 for a tetrakaidecahedron-shaped austenite grain [26].

Similar to f_{AGB}^{max}, the maximum fraction of bainite that can be formed by autocatalysis, f_{BA}^{max}, can be defined. However, unlike f_{AGB}^{max}, f_{BA}^{max} varies during

the transformation. At the beginning of the transformation, when no bainite is formed, it is not possible to have autocatalysis. Figure 2.1b shows that after the first sub-unit of bainite is formed at the austenite grain boundary, new nucleation sites are created at the B/A interface, and autocatalysis can start. Considering that the first bainite sub-unit nucleated at the grain boundary can give rise to $C_{\mathrm{A,AGB}}$ bainite sub-units by autocatalysis, the change in $f_{\mathrm{BA}}^{\mathrm{max}}$ promoted by a change in the fraction of bainite nucleated at the grain boundaries, f_{AGB}, can be calculated by Equation (2.16)

$$\mathrm{d}f_{\mathrm{BA}}^{\mathrm{max}} = C_{\mathrm{A,AGB}} \left(1 - f_{\mathrm{BA}}^{\mathrm{max}}\right) \mathrm{d}f_{\mathrm{AGB}}, \tag{2.16}$$

where $\mathrm{d}f_{\mathrm{BA}}^{\mathrm{max}}$ is an infinitesimal change to $f_{\mathrm{BA}}^{\mathrm{max}}$ induced by $\mathrm{d}f_{\mathrm{AGB}}$, an infinitesimal change to f_{AGB}. The term $\left(1 - f_{\mathrm{BA}}^{\mathrm{max}}\right)$ is inserted to account for hard impingement. Integrating both sides of Equation (2.16) with the boundary conditions of $f_{\mathrm{BA}}^{\mathrm{max}} = 0$ for $f_{\mathrm{AGB}} = 0$, and $f_{\mathrm{BA}}^{\mathrm{max}} = 1 - f_{\mathrm{AGB}}^{\mathrm{max}}$ for $f_{\mathrm{AGB}} = f_{\mathrm{AGB}}^{\mathrm{max}}$ (Figure 2.1c), results in Equations (2.17) and (2.18):

$$C_{\mathrm{A,AGB}} = \frac{\ln\left(f_{\mathrm{AGB}}^{\mathrm{max}}\right)}{f_{\mathrm{AGB}}^{\mathrm{max}}}, \tag{2.17}$$

$$f_{\mathrm{BA}}^{\mathrm{max}} = 1 - \exp\left(\frac{f_{\mathrm{AGB}}}{f_{\mathrm{AGB}}^{\mathrm{max}}} \ln f_{\mathrm{AGB}}^{\mathrm{max}}\right). \tag{2.18}$$

The boundary condition of $f_{\mathrm{BA}}^{\mathrm{max}} = 1 - f_{\mathrm{AGB}}^{\mathrm{max}}$ when $f_{\mathrm{AGB}} = f_{\mathrm{AGB}}^{\mathrm{max}}$ is not necessarily true. Sheaves of bainite may grow until they are halted by the austenite grain boundaries, such that the sheaves containing the plates marked as f_{BA} in Figure 2.1c actually occupy some of the area initially marked as $f_{\mathrm{AGB}}^{\mathrm{max}}$. The proposed boundary condition is then a simplification of a more complex problem, and it was chosen so that $f_{\mathrm{AGB}}^{\mathrm{max}} + f_{\mathrm{BA}}^{\mathrm{max}}$ tends towards unity as the reaction progresses.

After having defined $f_{\mathrm{AGB}}^{\mathrm{max}}$ and $f_{\mathrm{BA}}^{\mathrm{max}}$, the two terms can be combined with Equation (2.13), which includes carbon enrichment of the austenite, and used for calculating the density of potential nucleation sites at the austenite grain boundaries, n_{AGB}, and at the bainite/austenite interfaces, n_{BA}, at any given time t, as

$$n_{\mathrm{AGB}} = n_{\mathrm{S,AGB}} S_{\mathrm{AGB}} \left(1 - \frac{f_{\mathrm{AGB}}}{f_{\mathrm{AGB}}^{\mathrm{max}}}\right) \left(\frac{T_0' - T}{T_{0\overline{X}}' - T}\right), \tag{2.19}$$

$$n_{\mathrm{BA}} = n_{\mathrm{S,BA}} S_{\mathrm{BA}} \left(1 - \frac{f_{\mathrm{BA}}}{f_{\mathrm{BA}}^{\mathrm{max}}}\right) \left(\frac{T_0' - T}{T_{0\overline{X}}' - T}\right), \tag{2.20}$$

where $n_{\mathrm{S,AGB}}$ and $n_{\mathrm{S,BA}}$ are respectively the number of potential nucleation sites per unit area of austenite grain boundary and bainite/austenite interface, later discussed in Section 2.4.1, and S_{AGB} and S_{BA} are the area of the austenite grain boundaries and bainite/austenite interfaces per unit volume, respectively. The autocatalytic nucleation of bainite is commonly considered to take place at the tip of previously formed bainitic ferrite sub-units [2]. Thus, instead of considering the whole bainite/austenite interface area for calculating S_{BA}, only the interface

area of the tip of the sub-units is considered. The terms can then be calculated as

$$S_{\mathrm{AGB}} = \frac{Z}{d_\gamma}, \tag{2.21}$$

$$S_{\mathrm{BA}} = \frac{f}{u_{\mathrm{L}}}. \tag{2.22}$$

While the density of potential nucleation sites $n_{\mathrm{S,AGB}}$ and $n_{\mathrm{S,BA}}$ and the interface area of prior austenite grain boundaries, S_{AGB}, are constant, the interface area of the sub-units tip, S_{BA}, depends on the fraction of bainite existing at given time. In order to calculate the rate of bainite nucleation, Equations (2.19) and (2.20) are used in Equations (2.5) and (2.7), changing the way in which Ravi *et al.* calculated the number density of potential nucleation sites. By comparing Equations (2.19) and (2.20) with Equations (2.6), (2.8) and (2.13) it can be seen that in the proposed model the saturation of nucleation sites for grain boundary nucleation and autocatalysis are distinguished through the terms $1 - f_{\mathrm{AGB}}/f_{\mathrm{AGB}}^{\mathrm{max}}$ and $1 - f_{\mathrm{BA}}/f_{\mathrm{BA}}^{\mathrm{max}}$. In Ravi's model, site saturation is treated as if it were equal for both grain boundary and autocatalysis by the single term $1 - f$.

2.2.3. Input parameters

Most of the input parameters needed for the model can be measured, calculated from empirical equations, or extracted from thermodynamic databases as described by Ravi *et al.* [19]. However, because of the modifications proposed here, four new input parameters are needed: $n_{\mathrm{S,AGB}}$, $n_{\mathrm{S,BA}}$, V_{b}, and u_{L}. Note that although V_{b} appears in the equations from Ravi *et al.* [19], it gets cancelled out eventually – see Equations (2.5) to (2.8) and (2.14). For the purpose of the present work, both $n_{\mathrm{S,AGB}}$ and $n_{\mathrm{S,BA}}$ were taken as $10^{16}\,\mathrm{m}^{-2}$, following van Bohemen [27]. V_{b} is calculated as $u_{\mathrm{T}} \cdot u_{\mathrm{W}} \cdot u_{\mathrm{L}}$, where u_{T} and u_{W} are the thickness and the width of the bainite sub-unit. In the present work, the sub-unit was considered to be a plate with $u_{\mathrm{W}} = u_{\mathrm{L}} = 6 \cdot u_{\mathrm{T}}$, following Azuma *et al.* [28]. The values chosen for those parameters are discussed in Section 2.4.1. The fraction of carbon trapped in the bainite, X_{b}, and the activation energies, $Q_{\mathrm{AGB}\overline{X}}$ and $Q_{\mathrm{BA}\overline{X}}$, are fitting parameters, as in Ravi *et al.*'s model.

2.3. Results

This section starts with a theoretical analysis of the model, focusing on the predicted influence of the prior austenite grain size on the bainite formation, and the differences with respect to the results obtained following the model developed by Ravi *et al.* [19]. Then, the model is validated by comparison against the experimental data.

2.3.1. Theoretical analysis of the model

The model was first theoretically analyzed by simulating kinetic curves of bainite formation using hypothetical input parameter values that result in realistic

transformation rates. Then, the effect of prior austenite grain size was also theoretically studied for different model input parameter values. All the parameters used in the simulations of this section are given in the graphs and captions of Figures 2.2 and 2.3.

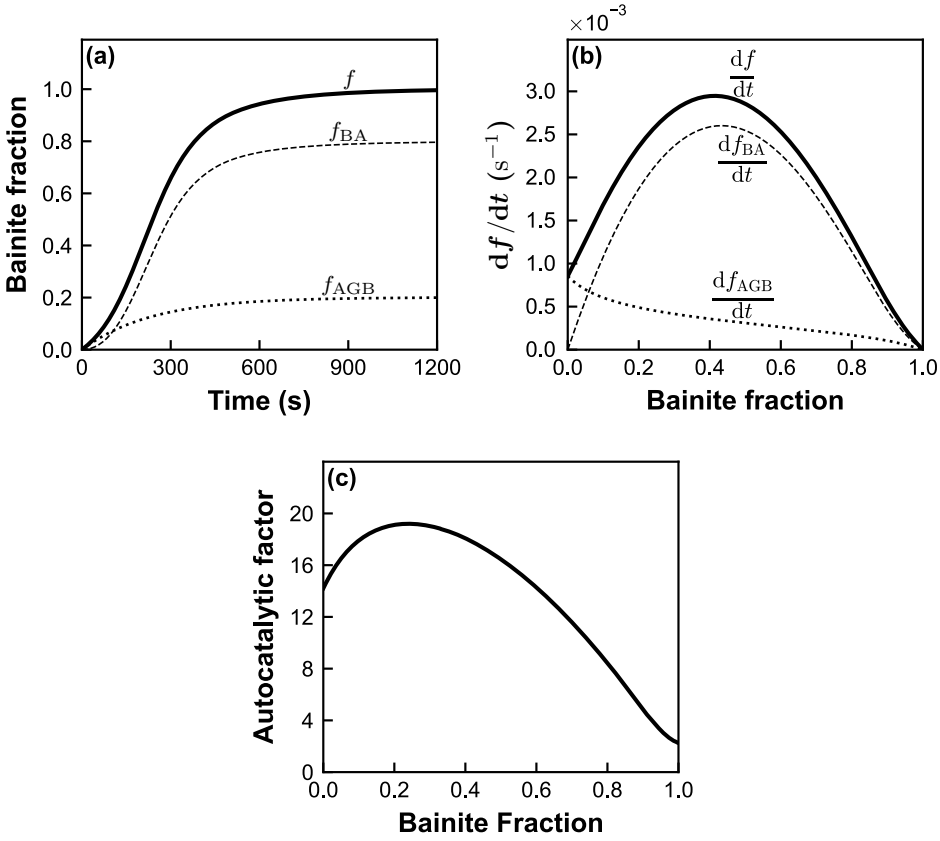

Figure 2.2. Simulated kinetics of bainite formation considering the parameters: $T = 300\,°C$, $d_\gamma = 10\,\mu m$, $Q_{AGB\overline{X}} = 200\,kJ\,mol^{-1}$, $Q_{BA\overline{X}} = 195\,kJ\,mol^{-1}$, $u_T = 0.100\,\mu m$, and $X_b = \overline{X}$. **a.** Fraction of bainite over time, distinguishing the total fraction, f, the fraction nucleated by autocatalysis, f_{BA}, and the fraction nucleated at austenite grain boundaries, f_{AGB}. **b.** Rate of bainite formation, also showing the total rate and distinguishing individual components by nucleation site. **c.** Autocatalytic factor calculated by Equation (2.23)

Figure 2.2 shows the simulated kinetics of bainite formation during isothermal holding. The simulated curve follows a sigmoidal-like shape, resembling the experimentally measured curves of bainite formation. Because the model distinguishes the fraction of bainite per nucleation site, the curves for bainite nucleated at the austenite grain boundaries and by autocatalysis can be calculated individually, as shown in Figure 2.2a. The curve for f_{AGB} follows a logarithmic shape approaching a limiting value. For the case presented in Figure 2.2, since

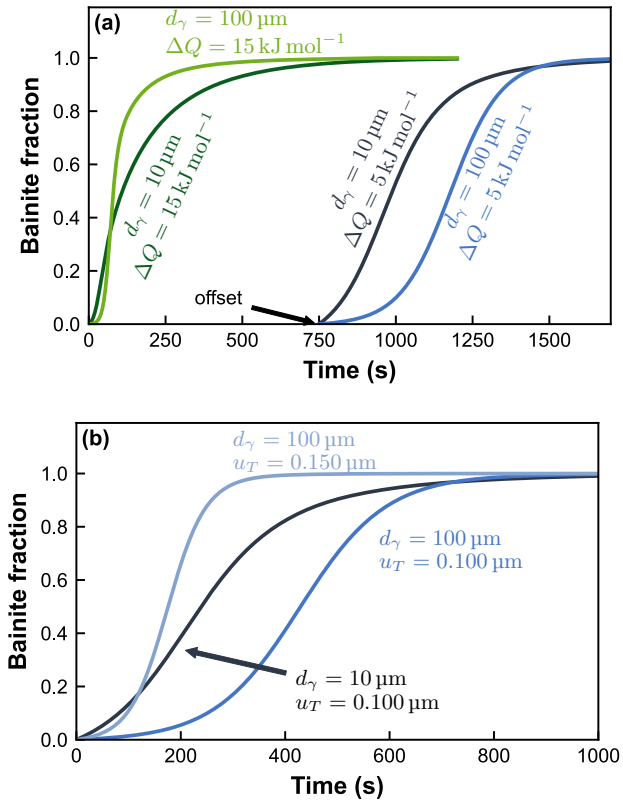

Figure 2.3. Simulated curves showing the predicted effect of varying the prior austenite grain size from 10 to 100 µm on the bainite formation kinetics. The fixed parameters used were $T = 300\,^{\circ}C$, $Q_{AGB\overline{X}} = 200\,kJ\,mol^{-1}$, and $X_b = \overline{X}$, while $\Delta Q(Q_{AGB} - Q_{BA})$ or u_T were varied. **a.** On the left, simulated curves for $\Delta Q = 15\,kJ\,mol^{-1}$. On the right and offset by 750 s, simulated curve for $\Delta Q = 5\,kJ\,mol^{-1}$. In all cases, u_T was taken as $0.100\,\mu m$. **b.** Curves for $\Delta Q = 5\,kJ\,mol^{-1}$. For $d_\gamma = 10\,\mu m, u_T = 0.100\,\mu m$. For $d_\gamma = 100\,\mu m$, two curves are shown: one considering the thickness of the sub-unit does not change by varying the grain size, and one considering that because of the increase in grain size the thickness of the sub-unit increases to $0.150\,\mu m$.

there is no carbon enrichment of the austenite ($X_b = \overline{X}$), the limiting value for f_{AGB} is given by f_{AGB}^{max}. The f_{BA} curve, on the other hand, follows a sigmoidal-like shape. For the present case, in which there is no carbon enrichment, f_{BA} approaches $1 - f_{AGB}^{max}$, so that the total fraction of bainite, f, tends towards unity.

Figure 2.2b shows the rate of bainite formation distinguished by nucleation site. At the beginning of the transformation, the rate of bainite formation comes from grain boundary nucleation only. As the reaction progresses, potential nucleation sites are created at the bainite/austenite interface, and autocatalysis starts con-

tributing to the total rate of bainite formation.

Many of the models that adopt the diffusionless theory of bainite formation use a so-called autocatalytic factor [19–21]. The autocatalytic factor, λ, is used to relate the rate of bainite nucleation at the grain boundaries, $\dot{N}_{\mathrm{AGB}}$, to the nucleation rate by autocatalysis, $\dot{N}_{\mathrm{BA}}$, through the general expression $\dot{N}_{\mathrm{BA}} = \lambda f \dot{N}_{\mathrm{AGB}}$. In the present model, no autocatalytic factor was used. However, by isolating λ in the general formula present in other models, an autocatalytic factor can be derived and calculated using the outcomes of the present model according to Equation (2.23).

$$\lambda = \frac{1}{f}\frac{\dot{N}_{\mathrm{BA}}}{\dot{N}_{\mathrm{AGB}}}. \tag{2.23}$$

The calculated autocatalytic factor is shown in Figure 2.2c. Unlike in other bainite models, where it is usually taken as a value to be fitted, in the present model the autocatalytic factor is an outcome. The autocatalytic factor is shown to depend on the interplay between parameters such as the prior austenite grain size, size of the bainite sub-unit, and the difference between the activation energies Q_{AGB} and Q_{BA}, which in turn depends on the chemical composition, temperature, and dislocations created during bainite formation. Also, the factor is not constant but varies throughout the whole transformation.

The predicted effect of the prior austenite grain size on the bainite formation kinetics is presented in Figure 2.3 . Depending on the difference between the activation energies for grain boundary and autocatalytic nucleation, $\Delta Q = Q_{\mathrm{AGB}} - Q_{\mathrm{BA}}$, and on the variation of the thickness of the bainite sub-unit as a function of the prior austenite grain size, different behaviors are observed.

When the activation energies Q_{AGB} and Q_{BA} were considered to differ by only $5\,\mathrm{kJ\,mol^{-1}}$, a smaller grain size led to faster bainite formation. But when Q_{BA} was smaller than Q_{AGB} by $15\,\mathrm{kJ\,mol^{-1}}$, a larger prior austenite grain size led to a faster bainite formation (see Figure 2.3). This indicates that as the difference ΔQ between activation energies increases, the kinetics of bainite formation by autocatalysis tends to overcome the kinetics of bainite formation at austenite grain boundaries, ultimately leading to the observation of a faster bainite formation for larger prior austenite grain sizes.

In Figure 2.3a, u_{T} was considered to be independent of the prior austenite grain size. But in reality u_{T} might be different for different austenite grain sizes. In the present model, the nucleation rate is multiplied by the volume of the sub-unit to yield the rate of bainite formation, and thus a larger sub-unit speeds up the transformation. This possibility was explored in the simulation shown in Figure 2.3b.

In Figure 2.3b, the two curves from Figure 2.3a corresponding to $\Delta Q = 5\,\mathrm{kJ\,mol^{-1}}$, for which smaller austenite grains led to a faster transformation, are shown again and complemented by a third simulated curve. In the latter, it is considered that by increasing the prior austenite grain size from 10 to $100\,\mu\mathrm{m}$ the thickness of the sub-unit increases from 0.100 to $0.150\,\mu\mathrm{m}$. As a result, the effect of the grain size was reversed, and a larger prior austenite grain size resulted in a faster overall bainite formation.

The theoretical analysis described in this section indicates that the proposed

model is capable of reproducing both the acceleration as well as the deceleration of bainite formation by the refinement of the prior austenite grain size. To our knowledge, and based on our analysis of other published models of bainite formation [19, 21, 28–30], the model proposed here is the only one that is able to simulate these two possible effects.

None of the results shown in this section considered the carbon enrichment of the austenite. However, repeating the simulations considering the carbon enrichment of austenite did not reveal any influence of the carbon enrichment of the austenite on the effect of the prior austenite grain size on bainite formation kinetics (see Appendix A and Figures A.1 to A.3).

2.3.2. Comparison to Ravi et al.'s model

The predicted effect of the prior austenite grain size was also analyzed for Ravi *et al.*'s model, and a comparison between their model and the model from the present work is shown in Figure 2.4. The simulations presented in this section use parameters similar to the ones used in Section 2.3.1 for the proposed model, and parameters for Ravi *et al.*'s model that led to similar kinetics. All parameters and values are given in the graphs and caption of Figure 2.4.

By comparing Figure 2.4a,c with Figure 2.4b,d, it is evident that the model from Ravi *et al.* predicts a much greater influence of the prior austenite grain size on the kinetics of bainite formation. In the present model, the effect of grain size depends on factors such as the difference in the activation energies and the size of the bainite sub-unit. Figure 2.4a,c thus represent only the specific case for the conditions used in the simulation. In Ravi *et al.*'s model, the rate of bainite formation is always inversely proportional to the prior austenite grain size, given that the activation energies are independent of the grain size. Hence, the trends shown in Figure 2.4b,d are general for Ravi *et al.*'s model and are is the only possible outcome, irrespective of the parameters used in the simulation.

As the rate of bainite nucleation at grain boundaries and by autocatalysis are distinguished in both models, it is possible to calculate the final fraction of grain boundary nucleated and autocatalytically nucleated bainite at the end of the transformation, and then calculate their ratio. Figure 2.4e shows this ratio as a function of the prior austenite grain size for both models. For the model developed in the present work, the ratio increases linearly with the prior austenite grain size, meaning that autocatalysis becomes more important for larger austenite grains. On the other hand, in the model from Ravi *et al.*, the ratio is constant with respect to the austenite grain size.

The linear relationship observed in Figure 2.4e was achieved in the present model by the introduction of the parameters $f_{\mathrm{AGB}}^{\max}$ and $f_{\mathrm{BA}}^{\max}$, both a function of the prior austenite grain size and the length of the bainite sub-unit. The linearity is a direct consequence of the assumption that f_{AGB} at the end of the transformation is proportional to the interface area of the prior austenite grain boundaries, S_{AGB}, which in turn is inversely proportional to the prior austenite grain size, d_γ – Equations (2.15) and (2.21). Such a relationship is derived in Appendix A.2. The two parameters control the relative contribution of grain boundary nucleation

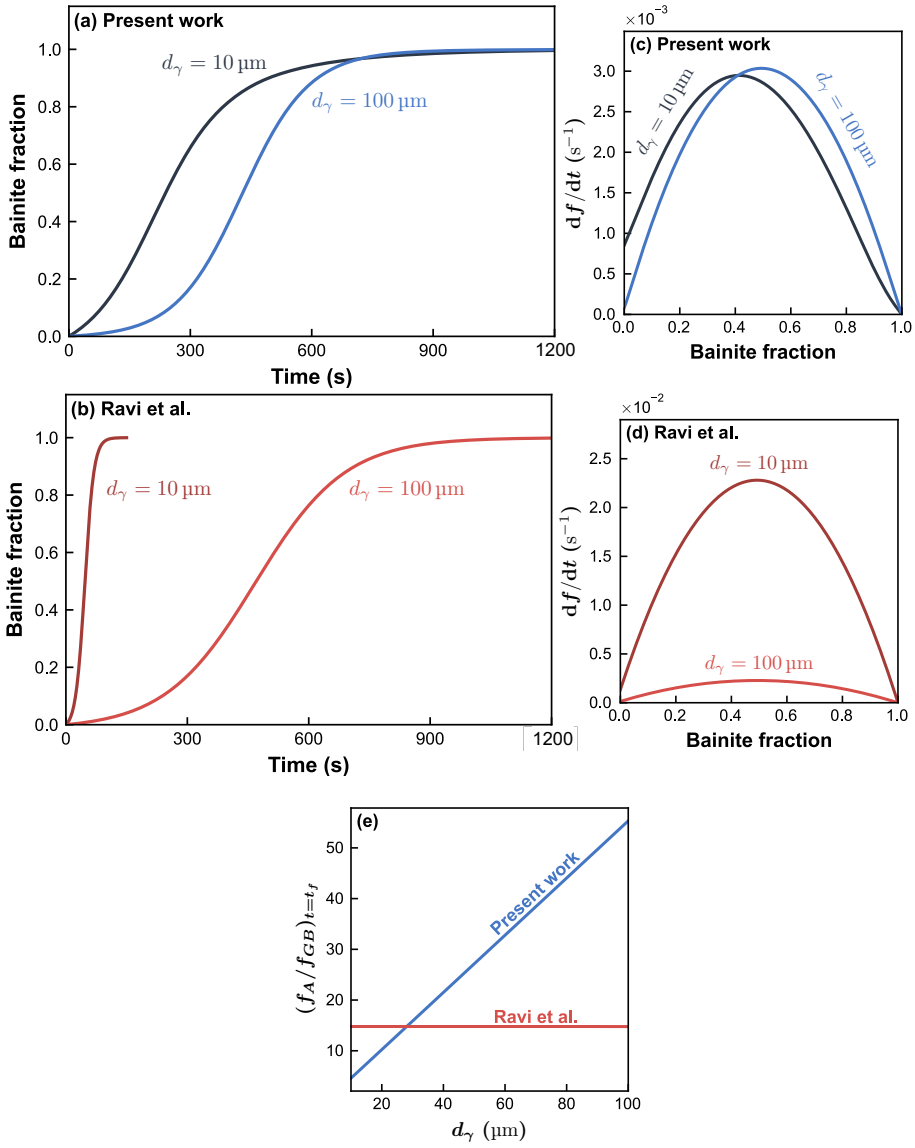

Figure 2.4. Effect of the prior austenite grain size on bainite formation according to the present model and Ravi *et al.*'s model. In all cases $T = 300\,^\circ\mathrm{C}$ and $X_\mathrm{b} = \overline{X}$ were considered. For the simulations using the model from the present work, $Q_{\mathrm{AGB}\overline{X}} = 200\,\mathrm{kJ\,mol^{-1}}$, $Q_{\mathrm{BA}\overline{X}} = 195\,\mathrm{kJ\,mol^{-1}}$, and $u_\mathrm{T} = 0.100\,\mu\mathrm{m}$ were used. In the simulations using Ravi *et al.*'s model, $Q_{\mathrm{AGB}\overline{X}} = 145\,\mathrm{kJ\,mol^{-1}}$, $Q_{\mathrm{BA}\overline{X}} = 125\,\mathrm{kJ\,mol^{-1}}$, $T_\mathrm{h} = 577\,^\circ\mathrm{C}$, and $\alpha_\mathrm{m} = 0.011\,\mathrm{K^{-1}}$ were used. **a-d.** Simulated bainite fraction as a function of time and the rate of bainite formation as a function of bainite fraction for both models and for $d_\gamma = 10\,\mu\mathrm{m}$ and $d_\gamma = 100\,\mu\mathrm{m}$. **e.** Ratio between the fraction of autocatalytic nucleated and grain boundary nucleated bainite at the end of the transformation as a function of prior austenite grain size for both models.

and autocatalysis, and also limit their overall fraction. In the model from Ravi *et al.*, on the other hand, there is no limit on the fraction of grain boundary nor autocatalytic nucleated bainite, and their relative contribution does not depend on the austenite grain size nor on the bainite sub-unit size. In Ravi *et al.*'s model, at any given point of the transformation, the ratio between the nucleation rates is

$$\frac{\mathrm{d}f_{\mathrm{BA}}/\mathrm{d}t}{\mathrm{d}f_{\mathrm{AGB}}/\mathrm{d}t} = f \exp\left(\frac{\Delta Q}{RT}\right), \tag{2.24}$$

which shows that the relative contribution of each type of nucleation site is determined solely by the difference in the activation energies and does not include the effect of the prior austenite grain size.

2.3.3. Comparison against experiments

Experimental data on the kinetics of bainite formation during isothermal holding measured by dilatometry was used to validate the present model. The chemical composition, prior austenite grain size, isothermal holding temperature, thickness of the bainite sub-unit and references to the original source of the data are in Table 2.1, alongside the given nomenclature. The curves of bainite fraction as a function of time were used for optimizing the fitting parameters ($Q_{\mathrm{AGB}\overline{X}}$, $Q_{\mathrm{BA}\overline{X}}$, and X_{b}), and the implementation of the differential evolution algorithm [31] in SciPy and Lmfit [32, 33] was used to find the best values.

In order to investigate the effect of the transformation temperature, Steels A and B, which were treated at holding temperatures in the range of 370 to $500\,^{\circ}\mathrm{C}$, were first fitted to the model. Figure 2.5a,b show that the present model was able to match well the experimentally observed data for both steels and at every temperature. The activation energies extracted from the fitting are shown in Figure 2.5c,d and listed in Table 2.1, and range from 220 to $270\,\mathrm{kJ\,mol^{-1}}$. Both $Q_{\mathrm{AGB}\overline{X}}$ and $Q_{\mathrm{BA}\overline{X}}$ increase linearly with the temperature.

The optimal fitted values for the activation energies bear uncertainties related to the fitting procedure itself and to the uncertainty in the input parameters. The uncertainty related to the fitting procedure is relatively small and estimated as less than $0.1\,\mathrm{kJ\,mol^{-1}}$. The uncertainty related to the input parameters, however, is much higher. By assuming there is a $10\,\%$ uncertainty in the values for the prior austenite grain size and for the sub-unit thickness, and a $50\,\%$ uncertainty in the sub-unit aspect ratio, the uncertainty for $Q_{\mathrm{AGB}\overline{X}}$ and $Q_{\mathrm{BA}\overline{X}}$ were estimated as $4\,\%$ and $2\,\%$, respectively. The estimation of the uncertainty in the activation energies is detailed in Appendix A.3.

Steels C and D were chosen for analyzing the effect of the prior austenite grain size because they show opposite behaviors. In the case of Steel C, bainite formation was accelerated by increasing the prior austenite grain size, while for Steel D the reaction was accelerated by decreasing the grain size. For each steel, samples with different grain sizes were treated isothermally at the same holding temperature.

Figure 2.6 shows the experimental and modeled fraction of bainite as a function of time for the steels C and D. Because all treatments for a given steel were

Table 2.1. Chemical composition, prior austenite grain size (d_γ), temperature of bainite formation (T), thickness of the bainite sub-unit (u_T), and model outputs ($Q_{\mathrm{AGB}\overline{X}}$, $Q_{\mathrm{BA}\overline{X}}$, and X_b) of the steels used for the validation. The grain size of steel A is not reported in the original paper [30] and thus the value estimated by [21] is used. The thickness of the bainite sub-unit for steels A and B were not reported, and thus were calculated using the model from [34] for steel A and from [35] for steel B. $Q_{\mathrm{AGB}\overline{X}}$, $Q_{\mathrm{BA}\overline{X}}$ and X_b result from fitting the data to the model and assuming that $Q_{\mathrm{AGB}\overline{X}}$ and $Q_{\mathrm{BA}\overline{X}}$ are independent of d_γ.

Steel	Chemical composition	d_γ	T	u_T	$Q_{\mathrm{AGB}\overline{X}}$	$Q_{\mathrm{BA}\overline{X}}$	X_b
	wt.%	µm	°C	µm	kJ/mol	kJ/mol	at.frac.
A[30]	Fe-0.53C-0.69Mn-0.29Cr-0.03Al	140	500	0.327	259	261	0.0241
		140	450	0.260	244	242	0.0241
		140	425	0.227	238	232	0.0241
		140	400	0.194	224	225	0.0241
		140	375	0.160	218	217	0.0240
B[36]	Fe-0.29C-2.39Mn-1.76Si	22	480	0.178	267	251	0.0060
		22	450	0.152	253	243	0.0077
		22	420	0.131	244	232	0.0089
		22	390	0.113	228	225	0.0086
		22	370	0.102	220	218	0.0096
C[17]	Fe-0.25C-1.6Mn-1.25Si-1Cr-0.3Mo	16	420	0.255	259	243	0.0114
		20	420	0.296	259	243	0.0096
		76	420	0.353	259	243	0.0079
		157	420	0.416	259	243	0.0075
D[15]	Fe-0.51C-0.83Mn-1.72Si-0.98Cr-0.25Mo-0.56Co-0.60Ni-0.04Nb	33	280	0.297	202	200	0.0068
		50	280	0.297	202	200	0.0068
		72	280	0.297	202	200	0.0068
		93	280	0.297	202	200	0.0068

performed at the same holding temperature, the values of $Q_{\mathrm{AGB}\overline{X}}$ and $Q_{\mathrm{BA}\overline{X}}$ were fitted considering that they are the same irrespective of the prior austenite grain size. The modeled curves were able to reproduce the opposing effects of the austenite grain size seen in both steels.

In the case in which bainite formation was faster for a larger prior austenite grain size (Steel C, Figure 2.6a), the activation energy for grain boundary nucleation was $16\,\mathrm{kJ\,mol^{-1}}$ higher than the activation energy for autocatalytic nucleation. For Steel D (Figure 2.6b), which shows the opposite effect, the difference between the activation energies was only $2\,\mathrm{kJ\,mol^{-1}}$. This can be taken as an indication that the lengthening of bainite sheaves by the successive nucleation of bainite sub-units is relatively faster than their nucleation at grain boundaries for Steel C than it is for Steel D. This result also matches the predictions from the simulations described in Figure 2.3 and the experimental observations made by Matsuzaki and Bhadeshia [10].

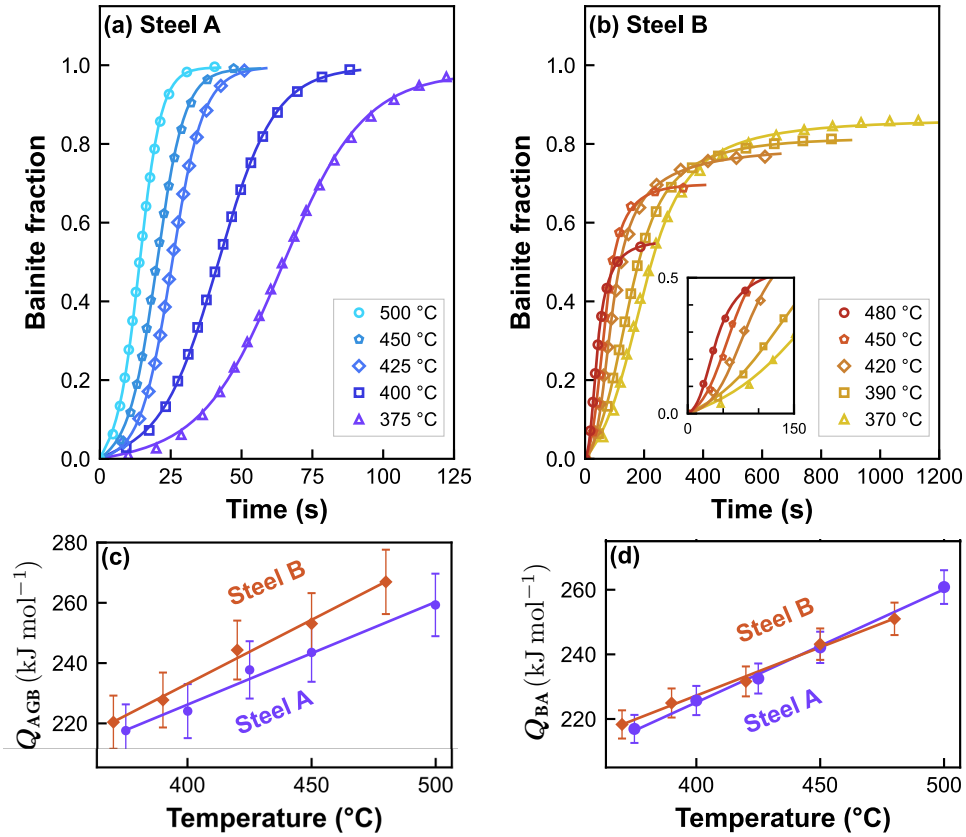

Figure 2.5. Model fitted to the experimental data from steels A and B for several different holding temperatures. In **a.** and **b.** the markers represent the experimental data and the lines represent the fitted model. Markers in **c.** and **d.** show the initial activation energies extracted from the fit for Steel A (purple circle) and Steel B (red diamond), while the solid lines show linear fits. The error bars in **c.** and **d.** were calculated considering an uncertainty of 10 % in d_γ and in u_T, and 50 % in the aspect ratio of the bainite sub-unit.

2.4. Discussion

2.4.1. Model parameters

Size of the bainite sub-unit

Both the length and the volume of the bainite sub-unit are an integral part of the present model. Their values are, however, difficult to measure. On the other hand, the thickness of the sub-units have been extensively measured and can be estimated using empirical equations available in the literature [34, 35]. Then, the length can be calculated by assuming an aspect ratio – which is, however, also difficult to estimate. Based on the images from Bhadeshia *et al.* [38], the

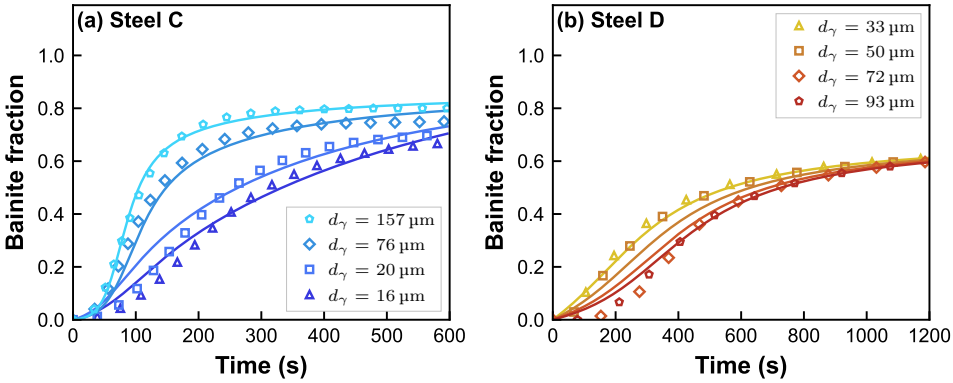

Figure 2.6. Experimental data (markers) and modeled curve (solid line) of bainite formation for **a.** steel C and **b.** steel D at different prior austenite grain sizes, alongside the best fit values for the initial activation energies. Since the retained austenite fraction for Steel D was not reported, it was estimated using the steel models from Thermo-Calc version 2023a with the thermodynamic database TCFE12 [37].

size of a sub-unit was estimated to be $0.2 \times 10 \times 10\,\mathrm{m}^3$, which indicates an aspect ratio of 50. In-depth analysis at a higher resolution indicated that the aspect ratio could actually be in the range from 2 to 15 [39–41]. All of these values are based on a few images from transmission electron microscopy, and thus should be interpreted with care. Also, the size of the sub-unit should not be confused with the size of a sheaf of bainite seen by optical microscopy [42], since a sheaf is an aggregate of several individual sub-units.

Azuma *et al.* [28] were able to model the change from upper to lower bainite assuming an aspect ratio of 6, a value that lies in the middle of the 2 to 15 range. For that reason, the aspect ratio was assumed to be 6 in the present work. Since this estimate bears much uncertainty and may vary depending on the chemical composition of the steel and the transformation temperature, a $50\,\%$ uncertainty on the aspect ratio was considered when calculating the errors in $Q_{\mathrm{AGB}\overline{X}}$ and $Q_{\mathrm{BA}\overline{X}}$.

The rate of bainite formation is proportional to the volume of the bainite sub-unit in the present model. Although this differs from Ravi *et al.*'s model [19], in which V_b has no influence, it is in line with other models of bainite formation, such as the one from Matsuda and Bhadeshia [43]. Given that a higher V_b means that each nucleation event will give rise to a correspondingly greater fraction of bainite, it seems reasonable to assume this linear relationship.

Correctly capturing the influence of the volume of the sub-unit on the rate of bainite formation is especially important in the present work because by changing the prior austenite grain size the volume of the sub-unit may also change. And, in turn, the correlation between V_b and d_γ could define the effect of the prior austenite grain size on the kinetics of bainite formation, as shown in the

simulation presented in Figure 2.3b. This relation between V_b, d_γ, and the kinetics of bainite formation will be further discussed in Section 2.4.2.

Density of potential nucleation sites

According to the displacive theory of bainite formation, nucleation happens by the dissociation of dislocations, similar to martensite formation [2, 44]. Because of this similarity, Magee's work on martensite nucleation [24] was used by van Bohemen [21] in order to estimate the density of initially present potential nucleation sites for bainite.

In the case of martensite, Magee assumed that there is a linear relationship between the driving force for the fcc → bcc transformation and the number of nucleation events of new martensite plates per unit volume of austenite. Following this simple assumption, Magee arrived at the same expression relating undercooling and fraction of martensite than the one found empirically by Koistinen and Marburger [45]. At small undercoolings below M_S, the number of martensite plates nucleated per unit volume of austenite is calculated as

$$N_m = \frac{\alpha_m}{V_m} (M_S - T), \tag{2.25}$$

where N_m is the number of martensite plates per unit volume of austenite and M_s is the martensite start temperature.

While martensite seems to nucleate in defects present inside the austenite grains, bainite seems to nucleate preferentially at the austenite grain boundaries. Thus, in order to calculate the potential nucleation sites for bainite, van Bohemen [21] scaled down Equation (2.25) by the factor $6\delta/d_\gamma$ and changed the martensite-related parameters M_S and V_m by the corresponding bainite-related parameters T_h and V_b, giving rise to Equation (2.6), which is also used in Ravi *et al.*'s model [19]. There are two factors, however, that could lead to errors in van Bohemen's approach.

First, in Magee's derivation of the Koistinen-Marburger, Equation (2.25), it is not the density of initially present potential nucleation sites that is calculated, but the density of plates of martensite that actually nucleate. When a potential nucleation site is activated, a plate of martensite nucleates and then grows to its final size, sweeping many other potential nucleation sites in the process. Thus, the real number of potential nucleation sites may be much higher than the number of plates that actually nucleate, and the two values should not be equated.

Also, the effect of autocatalysis has been overlooked in van Bohemen's derivation. Since Magee's equation considers the total number of martensite plates nucleated, it takes into account not only the martensite plates nucleated at pre-existing defects in austenite but the plates nucleated by autocatalysis at newly created nucleation sites (for more detail see Fig. 2.2 in [24]). But when adapting it to the case of bainite nucleation at defects initially present in the austenite, Equation (2.25) was used as if it concerned only nucleation at pre-existing defects and did not include autocatalysis – which is not the case.

Different approaches were used in other bainite models, mostly using the density of potential nucleation sites at the austenite grain boundaries, $n_{S,AGB}$, as a fitting parameter [27, 28, 30, 43, 46–50]. The values reported differ by a striking 46 orders of magnitude, varying from 10^{-30} [49] to 10^{16} per m^2 of austenite grain boundary [27]. The wide range may be partially caused by the difficulty of simultaneously fitting the activation energy and the density of potential nucleation sites.

In order to perform a quantitative analysis, the values of $n_{S,AGB}$ were compared to the physically-based limits – calculated for a single austenite grain – proposed in Figure 2.7. Considering that nucleation of bainite plates at the austenite grain boundaries takes place at pre-existing defects, the number of potential nucleation sites initially present should be at least as large as the number of nucleation events necessary to fully occupy the austenite grain boundary. The number of necessary nucleation events can be calculated by dividing the grain boundary area by the bainite sub-unit tip area. The upper limit for the potential nucleation sites is the number of atoms present at the austenite grain boundary.

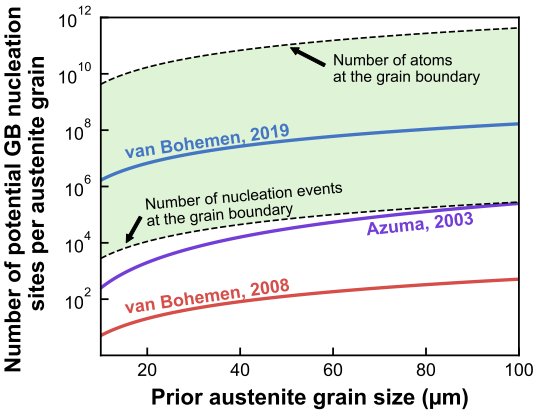

Figure 2.7. Potential sites for bainite nucleation per austenite grain as a function of grain size calculated according to the models from van Bohemen, 2008 [21], Azuma [28] and van Bohemen, 2019 [27]. The calculations were performed considering $u_T = 0.100\,\mu m, u_W = u_L = 0.600\,\mu m, T_h - T = 100\,K, \alpha_m = 0.011\,K^{-1}, Z = 3.35$, and 2.5×10^{19} atoms per m^2 of austenite grain boundary. The shaded area marks the region limited at the bottom by the number of nucleation events at the grain boundary necessary to occupy the whole austenite grain boundary and at the top by the number of atoms in the austenite grain boundary.

Figure 2.7 shows that the values reported by van Bohemen in 2019 [27], at $n_{S,AGB} = 10^{16}\,m^{-2}$ and at the top of the observed range, are the only ones that lie inside the range given by the proposed limits. The early values found by van Bohemen in 2008 [21], Equation (2.6), and used by Ravi *et al.* [19] and subsequent models [51, 52] are three to four orders of magnitude smaller than the lower limit. The curves for most of the other cited models are not shown in

Figure 2.7 because they are too far from the limiting range, with most resulting in less than one potential nucleation site per austenite grain.

From the above discussion it is clear that estimating $n_{S,AGB}$, either by using it as a fitting parameter or by relating it to martensite nucleation, is not straightforward. Also, the physical interpretation of the density of potential nucleation sites and the enormous discrepancy among the reported values have been overlooked in previous models of bainite nucleation. In the present work, $n_{S,AGB}$ was taken as $10^{16}\,m^{-2}$, following van Bohemen [27], because it is the only value reported so far that is within the limits shown in Figure 2.7. Additionally, this value, which is equivalent to one potential nucleation site every $100\,nm^2$ of austenite grain boundary, is consistent with the mechanism of bainite nucleation proposed by the displacive-diffusionless theory of bainite formation [2].

Considering that bainite nucleation is similar to that of martensite, the controlling mechanism is then the dissociation of dislocations. Although the structure of grain boundaries is not always well defined, it can be sometimes well represented in terms of arrays of dislocations or similar defects [53] separated by a few atomic distances [54]. The separation of these defects is in line with the density of potential nucleation sites used in the present work. Then, a similar argument can be made for nucleation at the tip of the bainite sub-units, $n_{S,BA}$, which in the present work was also taken as equal to $10^{16}\,m^{-2}$.

The initial density of potential nucleation sites for a steel with a prior austenite grain size of $50\,\mu m$, considering $n_{S,AGB}$ as $10^{16}\,m^{-2}$, is in the order of 10^{20} to $10^{21}\,m^{-3}$. Although it is physically consistent with the argument made in Figure 2.7, it is much higher than the values reported for martensite. Based on classical small particles experiments, the density of initially-present potential nucleation sites for martensite was estimated as 10^{11} to $10^{13}\,m^{-3}$ [24].

In the case of martensite, however, 10^{11} to $10^{13}\,m^{-3}$ initial potential nucleation sites per m^3 is enough to ensure a full transformation. This is because the volume of martensite plates can be much higher than that of bainite plates, and the creation of new potential sites for nucleation by autocatalysis is much higher for martensite than for bainite. While the autocatalytic factor for bainite is usually in the order of 3 to 200 [21, 29], for martensite it is reported to be in the range of 1000 [24, 55, 56]. Also, the fact that martensite formation is seen to start in the grain interiors and bainite formation in the grain boundaries indicates that, despite their mechanism of formation being similar, their nucleation sites are not exactly the same.

Finally, given the uncertainty in the values of $n_{S,AGB}$ and $n_{S,BA}$, it is important to know their effect in the model. Both values multiply the exponential term containing the activation energies for nucleation. Since the activation energies are fitted to the experimental data, any error in the density of potential nucleation sites results in an erroneous estimation of the activation energy – an overestimation of $n_{S,AGB}$ leads to an overestimation of $Q_{AGB\overline{X}}$, for instance. Since in all cases the same values of $n_{S,AGB}$ and $n_{S,BA}$ were used, any error in the assumed values resulted in roughly the same error in all values of $Q_{AGB\overline{X}}$ and $Q_{BA\overline{X}}$ extracted from fitting. This means that although the absolute values of $Q_{AGB\overline{X}}$ and $Q_{BA\overline{X}}$ reported

in the present work bear this uncertainty with it, none of the trends – such as the ones in Figures 2.5 and 2.6 – are affected by this uncertainty.

Activation energy

The activation energies for bainite nucleation for steels A-D were found to be in the range from 200 to $270\,\mathrm{kJ\,mol^{-1}}$. These values are higher than the ones reported in previous models, which usually range from 100 to $180\,\mathrm{kJ\,mol^{-1}}$ [19, 21, 43]. For steel A and B, the activation energies reported by Ravi *et al.* [19] were up to $120\,\mathrm{kJ\,mol^{-1}}$ lower than the ones found in the present work. This difference is due to the underestimation of the density of potential nucleation sites in previous models.

In Equations (2.5) and (2.7), the density of potential nucleation sites multiplies the exponential term containing the activation energy for nucleation. Hence, the activation energy found by fitting the model to experimental curves of bainite formation kinetics depends on the assumed density of potential nucleation sites. In the present work, the number of potential nucleation sites per interface area, $n_{\mathrm{S,AGB}}$ and $n_{\mathrm{S,BA}}$, was considered to be $10^{16}\,\mathrm{m^{-2}}$. Although the assumed values are the most realistic considering the physical conditions of the transformation, it is important to analyze the consequences of using other values of $n_{\mathrm{S,AGB}}$ and $n_{\mathrm{S,BA}}$ in the resulting activation energies.

Figure 2.8 shows the activation energy for bainite nucleation found for steel B isothermally treated at $420\,^{\circ}\mathrm{C}$ as a function of the assumed $n_{\mathrm{S,AGB}}$ and $n_{\mathrm{S,BA}}$, which were varied from 10^{6} to $10^{16}\,\mathrm{m^{-2}}$. Both $Q_{\mathrm{AGB}\overline{X}}$ and $Q_{\mathrm{BA}\overline{X}}$ vary by $130\,\mathrm{kJ\,mol^{-1}}$ within this range. At 10^{10} potential nucleation sites per $\mathrm{m^2}$, which is the order of magnitude used by Ravi *et al.*, $Q_{\mathrm{AGB}\overline{X}}$ and $Q_{\mathrm{BA}\overline{X}}$ are respectively 165 and $152\,\mathrm{kJ\,mol^{-1}}$, differing only by $3\,\mathrm{kJ\,mol^{-1}}$ from the values found by Ravi *et al.* (168 and $155\,\mathrm{kJ\,mol^{-1}}$). Thus, the lower values of activation energy for bainite previously reported in other models in the literature are a consequence of such models may having underestimated the density of potential nucleation sites for bainite nucleation.

According to the displacive theory of bainite formation, there are two thermally-activated events involved in the nucleation: carbon diffusion and dissociation of dislocations [2]. The activation energy for bainite nucleation, Q, can then be understood as the sum of the individual activation energies for carbon diffusion, Q_{D}, and for the dissociation of dislocations, Q^{*} [28, 57]. Rigorously, Q_{D} is the activation energy for a carbon atom to jump from a bainite embryo to the austenite matrix. Since this value is not known, Q_{D} can be approximated as the activation energy for carbon diffusion in the austenite, which is around $140\,\mathrm{kJ\,mol^{-1}}$ (from databases TCFE12 and MOBFE7 in Thermo-Calc). Thus, Q^{*} was found to vary from 60 to $130\,\mathrm{kJ\,mol^{-1}}$, which is smaller than the activation energy for the diffusional movement of ferrite/austenite interfaces, estimated as $140\,\mathrm{kJ\,mol^{-1}}$ [58].

According to Olson and Cohen's theory of martensite nucleation [59], which

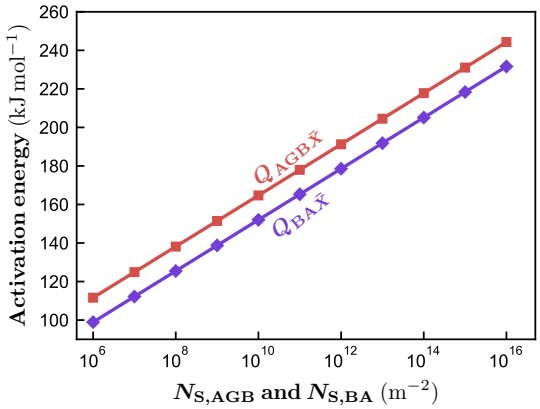

Figure 2.8. Estimated activation energies for bainite nucleation in steel B isothermally treated at $420\,^{\circ}\mathrm{C}$ as a function of the assumed values of the number of potential nucleation sites per interface area, $n_{\mathrm{S,AGB}}$ and $n_{\mathrm{S,BA}}$.

has been adopted in the theory of bainite nucleation [2], Q^* can be calculated as

$$Q^* = Q_0^* + \left(\tau_\mu + \frac{\rho_{\mathrm{A}}}{b} E_{\mathrm{str}} + \frac{2\sigma}{n_{\mathrm{p}} b}\right) V^* + \left(\frac{\rho_{\mathrm{A}}}{b} V^*\right) \Delta G_{\mathrm{m}}, \tag{2.26}$$

where Q_0^* is the activation energy for overcoming the short-range barriers to dislocation movement, τ_μ is the athermal resistance to dislocation movement, ρ_{A} is the number of atoms per unit area of the closed packed plane, b is the magnitude Burgers vector, E_{str} is the strain energy, σ is the bainite/austenite interfacial energy, n_{p} is the number of atomic planes of the embryo, and V^* is the activation volume [2, 44, 60].

Since Equation (2.26) has several unknown parameters (Q_0^*, τ_μ, E_{str}, σ, n_{p}, V^*), it cannot be directly used to calculate Q^*. The derivative of Equation (2.26) with respect to temperature, however, can be used to estimate the activation volume for bainite nucleation. If ΔG_{m} is assumed to be the only temperature-dependent parameter in Equation (2.26), then the derivative is calculated as

$$\frac{\mathrm{d}Q^*}{\mathrm{d}T} = \frac{\rho_{\mathrm{A}}}{b} V^* \frac{\mathrm{d}(\Delta G_{\mathrm{m}})}{\mathrm{d}T}. \tag{2.27}$$

Using the values of ΔG_{m} calculated in Thermo-Calc, the activation volume V^* for the grain boundary and autocatalytic nucleation of bainite in steel A is estimated as 55 and 57 Ω, respectively, and in steel B as 72 and 51 Ω, where Ω is the atomic volume of the Fe atom ($8.5 \times 10^{-30}\,\mathrm{m}^{-3}$). These values are in line with the range reported by Olson and Cohen for the isothermal martensite nucleation in Fe-Ni and Fe-Ni-Mn alloys, which was from 21 to 73 Ω [44].

The slopes $\mathrm{d}Q^*/\mathrm{d}T$ for steels A and B, calculated from the curves shown in Figure 2.5c,d, were in the range from 272 to $386\,\mathrm{kJ\,mol^{-1}}$. Again, these values are

close to those reported for isothermal martensite nucleation in Fe-Ni-Mn alloys, which were around 300 to 360 $\mathrm{kJ\,mol^{-1}}$ [55, 56].

Lengthening rate of sheaves

A sheaf of bainite is a structure formed by an aggregate of bainite sub-units that were nucleated one at the tip of the other by autocatalysis. The lengthening of bainite sheaves is not, according to the diffusionless theory, a continuous process, but rather a succession of several nucleation events. Although the present model is based on the individual nucleation events, the lengthening rate of bainite sheaves can be derived and compared with experimental values.

The apparent lengthening rate of a sheaf of bainite, v_{L}, can be calculated as the product of the length of a bainite sub-unit and the nucleation rate at the tip of a single sub-unit,

$$v_{\mathrm{L}} = u_{\mathrm{L}} \frac{kT}{h} n_{\mathrm{S,BA}} u_{\mathrm{T}} u_{\mathrm{W}} \ \exp\left(-\frac{Q_{\mathrm{BA}}}{RT}\right). \tag{2.28}$$

In Equation (2.28), the product $n_{\mathrm{S,BA}} \cdot u_{\mathrm{T}} \cdot u_{\mathrm{W}}$ is the number of potential nucleation sites at the tip of a single bainite sub-unit.

Figure 2.9 shows the lengthening rate for steel A and B calculated using the model from the present work, the model from Ravi *et al.*, and Thermo-Calc [61]. In Ravi's model $n_{\mathrm{S,BA}}$ is not defined, and thus the number of potential nucleation sites at the tip of the individual sub-units cannot be calculated. However, for the bainitic transformation to progress, it is necessary to have at least one potential nucleation site at the tip of every sub-unit. For that reason, the term $n_{\mathrm{S,BA}} \cdot u_{\mathrm{T}} \cdot u_{\mathrm{W}}$ was considered to be equal to one when calculating the lengthening rate according to Ravi's model. According to the model from the present work, the number of potential nucleation sites at the tip of the bainite sub-units varied from 600 to 6000 for Steels A and B.

The lengthening rates obtained for steel A and B, using the present model, were in the range from 10^{-8} to $10^{-6}\,\mathrm{m\,s^{-1}}$. In comparison, using Ravi *et al.*'s model, lengthening rates up to $10^{-2}\,\mathrm{m\,s^{-1}}$ were found, which is two orders of magnitude above the highest values reported in literature [2, 61]. The unrealistically high values from Ravi *et al.*'s model are due to the underestimation of potential nucleation sites. Although one potential nucleation site per bainite sub-unit was assumed in the present calculation, the values of n_{BA} calculated from Equation (2.8) suggest that in Ravi *et al.*'s model there is less than one potential nucleation site per tip of bainite sub-unit. This value is too low, since without at least one potential nucleation site per tip, the growth of a sheaf cannot progress.

For steel B, the lengthening rates calculated using the present model and using Thermo-Calc match well. For steel A, however, the rates calculated using the present model were 10 to 20 times lower. The results from Thermo-Calc simulation are closer to experimental values of steels with chemical composition similar to the one of steel B [61], indicating that the present model underestimated the lengthening rate of the bainitic sheaf. However, two critical aspects need to be considered when making this comparison.

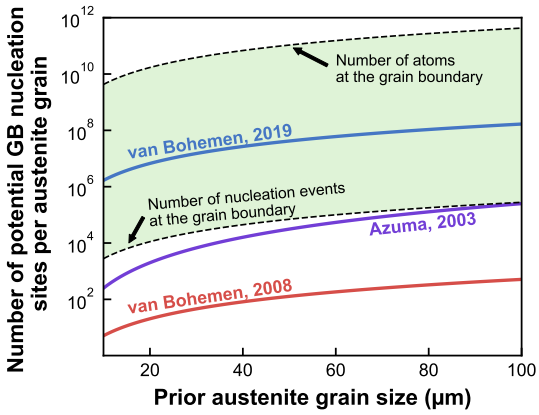

Figure 2.9. Lengthening rate of bainite sheaves in steel A and B calculated according to the model from the present work, to the model from Ravi *et al.* [19], and to Thermo-Calc [37, 61]. Shaded area represents the range of values reported in the literature so far for several steels [2, 61]. The error bars were estimated considering an uncertainty of $10\,\%$ in d_γ and in u_T, and $50\,\%$ in the aspect ratio of the bainite sub-unit. The error associated with the Thermo-Calc could not be estimated, but based on Ref. [61] it may span more than one order of magnitude.

First, the model from the present work and Thermo-Calc's model use different optimization strategies. While Thermo-Calc's model used for calculating the curves in Figure 2.9 was optimized to match the experimentally measured lengthening rates [61], the model from the present work was optimized to match the overall kinetics of bainite formation. Even so, the difference between Thermo-Calc's simulation and the experimentally measured lengthening rates can differ by a factor of 20 [61].

Second, the experimental data used for optimizing Thermo-Calc's model was measured by either *in situ* hot-stage microscopy or measuring the longest bainite sheaf after interrupted transformation. The former technique measures the lengthening rate on the surface, which can be faster than in the bulk because of free surface effects [61]. The later technique measures the rate of the fastest growing sheaf, not the average lengthening rate.

2.4.2. Effect of the prior austenite grain size on bainite formation

Refining the grain size of the parent phase usually accelerates the formation of the precipitating phase. In the case of bainite, not only acceleration but deceleration have been reported. In the present work, both behaviors were successfully replicated by a single model, as shown in Figures 2.3 and 2.6. In the model developed, the behavior that the steel will show depends on ΔQ – the difference between the activation energy for grain boundary and autocatalytic nucleation – and on how the thickness of the bainite sub-unit, u_T, varies with the prior austen-

ite grain size.

The effect of ΔQ has been verified experimentally by Matsuzaki and Bhadeshia [10], who analyzed the microstructure after interrupted bainitic treatment of two steels showing opposite behaviors. For the steel in which bainite formation was accelerated by increasing the austenite grain size, the lengthening of sheaves was faster than their nucleation at the grain boundaries, which is consistent with a high ΔQ. Conversely, for the steel in which bainite formation was accelerated by decreasing the austenite grain size, nucleation at the grain boundaries was faster than the growth of sheaves, consistent with a small ΔQ. It is important then to discuss which aspects of the steel influence ΔQ and u_{T}.

From Equation (2.26), the difference between $Q_{\mathrm{AGB}\overline{X}}$ and $Q_{\mathrm{BA}\overline{X}}$ can be understood in terms of different interfacial energies, σ, and different strain energies, E_{str}. While autocatalytic nucleation takes place at the α/γ interface, grain boundary nucleation takes place at a γ/γ interface, and hence they are expected to have different σ values for nucleation.

The strain energy caused by bainite formation can be decreased by self-accommodating variant pairing [62]. Hence, sub-units nucleated by autocatalysis might face a smaller strain energy barrier than the first sub-units formed at the austenite grain boundaries. This effect is of course expected to be less important at larger undercoolings, when the driving force for nucleation is much higher than the strain energy. Table 2.1 indeed shows that for Steel B ΔQ decreases with decreasing temperature, going from $16\,\mathrm{kJ\,mol^{-1}}$ at $480\,^{\circ}\mathrm{C}$ to $2\,\mathrm{kJ\,mol^{-1}}$ at $370\,^{\circ}\mathrm{C}$. This effect is not seen in Steel A, which shows a small ΔQ of $1\,\mathrm{kJ\,mol^{-1}}$ on average throughout the whole reported temperature range.

The first bainite model to distinguish the activation energy by nucleation site is that of Ravi *et al.* Previous models have used instead an autocatalytic factor (λ) [21, 29, 49], which depends on, among other terms, ΔQ, as shows Equation (2.23). A higher ΔQ translates to a higher λ. Rees and Bhadeshia [29] argued that the temporarily higher carbon concentration at the tip of bainite sub-units hinders autocatalysis, and hence proposed that the autocatalytic factor, λ, decreases linearly with the carbon content of the steel. In terms of the present model, this reasoning means a lower ΔQ as the carbon content increases.

Indeed, from analyzing the data for steel A-D, higher temperatures and lower carbon content seem to result in a higher ΔQ. The effect of carbon on ΔQ is also consistent with the work of Matsuzaki and Bhadeshia [10], in which the low carbon steel analyzed showed an acceleration of bainite formation by increasing the prior austenite grain size, and the high carbon steel showed the opposite behavior.

The reasoning above cannot explain, however, all experimental observations. There are reported cases of low carbon steel in which refining the prior austenite grain size accelerates bainite formation [11], and reported cases of high carbon steel in which refining the grain size decelerates the reaction [4, 18].

Alloying elements that segregate to austenite grain boundaries may also influence ΔQ. This segregation can change the austenite grain boundary energy and locally change the driving force for bainite nucleation, thus affecting $Q_{\mathrm{AGB}\overline{X}}$. Such

an effect was observed by Douguet *et al.* [63] by studying the addition of boron, a chemical element known for segregating to austenite grain boundaries [64]. In the boron-free version of the steel they analyzed, changing the prior austenite grain size had little impact on bainite formation kinetics. When $30\,\mathrm{ppm}$ of boron was added, larger prior austenite grains led to faster bainite formation kinetics, indicating that adding boron increased ΔQ.

Another aspect that defines the steel's behavior is how the size of the bainite sub-unit varies with changes in the prior austenite grain size. In martensite formation, larger austenite grains result in larger martensite plates. Consequently, increasing the prior austenite grain size accelerates the rate of isothermal martensite formation [65]. The relation between austenite grain size and size of the bainite plates, however, is not straightforward.

Since the sub-unit thickness is mainly controlled by the austenite yield strength [66], it could be expected that a smaller austenite grain size leads to finer sub-units. Note that, considering a fixed aspect ratio, a larger thickness (u_T) implies a greater volume (V_b). In van Bohemen's model for calculating the bainite plate thickness [35], the Hall-Petch effect is included when calculating the austenite yield strength, and thus the model predicts that smaller austenite grains result in finer bainite plates. This behavior has been verified experimentally for several steels, such as Steel C in the present work [17] and in the data used by van Bohemen in the model optimization.

However, the opposite effect has also been reported, in which a larger prior austenite grain size has led to the formation of finer bainite plates [67, 68]. The reason for this behavior is not well explained by the currently available models, which consider u_T to be a function of austenite strength, driving force for bainite formation, and temperature. Nonetheless, it has already been shown that these three are not the only factor that define the bainite plate thickness, and that dynamic, localized factors such as the creation of dislocations at the bainite/austenite interface and the inhomogeneous distribution of carbon could play a role [66].

Although the bainite model from the present work was able to replicate the effect of the prior austenite grain size on the bainite formation kinetics, its ability to quantitatively predict the effect for a given steel composition and temperature might be limited. If an experimental curve of bainite formation at a given austenite grain size is available, the curve can be fitted to the model and the calculated ΔQ can qualitatively point to which behavior the steel might follow (see Figure 2.3). For a more accurate prediction, it would be necessary to know beforehand how the size of the bainite sub-unit for the given steel changes with the prior austenite grain size – which is a short-coming of the currently available models for calculating u_T. Given the limited availability of data in the literature in which both the bainite formation curve and the size of the bainite sub-unit are reported, it was not possible to assess the predictive abilities of the model after extracting ΔQ for a given steel composition and temperature from a single curve.

The predictive abilities of the model can be improved by the atomic scale investigation of grain boundary and autocatalytic nucleation. The segregation of

elements to austenite grain boundaries can influence $Q_{\mathrm{AGB}\overline{X}}$ by locally changing the driving force for bainite nucleation and the boundary's interface energy. Similarly, the buildup of carbon at the tip of bainite sub-units influences $Q_{\mathrm{BA}\overline{X}}$ by locally decreasing the driving force for bainite nucleation. Understanding such effects can give a better insight into the factors controlling ΔQ and how it varies with temperature and chemical composition.

Another important factor that needs to be better understood is how the prior austenite grain size influences the size of the bainite sub-unit. Currently there is no single theory capable of explaining the opposing trends reported in the literature.

2.5. Conclusion

In this Chapter, a new model for bainite formation was developed. The proposed model is capable of replicating both the acceleration and deceleration of the bainite formation kinetics by the refinement of the prior austenite grain size. The model also closely matched experimental curves of bainite formation both for steels that showed acceleration and steels that showed deceleration of bainite formation by austenite grain refinement. Two factors were found to define the effect of the prior austenite grain size on the bainite kinetics:

- The difference in the activation energies for grain boundary and autocatalytic nucleation, ΔQ. The larger the ΔQ, the faster the autocatalytic nucleation in comparison to grain boundary nucleation, and the more the bainite formation tends to be accelerated by grain coarsening. Low carbon content and low undercooling seem to increase ΔQ.

- The correlation between the thickness of the bainite sub-unit, u_{T}, and the prior austenite grain size, d_{γ}. If u_{T} increases with increasing d_{γ}, bainite formation tends to be faster for larger prior austenite grain sizes. The factors that define the correlation between u_{T} and d_{γ} are not yet clear.

In addition, the input and output parameters of bainite formation models were analyzed. Most importantly, it was shown that most of the models published in the literature have underestimated the density of initially present potential nucleation sites, resulting in an underestimation of the activation energies for bainite nucleation and overestimation of the lengthening rate of bainite sheaves.

References

[1] D. d. S. Avila, S. E. Offerman, and M. J. Santofimia. “Modeling the effect of prior austenite grain size on bainite formation kinetics”. In: *Acta Materialia* 266 (Mar. 1, 2024), p. 119656. doi: 10.1016/j.actamat.2024.119656.

[2] H. K. D. H. Bhadeshia. *Bainite in Steels: Theory and Practice, Third Edition*. 3rd ed. London: CRC Press, Mar. 6, 2015. 616 pp. doi: 10.1201/9781315096674.

[3] C. Garcia-Mateo, F. G. Caballero, and H. K. D. H. Bhadeshia. “Acceleration of Low-temperature Bainite”. In: *ISIJ International* 43.11 (2003), pp. 1821–1825. doi: 10.2355/isijinternational.43.1821.

[4] F. Hu, P. D. Hodgson, and K. M. Wu. “Acceleration of the super bainite transformation through a coarse austenite grain size”. In: *Materials Letters* 122 (May 1, 2014), pp. 240–243. doi: 10.1016/j.matlet.2014.02.051.

[5] E. S. Davenport, R. A. Grange, and R. Hafsten. “Influence of austenite grain size upon isothermal transformation behavior of SAE 4140 steel”. In: *Trans. AIME* 145 (1941), p. 301.

[6] J. Barford and W. Owen. “The effect of austenite grain size and temperature on the rate of bainite formation”. In: *Journal Iron and Steel Institute* 197 (1961).

[7] M. Umemoto, K. Horoichi, and I. Tamura. “Transformation Kinetics of Bainite During Isothermal Holding and Continuous Cooling”. In: *Tetsu-To-Hagane/Journal Iron Steel Inst. Japan.* 68.3 (1982), pp. 461–470. doi: 10.2355/tetsutohagane1955.68.3_461.

[8] L. Graham and H. Axon. “The effect of austenitizing treatment on formation of lower bainite in a plain carbon steel”. In: *Journal Iron and Steel Institute* 191 (1959), pp. 361–365.

[9] P. Chráska and J. Dubský. “Cyclic re-austenitizing”. In: *Materials Science and Engineering* 41.2 (Dec. 1, 1979), pp. 217–224. doi: 10.1016/0025-5416(79)90141-1.

[10] A. Matsuzaki and H. Bhadeshia. “Effect of austenite grain size and bainite morphology on overall kinetics of bainite transformation in steels”. In: *Materials Science and Technology* 15.5 (May 1, 1999). Publisher: SAGE Publications, pp. 518–522. doi: 10.1179/026708399101506210.

[11] L. Y. Lan, C. L. Qiu, D. W. Zhao, X. H. Gao, and L. X. Du. “Effect of austenite grain size on isothermal bainite transformation in low carbon microalloyed steel”. In: *Materials Science and Technology* 27.11 (Nov. 1, 2011). Publisher: SAGE Publications, pp. 1657–1663. doi: 10.1179/1743284710Y.0000000026.

[12] T. Jiang, H. Liu, J. Sun, S. Guo, and Y. Liu. “Effect of austenite grain size on transformation of nanobainite and its mechanical properties”. In: *Materials Science and Engineering: A* 666 (June 1, 2016), pp. 207–213. doi: 10.1016/j.msea.2016.04.041.

[13] R. Ueji, Y. Kimura, K. Ushioda, T. Ohmura, and T. Inoue. “Bainite Transformation and Resultant Tensile Properties of 0.6%C Low Alloyed Steels with Different Prior Austenite Grain Sizes”. In: *ISIJ International* 61.2 (2021), pp. 582–590. doi: 10.2355/isijinternational.ISIJINT-2020-389.

[14] G. Xu, F. Liu, L. Wang, and H. Hu. “A new approach to quantitative analysis of bainitic transformation in a superbainite steel”. In: *Scripta Materialia* 68.11 (June 1, 2013), pp. 833–836. doi: 10.1016/j.scriptamat.2013.01.033.

[15] Z. Li, P. Li, Y. Luo, X. Zhou, L. Qi, S. Li, and Z. Wang. “Effect of Austenitizing Temperature and Prior Martensite on Ultra-Fine Bainite Transformation Kinetics”. In: *Metals* 9.12 (Dec. 2019). Number: 12 Publisher: Multidisciplinary Digital Publishing Institute, p. 1309. doi: 10.3390/met9121309.

[16] S. Chen, X. Zhao, and W. Xu. “Effect of prior austenite grain size on bainitic transformation above and below Ms in medium Mn steel”. In: *Journal of Physics: Conference Series* 1653.1 (Oct. 2020). Publisher: IOP Publishing, p. 012043. doi: 10.1088/1742-6596/1653/1/012043.

[17] S. M. Hasan, S. Kumar, D. Chakrabarti, and S. B. Singh. “Effect of prior austenite grain size on the formation of carbide-free bainite in low-alloy steel”. In: *Philosophical Magazine* 100.18 (Sept. 16, 2020). Publisher: Taylor & Francis _eprint: https://doi.org/10.1080/14786435.2020.1764653, pp. 2320–2334. doi: 10.1080/14786435.2020.1764653.

[18] D. San-Martin, M. Kuntz, F. G. Caballero, and C. Garcia-Mateo. “A New Systematic Approach Based on Dilatometric Analysis to Track Bainite Transformation Kinetics and the Influence of the Prior Austenite Grain Size”. In: *Metals* 11.2 (Feb. 2021). Number: 2 Publisher: Multidisciplinary Digital Publishing Institute, p. 324. doi: 10.3390/met11020324.

[19] A. Ravi, J. Sietsma, and M. Santofimia. “Exploring bainite formation kinetics distinguishing grain-boundary and autocatalytic nucleation in high and low-Si steels”. In: *Acta Materialia* 105 (2016), pp. 155–164. doi: 10.1016/j.actamat.2015.11.044.

[20] M. J. Santofimia, F. G. Caballero, C. Capdevila, C. García-Mateo, and C. G. d. Andrés. “Evaluation of Displacive Models for Bainite Transformation Kinetics in Steels”. In: *Materials Transactions* 47.6 (2006), pp. 1492–1500. doi: 10.2320/matertrans.47.1492.

[21] S. van Bohemen and J. Sietsma. “Modeling of isothermal bainite formation based on the nucleation kinetics.” In: *International Journal of Materials Research* 99 (2008), pp. 739–747. doi: 10.3139/146.101695.

[22] L. C. D. Fielding. “The Bainite Controversy”. In: *Materials Science and Technology* 29.4 (Apr. 1, 2013), pp. 383–399. doi: 10.1179/1743284712Y.0000000157.

[23] S. Lin, A. Borgenstam, A. Stark, and P. Hedström. “Effect of Si on bainitic transformation kinetics in steels explained by carbon partitioning, carbide formation, dislocation densities, and thermodynamic conditions”. In: *Materials Characterization* 185 (Mar. 1, 2022), p. 111774. doi: 10.1016/j.matchar.2022.111774.

[24] C. L. Magee. “The nucleation of martensite”. In: *Phase Transformations*. ASM, 1970, pp. 115–156.

[25] S. Van Bohemen. “Modeling Start Curves of Bainite Formation”. In: *Metallurgical and Materials Transactions A* 41.2 (Feb. 1, 2010), pp. 285–296. doi: 10.1007/s11661-009-0106-9.

[26] J. W. Cahn. “The kinetics of grain boundary nucleated reactions”. In: *Acta Metallurgica* 4.5 (Sept. 1, 1956), pp. 449–459. doi: 10.1016/0001-6160(56)90041-4.

[27] S. M. C. van Bohemen. “Bainite growth retardation due to mechanical stabilisation of austenite”. In: *Materialia* 7 (Sept. 1, 2019), p. 100384. doi: 10.1016/j.mtla.2019.100384.

[28] M. Azuma, N. Fujita, M. Takahashi, and T. Iung. “Modelling Upper and Lower Bainite Transformation in Steels”. In: *Materials Science Forum* 426-432 (2003). Publisher: Trans Tech Publications Ltd, pp. 1405–1412. doi: 10.4028/www.scientific.net/MSF.426-432.1405.

[29] G. I. Rees and H. K. D. H. Bhadeshia. “Bainite transformation kinetics Part 1 Modified model”. In: *Materials Science and Technology* 8.11 (Nov. 1, 1992). Publisher: SAGE Publications, pp. 985–993. doi: 10.1179/mst.1992.8.11.985.

[30] D. Quidort and Y. J. M. Brechet. “A Model of Isothermal and Non Isothermal Transformation Kinetics of Bainite in 0.5% C Steels”. In: *ISIJ International* 42.9 (2002), pp. 1010–1017. doi: 10.2355/isijinternational.42.1010.

[31] R. Storn and K. Price. “Differential Evolution – A Simple and Efficient Heuristic for global Optimization over Continuous Spaces”. In: *Journal of Global Optimization* 11.4 (Dec. 1, 1997), pp. 341–359. doi: 10.1023/A:1008202821328.

[32] M. Newville, R. Otten, A. Nelson, T. Stensitzki, A. Ingargiola, D. Allan, A. Fox, F. Carter, Michał, R. Osborn, D. Pustakhod, S. Weigand, Ineuhaus, A. Aristov, Glenn, Mark, mgunyho, C. Deil, A. L. R. Hansen, G. Pasquevich, L. Foks, N. Zobrist, O. Frost, Stuermer, J.-C. Jaskula, S. Caldwell, P. Eendebak, M. Pompili, J. H. Nielsen, and A. Persaud. *lmfit/lmfit-py: 1.3.2*. Version 1.3.2. July 19, 2024. doi: 10.5281/zenodo.12785036.

[33] P. Virtanen, R. Gommers, T. E. Oliphant, M. Haberland, T. Reddy, D. Cournapeau, E. Burovski, P. Peterson, W. Weckesser, J. Bright, S. J. van der Walt, M. Brett, J. Wilson, K. J. Millman, N. Mayorov, A. R. J. Nelson, E. Jones, R. Kern, E. Larson, C. J. Carey, İ. Polat, Y. Feng, E. W. Moore, J. VanderPlas, D. Laxalde, J. Perktold, R. Cimrman, I. Henriksen, E. A. Quintero, C. R. Harris, A. M. Archibald, A. H. Ribeiro, F. Pedregosa, and P. van Mulbregt. "SciPy 1.0: fundamental algorithms for scientific computing in Python". In: *Nature Methods* 17.3 (Mar. 2020). Publisher: Nature Publishing Group, pp. 261–272. doi: 10.1038/s41592-019-0686-2.

[34] S. V. Parker. "Modelling of Phase Transformations in Hot-Rolled Steels". PhD thesis. University of Cambridge, Jan. 27, 1998.

[35] S. M. C. van Bohemen. "Exploring the correlation between the austenite yield strength and the bainite lath thickness". In: *Materials Science and Engineering: A* 731 (July 25, 2018), pp. 119–123. doi: 10.1016/j.msea.2018.06.041.

[36] S. M. C. van Bohemen and D. N. Hanlon. "A physically based approach to model the incomplete bainitic transformation in high-Si steels". In: *International Journal of Materials Research* 103.8 (Aug. 1, 2012). Publisher: De Gruyter, pp. 987–991. doi: 10.3139/146.110744.

[37] J.-O. Andersson, T. Helander, L. Höglund, P. Shi, and B. Sundman. "Thermo-Calc & DICTRA, computational tools for materials science". In: *Calphad* 26.2 (June 1, 2002), pp. 273–312. doi: 10.1016/S0364-5916(02)00037-8.

[38] H. K. D. H. Bhadeshia and D. V. Edmonds. "The mechanism of bainite formation in steels". In: *Acta Metallurgica* 28.9 (Sept. 1, 1980), pp. 1265–1273. doi: 10.1016/0001-6160(80)90082-6.

[39] I. B. Timokhina, K. D. Liss, D. Raabe, K. Rakha, H. Beladi, X. Y. Xiong, and P. D. Hodgson. "Growth of bainitic ferrite and carbon partitioning during the early stages of bainite transformation in a 2 mass% silicon steel studied by in situ neutron diffraction, TEM and APT". In: *Journal of Applied Crystallography* 49.2 (Apr. 1, 2016). Publisher: International Union of Crystallography, pp. 399–414. doi: 10.1107/S1600576716000418.

[40] Q. Liu, X. Zhao, X. Zhang, and H. Wang. "Effect of cooling temperature field on formation of shelf-like bainite in high carbon silicon steel". In: *Materials Science and Engineering: A* 720 (Mar. 21, 2018), pp. 176–179. doi: 10.1016/j.msea.2018.02.061.

[41] J. Nutter, J. Qi, H. Farahani, W. M. Rainforth, and S. van der Zwaag. “In situ TEM observations of the growth of bainitic ferrite in an Fe-0.3C-3Mn-1.5Si-0.15Mo steel”. In: *Acta Materialia* 252.118924 (2023). doi: 10.1016/j.actamat.2023.118924.

[42] J. Wang, S. van der Zwaag, Z. Yang, and H.-S. Fang. “Aspect ratio of bainite in steels”. In: *Materials Letters* 45.3 (Sept. 1, 2000), pp. 228–234. doi: 10.1016/S0167-577X(00)00110-5.

[43] H. Matsuda and H. K. D. H. Bhadeshia. “Kinetics of the Bainite Transformation”. In: *Proceedings: Mathematical, Physical and Engineering Sciences* 460.2046 (2004). Publisher: The Royal Society, pp. 1707–1722. doi: 10.1098/rspa.2003.1225.

[44] G. B. Olson and M. Cohen. “A general mechanism of martensitic nucleation: Part I. General concepts and the FCC $\rightarrow$ HCP transformation”. In: *Metallurgical Transactions A* 7.12 (Dec. 1, 1976), pp. 1897–1904. doi: 10.1007/BF02659822.

[45] D. P. Koistinen and R. E. Marburger. “A general equation prescribing the extent of the austenite-martensite transformation in pure iron-carbon alloys and plain carbon steels”. In: *Acta Metallurgica* 7.1 (Jan. 1, 1959), pp. 59–60. doi: 10.1016/0001-6160(59)90170-1.

[46] D. Gaude-Fugarolas and P. J. Jacques. “A New Physical Model for the Kinetics of the Bainite Transformation”. In: *ISIJ International* 46.5 (2006), pp. 712–717. doi: 10.2355/isijinternational.46.712.

[47] N. V. Luzginova, L. Zhao, and J. Sietsma. “Bainite formation kinetics in high carbon alloyed steel”. In: *Materials Science and Engineering: A*. Proceedings of the 7th European Symposium on Martensitic Transformations, ESOMAT 2006 481-482 (May 25, 2008), pp. 766–769. doi: 10.1016/j.msea.2006.11.173.

[48] G. Sidhu, S. D. Bhole, D. L. Chen, and E. Essadiqi. “An improved model for bainite formation at isothermal temperatures”. In: *Scripta Materialia* 64.1 (Jan. 1, 2011), pp. 73–76. doi: 10.1016/j.scriptamat.2010.09.009.

[49] S. Singh. “Phase Transformations from Deformed Austenite”. PhD thesis. University of Cambridge, 1998.

[50] M. J. Santofimia, F. G. Caballero, C. Capdevila, C. García-Mateo, and C. G. d. Andrés. “New Model for the Overall Transformation Kinetics of Bainite. Part 1: the Model”. In: *Materials Transactions* 47.10 (2006), pp. 2465–2472. doi: 10.2320/matertrans.47.2465.

[51] W. Wei, P. Retzl, E. Kozeschnik, and Erwin Povoden-Karadeniz. “A semi-physical α-β model on bainite transformation kinetics and carbon partitioning”. In: *Acta Materialia* 207 (Apr. 1, 2021), p. 116701. doi: 10.1016/j.actamat.2021.116701.

[52] Y. Zhang, Y. He, Y. Zhang, S. Song, and F. Liu. “Bainitic transformation and generalized stability”. In: *Scripta Materialia* 227 (Apr. 1, 2023), p. 115311. doi: 10.1016/j.scriptamat.2023.115311.

[53] I. S. Winter, T. Oppelstrup, T. Frolov, and R. E. Rudd. “Characterization and visualization of grain boundary disconnections”. In: *Acta Materialia* 237 (Sept. 15, 2022), p. 118067. doi: 10.1016/j.actamat.2022.118067.

[54] Y. Ishida, T. Hasegawa, and F. Nagata. “Grain-Boundary Fine Structure in an Iron Alloy”. In: *Journal of Applied Physics* 40.5 (Apr. 1, 1969), pp. 2182–2186. doi: 10.1063/1.1657955.

[55] G. Ghosh and V. Raghavan. “The kinetics of isothermal martensitic transformation in an Fe-23.2wt.%Ni-2.8wt.%Mn alloy”. In: *Materials Science and Engineering* 80.1 (June 1, 1986), pp. 65–74. doi: 10.1016/0025-5416(86)90303-4.

[56] S. R. Pati and M. Cohen. “Nucleation of the isothermal martensitic transformation”. In: *Acta Metallurgica* 17.3 (Mar. 1, 1969), pp. 189–199. doi: 10.1016/0001-6160(69)90058-3.

[57] S. E. Offerman, N. H. van Dijk, J. Sietsma, S. Grigull, E. M. Lauridsen, L. Margulies, H. F. Poulsen, M. T. Rekveldt, and S. van der Zwaag. “Grain Nucleation and Growth During Phase Transformations”. In: *Science* 298.5595 (Nov. 2002). Publisher: American Association for the Advancement of Science, pp. 1003–1005. doi: 10.1126/science.1076681.

[58] G. P. Krielaart and S. van der Zwaag. “Kinetics of $\gamma \rightarrow \alpha$ phase transformation in Fe-Mn alloys containing low manganese”. In: *Materials Science and Technology* 14.1 (Jan. 1, 1998). Publisher: SAGE Publications, pp. 10–18. doi: 10.1179/mst.1998.14.1.10.

[59] G. B. Olson and M. Cohen. “A general mechanism of martensitic nucleation: Part III. Kinetics of martensitic nucleation”. In: *Metallurgical Transactions A* 7.12 (Dec. 1, 1976), pp. 1915–1923. doi: 10.1007/BF02659824.

[60] H. Conrad. “Thermally activated deformation of metals”. In: *JOM* 16.7 (July 1, 1964), pp. 582–588. doi: 10.1007/BF03378292.

[61] L. Leach, J. Ågren, L. Höglund, and A. Borgenstam. “Diffusion-Controlled Lengthening Rates of Bainitic Ferrite a Part of the Steel Genome”. In: *Metallurgical and Materials Transactions A* 50.6 (June 1, 2019), pp. 2613–2618. doi: 10.1007/s11661-019-05208-x.

[62] N. Takayama, G. Miyamoto, and T. Furuhara. “Effects of transformation temperature on variant pairing of bainitic ferrite in low carbon steel”. In: *Acta Materialia* 60.5 (Mar. 1, 2012), pp. 2387–2396. doi: 10.1016/j.actamat.2011.12.018.

[63] P. Douguet, G. Da Rosa, P. Maugis, J. Drillet, and K. Hoummada. “Effect of boron segregation on bainite nucleation during isothermal transformation”. In: *Scripta Materialia* 207 (Jan. 15, 2022), p. 114286. doi: 10.1016/j.scriptamat.2021.114286.

[64] T. S. Prithiv, B. Gault, Y. Li, D. Andersen, N. Valle, S. Eswara, D. Ponge, and D. Raabe. “Austenite grain boundary segregation and precipitation of boron in low-C steels and their role on the heterogeneous nucleation of ferrite”. In: *Acta Materialia* 252 (June 15, 2023), p. 118947. doi: 10.1016/j.actamat.2023.118947.

[65] V. Raghavan and M. Cohen. “Measurement and interpretation of isothermal martensitic kinetics”. In: *Metallurgical Transactions* 2.9 (Sept. 1, 1971), pp. 2409–2418. doi: 10.1007/BF02814878.

[66] A. Eres-Castellanos, J. Hidalgo, M. Zorgani, M. Jahazi, I. Toda-Caraballo, F. G. Caballero, and C. Garcia-Mateo. “Assessing the scale contributing factors of three carbide-free bainitic steels: A complementary theoretical and experimental approach”. In: *Materials & Design* 197 (Jan. 1, 2021), p. 109217. doi: 10.1016/j.matdes.2020.109217.

[67] B. Chhajed, K. Mishra, K. Singh, and A. Singh. “Effect of prior austenite grain size on the tensile properties and fracture toughness of nano-structured bainite”. In: *Materials Characterization* 192 (Oct. 1, 2022), p. 112214. doi: 10.1016/j.matchar.2022.112214.

[68] K. Singh, A. Kumar, and A. Singh. “Effect of Prior Austenite Grain Size on the Morphology of Nano-Bainitic Steels”. In: *Metallurgical and Materials Transactions A* 49.4 (Apr. 1, 2018), pp. 1348–1354. doi: 10.1007/s11661-018-4492-8.

3

Modeling the effect of prior martensite on bainite formation kinetics

The presence of prior martensite accelerates the kinetics of bainite formation. The reported magnitude of such an acceleration in the rate of bainite nucleation ranges from the same magnitude as the autocatalytic effect of bainite to two orders of magnitude higher. However, the mechanism behind the acceleration and the factors controlling the magnitude of the acceleration are unknown. In this Chapter, the kinetic model of bainite formation developed in Chapter 2 is expanded to include the nucleation of bainite sub-units at the interface between prior martensite and austenite (M/A interface). The expanded model captures the accelerating effect of prior martensite and, by comparison against experimental measurements, indicates that the acceleration originates from the large number of potential nucleation sites created at the M/A interfaces. The magnitude of the acceleration is shown to be stronger at higher temperatures. However, the two order of magnitude increase in the rate of bainite nucleation is shown to be possibly an overestimation due to measuring artifacts caused by thermal gradients in the dilatometry samples. The finding that M/A interfaces are the dominant site for bainite nucleation allows to increase the hardenability of steels without slowing down the kinetics of bainite formation in the presence of martensite by alloying the steels with elements that strongly segregate to austenite grain boundaries, such as boron.

To be submitted for publication.

3.1. Introduction

The partial decomposition of austenite to martensite before bainite formation strongly influences the subsequent transformation kinetics. The presence of prior martensite reduces or even mitigates the incubation period for bainite formation [1], significantly accelerating the transformation [2]. Hence, the formation of prior martensite is being investigated as a strategy to expand the industrial applicability of steels containing low-temperature [3] and carbide-free bainite [4] by shortening their heat treatment time. However, there is no satisfactory explanation for the mechanism and the different levels of acceleration reported. While Navarro-López *et al.* [2] reported that the presence of prior martensite induced a two-order-of-magnitude increase in the maximum nucleation rate of bainite, Smanio *et al.* [5] reported no increase in the maximum nucleation rate, with the prior martensite having the same accelerating effect as the typical autocatalytic effect present in bainite formation.

Here, the kinetic model of bainite formation developed in Chapter 2 is expanded to include the effect of prior martensite. The results show that the creation of new potential sites for bainite nucleation at the martensite/austenite (M/A) interface can fully explain the influence of prior martensite on the subsequent kinetics of bainite formation. The model indicates that even at martensite fractions as low as 0.05, bainite nucleation at the M/A interface becomes more important than at austenite grain boundaries, and at a martensite fraction of 0.10, most of bainite is nucleated at the M/A interface.

3.2. Model

The model developed in Chapter 2 calculates the kinetics of bainite formation considering that the rate-controlling factor is the nucleation of bainite plates. The nucleation rate of bainite plates is separated into nucleation at austenite grain boundaries (AGB) and nucleation at bainite/austenite (B/A) interfaces. Site saturation is calculated independently for nucleation at AGBs and B/A interfaces. Here, the model is expanded by assuming that, when martensite is formed prior to bainite formation, potential sites for bainite nucleation are present at the martensite/austenite (M/A) interface, as illustrated in Figure 3.1. No prior assumptions are made on whether such sites are present in the interface itself or in dislocations near the interface. Also, no prior assumptions about the role of residual stress induced by the martensitic transformation are made. The nucleation rate at the M/A interface, $\mathrm{d}N_{\mathrm{MA}}/\mathrm{d}t$, is given by

$$\frac{\mathrm{d}N_{\mathrm{MA}}}{\mathrm{d}t} = \frac{kT}{h} n_{\mathrm{MA}} \exp\left(-\frac{Q_{\mathrm{MA}}}{RT}\right), \tag{3.1}$$

where Q_{MA} is the activation energy for bainite nucleation at the M/A interface at time t, calculated similarly to Equation (2.11) as

$$Q_{\mathrm{MA}} = Q_{\mathrm{MA}\overline{X}} + K_{\gamma} C_1 \left(X_{\gamma} - \overline{X}\right), \tag{3.2}$$

where $Q_{\mathrm{MA}\overline{X}}$ is the initial activation energy bainite nucleation at the M/A interface, and n_{MA} is the density of potential nucleation sites at the M/A interface at time t, calculated as

$$n_{\mathrm{MA}} = n_{\mathrm{S,MA}} S_{\mathrm{MA}} \left(1 - \frac{f_{\mathrm{MA}}}{f_{\mathrm{MA}}^{\max}}\right) \left(\frac{T_0' - T}{T'_{0\overline{X}} - T}\right), \tag{3.3}$$

where $n_{\mathrm{S,MA}}$ is the number of potential nucleation sites per unit area of M/A interface, taken as $10^{16}\,\mathrm{m}^{-2}$, S_{MA} is the area of the M/A interface per unit volume, f_{MA} is the fraction of bainite nucleated at the M/A interface, and $f_{\mathrm{MA}}^{\max}$ is the maximum fraction of bainite that can be formed by nucleation at the M/A interface, which is assumed to be

$$f_{\mathrm{MA}}^{\max} = S_{\mathrm{MA}} u_{\mathrm{L}} \left[1 - f_{\mathrm{AGB}}^{\max} \frac{\exp\left(-\frac{Q_{\mathrm{AGB}}}{RT}\right)}{\exp\left(-\frac{Q_{\mathrm{AGB}}}{RT}\right) + \exp\left(-\frac{Q_{\mathrm{MA}}}{RT}\right)}\right]. \tag{3.4}$$

The expression in square brackets in Equation (3.4) accounts for the overlap in regions of the austenite grain that are close to both austenite grain boundaries and M/A interfaces, as shown in Figure 3.1b. This overlap region can be consumed both by bainite nucleating at austenite grain boundaries and at M/A interfaces, and it is considered that the rate of nucleation (represented in Equation (3.4) by the activation energies) at each site will determine the relative dominance of one site over the other. Similarly, $f_{\mathrm{AGB}}^{\max}$ needs to be updated as

$$f_{\mathrm{AGB}}^{\max} = S_{\mathrm{AGB}} u_{\mathrm{L}} \left[1 - f_{\mathrm{MA}}^{\max} \frac{\exp\left(-\frac{Q_{\mathrm{MA}}}{RT}\right)}{\exp\left(-\frac{Q_{\mathrm{AGB}}}{RT}\right) + \exp\left(-\frac{Q_{\mathrm{MA}}}{RT}\right)}\right]. \tag{3.5}$$

Figure 3.1 illustrates the separation of bainite fraction by nucleation site at the end of the transformation with and without prior martensite. In addition to creating new potential nucleation sites, the presence of martensite consumes a fraction of the austenite. Therefore, the equations for the nucleation rate at prior austenite grain boundaries and by autocatalysis need to be modified.

Since martensite plates and laths can span across the whole austenite grain, a fraction of the austenite grain boundaries is consumed by the martensite. Thus, S_{AGB} is calculated as

$$S_{\mathrm{AGB}} = \frac{Z}{d_\gamma} \left(1 - f_{\mathrm{m}}\right), \tag{3.6}$$

where f_{m} is the fraction of martensite. Because n_{AGB} and $f_{\mathrm{AGB}}^{\max}$ are proportional to S_{AGB}, both are reduced by the presence of prior martensite.

Autocatalysis can only start after sub-units of bainite have been formed. When martensite is present, there are two possible sites for nucleating the initial sub-units that give rise to autocatalysis: prior austenite grain boundaries and the M/A interface. To also account for autocatalysis that can start from bainite nucleated

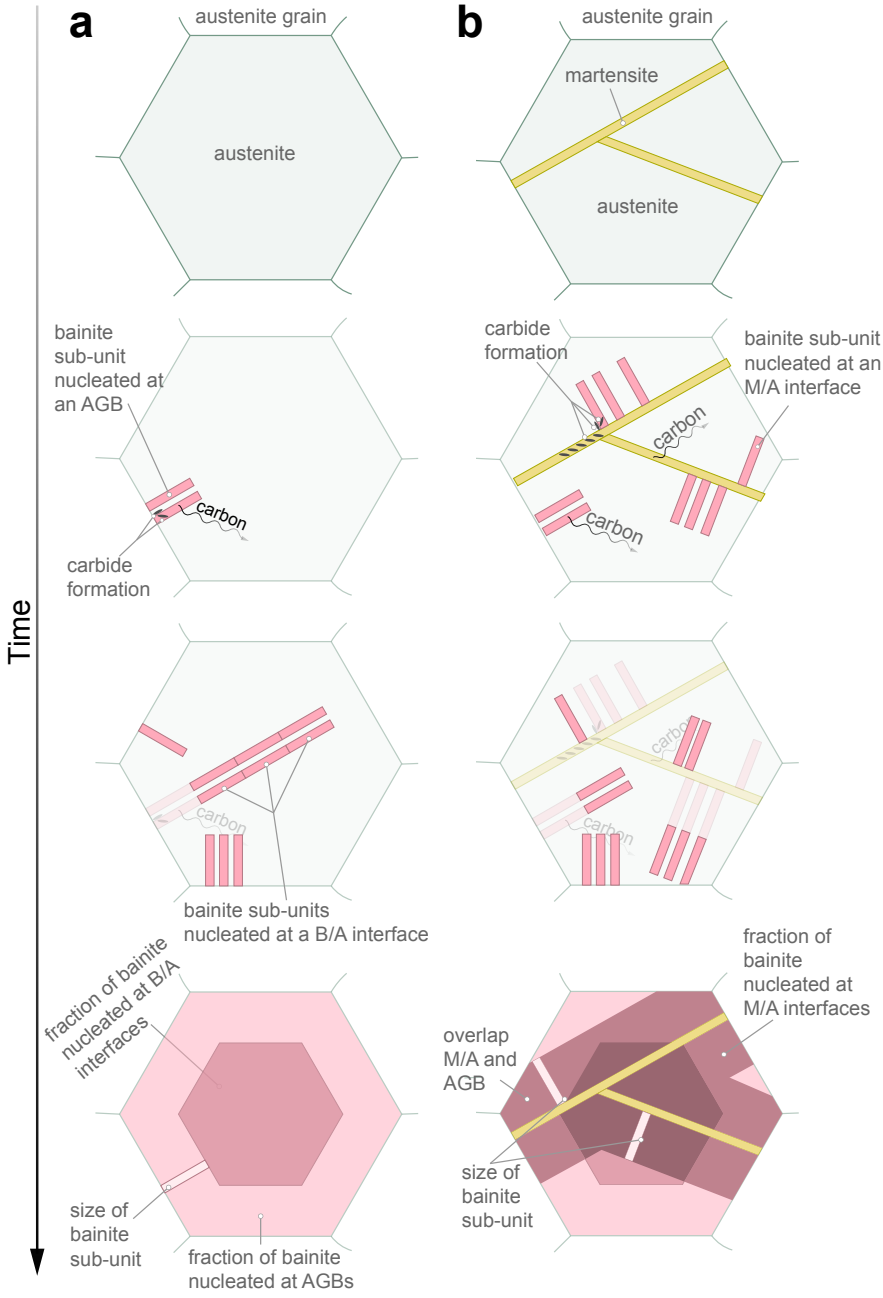

Figure 3.1. Schematics of a single austenite grain during a complete bainitic transformation **a.** without prior martensite and **b.** with prior martensite. On the bottom, the prior austenite grain is dived into different regions based on the nucleation site of bainite that has occupied such region.

at the M/A interface, f_{BA}^{max} needs to be rederived with respect to what was derived in Chapter 2 as

$$\mathrm{d}f_{BA}^{max} = C_{A,AGB}\left(1 - f_{BA}^{max}\right)\mathrm{d}f_{AGB} + C_{A,MA}\left(1 - f_{BA}^{max}\right)\mathrm{d}f_{MA}, \tag{3.7}$$

where $C_{A,MA}$ is the number of bainite sub-units that can be formed by autocatalysis from the first bainite sub-unit nucleated at the M/A interface, and $\mathrm{d}f_{MA}$ is an infinitesimal change to f_{MA}. $C_{A,MA}$ can be found by integrating Equation (3.7) considering $f_{AGB} = 0$ and applying the boundary conditions that $f_{BA}^{max} = 0$ when no bainite has yet nucleated at the M/A interface and $f_{BA}^{max} = 1 - f_{AGB}^{max} - f_{MA}^{max} - f_m$ when $f_{MA} = f_{MA}^{max}$. The latter boundary condition states that once all the M/A interface has been consumed by bainite nucleation, all the area marked as the fraction of bainite nucleated at B/A interfaces in Figure 3.1b becomes available for autocatalysis, even if no bainite has nucleated at the austenite grain boundaries yet. Then, $C_{A,MA}$ is found to be

$$C_{A,MA} = -\frac{\ln\left(f_{AGB}^{max} + f_{MA}^{max} + f_m\right)}{f_{MA}^{max}}. \tag{3.8}$$

Although $C_{A,AGB}$ was previously derived in Chapter 2, it needs to be reassessed because the presence of martensite changes the boundary conditions used in its previous derivation. The boundary conditions applied in the presence of martensite are analogous to those used for deriving $C_{A,MA}$. At $f_{MA} = 0$, $f_{BA}^{max} = 0$ when no bainite has nucleated at AGBs, and $f_{BA}^{max} = 1 - f_{AGB}^{max} - f_{MA}^{max} - f_m$ when $f_{AGB} = f_{AGB}^{max}$. Then, integrating Equation (3.7) and applying the proposed boundary conditions yields

$$C_{A,AGB} = -\frac{\ln\left(f_{AGB}^{max} + f_{MA}^{max} + f_m\right)}{f_{AGB}^{max}}. \tag{3.9}$$

By integrating Equation (3.7), solving for f_{BA}^{max}, and including the condition that f_{BA}^{max} can never be greater than $1 - f_{AGB}^{max} - f_{MA}^{max} - f_m$, the final expression becomes

$$f_{BA}^{max} = \begin{cases} 1 - \exp\left[\left(\frac{f_{AGB}}{f_{AGB}^{max}} + \frac{f_{MA}}{f_{MA}^{max}}\right)\ln\left(f_{AGB}^{max} + f_{MA}^{max} + f_m\right)\right] & \frac{f_{AGB}}{f_{AGB}^{max}} + \frac{f_{MA}}{f_{MA}^{max}} < 1 \\ 1 - f_{AGB}^{max} - f_{MA}^{max} - f_m & \frac{f_{AGB}}{f_{AGB}^{max}} + \frac{f_{MA}}{f_{MA}^{max}} \geq 1 \end{cases} \tag{3.10}$$

The carbon enrichment of the austenite is another aspect that needs to be reevaluated when prior martensite is present, as carbon can partition from martensite to austenite. To accurately calculate the kinetics of carbon partitioning from martensite to austenite, it is necessary to solve diffusion equations for a 1, 2, or 3D representation of the microstructure. In the present work, the calculation is simplified by assuming that the kinetics of carbon partitioning from martensite follows the previously assumed kinetics of carbon partitioning from bainite. At any time, the carbon content in the austenite can be calculated as

$$X_\gamma = \overline{X} + \frac{X_{part}}{f_\gamma}, \tag{3.11}$$

where X_{part} is the total carbon partitioned from bainite and martensite to austenite, and f_γ is the fraction of austenite.

Figure 3.2 shows the calculated fraction of carbon partitioned to the austenite, X_{part}, as a function of bainite fraction for a theoretical case in which prior martensite is present. The parameters used in the calculation are given in the Figure's caption. At the beginning of the transformation, carbon partitioning is still negligible. The total carbon partitioned then increases linearly with respect to the bainite fraction, until the reaction reaches stasis. At the end of the transformation, the total fraction of carbon partitioned to austenite is $f_{\text{b}}^{\text{stasis}}\left(\overline{X}-X_{\text{b}}\right)+f_{\text{m}}\left(\overline{X}-X_{\text{m}}\right)$, where $f_{\text{b}}^{\text{stasis}}$ is the fraction of bainite at stasis – which can be calculated from the equations for T_0' from Chapter 2 – Equation (2.10). At any point of the transformation, the carbon content in austenite can be calculated as

$$X_\gamma=\overline{X}+\frac{f_{\text{b}}^{\text{stasis}}\left(\overline{X}-X_{\text{b}}\right)+f_{\text{m}}\left(\overline{X}-X_{\text{m}}\right)}{1-f_{\text{b}}-f_{\text{m}}}\frac{f_{\text{b}}}{f_{\text{b}}^{\text{stasis}}}. \tag{3.12}$$

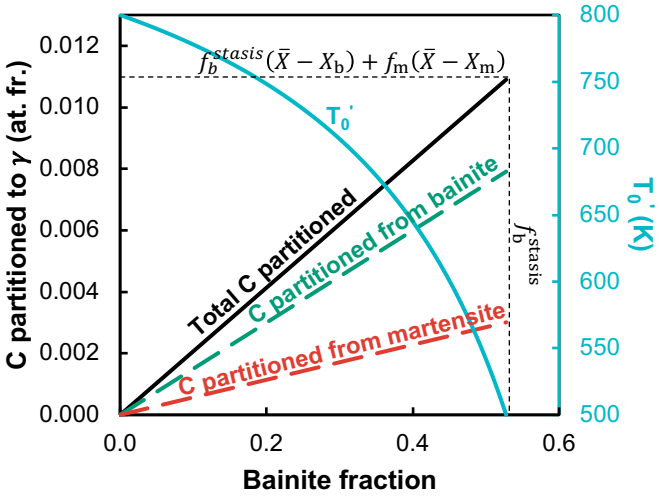

Figure 3.2. Calculated curves of carbon partitioned to austenite and T_0' as a function of bainite fraction for a theoretical case. The total fraction of carbon partitioned to austenite (X_{part}, solid black curve) is the sum of the carbon partitioned from bainite (dashed green curve) and carbon partitioned from martensite (dashed red curve). When T_0' (solid cyan curve) reaches the temperature at which bainite is being formed, the reaction halts. The parameters used in the calculation were: $\overline{X}=0.02\,\text{at. fr.}, X_{\text{b}}=X_{\text{m}}=0.005\,\text{at. fr.}, f_{\text{m}}=0.2, T'_{0\overline{X}}=800\,\text{K}, T=500\,\text{K}, C_2=7500\,\text{K/at. fr.}$.

The total nucleation rate of bainite is calculated then as

$$\frac{\text{d}N}{\text{d}t}=\frac{\text{d}N_{\text{AGB}}}{\text{d}t}+\frac{\text{d}N_{\text{BA}}}{\text{d}t}+\frac{\text{d}N_{\text{MA}}}{\text{d}t}. \tag{3.13}$$

Equation (3.13) can be generalized as

$$\frac{\mathrm{d}N}{\mathrm{d}t} = \sum_i \frac{\mathrm{d}N_i}{\mathrm{d}t} = \sum_i \frac{kT}{h} n_i \exp\left(-\frac{Q_i}{RT}\right) \tag{3.14}$$

where N_i is the nucleation rate of bainite at site i, Q_i is the activation energy for bainite nucleation at site i, and n_i is the density of potential sites of bainite nucleation, calculated as

$$n_i = n_{\mathrm{S},i} S_i \left(1 - \frac{f_i}{f_i^{\max}}\right)\left(\frac{T_0' - T}{T_{0\overline{X}}' - T}\right) \tag{3.15}$$

where $n_{\mathrm{S},i}$ is the number of potential nucleation sites per area of interface i, S_i is the area of interface i per volume of material, f_i is the fraction of bainite nucleated at site i, and $f_i^{\max}$ is the maximum fraction of bainite that can nucleate at site i.

The general Equations (3.14) and (3.15) may be used to expand the model to cases in which there are other interfaces that can act as a nucleation site for bainite, such as ferrite/austenite interfaces [6] or precipitate/austenite interfaces, as in the formation of acicular ferrite, for instance [7]. However, in doing so, the equations for $f_{\mathrm{AGB}}^{\max}$ and $f_{\mathrm{BA}}^{\max}$ should be reevaluated accordingly, as done in the present work in Equations (3.5) to (3.10).

The model contains five unknown parameters that are found by fitting to the experimentally measured kinetics of bainite formation. The parameters are:

- Activation energies for bainite nucleation at the three possible nucleation sites: austenite grain boundaries (AGB), bainite/austenite (B/A) interface, and martensite/austenite (M/A) interface;
- Area of martensite/austenite (M/A) interface per unit volume, S_{MA};
- Fraction of carbon trapped in bainite and martensite either in solid solution, segregated to defects, or in carbides, X_{bm}.

The activation energies were considered to be a linear function of temperature, in accordance with the theory of nucleation by the thermally activated dissociation of dislocations discussed in Chapter 2. For each steel, the experimental curves were split into a group with prior martensite and a group without prior martensite, and all curves from a given group were fitted simultaneously. The groups without prior martensite were used to find the linear equations that represent the activation energies of nucleation at AGBs and B/A interface (Q_{AGB} and Q_{BA}), and the groups with martensite to find S_{MA} and the linear equation for the activation energy of nucleation at the M/A interface (Q_{MA}). While the activation energies were fitted as a linear function of temperature, no specific relationship was imposed for S_{MA} and X_{bm}. The algorithms used for fitting were the ones described in Chapter 2.

3.3. Experimental procedure

Table 3.1 shows the chemical composition of the steels used to validate the model proposed in the present work. Low carbon steels (1.5Si, 0.6Si, 3B, 17B, and 0.3C) were supplied by Tata Steel Europe as $10 \times 5 \times 1\,\mathrm{mm}^3$ plates cut from larger cold rolled sheets. The high carbon steel (0.8C) was supplied by Ascometal as $10\,\mathrm{mm}$ long cylinders $4\,\mathrm{mm}$ in diameter. The kinetics of bainite formation and the phase fractions were measured by a combination of dilatometry and X-ray diffraction for the heat treatments shown in Figure 3.3. A detailed description of the steels' manufacturing route and experimental methods can be found in Chapter 4 for the low carbon steels and in the work of Garcia-Mateo *et al.* for steel 0.8C [8]. The prior austenite grain size was estimated using the model by van Bohemen and Morsdorf [9] as $13\,\mu\mathrm{m}$ for steels 1.5Si and 0.6Si, and as $11\,\mu\mathrm{m}$ for steel 0.8C.

Table 3.1. Chemical composition of steels used for validating the analytical model. For Steel 0.8C, both the nominal and the austenite composition at the austenitization temperature ($860\,^\circ\mathrm{C}$) calculated using Thermo-Calc (database TCFE12) are given.

Steel		Chemical composition (wt.%)					
		C	Mn	Si	Cr	Mo	B(ppm)
1.5Si		0.246	2.28	1.51	–	–	–
0.6Si		0.246	2.26	0.61	–	–	–
3B		0.243	1.31	1.49	0.60	0.20	3
17B		0.236	1.29	1.48	0.60	0.20	17
0.3C		0.304	1.30	1.48	0.56	–	3
0.8C	nominal	0.80	1.2	1.3	1.75	0.3	–
	γ at T_{aus}	0.76	1.2	1.3	1.67	0.3	–

In the low carbon steels 0.6Si and 1.5Si, the samples were heated to the respective austenitization temperatures and quenched to temperatures ranging from 305 to $455\,^\circ\mathrm{C}$ for isothermal bainite formation. Martensite was formed during quenching only for isothermal holding temperatures below $380\,^\circ\mathrm{C}$. High carbon steel samples were divided into two groups. The first group of samples was heated to $860\,^\circ\mathrm{C}$ for partial austenitization (0.993 volume fraction of austenite and 0.007 volume fraction of cementite at thermodynamic equilibrium according to Thermo-Calc simulations) and quenched to temperatures ranging from 230 to $330\,^\circ\mathrm{C}$ for isothermal bainite formation without the presence of prior martensite (heat treatment B). The second group was quenched to $170\,^\circ\mathrm{C}$ after partial austenitization to form a 0.15 volume fraction of martensite and reheated to 230, 280, or $330\,^\circ\mathrm{C}$ for bainite formation in the presence of martensite (heat treatment MB). In the low carbon steel, the martensite fraction and the temperature of bainite formation varied simultaneously; in the high carbon steel, at each temperature, the kinetics of bainite formation with and without the presence of martensite was measured. Steels 3B, 17B, and 0.3C were used specifically to investigate the effect of austenite grain boundaries, discussed in Section 3.4.2.

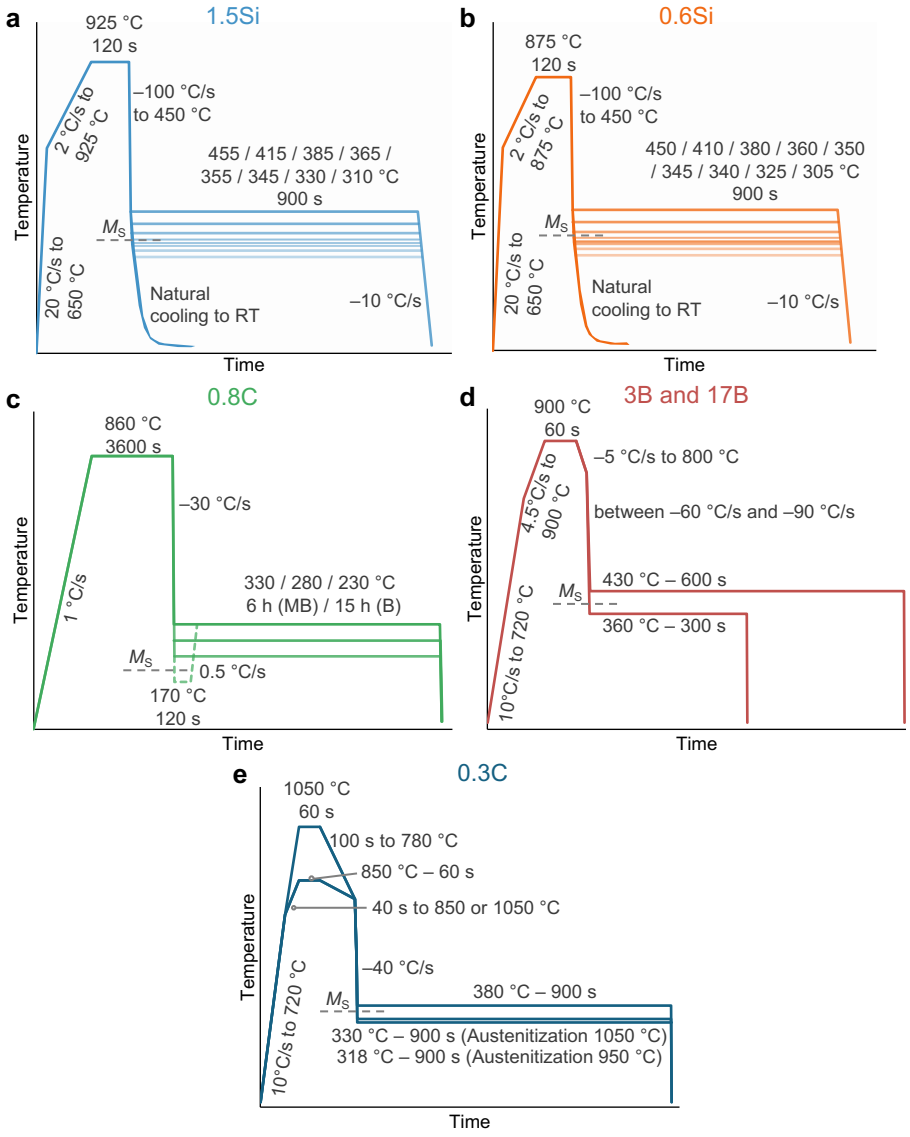

Figure 3.3. Heat treatments applied to steel **a.** 1.5Si, **b.** 0.6Si, **c.** 0.8C, **d.** 3B and 17B, and **e.** 0.3C. In **c.**, solid lines represent treatment B, in which bainite formation took place without prior martensite, and dashed lines represent treatment MB, in which martensite was formed prior to bainite formation.

3.4. Results

3.4.1. Initial validation of the model

Figure 3.4a shows the experimental and the modeled kinetics of bainite formation with and without the presence of prior martensite for a representative selection of conditions for low and high carbon steels. The fitted curves, represented by solid lines, match well the experimentally measured kinetics of bainite formation with and without the presence of prior martensite. The activation energy of bainite nucleation at the M/A interface, shown in Figure 3.4b, lies between the activation energies for nucleation at AGB and B/A interfaces, which indicates that the acceleration induced by prior martensite is not because of a lower activation energy for bainite nucleation at the M/A interface.

In the model, the rate of bainite formation at each nucleation site is distinguished, and thus the relative fraction of bainite formed at each site can be calculated. Figure 3.4c shows such relative fractions. At 0.04 martensite fraction, for steel 1.5Si, 16% of the total bainite formed at stasis was nucleated at M/A sites; at 0.09 martensite fraction, for steel 0.6Si, it was 75%. The high relative fraction of bainite nucleated at the M/A interface is because the area of M/A interfaces, S_{MA}, is much higher than that of austenite grain boundaries, S_{AGB}, as Figure 3.4d shows. This indicates that the origin of the acceleration is that the area density of M/A interface is high enough to form a major fraction of bainite. S_{MA} was found by fitting the model to the experimentally measured kinetics of bainite formation, and its value is discussed in Section 3.5.1.

The prominence of bainite nucleation at M/A interfaces also explains the change in the shape of the kinetic curve of bainite formation when martensite is present. In the absence of prior martensite, bainite nucleates either at AGBs or B/A interfaces. Figure 3.5a shows this distinction for steel 0.6Si transformed at $380\,^{\circ}\mathrm{C}$, a temperature above M_{S}, and for which there is no prior martensite. The curve for the total fraction of bainite as a function of temperature can be split using the model into two separate curves with different shapes: fraction of bainite nucleated at AGBs and at B/A interfaces. The curve for f_{BA} has a sigmoidal shape because the nucleation sites at B/A interfaces are created as the transformation is progressing, in a phenomenon called autocatalysis. In the case shown in Figure 3.5a, most of the bainite is nucleated at B/A interfaces, and thus the curve for the total fraction of bainite as a function of time is dominated by f_{BA} and has a sigmoidal-like shape – as discussed in Chapter 2.

Conversely, in the case shown in Figure 3.5b, in which there is a 0.20 volume fraction of martensite present, most of the bainite is nucleated at M/A interfaces. The curve of the total fraction of bainite as a function of time is then dominated by the curve for f_{MA}. Unlike for B/A interfaces, the potential nucleation sites at M/A interfaces are present from the beginning of the transformation, and there is no autocatalysis involved. Thus, the curve of f_{MA} has a similar shape to that of f_{AGB}. The rate of bainite formation is faster at the beginning and tends toward zero as the reaction progresses. Consequently, when M/A interfaces are the dominating nucleation site for bainite, the kinetic curve of bainite formation loses its traditional sigmoidal shape and assumes the shape shown in Figure 3.5b.

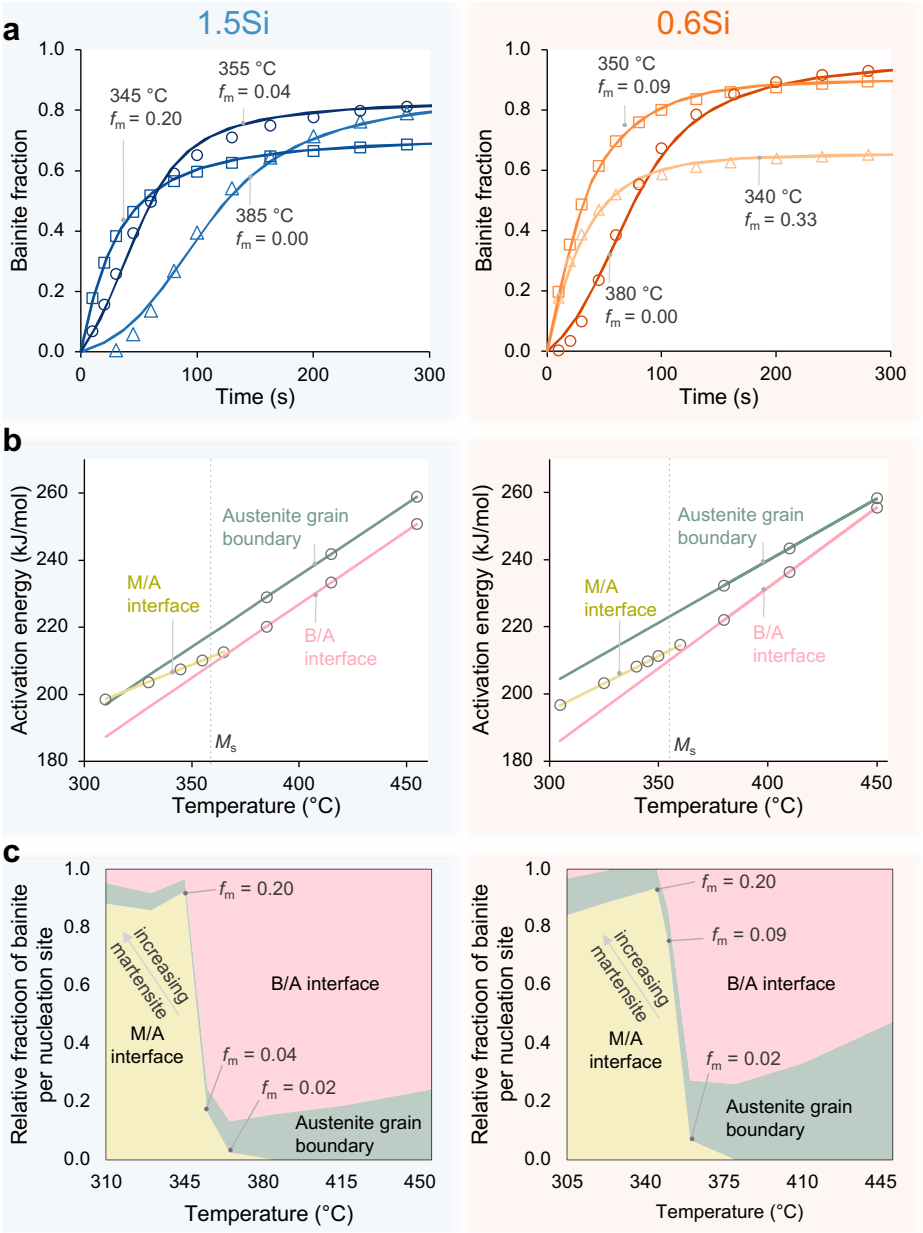

Figure 3.4. Summary of results of the analytical model. **a.** Experimental (markers) and modeled (solid lines) kinetics of bainite formation. **b.** Activation energy for bainite nucleation at the different activation sites as a function of temperature. Markers indicate the data points used for fitting. **c.** Relative fraction of bainite per nucleation site at the end of the transformation. **d.** Area of M/A interface per unit volume. **e.** Normalized fraction of carbon trapped in bainite and martensite (continues on the next page).

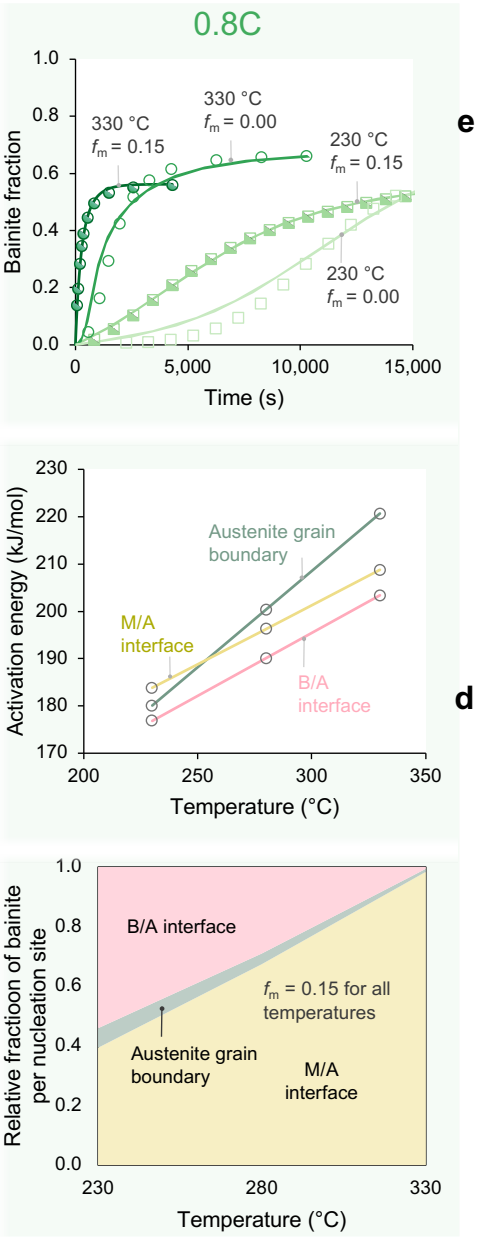

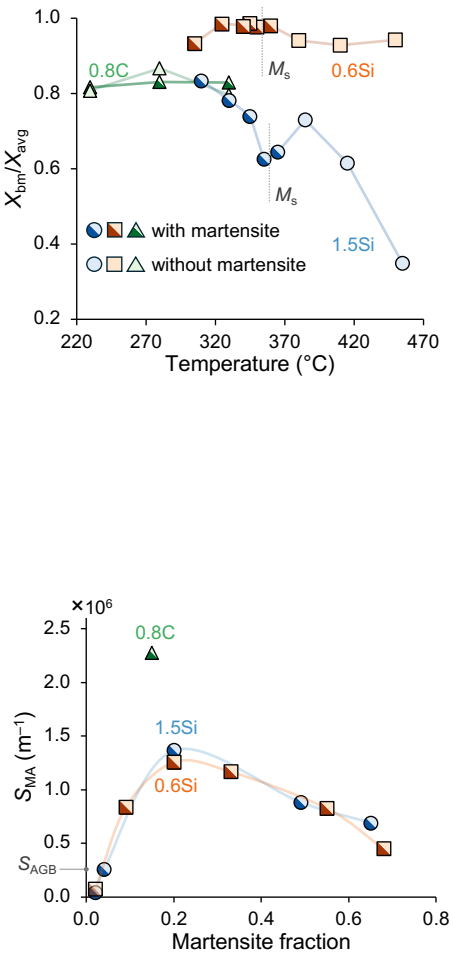

Figure 3.4. Part 2 of the figure (continued).

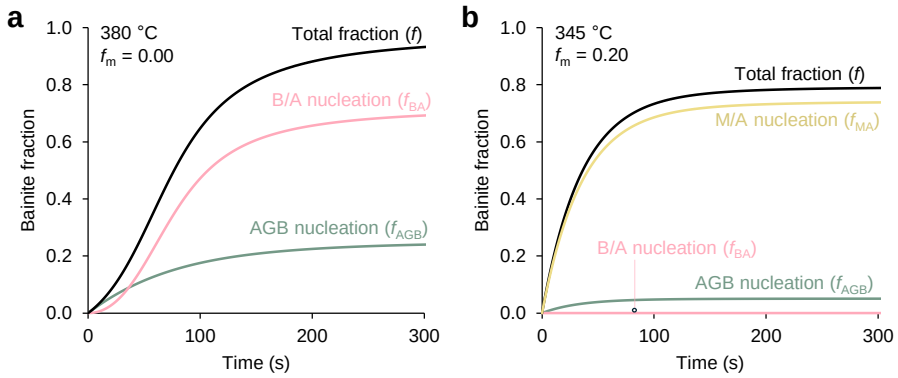

Figure 3.5. Kinetic curve of bainite formation for steel 0.6Si at **a.** $380\,^{\circ}\mathrm{C}$ and **b.** $345\,^{\circ}\mathrm{C}$. The total fraction of bainite is split into separate curves depending on their nucleation site (AGBs, B/A interfaces, M/A interfaces) using the output from the model.

At $365\,^{\circ}\mathrm{C}$, for steel 1.5Si, and at $360\,^{\circ}\mathrm{C}$, for steel 0.6Si, around 0.02 volume fraction of martensite is formed, despite these temperatures being slightly above their measured M_S ($359\,^{\circ}\mathrm{C}$ for 1.5Si and $355\,^{\circ}\mathrm{C}$ for 0.6Si). This is because the temperatures at the border of the samples, which are in contact with the cold pushrods of the dilatometer, cool down to $15\,^{\circ}\mathrm{C}$ below the programmed temperature. Even at such a small fraction of martensite, the kinetics of bainite formation was accelerated (see Figure 4.2c, for instance). This accelerating effect supposedly above M_S has been reported by Radcliffe and Rollason and was termed the swing-back effect [10]. The results presented here show that a swing-back effect can be induced by the formation of a small fraction of martensite prior to bainite formation.

Figure 3.4e shows the carbon content trapped in bainite and martensite as a function of temperature. For steel 0.6Si, this value is close to the nominal carbon content because the silicon content is not high enough to significantly prevent carbide precipitation. For steel 1.5Si, X_{bm} increases at lower temperatures, which can be because of more carbon in solid solution, trapped in dislocations, and more carbide precipitation. Both the solubility of carbon in bainitic ferrite and the dislocation density of bainitic ferrite are expected to increase with decreasing temperature.

Most importantly, Figure 3.4e shows that a single, common value for carbon trapped in bainite and martensite successfully represented the incomplete reaction phenomenon in such steels. In steel 0.8C, X_{bm} was virtually unchanged by the presence of 0.15 volume fraction of prior martensite. From a theoretical point of view, this result can be explained by the diffusionless theory. If both martensite and bainite grow supersaturated in carbon by a displacive, diffusionless mechanism, they should have similar dislocation density, solubility of carbon, and kinetics of carbide precipitation. Thus, the carbon trapped in both should be similar.

3.4.2. Effect of austenite grain boundaries

Since the M/A interface is the dominant nucleation site when prior martensite is present at fractions higher than around 0.10, the model predicts that, in those conditions, any parameter that influences the nucleation rate at AGBs loses its influence on the overall kinetics of bainite formation. This was investigated theoretically, by performing new simulations based on the parameters of steel 1.5Si, and experimentally, using steels 3B, 17B, and 0.3C. Two different strategies that change the rate of bainite nucleation at austenite grain boundaries were tested. The first strategy is alloying the steel with boron, which is an element that strongly segregates to austenite grain boundaries and retards the formation of ferrite and bainite [11]. It is assumed in the simulation that boron only affects the kinetics of bainite formation by increasing the activation energy for nucleation at austenite grain boundaries. The second strategy is increasing the prior austenite grain size, which decreases the density of potential nucleation sites n_{AGB}.

Figure 3.6 shows the simulated and experimentally measured effect of boron on the kinetics of bainite formation with and without the presence of prior martensite. By alloying the steel with boron, which is implemented into the model by considering a higher $Q_{\mathrm{AGB}\overline{X}}$, bainite formation is predicted to be slowed down if there is no prior martensite present (Figure 3.6a). However, if there is prior martensite present (Figure 3.6b), then the model predicts alloying the steel with boron has no effect on the kinetics of bainite formation.

In this simulation, boron is considered to affect the activation energy for nucleation at austenite grain boundaries based on numerous reports showing strong boron segregation to austenite grain boundaries and its influence on nucleation [11–13]. Experiments using atom probe tomography show that boron, despite segregating to AGBs, does not segregate to martensite/martensite nor bainite/bainite boundaries [14–16]. Therefore, it was considered that boron does not affect the activation energies for nucleation at B/A and M/A interfaces.

The model's predictions were confirmed by the experiments with steel 3B and 17B. Both steels differ in chemical composition only on their boron content – steel 3B has $3\,\mathrm{ppm}$ boron, and steel 17B has $17\,\mathrm{ppm}$ boron. Figure 3.6c shows that at $430\,^{\circ}\mathrm{C}$, which is above M_{S} for both steels, bainite formation is slower for steel 17B. The retarding effect of boron is likely caused by its segregation to austenite grain boundaries. At $360\,^{\circ}\mathrm{C}$, which is below M_{S} and around 0.20 volume fraction of martensite is formed prior to isothermal holding, the kinetics of bainite formation is similar in both steels (Figure 3.6d).

A similar effect emerges from changing the prior austenite grain size. The simulations predict that while increasing the prior austenite grain size by austenitizing at a higher temperature slows down bainite formation when there is no prior martensite (Figure 3.7a), it does not influence the kinetics when bainite is formed in the presence of prior martensite (Figure 3.7b). This prediction was tested against experiments made with steel 0.30C. Increasing the prior austenite grain size slowed down bainite formation above M_{S} (Figure 3.7c), but had little effect below M_{S} once around 0.10 volume fraction of martensite was formed (Figure 3.7d).

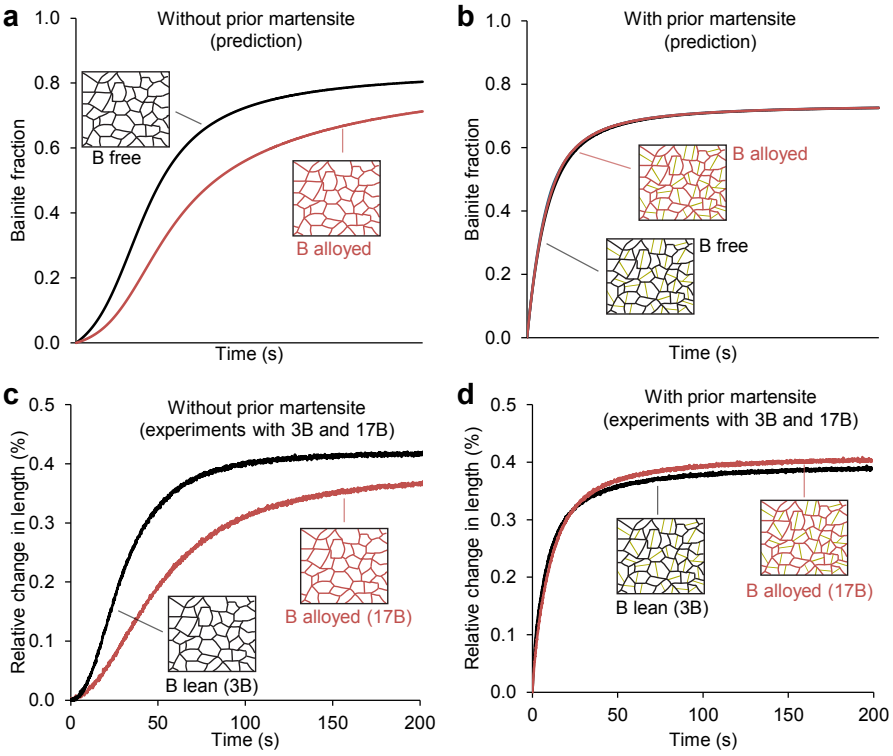

Figure 3.6. Effect of boron on the kinetics of bainite formation. **a, b.** Simulations using the parameters of steel 1.5Si as the basis for the B free steel. Curves without prior martensite **a.** were simulated at $415\,^{\circ}\mathrm{C}$, and curves with prior martensite **b.** at $345\,^{\circ}\mathrm{C}$, with 0.20 volume fraction of prior martensite. The effect of boron on the kinetics was simulated as a $5\,\mathrm{kJ\,mol^{-1}}$ increase in the activation energy for grain boundary nucleation. **c, d.** Experimentally measured effect of boron for steels 3B and 17B. **c.** shows curves at $430\,^{\circ}\mathrm{C}$, which is above M_{S}. **d.** shows curves at $360\,^{\circ}\mathrm{C}$, which is below M_{S} and around 0.20 volume fraction of prior martensite is present.

The combination of predictions based on the model and experiments shown in Figure 3.6 and Figure 3.7 indicates that when prior martensite is present (0.1 to 0.2 volume fraction), the dominating sites for bainite nucleation are at the martensite/austenite interface.

3.4.3. Initial rate of bainite formation

For the low carbon steels, the samples were quenched from the austenitization temperature to an isothermal holding temperature below M_{S}. Because of its athermal nature, martensite is expected to form only during this quenching. Bainite, on the other hand, is expected to form not during quenching but during isothermal holding, as it is a thermally activated transformation. To distinguish

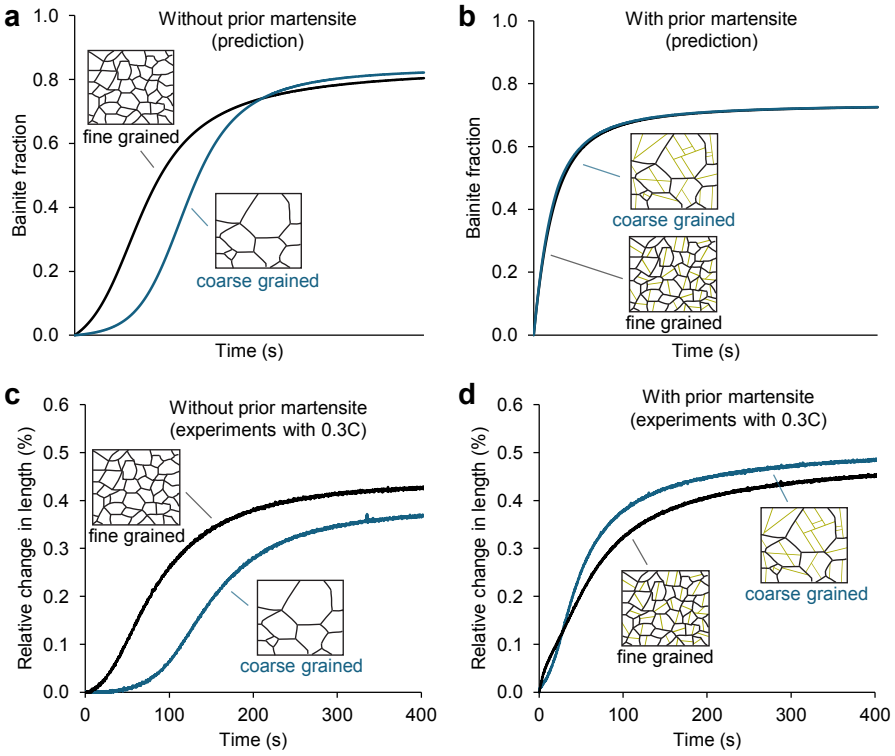

Figure 3.7. Effect of prior austenite grain size on the kinetics of bainite formation. **a, b.** Simulations using the parameters of steel 1.5Si as the basis for fine grained steel. Curves without prior martensite **a.** were simulated at $415\,^{\circ}\mathrm{C}$, and curves with prior martensite **b.** at $345\,^{\circ}\mathrm{C}$, with 0.20 volume fraction of prior martensite. The fine grained steel has a PAGS of $13\,\mu\mathrm{m}$, and the coarse grained steel of $100\,\mu\mathrm{m}$. **c, d.** Experimentally measured effect of PAGS for steel 0.3C, with the coarse grained sample austenitized at a higher temperature than the fine grained sample. **c.** shows curves at $380\,^{\circ}\mathrm{C}$, which is above M_{S}. **d.** shows curves at $318\,^{\circ}\mathrm{C}$ for the fine grained steel and $330\,^{\circ}\mathrm{C}$ for the coarse grained steel. In both cases, a volume fraction of around 0.10 of prior martensite is present. Different holding temperatures were used because changing the PAGS changes the M_{S} of the steel, and if the same holding temperature was used for both steels, they would have different fractions of martensite. The temperature difference might be the reason for the slight difference in the kinetics between the fine and coarse grained steels.

the phase fraction of martensite and bainite, it is therefore important to accurately choose a point in time that marks the transition between quenching and isothermal holding. Before this point, any transformation product is considered martensite. After this point and during holding, any transformation product is considered bainite. This seemingly simple distinction is, in fact, not trivial.

Navarro-López *et al.* [2] used the temperature measured by a thermocouple welded to the center of the samples to differentiate cooling from isothermal hold-

ing. They considered the point zero for the start of bainite formation as the time at which the temperature reached its lowest value during cooling. Following this procedure, they found that prior martensite accelerated the initial nucleation rate of bainite by two orders of magnitude.

The procedure of Navarro-López *et al.*, however, overlooks the thermal gradients present in the dilatometry sample. The thermocouple in the center is used for temperature control, and thus it closely follows the programmed time-temperature profile. On the other hand, the border of the samples, which is in contact with the cold pushrods, is always at a lower temperature than the center [17, 18] and is not automatically controlled by the dilatometer. Hence, at the time zero chosen by Navarro-López et al, the border of the sample could still be cooling down and forming martensite.

In the experiments for steel 0.6Si and 1.5Si, in addition to the thermocouple welded to the center of the sample for temperature control, a second thermocouple was welded at approximately $1\,\mathrm{mm}$ from the border of the sample. The temperature reading from the second thermocouple was recorded but not used for temperature control. Figure 3.8a shows the temperature at the center and at the border of the sample for steel 1.5Si treated at $345\,^{\circ}\mathrm{C}$. Time zero is chosen following the procedure of Navarro-López. During the first seconds of isothermal holding, the temperature at the center of the sample is stable; at the border of the sample, the temperature is still decreasing for around five seconds, and it cools down to $325\,^{\circ}\mathrm{C}$. During these five seconds, martensite is forming at the border of the sample. The rate of martensite formation can be calculated as:

$$\frac{\mathrm{d}f_{\mathrm{m,border}}}{\mathrm{d}t} = \frac{\mathrm{d}T_{\mathrm{border}}}{\mathrm{d}t}\left.\frac{\mathrm{d}f_{\mathrm{m}}}{\mathrm{d}t}\right|_{T_{\mathrm{border}}}, \tag{3.16}$$

where $f_{\mathrm{m,border}}$ is the fraction of martensite at the border of the sample and T_{border} is the temperature at the border of the sample. If the average temperature of the sample is estimated to be the average between the temperature at the center (which is constant during isothermal holding) and at the border, the rate of martensite formation during the first seconds of isothermal holding can be estimated as half of the rate calculated from Equation (3.16),

$$\frac{\mathrm{d}f_{\mathrm{m}}}{\mathrm{d}t} \approx \frac{1}{2}\frac{\mathrm{d}f_{\mathrm{m,border}}}{\mathrm{d}t}. \tag{3.17}$$

Figure 3.8b shows that the rate of transformation at the beginning of isothermal holding at $345\,^{\circ}\mathrm{C}$ for steel 1.5Si is $0.08\,\mathrm{s}^{-1}$. This rate of transformation is calculated based on the change in length of the sample, ΔL. Since bainite and martensite cause the same change in length, which is dictated by the difference in molar volume between FCC and BCC, the rate of transformation calculated using ΔL is the sum of the rate of bainite and martensite formation. While the experimental rate is $0.08\,\mathrm{s}^{-1}$, the rate of bainite formation calculated from the model is only $0.02\,\mathrm{s}^{-1}$. However, the sum of the rate of bainite formation, calculated from the model, and of martensite formation, calculated using Equation (3.17), matches

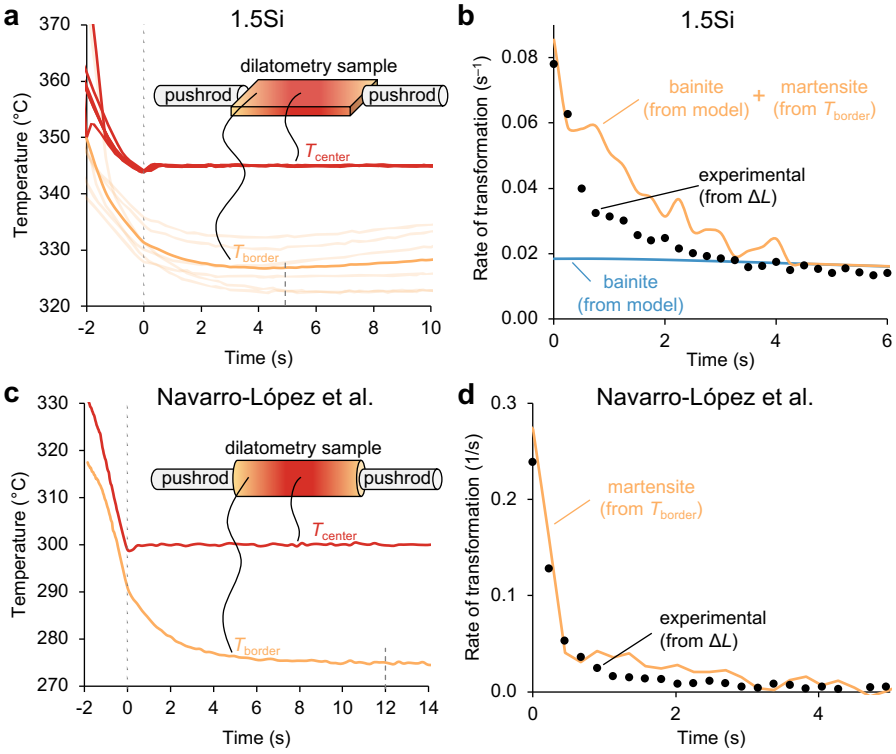

Figure 3.8. Borders of dilatometry samples, which are in contact with cold pushrods, are still cooling during the first seconds of isothermal holding, and thus martensite is still forming and accounts for the high initial rate of transformation. **a, c.** Temperatures measured by thermocouples welded to the center of the sample and at $1\,\mathrm{mm}$ from the border of the sample for steel 1.5Si and the steel used by Navarro-López *et al.*, respectively. **b, d.** Initial rate of transformation (bainite and martensite) calculated using the measured ΔL, rate of martensite formation calculated using Equation (3.17), and rate of bainite formation calculated using the model for steel 1.5Si and the steel used by Navarro-López *et al.*, respectively. For steel 1.5Si, six repetitions of the experiment were made. Three repetitions followed the cooling profile from Figure 3.3, and the other three had constant cooling rate of 50, 100, and $200\,^{\circ}\mathrm{C\,s^{-1}}$. All six experiments gave fairly similar results and are shown in **a** by transparent lines. The solid, opaque line in **a** and **b** is the average from all six experiments.

well the experimental rate of transformation. Therefore, the high initial transformation rate originates from martensite forming at the border of the samples rather than from bainite formation.

To confirm if martensite formation at the border of the sample was also the reason for the extremely high initial transformation rate found by Navarro-López *et al.*, we repeated their experiments using a second thermocouple welded at $1\,\mathrm{mm}$ from the border of the sample. The same samples, dilatometer, and pa-

rameters from Navarro-López were used. Figure 3.8c shows again that during the first seconds, the temperature is stable at the center of the sample, but it is still cooling down at the border. The temperature at the border took around 12 seconds to stabilize, which is longer than the five seconds for steel 1.5Si. The difference might be because of the different sample geometry (plate vs cylinder) and atmosphere. In the experiments of Navarro-López, a helium atmosphere is kept during the beginning of isothermal holding. For steel 1.5Si, the chamber starts being pumped after fast cooling to $450\,^{\circ}\mathrm{C}$ (Figure 3.3a). Longitudinal thermal gradients are milder when the dilatometer chamber is under vacuum than when it is filled with helium [18].

The initial rate of transformation for Navarro-López *et al.*'s steel is $0.23\,\mathrm{s}^{-1}$. Figure 3.8d shows that this high initial rate can be fully accounted for by the martensite formation calculated using Equation (3.17). After 12 seconds, when the temperature at the border is stable, the rate decreases by a factor of 200 to less than $0.001\,\mathrm{s}^{-1}$, which is in the same order of magnitude as for the samples without prior martensite [2, 19]. Because the second thermocouple was welded at $1\,\mathrm{mm}$ from the border of the sample, it cannot be ruled out that even after 12 seconds the regions closer to the border are still cooling down and a small fraction of martensite is still forming.

The results presented in Figure 3.8 show that the acceleration of bainite nucleation by a factor of two orders of magnitude reported by Navarro-López *et al.* was, in reality, an overestimation resulting from an artifact of measurement. Such an artifact is inherent to the quenching dilatometers based on induction heating, which are routinely used in scientific and technological works to measure the kinetics of phase transformations. Thus, the incorrect interpretation by Navarro-López *et al.*, used here to illustrate this artifact, might be present in similar studies carried out by other researchers. For instance, Ravi *et al.* [19] modeled bainite formation at the M/A interface using the high initial nucleation rate, which may be, in reality, mostly martensite formation. Therefore, Ravi's model represents martensite formation rather than bainite formation.

Given this artifact, it is difficult to accurately measure the initial rate of bainite formation and to differentiate martensite and bainite formation. In steels in which bainite formation is slow and a negligible fraction is expected to form in the first 10 to 20 seconds of isothermal holding, all the transformation that happens during this time can be considered to be martensite. However, that is not the case for steel 1.5Si. The rate of bainite formation is estimated to be around $0.02\,\mathrm{s}^{-1}$ during the first seconds of isothermal holding, and thus, in the first 10 seconds, up to 0.20 volume fraction of bainite could be formed. To better differentiate bainite and martensite in this case, it is useful to use the model presented in this Chapter to estimate the rate of bainite formation. The rate of martensite formation can be modeled using an exponential decay type expression, such as the expression Ravi *et al.* used to model bainite nucleation at the M/A interface [19]. In either case, it is good practice to use a second thermocouple welded to the border of the sample.

3.4.4. Acceleration by martensite and autocatalysis in bainite formation

Figure 3.9 compares the kinetics of bainite formation with and without the presence of martensite for steel 1.5Si, 0.6Si, and 0.8C at different isothermal holding temperatures. The y-axis on the graph in Figure 3.9a is the combined fraction of martensite and bainite, and the curve with prior martensite is shifted in time so that it starts from the same point as the curve without prior martensite, as proposed in the work of Smanio and Sourmail [5]. The plot in Figure 3.9a directly compares the accelerating effect of prior martensite with the accelerating effect of an equal fraction of bainite (autocatalysis). In Figure 3.9b, the difference between the curves is plotted.

For Steel 0.8C, the samples were either transformed to bainite directly after austenitization by quenching to the desired temperature of bainite formation ($230\,^{\circ}\mathrm{C}$ to $330\,^{\circ}\mathrm{C}$) or by quenching to $170\,^{\circ}\mathrm{C}$ to form prior martensite and reheating the desired temperature of bainite formation ($230\,^{\circ}\mathrm{C}$ to $330\,^{\circ}\mathrm{C}$). This approach allows directly comparing the kinetics of bainite formation with and without the presence of prior martensite. However, for the low carbon steels, bainite was formed in the presence of martensite by a one-step treatment below M_{S}, and it is not possible to experimentally make the same comparison as for Steel 0.8C. Thus, the model developed in the present chapter was used to simulate the kinetics of bainite formation without the presence of martensite in treatments below M_{S} for the low carbon steels.

For the three steels, the acceleration by martensite is stronger at higher temperatures. The difference does not seem to be controlled by the fraction of martensite or the area of M/A interface. For steel 0.6Si, the difference in acceleration by prior martensite and the autocatalysis in bainite formation is higher at $350\,^{\circ}\mathrm{C}$ than at $345\,^{\circ}\mathrm{C}$, despite S_{MA} being higher at $345\,^{\circ}\mathrm{C}$ than at $350\,^{\circ}\mathrm{C}$. For steel 0.8C, S_{MA} is the same regardless of the temperature at which bainite is formed; still, the acceleration is more pronounced at higher temperatures.

Smanio and Sourmail [5] reported that for a 100Cr6 steel the accelerating effect of 0.15 or 0.30 volume fraction of prior martensite was the same as the autocatalytic acceleration from a similar fraction of bainite for bainite formation at $220\,^{\circ}\mathrm{C}$ and $250\,^{\circ}\mathrm{C}$. The same effect was observed in steel 0.8C at $280\,^{\circ}\mathrm{C}$. However, at $230\,^{\circ}\mathrm{C}$, martensite accelerates less than a similar fraction of bainite; and at $330\,^{\circ}\mathrm{C}$, it accelerates more. Thus, the effect reported by Smanio and Sourmail is rather a temperature-dependent effect than a general one.

According to the proposed model, one important aspect that may change the intensity of the acceleration by prior martensite is the size of the bainite sub-units. The maximum fraction of bainite that can nucleate at the M/A interfaces is calculated as $f_{\mathrm{MA}}^{\max} = S_{\mathrm{MA}} u_{\mathrm{L}}$, where u_{L} is the average length of the bainite sub-units. The size of bainite sub-units increases with temperature, and thus $f_{\mathrm{MA}}^{\max}$ also increases with temperature for a fixed S_{MA}. This is visible in Figure 3.4c for Steel 0.8C. Even though S_{MA} was the same for all three temperatures of bainite formation, the relative fraction of bainite nucleated at the M/A interface increased with temperature.

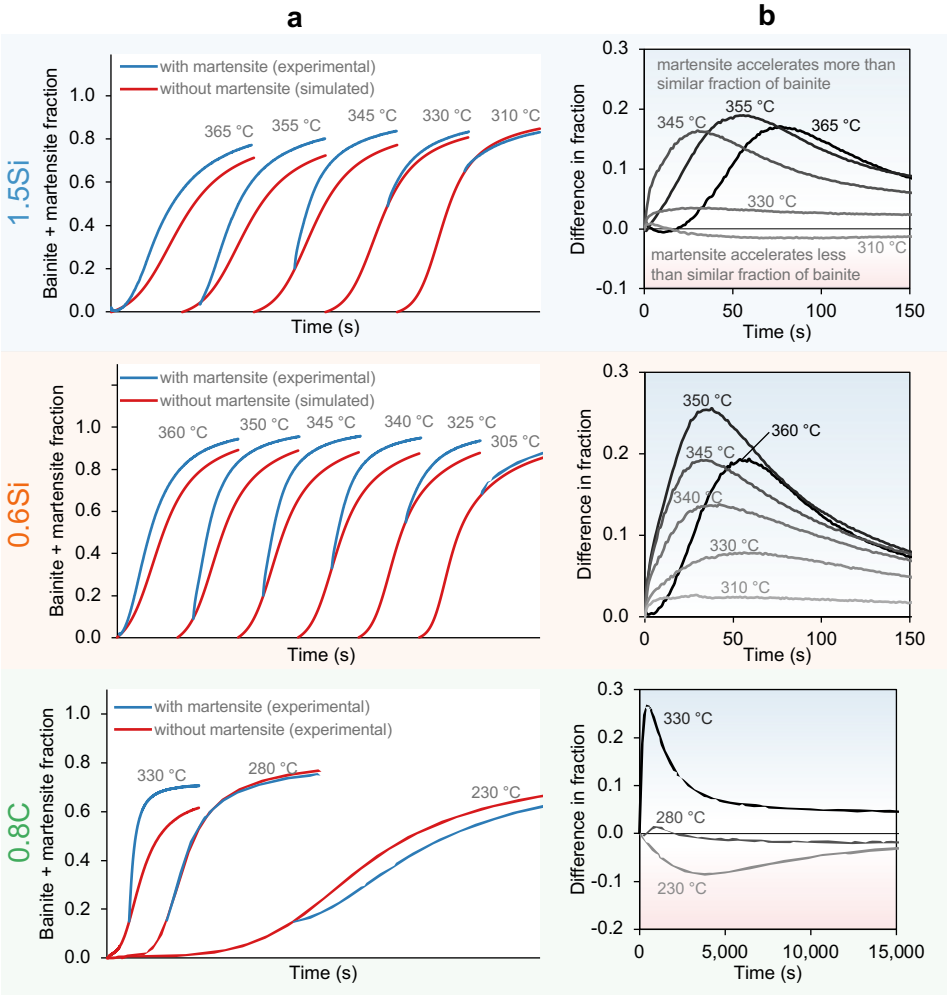

Figure 3.9. Comparison between acceleration by martensite and autocatalysis in bainite formation for steels 1.5Si (top), 0.6Si (middle), and 0.8C (bottom). **a.** kinetics of bainite formation with and without prior martensite, with the curves with prior martensite shifted in time to match those without prior martensite. **b.** difference between the curves with and without prior martensite.

While larger sub-units may enhance the accelerating effect of prior martensite, they may have the opposite effect on the acceleration by autocatalysis. The density of potential nucleation sites for autocatalysis is proportional to the area of B/A interface at the tip of the sub-units. This area is calculated from Equation (2.22) as f/u_{L}. Thus, at lower temperatures, more nucleation sites for autocatalysis are created because u_{L} is smaller, and autocatalysis becomes more pronounced.

Other aspects that might influence the intensity of the martensite-induced acceleration are martensite tempering, carbon partitioning to the austenite, carbon segregation to M/A interfaces, and stress relaxation. At higher temperatures, martensite tempering, carbon homogenization in austenite, and stress relaxation are accelerated. To investigate the influence of such aspects, an extra experiment, shown in Figure 3.10, was carried out using steel 0.8C. In this extra experiment, after quenching to $170\,^{\circ}\mathrm{C}$, the specimen was heated to $330\,^{\circ}\mathrm{C}$, held for $10\,\mathrm{s}$, and cooled back down to $230\,^{\circ}\mathrm{C}$, as shown in Figure 3.10a. The results of the experiment were compared to the results of the treatment in which the steel was heated directly to $230\,^{\circ}\mathrm{C}$ after quenching to $170\,^{\circ}\mathrm{C}$.

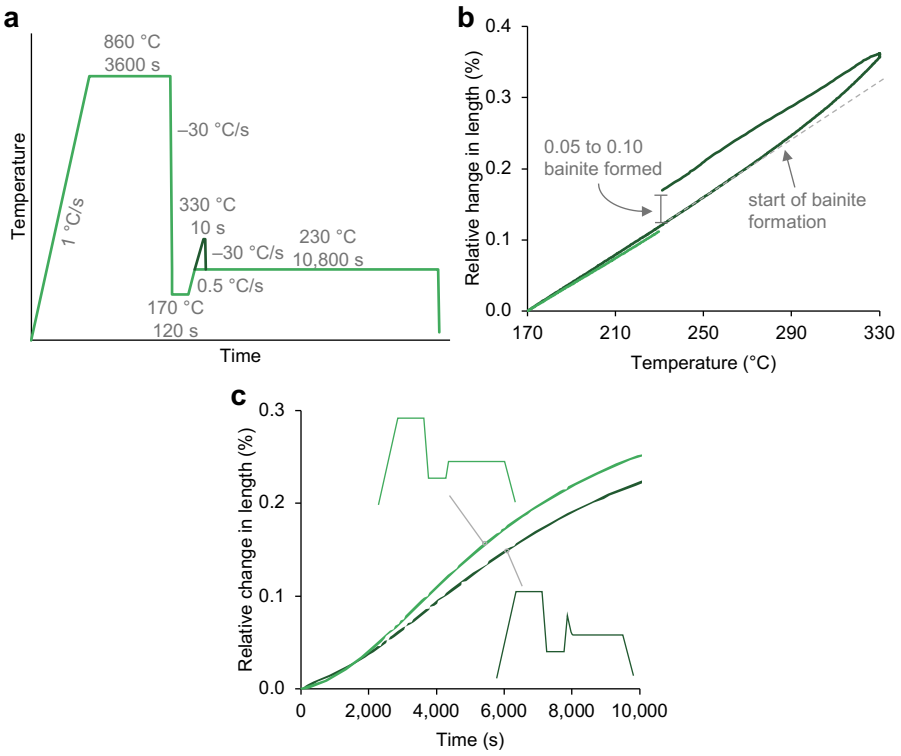

Figure 3.10. Kinetics of bainite formation in the presence of martensite at $230\,^{\circ}\mathrm{C}$ for steel 0.8C with and without an intermediate heating to $330\,^{\circ}\mathrm{C}$. **a.** Time temperature profile of the two treatments. **b.** Relative change in length during heating to 230 or $330\,^{\circ}\mathrm{C}$ after quenching to $170\,^{\circ}\mathrm{C}$. **c.** Relative change in length during isothermal holding at $230\,^{\circ}\mathrm{C}$

Figure 3.10b shows the relative change in length (RCL) for the two treatments during reheating from the quenching temperature of $170\,^{\circ}\mathrm{C}$. At around $280\,^{\circ}\mathrm{C}$, a deviation from linearity indicates that bainite started to form in the steel that was being heated to $330\,^{\circ}\mathrm{C}$. A volume fraction of 0.05 to 0.10 of bainite was formed during heating to $330\,^{\circ}\mathrm{C}$ and holding for $10\,\mathrm{s}$. Thus, if the higher intensity

of acceleration at higher temperatures is due to the aspects that are related to martensite tempering, as discussed above, then these phenomena have already started taking place during heating to $330\,^{\circ}\mathrm{C}$.

Figure 3.10c shows that the kinetics of bainite formation during holding at $230\,^{\circ}\mathrm{C}$ is mostly unaffected by reheating to $330\,^{\circ}\mathrm{C}$. The main difference between the two curves is that the RCL at the end of the treatment is slightly smaller for the sample reheated to $330\,^{\circ}\mathrm{C}$, possibly because this sample already had some 0.05 to 0.10 of bainite formed before the start of isothermal holding. Such a result indicates that the stronger acceleration induced by martensite at higher temperatures is related to an intrinsic effect of temperature and not to other aspects such as martensite tempering, redistribution of carbon, or stress relief.

3.5. Discussion

3.5.1. Area per volume of martensite/austenite interfaces

The results presented so far point out that when prior martensite is present, most of the bainite nucleation events take place at the M/A interface. This is evident in Figure 3.4c, which shows the relative fraction of bainite per nucleation site. According to the proposed model, the parameter that controls the maximum fraction of bainite that can nucleate at M/A interfaces is the area per volume of such interfaces, S_{MA}. This value is particularly difficult to measure experimentally. When analyzing the final microstructure, it is not trivial to distinguish the martensite that was formed prior to bainite formation from bainite itself. The only measurement of S_{MA} reported in the literature, to our knowledge, is from Chang *et al.* [20]. They analyzed the microstructure of quenched and tempered high carbon steels at different fractions of martensite by optical microscopy. The highest values of S_{MA} they found for the different steels ranged from 1.2×10^{6} to $1.7\times10^{6}\,\mathrm{m}^{-1}$, which is close to the values found in the present work (1.3×10^{6} to $2.4\times10^{6}\,\mathrm{m}^{-1}$). However, the values measured by Chang *et al.* may be an underestimation, as they analyzed the microstructure using only optical microscopy, which does not have the resolution to distinguish thin laths and plates of martensite.

A theoretical estimate of S_{MA} can be derived by considering that bainite nucleates at the broad faces of martensite laths or plates. The surface area of the broad face per volume of martensite, S_{M}, can be calculated as $2/t_{\mathrm{m}}$, where t_{m} is the thickness of the martensite laths or plates. To calculate S_{MA}, it is also necessary to know the distribution of martensite within austenite grains. Although it is known that at the end of the transformation martensite is organized into packets and blocks, the initial sequence of martensite formation is less understood because it is experimentally difficult to observe. A reasonable approximation is that during the initial stage laths or plates of martensite grow in different crystallographic directions inside austenite grains, and during the final stage martensite forms in the untransformed region as parallel laths or plates. This sequence of formation was proposed by Raghavan, McMurtrie, and Magee [21, 22] and has some experimental support in the work of Nambu *et al.* [23]. During the initial

stage of martensite formation, S_{MA} can then be approximated by Equation (3.18)

$$S_{MA} = S_M f_m f_\gamma, \tag{3.18}$$

where f_m is the fraction of martensite and f_γ is the fraction of austenite. By substituting S_M for $2/t_m$, Equation (3.18) can be rewritten as

$$\frac{S_{MA}}{f_\gamma} = \frac{2}{t_m} f_m. \tag{3.19}$$

Figure 3.11 shows S_{MA}/f_γ as a function of martensite fraction for all three steels for martensite fractions up to 0.20. For each steel, a linear curve was fitted, and the slope of such curves were used to calculate the thickness of the martensite lath, t_m, using Equation (3.19). Table 3.2 shows the values of t_m calculated using Equation (3.19) and using the model for martensite lath thickness developed by Galindo-Nava and Rivera-Díaz-del-Castillo [24], model which was validated against experimental measurements of martensite lath thickness.

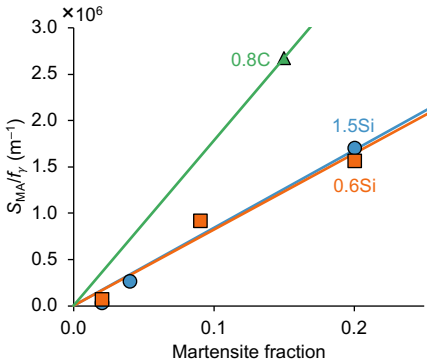

Figure 3.11. Area of M/A interface per volume of remaining austenite as a function of martensite fraction. Markers represent points calculated using the values of S_{MA} found using the analytical model presented here, and solid lines are the best fit linear curves for each steel.

Table 3.2. Thickness of martensite laths or plates.

Steel	Martensite lath or plate thickness (μm)	
	Calculated from S_{MA}	Calculated from ref. [24]
0.8C	0.112	0.066
1.5Si	0.238	0.143
0.6Si	0.243	0.143

The martensite lath thickness – calculated using the values of S_{MA} of the model from this chapter – of Steels 1.5Si and 0.6Si are similar, at 0.240 μm on aver-

age, while that of Steel 0.8C is finer, at $0.112\,\mu m$. This trend is in close agreement with the prediction of Galindo-Nava's model. The thickness calculated using the present model is consistently thicker than the thickness calculated using Galindo-Nava's model. This overestimation is possibly due to the assumption that martensite initially nucleates in different crystallographic directions inside each austenite grain. If some laths or plates nucleate parallel to each other and share a martensite/martensite interface instead of a martensite/austenite interface, Equation (3.18) will overestimate S_{MA} and, consequently, Equation (3.19) will overestimate t_m. A correction factor, K_{MM}, can be applied to Equation (3.18) to account for the fraction of parallel martensite laths sharing a martensite-martensite interface, which then becomes

$$S_{MA} = K_{MM} S_M f_m f_\gamma, \tag{3.20}$$

with K_{MM} equal to 0.59 in the case of the steels in Table 3.2 – if the thickness calculated using Galindo-Nava's model is considered to be the true value of the thickness.

The approach above allows to estimate S_{MA} during the initial stage of martensite formation, possibly to fractions up to 0.20, but it overestimates S_{MA} at larger fractions. Nonetheless, a good correlation was found between S_{MA} and the rate of martensite formation for fractions of martensite of up to 0.68, as shown in Figure 3.12. The kinetics of martensite formation is generally represented by the Koistinen-Marburger (KM) equation [25, 26], which can be written as

$$f_m = 1 - \exp\left[-\alpha_m \left(T_{KM} - T\right)\right], \tag{3.21}$$

where α_m is the composition-dependent KM exponent term, T_{KM} is the KM martensite start temperature, which can be around 10 to $30\,^\circ C$ below the experimentally measured M_S. While Equation (3.21) can yield a fair estimate of the fraction of martensite for a given temperature, it does not capture the evolution of the rate of martensite formation throughout the transformation.

Magee [27] showed that the Koistinen-Marburger equation can be theoretically derived by assuming the number of nucleation events of martensite laths or plates per available austenite fraction is proportional to the undercooling, that is,

$$\mathrm{d}N = \frac{\mathrm{d}f_m}{\overline{V}} = \varphi\left(1 - f_m\right)\mathrm{d}\left(\Delta T\right), \tag{3.22}$$

where N is the number of laths or plates of martensite nucleated, $\overline{V}$ is the average volume of martensite laths or plates, and φ is a proportionality constant. Following Magee's assumption that $\overline{V}$ is constant throughout most of the transformation, Equation (3.22) can be integrated to yield Equation (3.21).

The assumption in Magee's work, and in the Koistinen-Marburger equation, is that the rate of martensite formation per available austenite fraction is constant, which can be represented as

$$\frac{\mathrm{d}f_m}{\mathrm{d}t}\frac{1}{1 - f_m} = \alpha_m. \tag{3.23}$$

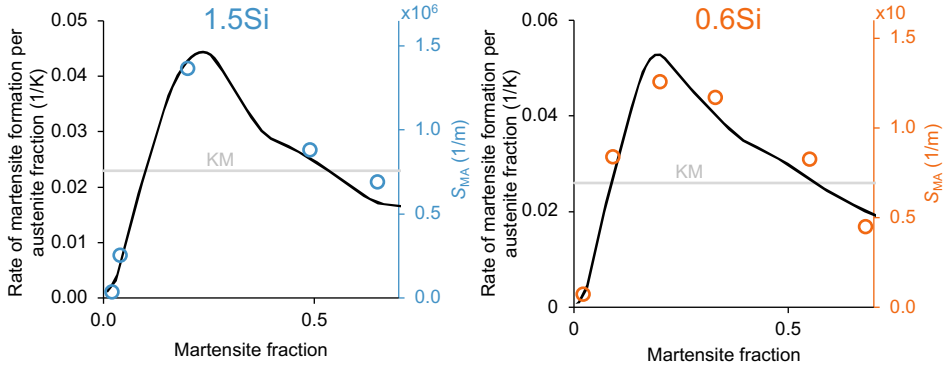

Figure 3.12. Correlation between the rate of martensite formation per austenite fraction and the values of S_{MA} found using our model for steels 1.5Si and 0.6Si. The rate of martensite formation predicted by the Koistinen-Marburger equation is plotted as the grey line marked as KM

However, Equation (3.23) does not match the experimentally measured kinetics of martensite formation. The rate of martensite formation per available fraction of austenite is not constant, as Figure 3.12 shows. Instead, the rate first increases linearly with martensite fraction, reaches a maximum at a fraction of around 0.20, and then slowly decreases. The inability of the KM equation and Magee's theory to represent the rate of martensite formation might be because they do not include the effect of autocatalysis, which is a crucial aspect of martensite formation.

When a martensite lath or plate forms, it deforms the surrounding austenite. The deformation creates defects in the austenite at which more martensite can nucleate, thus creating the autocatalytic effect in martensite formation. Most of the martensite laths or plates nucleate by autocatalysis from these sites that are created during the transformation, not from initially present defects [27–29]. To introduce autocatalysis in Magee's theory, φ in Equation (3.22) needs to be dependent on the number density of potential nucleation sites for martensite. Since the new potential nucleation sites are created in the austenite surrounding the martensite, the number density of these new potential nucleation sites can be considered proportional to the area per volume of the M/A interface. With this modification, Equation (3.22) becomes

$$\mathrm{d}N = \frac{\mathrm{d}f_{\mathrm{m}}}{\overline{V}} = (\varphi_{\mathrm{i}} + \varphi_{\mathrm{A}} S_{\mathrm{MA}})\,(1 - f_{\mathrm{m}})\,\mathrm{d}\,(\Delta T)\,, \tag{3.24}$$

where φ_{i} is the initial value of φ, which is related to the initial potential nucleation sites, and φ_{A} is a proportionality constant related to the potential nucleation sites created by autocatalysis. Since autocatalysis dominates over the initial nucleation rate even at martensite fractions as low as 0.01 (see the slow initial rate in Figure 3.12, and the works of refs. [27–29]), Equation (3.24) can be approximated

as

$$\mathrm{d}N = \frac{\mathrm{d}f_\mathrm{m}}{\overline{V}} \approx \varphi_\mathrm{A} S_\mathrm{MA} \left(1 - f_\mathrm{m}\right) \mathrm{d}\left(\Delta T\right), \tag{3.25}$$

and, from Equation (3.25) and following Magee's assumption of approximately constant $\overline{V}$ throughout most of the martensitic transformation,

$$\frac{\mathrm{d}f_\mathrm{m}}{\mathrm{d}t} \frac{1}{\left(1 - f_\mathrm{m}\right)} \approx K S_\mathrm{MA}, \tag{3.26}$$

where K is a proportionality constant.

Equations (3.24) to (3.26) give the theoretical background for the correlation shown in Figure 3.12. Physically, this correlation indicates that when martensite forms, the surrounding austenite is strained, and the defects created (such as dislocations and the M/A interface itself) can act as nucleation sites for both bainite and martensite.

3.5.2. Mechanism of acceleration

The mechanism by which prior martensite accelerates bainite formation has been extensively discussed in the literature, and this discussion was recently reviewed and summarized by Dhara *et al.* [1]. The main point of discussion is whether the acceleration is caused by bainite nucleation at the M/A interface itself or at dislocations introduced in the austenite during martensite formation.

The model proposed in this chapter assumes that the number density of new potential nucleation sites created by the presence of martensite is proportional to the area per volume of M/A interface. This assumption does not mean, however, that the nucleation sites are at the interface itself. The strain caused by martensite formation is most intense in the regions adjacent to the M/A interfaces [30]. Therefore, if bainite nucleates at dislocations generated by martensite formation, it is still valid to assume that the number density of potential nucleation sites is proportional to the area of M/A interface per volume. Consequently, it is not possible to distinguish, based on the present model, if the dominating nucleation site for bainite is at dislocations in the austenite close to the interface or at the interface itself.

According to the diffusionless theory of bainite formation proposed by Bhadeshia [7], bainite nucleates by the thermally-activated dissociation of dislocations proposed by Olson and Cohen originally for martensite nucleation [31]. The broad faces of martensite hold a glissile interface with austenite and have interface dislocations spaced at a few nanometers [32, 33]. Hence, in addition to dislocations in the austenite originating from strain accommodation, there are dislocations at the interface itself. If bainite nucleates at M/A interfaces, then the nucleation might be assisted by such interface dislocations. As there are dislocations both at the interface and in the austenite surrounding the interface, it is possible that bainite nucleates at both sites.

The discussion on the nucleation site for bainite is not restricted to bainite formation in the presence of martensite. As stated in Chapter 2, similar questions

can be posed regarding bainite nucleation at austenite grain boundaries. Does bainite nucleate at the austenite grain boundaries themselves, or at dislocations piled up at the grain boundaries? And in autocatalysis, does bainite nucleate at the B/A interface itself, or at dislocations close to the interface? And how can the nucleation at interfaces be combined with the theory of nucleation by the dissociation of dislocations?

Such questions cannot be answered by the model proposed in this dissertation. A satisfactory answer may require near atomic resolution *in situ* experiments, high fidelity atomistic simulations, or a combination of both. However, the model presented here gives important insights.

First, the kinetics of bainite formation was successfully replicated by considering a linear relationship between temperature and activation energy for nucleation (Figure 3.4). Such a relationship is consistent the mechanism of nucleation by dissociation of dislocations.

Second, the activation energies for bainite nucleation at the different sites were found to differ by usually less than $5\,\%$. Such a small difference may indicate that the same mechanism operates during bainite nucleation at or near AGBs, B/A interfaces, and M/A interfaces. The difference between activation energies might then be because of different localized factors, such as carbon segregation changing the local driving force for nucleation.

Third, there is a correlation between the bainite acceleration induced by prior martensite and autocatalysis in martensite formation. A possible explanation for the correlation is that both bainite and martensite nucleate at or near the M/A interface. The correlation is shown in Figure 3.12 by plotting the values of S_{MA}, found using the bainite model, and the rate of martensite formation. However, this correlation can be qualitatively verified even without recurring to the model. Figure 3.13 shows the fraction of bainite normalized by the remaining austenite after martensite formation as a function of holding time at different temperatures for steel 1.5Si (Figure 3.13a) and 0.6Si (Figure 3.13b). For both steels, the fastest kinetics of bainite formation is at $345\,^{\circ}\mathrm{C}$, with a 0.20 volume fraction of prior martensite. Also, for both steels, the rate of martensite formation is at its maximum at a 0.20 volume fraction of martensite, as shown in Figure 3.12.

Another aspect that might influence the intensity of the acceleration is the residual stress introduced by martensite formation. However, at least for the conditions tested in this chapter, stress does not seem to play a major role. This is verified by the result shown in Figure 3.10. A significant stress relaxation is expected to have occurred in steel 0.8C during heating to $330\,^{\circ}\mathrm{C}$. Ribamar *et al.* [34] studied the stress relief in austenite during tempering of a steel similar in chemical composition to steel 0.8C by *in situ* synchrotron X-ray diffraction. While at $230\,^{\circ}\mathrm{C}$ almost no stress relief had taken place, at around $300\,^{\circ}\mathrm{C}$ a sharp drop in residual stress started taking place. Therefore, even though the sample heated to $330\,^{\circ}\mathrm{C}$ underwent stress relief, the kinetics of bainite formation at $230\,^{\circ}\mathrm{C}$ in this sample was similar to that of the sample directly heated to $230\,^{\circ}\mathrm{C}$ after quenching (Figure 3.10).

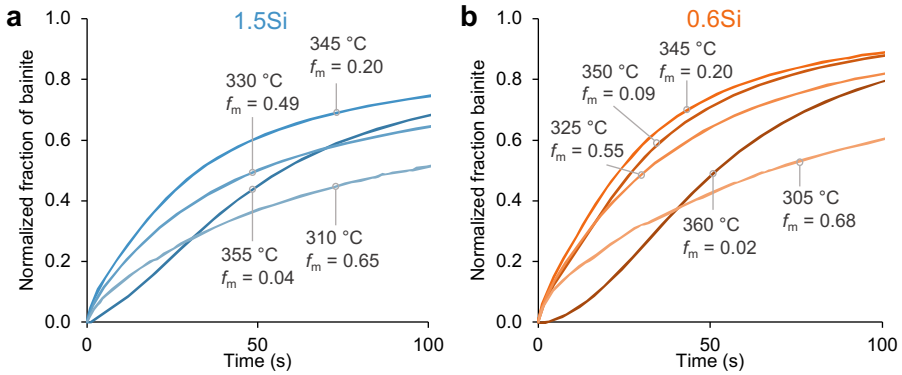

Figure 3.13. Kinetics of bainite formation in the presence of martensite for steels **a.** 1.5Si and **b.** 0.6Si.

3.5.3. Uncertainties in the model

In Chapter 2, it was shown that the uncertainty in the activation energies for nucleation mainly arises from the uncertainty in the input parameters, not from the fitting procedure itself. The same is true for the new parameters included to account for the presence of prior martensite. For instance, S_{MA} is multiplied by u_L to calculate f_{MA}max according to Equation (3.4). Thus, a $50\,\%$ uncertainty for the input value of u_L may result in a $50\,\%$ uncertainty in the output S_{MA}. However, given the correlation between S_{MA}, kinetics of bainite formation, and autocatalysis in martensite shown in Figure 3.12 and Figure 3.13, and the trend for different steels shown in Table 3.2, the relationship between S_{MA}, fraction of martensite, and steel composition seems to have been correctly captured.

Despite the possible high uncertainty in the value of S_{MA}, the fraction of bainite nucleated at the M/A interface also seems to have been correctly captured. This is confirmed by the shape of the curves of bainite formation (Figure 3.5), the effect of boron alloying (Figure 3.6), and the effect of prior austenite grain size (Figure 3.7).

3.6. Conclusion

This chapter introduced a new analytical model for the kinetics of bainite formation in the presence of martensite, which was developed by expanding the model presented in Chapter 2. The proposed model correctly captured the influence of prior martensite on the kinetics of bainite formation. This was achieved by distinguishing the fraction of bainite nucleated at each type of nucleation site: austenite grain boundaries, bainite/austenite interfaces, and martensite/austenite interfaces.

Applying the model to experimental data revealed that when prior martensite was present at a volume fraction higher than 0.10, most bainite nucleation events occurred at or near the martensite/austenite interface. The origin of the acceler-

ation induced by prior martensite is the large area per volume of M/A interfaces (in the order of $10^6\,\mathrm{m}^{-1}$), which can serve as nucleation site for most of the bainite sub-units. Such acceleration is more pronounced at higher temperatures, possibly because bainite sub-units are larger the higher the temperature.

Combining the model with measuring the thermal gradients in the dilatometry samples showed that the two-order-of-magnitude increase in the initial rate of bainite nucleation previously reported in the literature [2] is a measuring artifact from quenching dilatometers. Instead of bainite formation, the high rate of transformation comes from martensite formation at the colder regions of the dilatometry sample. Additionally, because of thermal gradients, a small fraction of martensite (< 0.05) formed even when the holding temperature was above M_S. This resulted in a bainite acceleration above M_S which is similar to the swing-back effect reported in the literature [10].

When M/A interfaces are the main nucleation site, changing the austenite grain size or the chemistry of the austenite grain boundaries, such as by boron segregation, does not influence the kinetics of bainite formation. This opens up new possibilities for steel design. Traditionally, bainitic steels need to be alloyed with elements that increase the steel's hardenability, such as manganese, nickel, chromium, or molybdenum. However, such elements slow down bainite formation. Unlike such elements, the effect of boron on hardenability originates from its segregation to austenite grain boundaries. Therefore, when prior martensite is present, boron loses its retarding effect on bainite formation. Thus, boron can be used in a unique way, which increases the hardenability of the steel without jeopardizing the kinetics of bainite formation. Additionally, boron is the most effective element in increasing the hardenability, with $20\,\mathrm{ppm}$ yielding the same increase in hardenability as $0.6\,\mathrm{wt.\%}$ Mn or $2\,\mathrm{wt.\%}$ Ni [35]. Substituting $2\,\mathrm{wt.\%}$ Ni by $20\,\mathrm{ppm}$ of B decreases the equivalent CO_2 emissions by $200\,\mathrm{kg}$ per ton of steel while also reducing the associated costs by $44\,\mathrm{USD}$ per ton of steel [36]. Boron also increases the cohesion of austenite grain boundaries, which might increase the steel's toughness and resistance to hydrogen embrittlement [37–39].

References

[1] S. Dhara, S. M. C. van Bohemen, and M. J. Santofimia. “Isothermal decomposition of austenite in presence of martensite in advanced high strength steels: A review”. In: *Materials Today Communications* 33 (Dec. 1, 2022), p. 104567. doi: 10.1016/j.mtcomm.2022.104567.

[2] A. Navarro-López, J. Sietsma, and M. J. Santofimia. “Effect of Prior Athermal Martensite on the Isothermal Transformation Kinetics Below Ms in a Low-C High-Si Steel”. In: *Metallurgical and Materials Transactions A* 47.3 (Mar. 1, 2016), pp. 1028–1039. doi: 10.1007/s11661-015-3285-6.

[3] W. Gong, Y. Tomota, S. Harjo, Y. Su, and K. Aizawa. “Effect of prior martensite on bainite transformation in nanobainite steel”. In: *Acta Materialia* 85 (Feb. 2015), pp. 243–249. doi: 10.1016/j.actamat.2014.11.029.

[4] A. Navarro-López, J. Hidalgo, J. Sietsma, and M. J. Santofimia. “Unravelling the mechanical behaviour of advanced multiphase steels isothermally obtained below *Ms*”. In: *Materials & Design* 188 (Mar. 1, 2020), p. 108484. doi: 10.1016/j.matdes.2020.108484.

[5] V. Smanio and T. Sourmail. “Effect of Partial Martensite Transformation on Bainite Reaction Kinetics in Different 1%C Steels”. In: *Solid State Phenomena* 172-174 (June 30, 2011), pp. 821–826. doi: 10.4028/www.scientific.net/SSP.172-174.821.

[6] A. M. Ravi, A. Kumar, M. Herbig, J. Sietsma, and M. J. Santofimia. “Impact of austenite grain boundaries and ferrite nucleation on bainite formation in steels”. In: *Acta Materialia* 188 (Apr. 15, 2020), pp. 424–434. doi: 10.1016/j.actamat.2020.01.065.

[7] H. K. D. H. Bhadeshia. *Bainite in Steels: Theory and Practice, Third Edition*. 3rd ed. London: CRC Press, Mar. 6, 2015. 616 pp. doi: 10.1201/9781315096674.

[8] C. Garcia-Mateo, T. Sourmail, A. Philippot, L. Morales-Rivas, and J. A. Jimenez. “Effect of prior martensite on bainitic transformation of high Si hypereutectoid steel”. In: *Journal of Materials Research and Technology* 30 (May 1, 2024), pp. 6995–7005. doi: 10.1016/j.jmrt.2024.05.090.

[9] S. M. C. van Bohemen and L. Morsdorf. “Predicting the Ms temperature of steels with a thermodynamic based model including the effect of the prior austenite grain size”. In: *Acta Materialia* 125 (Feb. 15, 2017), pp. 401–415. doi: 10.1016/j.actamat.2016.12.029.

[10] S. V. Radcliffe and E. C. Rollason. “The kinetics of the formation of bainite in high-purity iron-carbon alloys”. In: *Journal of the Iron and Steel Institute* (Jan. 1959), pp. 56–65.

[11] P. Douguet, G. Da Rosa, P. Maugis, J. Drillet, and K. Hoummada. “Effect of boron segregation on bainite nucleation during isothermal transformation”. In: *Scripta Materialia* 207 (Jan. 15, 2022), p. 114286. doi: 10.1016/j.scriptamat.2021.114286.

[12] T. S. Prithiv, B. Gault, Y. Li, D. Andersen, N. Valle, S. Eswara, D. Ponge, and D. Raabe. “Austenite grain boundary segregation and precipitation of boron in low-C steels and their role on the heterogeneous nucleation of ferrite”. In: *Acta Materialia* 252 (June 15, 2023), p. 118947. doi: 10.1016/j.actamat.2023.118947.

[13] G. Da Rosa, P. Maugis, A. Portavoce, J. Drillet, N. Valle, E. Lentzen, and K. Hoummada. “Grain-boundary segregation of boron in high-strength steel studied by nano-SIMS and atom probe tomography”. In: *Acta Materialia* 182 (Jan. 1, 2020), pp. 226–234. doi: 10.1016/j.actamat.2019.10.029.

[14] G. Da Rosa, P. Maugis, A. Portavoce, S. Lartigue-Korinek, N. Valle, E. Lentzen, J. Drillet, and K. Hoummada. “Boron segregation at austenite grain boundaries: An equilibrium phenomenon”. In: *Acta Materialia* 255 (Aug. 15, 2023), p. 119098. doi: 10.1016/j.actamat.2023.119098.

[15] J. Takahashi, K. Ishikawa, K. Kawakami, and M. Fujioka. “Hardenability Improvement Mechanisms and Hardenability-Controlling Factors in Steels With Combined Mo–B Addition”. In: *Metallurgical and Materials Transactions A* 54.2 (Feb. 1, 2023), pp. 526–536. doi: 10.1007/s11661-022-06895-9.

[16] Y. J. Li, D. Ponge, P. Choi, and D. Raabe. “Atomic scale investigation of non-equilibrium segregation of boron in a quenched Mo-free martensitic steel”. In: *Ultramicroscopy*. 1st International Conference on Atom Probe Tomography & Microscopy 159 (Dec. 1, 2015), pp. 240–247. doi: 10.1016/j.ultramic.2015.03.009.

[17] S. M. C. van Bohemen and J. Sietsma. “Kinetics of martensite formation in plain carbon steels: critical assessment of possible influence of austenite grain boundaries and autocatalysis”. In: *Materials Science and Technology* 30.9 (July 1, 2014). Publisher: Taylor & Francis _eprint: https://doi.org/10.1179/1743284714Y.0000000532, pp. 1024–1033. doi: 10.1179/1743284714Y.0000000532.

[18] S. D. Catteau, T. Sourmail, and A. Moine. “Dilatometric Study of Phase Transformations in Steels: Some Issues”. In: *Materials Performance and Characterization* 5.5 (Dec. 22, 2016), pp. 564–584. doi: 10.1520/MPC20160069.

[19] A. M. Ravi, A. Navarro-López, J. Sietsma, and M. J. Santofimia. “Influence of martensite/austenite interfaces on bainite formation in low-alloy steels below *Ms*”. In: *Acta Materialia* 188 (Apr. 15, 2020), pp. 394–405. doi: 10.1016/j.actamat.2020.02.003.

[20] P. H. Chang, P. G. Winchell, and G. L. Liedl. “Quantitative geometric characterization of high carbon martensite”. In: *Metallurgical Transactions A* 14.1 (Feb. 1, 1983), pp. 163–173. doi: 10.1007/BF02651612.

[21] V. Raghavan. “Formation sequence of plates in isothermal martensite transformation”. In: *Acta Metallurgica* 17.10 (1969). Publisher: Elsevier, pp. 1299–1303.

[22] D. G. McMurtrie and C. L. Magee. “The average volume of martensite plates during transformation”. In: *Metallurgical Transactions* 1.11 (Nov. 1, 1970), pp. 3185–3191. doi: 10.1007/BF03038436.

[23] S. Nambu, N. Shibuta, M. Ojima, J. Inoue, T. Koseki, and H. Bhadeshia. “In situ observations and crystallographic analysis of martensitic transformation in steel”. In: *Acta Materialia* 61.13 (Aug. 2013), pp. 4831–4839. doi: 10.1016/j.actamat.2013.04.065.

[24] E. Galindo-Nava and P. Rivera-Díaz-del-Castillo. “A model for the microstructure behaviour and strength evolution in lath martensite”. In: *Acta Materialia* 98 (Oct. 2015), pp. 81–93. doi: 10.1016/j.actamat.2015.07.018.

[25] D. P. Koistinen and R. E. Marburger. “A general equation prescribing the extent of the austenite-martensite transformation in pure iron-carbon alloys and plain carbon steels”. In: *Acta Metallurgica* 7.1 (Jan. 1, 1959), pp. 59–60. doi: 10.1016/0001-6160(59)90170-1.

[26] S. M. C. van Bohemen. “Bainite and martensite start temperature calculated with exponential carbon dependence”. In: *Materials Science and Technology* 28.4 (Apr. 1, 2012). Publisher: Taylor & Francis _eprint: https://doi.org/10.1179/1743284711Y.0000000097, pp. 487–495. doi: 10.1179/1743284711Y.0000000097.

[27] C. L. Magee. “The nucleation of martensite”. In: *Phase Transformations*. ASM, 1970, pp. 115–156.

[28] V. Raghavan and A. R. Entwisle. “Isothermal martensite kinetics in iron alloys”. In: *Physical Properties of Martensite and Bainite*. Iron and Steel Institute, 1965, pp. 30–37.

[29] S. R. Pati and M. Cohen. “Nucleation of the isothermal martensitic transformation”. In: *Acta Metallurgica* 17.3 (Mar. 1, 1969), pp. 189–199. doi: 10.1016/0001-6160(69)90058-3.

[30] G. Miyamoto, A. Shibata, T. Maki, and T. Furuhara. “Precise measurement of strain accommodation in austenite matrix surrounding martensite in ferrous alloys by electron backscatter diffraction analysis”. In: *Acta Materialia* 57.4 (Feb. 1, 2009), pp. 1120–1131. doi: 10.1016/j.actamat.2008.10.050.

[31] G. B. Olson and M. Cohen. “A general mechanism of martensitic nucleation: Part III. Kinetics of martensitic nucleation”. In: *Metallurgical Transactions A* 7.12 (Dec. 1, 1976), pp. 1915–1923. doi: 10.1007/BF02659824.

[32] T. Moritani, N. Miyajima, T. Furuhara, and T. Maki. “Comparison of interphase boundary structure between bainite and martensite in steel”. In: *Scripta Materialia* 47.3 (Aug. 2, 2002), pp. 193–199. doi: 10.1016/S1359-6462(02)00128-8.

[33] B. P. J. Sandvik and C. M. Wayman. “Characteristics of lath martensite: Part III. Some theoretical considerations”. In: *Metallurgical Transactions A* 14.4 (Apr. 1, 1983), pp. 835–844. doi: 10.1007/BF02644286.

[34] G. G. Ribamar, G. Miyamoto, T. Furuhara, J. D. Escobar, J. A. Ávila, E. Maawad, N. Schell, J. P. Oliveira, and H. Goldenstein. “On the Evolution of Austenite During Tempering in High-Carbon High-Silicon Bearing Steel by High Energy X-Ray Diffraction”. In: *Metallurgical and Materials Transactions A* 55.1 (Jan. 1, 2024), pp. 93–100. doi: 10.1007/s11661-023-07229-z.

[35] A. Gramlich, C. van der Linde, M. Ackermann, and W. Bleck. “Effect of molybdenum, aluminium and boron on the phase transformation in 4 wt.–% manganese steels”. In: *Results in Materials* 8 (Dec. 1, 2020), p. 100147. doi: 10.1016/j.rinma.2020.100147.

[36] A. Gramlich, C. Helbig, M. Schmidt, and W. Hagedorn. “A comprehensive design approach to increase the performance of steels under minimal costs and environmental impacts”. In: *Sustainable Materials and Technologies* 41 (Sept. 1, 2024), e01040. doi: 10.1016/j.susmat.2024.e01040.

[37] G. Hachet, A. Tehranchi, H. Shi, M. Prabhakar, S. Wei, K. Angenendt, S. Zaefferer, B. Gault, B. Sun, D. Ponge, and D. Raabe. “Segregation at prior austenite grain boundaries: The competition between boron and hydrogen”. In: *International Journal of Hydrogen Energy* 95 (Dec. 18, 2024), pp. 734–746. doi: 10.1016/j.ijhydene.2024.11.166.

[38] M. Kuzmina, D. Ponge, and D. Raabe. “Grain boundary segregation engineering and austenite reversion turn embrittlement into toughness: Example of a 9wt.% medium Mn steel”. In: *Acta Materialia* 86 (Mar. 1, 2015), pp. 182–192. doi: 10.1016/j.actamat.2014.12.021.

[39] R. Wu, A. J. Freeman, and G. B. Olson. “First Principles Determination of the Effects of Phosphorus and Boron on Iron Grain Boundary Cohesion”. In: *Science* 265.5170 (July 15, 1994). Publisher: American Association for the Advancement of Science, pp. 376–380. doi: 10.1126/science.265.5170.376.

4

Shortening the heat treatment of third generation advanced high strength steels by forming carbide free bainite in the presence of martensite

Successful implementation of third generation advanced high strength steels (3rd gen AHSS) can be accelerated by developing steels that can be heat treated in existing industrial lines. Here, we develop new carbide free bainitic (CFB) steels in which bainite formation is accelerated by a 0.2 volume fraction prior martensite and thus can be realized in 5 minutes, making them suitable for manufacturing in modern continuous annealing lines for bare steel strips. The resulting microstructure consists of bainitic ferrite, tempered martensite, and retained austenite. Carbon and silicon had the most pronounced effect on the mechanical properties among the studied alloying elements (niobium, chromium, molybdenum) because of their influence on the fraction and stability of retained austenite. Our proposed treatment, called here bainite accelerated by martensite (BAM), showed higher strength and lower global formability than traditional CFB without prior martensite (also called TRIP-assisted bainitic ferrite, TBF) and quenched and partitioned (Q&P) steels. Five of the designed steels showed tensile strength higher than 1370 MPa, a total elongation higher than 8 %, and hole expansion capacity higher than 30 %, and thus meet the requirements for the strongest commercial grades of complex phase steels with improved formability. This work broadens the possibilities of using existing industrial lines for manufacturing novel 3rd gen AHSS.

To be submitted for publication.

4.1. Introduction

The pressure on the automotive industry to simultaneously decrease car weight and increase passenger safety has stimulated the quick development of novel high strength sheet steels in the past 30 years, such as the so-called advanced high strength steels (AHSS) [1]. The first generation (1st gen) of AHSS achieved higher ultimate tensile strength (UTS) than the then-available commercial steels, although with limited ductility (e.g. 5 % total elongation at 1180 MPa ultimate tensile strength – UTS – for a complex-phase grade [2]). The balance of strength and ductility came by combining a soft ferrite matrix with hard martensite or bainite regions and, in some cases, regions of retained austenite. The family of 1st gen AHSS includes dual phase (DP) [3], transformation induced plasticity aided (TRIP) [4], and complex phase (CP) [5] steels.

As there is still a large pressure to reduce carbon emissions in the automotive industry by reducing car weight, the combination of strength and ductility achievable in 1st gen AHSS is not sufficient for current and future demands. Highly alloyed austenitic steels exhibiting twinning induced plasticity (TWIP) achieve a much higher combination of ductility and strength (e.g. 70 % total elongation at 1200 MPa of UTS [6]). These alloys were called 2nd gen AHSS. However, the elevated cost associated with high alloying restricted the widespread industrial application of such steels [1].

A 3rd generation of AHSS started being developed in the mid 2000s with the goal of achieving better strength-ductility balance than the 1st gen AHSS but with much lower alloying than 2nd gen AHSS. The improved mechanical properties with respect to 1st gen AHSS were achieved by avoiding or drastically reducing ferrite formation and introducing a larger fraction of retained austenite. Prominent members of the third generation of AHSS family are carbide-free bainitic (CFB) [7] – also called TRIP-assisted bainitic ferrite, TBF – and quenched and partitioned (Q&P) [8] steels. Medium manganese steels, which are also members of the 3rd gen AHSS family, still have a significant ferrite fraction, such as in 1st gen AHSS, but have a large fraction of manganese-enriched retained austenite [9].

Despite 3rd gen AHSS being intensively researched since 2005, their global commercialization started only around 2020 [10]. One of the reasons for this delay is that, despite such steels having lower alloying content than 2nd gen AHSS, the necessary heat treatment could not be directly performed in existing industrial lines dedicated to 1st gen AHSS. The general treatment of Q&P steels is two-step, which involves quenching to a temperature T_{Q}, which controls the martensite fraction, and reheating to a temperature T_{P} for carbon diffusion and partitioning [11–13]. It is possible to achieve mechanical properties suitable for 3rd gen AHSS with a one-step Q&P ($T_{\mathrm{P}} = T_{\mathrm{Q}}$), which does not require reheating, but, at low T_{P}, carbon may not sufficiently homogenize in the remaining austenite [14]. Therefore, the alloy design should be tuned to avoid the formation of fresh martensite during cooling to room temperature, which can compromise the local formability of the steel.

TBF steels adopt a heat treatment comparable to 1st gen TRIP steels, with the main difference being that in TBF steels, bainite is formed after full austenitiza-

tion, while in 1st gen TRIP steels bainite is formed after intercritical annealing. To achieve sufficient hardenability and avoid ferrite formation, the alloying content in TBF steels is higher than in 1st gen TRIP steels, which in turn slows down the kinetics of bainite formation, rendering it too long to be used in some industrial lines. In continuous annealing lines for bare cold-rolled steels, bainite formation happens in the overaging section and is restricted to a maximum of $10\,\mathrm{min}$ for $2\,\mathrm{mm}$ thickness strips and $6\,\mathrm{min}$ for $1\,\mathrm{mm}$ thickness strips [1]. However, in many recently developed TBF steels with mechanical properties compatible with 3rd gen AHSS, the required time for bainite formation is between 7 and $90\,\mathrm{min}$ [15–22]. Short times (below $7\,\mathrm{min}$) were tested in the works of Sugimoto *et al.* [7, 23–27] and Ebner *et al.* [28]. Despite being restricted to such short times, Sugimoto *et al.* achieved a 1370 MPa tensile strength with $30\,\%$ hole expansion capacity (HEC) – which is a measure of local formability [29] – and $8\,\%$ total elongation [26]. Such results, which were the best combination of strength and formability, were achieved for a single condition out of 50 tested combinations of different niobium contents and isothermal holding temperatures. Moreover, the isothermal holding temperature that led to these specific mechanical properties was $100\,^{\circ}\mathrm{C}$ below the martensite start temperature (M_S), and hence the majority phase was tempered martensite – not bainite.

This Chapter studies the influence of alloying elements (C, Si, Mn, Cr, Mo, and Nb) on the microstructure, kinetics, and mechanical properties of 3rd gen advanced high strength sheet steels designed to be manufactured in continuous annealing lines. A careful balance between the elements is needed because the alloying should be high enough to ensure sufficient hardenability and avoid ferrite formation but lean enough so that bainite can be formed in the overaging section of existing modern continuous annealing lines. To help achieve this balance, bainite was formed at around $20\,^{\circ}\mathrm{C}$ below M_S in the presence of around 0.2 volume fraction of prior martensite to take advantage of the martensite-induced bainite acceleration discussed in Chapter 3 and by Dhara *et al.* [30]. This heat treatment, called here bainite accelerated by martensite (BAM), is benchmarked against conventional TBF and two-step Q&P heat treatments. The proposed material and heat treatment achieves a UTS of $1420\,\mathrm{MPa}$, a total elongation of $9\,\%$, and a HEC of $30\,\%$ after isothermal bainite formation for $300\,\mathrm{s}$. Such properties meet the requirements of the new steel grade CR1000Y1370T-CH, which is the strongest complex phase steel with improved formability in VDA's (German Association of the Automotive Industry) recent standard for 3rd gen AHSS [31], while having a heat treatment suitable for modern continuous annealing lines.

4.2. Experimental procedure

Steel ingots with eight different chemical compositions (Table 4.1) and $25\,\mathrm{kg}$ each were manufactured at Tata Steel (IJmuiden, The Netherlands) using a vacuum induction melting furnace. The compositions were selected to allow the study of the effects of C, Mn, Si, Cr, Mo, and Nb content. The ingots were reheated to $1230\,^{\circ}\mathrm{C}$, annealed for $45\,\mathrm{min}$, and rough milled from 100 to $40\,\mathrm{mm}$ thick. Each

roughed ingot was cut into 70 mm long blocks and each block was reheated to 1230 °C for 30 min and hot rolled in five steps from 40 to 3.8 mm thick. Hot rolling started at 1170 °C and finished at 900 °C. The hot rolled slabs were transported to a Run-Out-Table simulator in which slabs were cooled with a cooling rate of 30–40 °C s^{-1} to arrive at a coiling temperature of about 630 °C. The slabs were put in the furnace, and a standard coiling simulation program was applied. The coiling temperature of 630 °C and slow furnace cooling ensure that a ferrite-pearlite microstructure is formed in the hot rolled slabs. Finally, the pickled slabs were cold rolled to a final thickness of 1 mm and cut to appropriate sizes for dilatometry and annealing in a continuous annealing simulator (CASim).

Table 4.1. Chemical composition of the steels tested and relevant temperatures of the heat treatment in the CASim. Ref is the reference composition, and all other steels are named based on the change in their composition with respect to the reference material. M_S is the martensite start temperature, and the meaning of the other temperatures is found in the heat treatment scheme in Figure 4.1b.

Steel		Ref	0.6Si	1.0Si	0.02Nb	1.7Mn-0.6Cr	1.7Mn-0.6Cr-0.2Mo	0.27C-1.7Mn-0.6Cr	0.30C-1.7Mn-0.6Cr
Chemical composition (wt.%)	C	0.240	0.246	0.246	0.241	0.241	0.234	0.273	0.304
	Mn	2.28	2.26	2.34	2.31	1.68	1.73	1.73	1.71
	Si	1.51	0.61	1.05	1.55	1.54	1.56	1.49	1.46
	Cr	-	-	-	-	0.59	0.59	0.59	0.58
	Mo	-	-	-	-	-	0.18	-	-
	Nb	-	-	-	0.026	-	-	-	-
Temperature (°C)	M_S	359	355	370	370	374	370	351	330
	T_{aus}	900	840	865	900	910	910	900	890
	T_{TBF}	390	390	390	390	390	390	390	390
	T_{BAM}	340	340	340	340	350	350	330	310
	T_Q	280	280	280	280	290	290	270	250
	T_P	400	400	400	400	400	400	400	400

Phase fractions (retained austenite, tempered martensite, fresh martensite, and bainite) and the kinetics of bainite formation were measured using dilatometry and X-ray diffraction (XRD). A Bähr 805 A/T dilatometer was used in quench mode with quartz rods, He-flow cooling, and $10 \times 5 \times 1\,\mathrm{mm}^3$ samples cut from the cold rolled sheets, with the long direction of the sample parallel to the rolling direction. One thermocouple was spot-welded at the center of the sample, which was used for temperature control, and one spot-welded 1 mm from the border of the sample, which was used to measure the thermal gradient at the sample [32]. XRD experiments were performed in a Bruker D8 Advance diffractometer in a Bragg-Bretano geometry with graphite monochromator and Vantec position-sensitive detector using Co K_α radiation and operating at 40 kV and 40 mA with a divergence slit V4. The step size was 0.035° (2θ), and the counting time per step was 3 s.

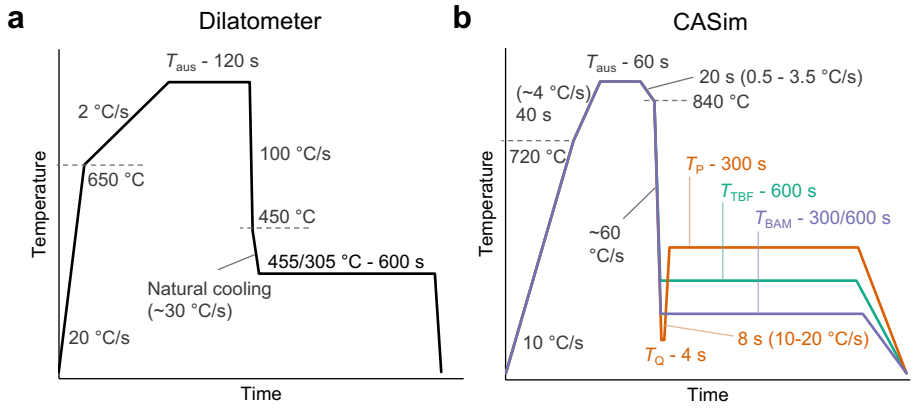

Figure 4.1. Heat treatments applied in **a.** the dilatometer and **b.** the CASIM. Natural cooling was used in the dilatometer for isothermal treatments below $450\,^{\circ}\mathrm{C}$ to minimize the thermal gradients in the sample [32]. T_{aus}, T_{Q}, T_{P}, T_{TBF}, and T_{BAM} for the CASim are given for each steel in Table 4.1. T_{aus} for the dilatometer is similar to T_{aus} for the CASim, unless otherwise stated.

Samples of selected steels were heat treated in the dilatometer, according to the thermal profiles of Figure 4.1a, to measure the fraction of austenite decomposed as a function of temperature during cooling and of time during isothermal holding. The phase fractions were calculated using the lever rule with the non-linear coefficients of thermal expansion of iron [33]. The distance between the expansion curves for austenite and martensite/bainite was adjusted to match the fraction of retained austenite at room temperature measured by XRD. The same procedure was applied in previous works [34]. The fraction of retained austenite was measured from the XRD experiments following the procedure of Jatczak [35]. Three body-centered cubic (BCC) peaks – $\{110\}$, $\{200\}$, and $\{211\}$ – and four face-centered cubic (FCC) peaks – $\{111\}$, $\{200\}$, $\{220\}$, and $\{311\}$ – were integrated using xrdfit [36].

To analyze the mechanical properties, the cold rolled sheets were heat treated in a continuous annealing simulator (CASim) according to the heat treatments shown in Figure 4.1b, which are named BAM (bainite accelerated by martensite), TBF (TRIP-assisted bainitic ferrite), and Q&P (quenched and partitioned). BAM also stands for the initials of the expected phases: bainite, austenite, and martensite. In the CASim, the extremities of the steel sheet ($550\,\mathrm{mm}$ in length and $100\,\mathrm{mm}$ in width) are clamped by metallic grips, and the heat treatment is applied by Joule heating. Two sheets were made for each combination of steel and heat treatment. Two JIS5 tensile samples [37] were cut from one of the sheets, and two HEC samples ($90 \times 90\,\mathrm{mm}^2$) were cut from the other sheet. After tensile testing, one $10\times10\times1\,\mathrm{mm}^3$ sample was cut from the head of the specimen, which was undeformed, and one was cut from the deformed part of the specimen, close to – but not including – the neck. The cross-sections normal to the transversal

direction of such samples were ground and polished, using the same procedure used for microstructural characterization described in the following paragraph, and analyzed in the XRD to measure the fraction of retained austenite.

Microstructural characterization was carried out in the scanning electron microscopes (SEM) JEOL JSM-6500F and Thermo Fisher Helios G4 UXe PFIB. Samples were cut from the head of the tensile test specimens, and the cross-section normal to the transversal direction was analyzed. All samples were ground up to $2000\,\mathrm{mesh}$ silicon carbide grinding paper, polished up to $1\,\mu\mathrm{m}$ diamond suspension, and etched with Nital $2\,\%$.

4.3. Results

4.3.1. Kinetics of bainite formation

Figure 4.2 shows the kinetics of bainite formation for the reference steel and steel 0.6Si. Based on the dilatometry cooling curves, no austenite decomposition took place during cooling from austenitization to the isothermal holding temperature. In the reference steel, which is alloyed with 1.5Si, the transformation reaches stasis before austenite is fully decomposed. The bainite fraction formed at stasis increases with decreasing temperature. This phenomenon, referred to as incomplete reaction, is common in steels alloyed with silicon. Silicon retards cementite formation, and carbon which is in excess of the carbon solubility in bainitic ferrite is partitioned to the austenite. The driving force for bainite nucleation and growth decreases as austenite is enriched with carbon, until the point at which bainite cannot form anymore. The carbon content in austenite at stasis can be calculated either using the T_0 or T_0' temperatures, which assume the diffusionless theory of bainite formation [38], or using the WB_s temperature, which assumes the diffusional theory [39]. Both theories indicate that the lower the temperature the higher the carbon content in austenite at stasis and the higher the fraction of bainite at stasis.

The austenite remaining after bainite formation in the reference steel can transform to martensite upon cooling to room temperature. Figure 4.2b shows the change in length during the final cooling for the different isothermal temperatures tested. The volume fraction of martensite formed during cooling, calculated from the lever rule, was 0.26 for isothermal holding at $455\,^\circ\mathrm{C}$, 0.08 for isothermal holding at $415\,^\circ\mathrm{C}$, and less than 0.05 for all other temperatures. The fraction of martensite formed during cooling decreases with isothermal holding temperature because the remaining austenite is more enriched in carbon after bainite formation at lower temperatures (based on the T_0' and WB_S temperatures) and, consequently, its martensite start temperature is lower [40].

Figure 4.2a shows that the kinetics of bainite formation is accelerated by decreasing the isothermal holding temperature in steel Ref even without the presence of prior martensite. This effect is because of the incomplete transformation, as less bainite is formed at higher temperatures. For steel 0.6Si, which almost fully transforms to bainite at any given temperature, the kinetics of bainite formation slows down when the temperature is decreased from $450\,^\circ\mathrm{C}$ down to $380\,^\circ\mathrm{C}$,

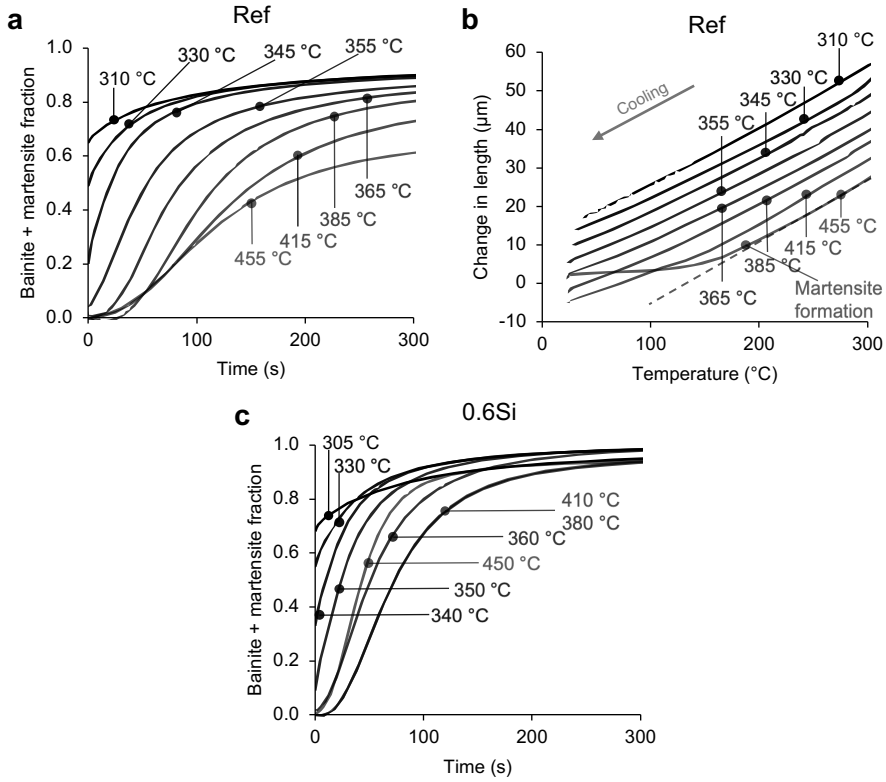

Figure 4.2. Kinetics of bainite formation at different isothermal temperatures for steel **a.** Ref and **c.** 0.6Si; and **b.** change in length during cooling after bainite formation for steel Ref, in which a deviation from the nonlinear expansion coefficient indicates the formation of martensite. T_{aus} was $925\,^{\circ}\mathrm{C}$ for steel Ref and $875\,^{\circ}\mathrm{C}$ for steel 0.6Si.

as Figure 4.2c shows. The opposite trend to steel Ref indicates that the incomplete reaction phenomenon played a strong role in accelerating bainite formation at lower temperatures for steel Ref.

In Steel 0.6Si, from $360\,^{\circ}\mathrm{C}$ and below, some martensite is formed prior to bainite formation, and the kinetics of bainite formation is accelerated. Despite $360\,^{\circ}\mathrm{C}$ being $5\,^{\circ}\mathrm{C}$ above M_{S} for steel 0.6Si, there was an undershoot in the temperature during cooling – especially at the border of the sample, which was in contact with the cold dilatometer rods –, and a volume fraction of 0.02 to 0.05 of martensite was formed. Such a low fraction was already efficient in accelerating bainite formation. At $350\,^{\circ}\mathrm{C}$, with a prior martensite fraction of 0.09, bainite formation is faster than at $450\,^{\circ}\mathrm{C}$. Such results confirm that the effect of bainite acceleration by the presence of prior martensite operates in these steels. The curves of bainite formation for steels Ref and 0.6Si are presented here to illustrate the bainite-accelerating effect induced by prior martensite. All other

compositions were also tested, and a similar accelerating effect was observed for all steels.

4.3.2. Microstructure

Figure 4.3 shows the microstructure of the different steels after being treated in the CASim. The microstructures consist of bainitic ferrite, films of retained austenite, martensite/austenite (MA) islands, and, for the heat treatments BAM and Q&P, tempered martensite. Some carbides may be present, especially in the steel 0.6Si. The fraction of retained austenite measured by XRD is presented in Figure 4.4. No proeutectoid ferrite was observed in any of the samples.

The reference steel showed large MA islands after the TBF treatment. After the BAM treatment, the MA islands are smaller and more dispersed. Such MA islands are formed from the austenite remaining after the end of the isothermal holding step. This remaining austenite partly transforms to martensite upon cooling to room temperature. In the BAM treatment, bainite formation is faster, and the fraction of remaining austenite is lower than in the TBF (Figure 4.2a), which contributes to having fewer and smaller islands of remaining austenite.

The size of MA islands in the Q&P treatment was similar to those in TBF for the reference steel. Such MA islands are formed from the austenite remaining after quenching to T_{Q} that did not decompose into bainite during partitioning at T_{P}. The martensite fraction formed upon quenching to T_{Q} was estimated to be 0.80, and the volume fraction of retained austenite was measured as 0.14 by XRD. Thus, most of the austenite remaining after quenching to T_{Q} does not decompose into bainite during partitioning and is retained at room temperature.

In steel 0.6Si, the low silicon content resulted in less retained austenite, as shown in Figure 4.4, and possibly more carbide formation. However, a few MA islands were still found in steel 0.6Si, as can be observed in Figure 4.3. Such MA islands mostly lie in bands parallel to the rolling direction and are probably in regions with pronounced chemical segregation of alloying elements, such as manganese. These regions are formed during the solidification of the steel ingots.

The addition of $0.026\,\mathrm{wt.\%}$ Nb changed the morphology of the MA islands and of the films of retained austenite. In the reference steel with the TBF treatment, there were thin, elongated films of retained austenite, and the MA islands were large and blocky. Conversely, in steel 0.02Nb, there were significantly fewer films of retained austenite, and the MA islands were smaller and globular.

The mechanism by which niobium changed the morphology of the MA islands and the films of retained austenite is not clear. One possibility is that the presence of niobium carbides induces the intragranular nucleation of bainite at the carbide/austenite interface. According to Thermo-Calc equilibrium simulations using the database TCFE12 [41], $98\,\%$ of the niobium atoms are in undissolved NbC carbides at the austenitization temperature ($900\,^{\circ}\mathrm{C}$). Additionally, niobium strongly segregates to austenite grain boundaries and hinders grain growth [42]. Therefore, the change in morphology could also be caused by the change in prior

austenite grain size or by a change in the nucleation rate of bainite at austenite grain boundaries caused by the higher niobium content at such boundaries.

The substitution of $0.6\,\mathrm{wt.\%}$ Mn for $0.6\,\mathrm{wt.\%}$ Cr in steel 1.7Mn-0.6Cr refined the MA islands in the TBF treatment, possibly due to faster kinetics of bainite formation, as Figure 4.5 shows. In the BAM treatment, a few large regions with carbide precipitation inside were present, as indicated in Figure 4.3. Such areas are typical of tempered martensite [43] formed slightly below M_S [44].

4.3.3. Mechanical properties

Figure 4.6 shows the plot of the total elongation (TE), which is a measurement of the global formability, and of the hole expansion capacity (HEC), which is a measurement of the global formability, against the ultimate tensile strength (UTS) of the steels annealed in the CASim. The highest UTS was achieved by the BAM steels, followed by the Q&P and the TBF steels. The trend for total elongation was the opposite, with the TBF steels having the highest elongation, followed by the Q&P and the BAM steels. The highest HEC was achieved by the Q&P steels, followed by the BAM and the TBF steels. Table 4.2 presents the average mechanical properties grouped by heat treatment, also including the BAM treatment with $300\,\mathrm{s}$ of isothermal holding time. The mechanical properties for each individual combination of steel and heat treatment are shown in Appendix B.

Table 4.2. Mechanical properties of the steels heat treated in the CASim for each heat treatment. Values are the average and standard deviation for each group, with each heat treatment group including the eight chemical compositions from Table 4.1.

Heat treatment	YS (MPa)	UTS (MPa)	TE (%)	HEC (%)
BAM (600 s)	1083 ± 18	1405 ± 79	8 ± 1	35 ± 10
BAM (300 s)	1023 ± 55	1451 ± 102	9 ± 1	30 ± 8
TBF	854 ± 54	1201 ± 98	12 ± 2	28 ± 9
Q&P	1116 ± 36	1276 ± 60	11 ± 2	39 ± 14

From an industrial and commercial point of view, the mechanical properties achieved can be benchmarked against the recently approved VDA standard 239-100, which includes requirements for complex and dual phase steels with improved formability (CH and DH, respectively). Despite the different naming, CH and DH grades can be considered to encompass TBF and Q&P steels [47, 48]. The stronger grade in these families is called CR1000Y1370T-CH, with YS between $1000\,\mathrm{MPa}$ and $1250\,\mathrm{MPa}$, UTS between $1370\,\mathrm{MPa}$ and $1550\,\mathrm{MPa}$, and total elongation above $5\,\%$. Including an extra requirement of HEC $> 30\,\%$, to ensure sufficient local formability, five steels with the BAM $300\,\mathrm{s}$ treatment meet these specifications and deliver a surplus in total elongation, which goes up to $9\,\%$: Ref, 0.6Si, 1.0Si, 1.7Mn-0.6Cr, and 1.7Mn-0.6Cr-0.2Mo.

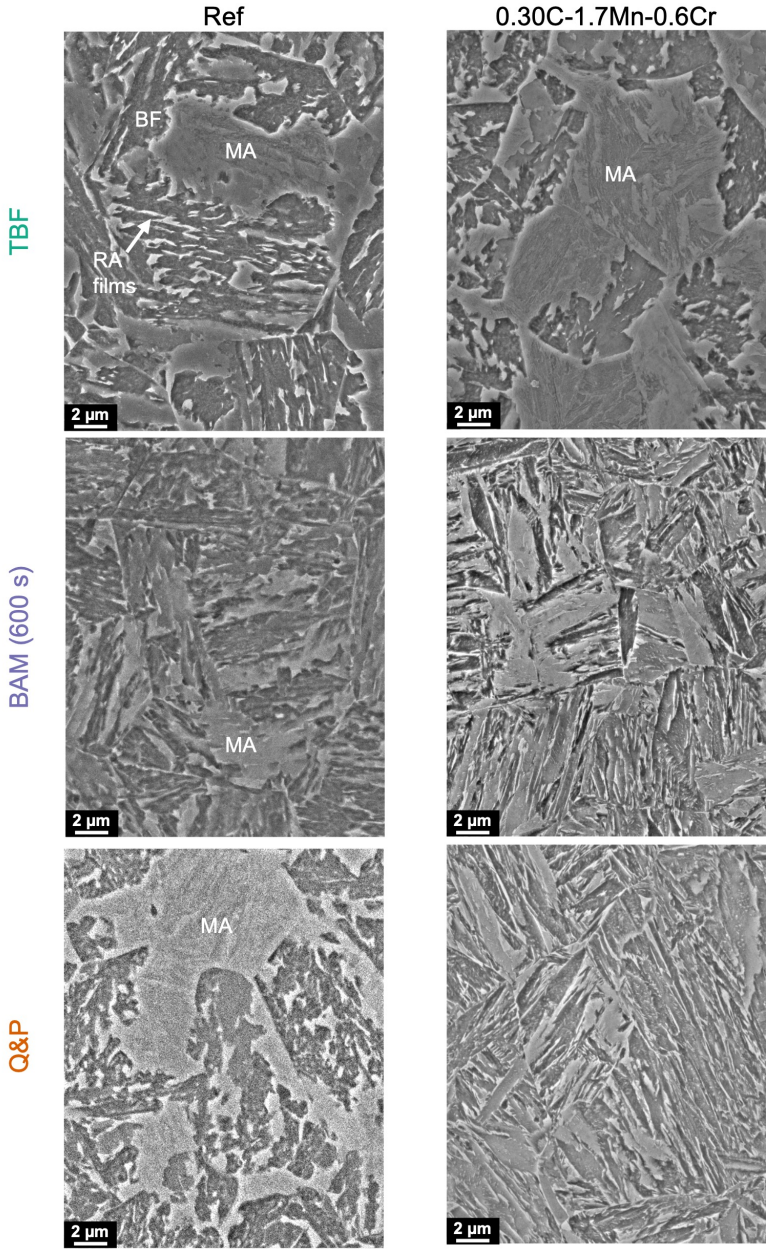

Figure 4.3. Microstructure of samples treated in the CASim. Columns indicate the steel and rows indicate the heat treatment. Annotations indicate bainitic ferrite (BF), tempered martensite (TM), islands of martensite and austenite (MA), and films of retained austenite (RA). Images were acquired in the SEM and the samples were etched with Nital 2%. The isothermal holding time for the BAM samples was $600\,\mathrm{s}$ (continues on the next page)

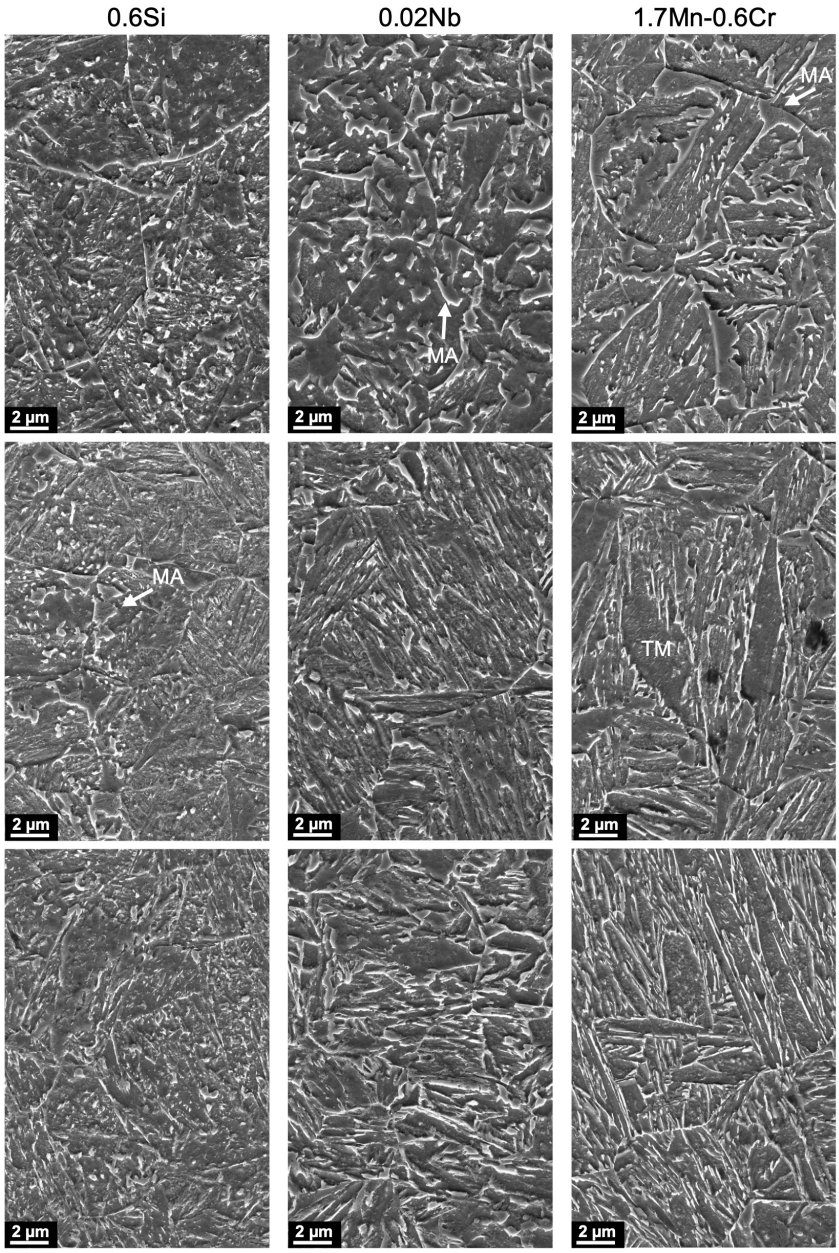

Figure 4.3. Part 2 of the Figure (continued).

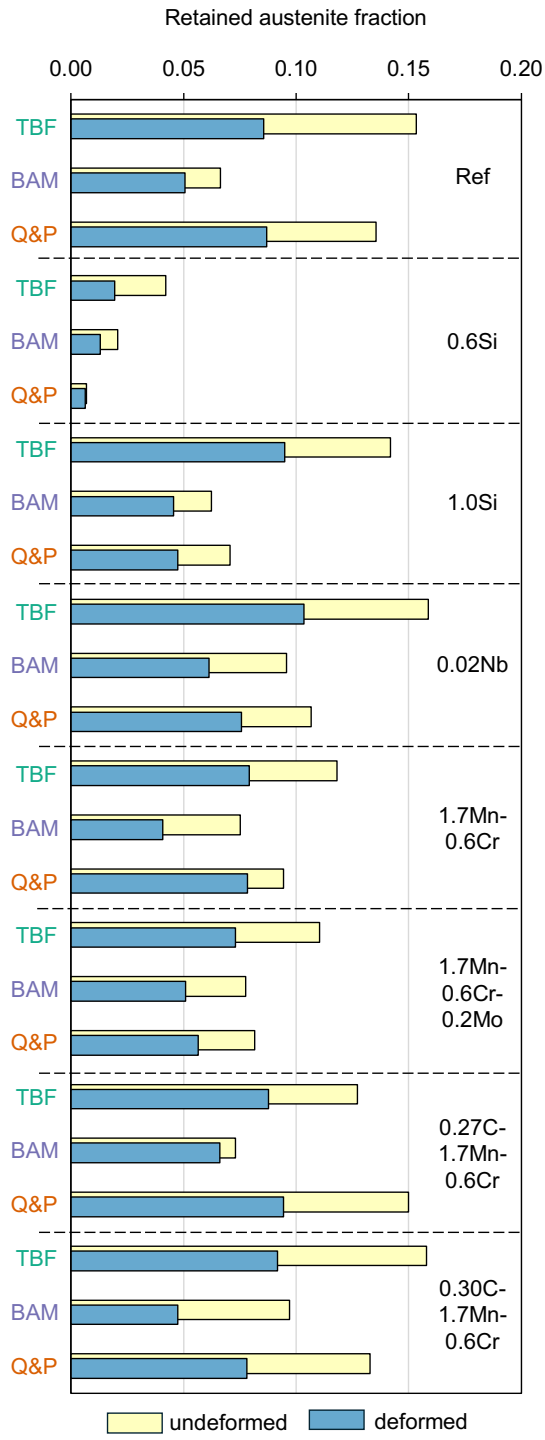
Retained austenite fraction
0.00
0.05
0.10
0.15
0.20
TBF
BAM
Q&P
Ref
0.6Si
1.0Si
0.02Nb
1.7Mn-
0.6Cr
1.7Mn-
0.6Cr-
0.2Mo
0.27C-
1.7Mn-
0.6Cr
0.30C-
1.7Mn-
0.6Cr
undeformed
deformed

Figure 4.4. Volume fraction of retained austenite measured in the specimens for tensile testing in the undeformed and in the deformed region of the specimens. The isothermal holding time for the BAM samples was 600 s. The reduced fraction in the deformed regions indicates that austenite transformed to martensite during tensile testing. The absolute uncertainty of the measured fractions is largely influenced by the texture resulting from cold rolling [45], which could not be estimated because it would require multiple experiments. However, as the production and rolling parameters of all steels were the same and the XRD patterns were taken from the same orientation in all samples, the uncertainty in the difference in the austenite fraction between steels should be much smaller (around 0.01–0.02 [46].)

4.4. Discussion

4.4.1. Effect of the heat treatment

The macroscopic mechanical properties depend on the mechanical properties of the individual phases that constitute the steel's microstructure, and on how these different microstructural constituents interact. A simple yet reasonably accurate assumption is that the strength is given by the average of the individual strength of the microstructure constituents – retained austenite, bainite, tempered martensite, and fresh martensite, in the present case – weighted by their volume fraction [15].

BAM steels achieved 200 MPa higher UTS and YS than TBF steels. In both groups of steels, bainite constitutes the major phase (70 to 90 %) and is thus expected to be the most important microstructure constituent controlling the strength. While bainite was formed at 390 °C for all TBF steels, it was formed at 310 to 350 °C in BAM steels. Bainite formed at lower temperatures is finer and, consequently, stronger. The thickness of bainite plates can be estimated as a function of temperature as [49]

$$u_{\mathrm{T}} = 0.2\frac{(T-528)}{150}, \tag{4.1}$$

where u_{T} is the thickness in µm and T is the temperature in kelvin. The strengthening contribution from the size of bainite plates is estimated as [50]

$$\sigma_{\mathrm{T}} = \frac{115}{2u_{\mathrm{T}}}, \tag{4.2}$$

where σ_{T} is the strengthening contribution in MPa.

From Figure 4.1, the average thickness of bainite plates is 0.180 µm at 390 °C (average TBF temperature) and 0.111 µm at 338 °C (average BAM temperature). From Equation (4.2), the size contribution to the strength of bainite is 319 MPa for TBF and 519 MPa for BAM. The 200 MPa increase in strength predicted for bainite is consistent with the experimental measurements summarized in Table 4.2: On average, UTS increased by 200 MPa and YS increased by 230 MPa from TBF to BAM with 600 s isothermal holding. Figure 4.7 shows the change in UTS and YS for individual steels, and such a strengthening was seen in all cases. The increase in UTS varied from 102 MPa (1.7Mn-0.6Cr-0.2Mo) to 284 MPa (1.0Si), and

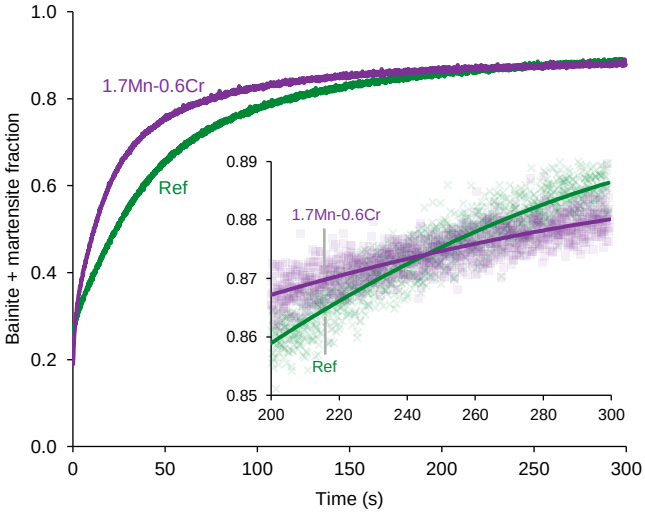

Figure 4.5. Kinetics of bainite formation in the presence of martensite for steel Ref and 1.7Mn-0.6Cr. T_{aus} was $850\,^{\circ}\mathrm{C}$ for steel Ref and $860\,^{\circ}\mathrm{C}$ for 1.7Mn-0.6Cr, and the holding time at T_{aus} was $60\,\mathrm{s}$. Isothermal bainite formation was for $300\,\mathrm{s}$ at $340\,^{\circ}\mathrm{C}$ for steel Ref and $350\,^{\circ}\mathrm{C}$ for steel 1.7Mn-0.6Cr. For both steels, the volume fraction of prior martensite was around 0.25. Inset shows the final $100\,\mathrm{s}$ of isothermal holding.

the increase in YS varied from $150\,\mathrm{MPa}$ (1.7Mn-0.6Cr-0.2Mo) to $330\,\mathrm{MPa}$ (0.30C-1.7Mn-0.6Cr).

The higher strength for BAM compared to TBF reported here contrasts with the work of Navarro-López *et al.* [16], who reported the same UTS for BAM and TBF. However, in their work, a higher fraction of fresh martensite (≈ 0.12) was formed for TBF than for BAM (≈ 0.03 to 0.05). Such fresh martensite is formed from the carbon-enriched austenite and hence is expected to be much stronger than the bainitic ferrite or the tempered martensite. Conversely, in the present work only a low fraction of fresh martensite (< 0.05) is formed after both TBF and BAM treatments.

Retained austenite is a minority phase, with a volume fraction of up to 0.16. However, thanks to the TRIP effect, it can have a pronounced effect on the global formability of steels. The XRD results presented in Figure 4.4 show that the fraction of retained austenite is, on average, $33\,\%$ lower in the deformed regions of the tensile specimen than in the undeformed regions. This result confirms that part of the austenite transformed into martensite during deformation, which indicates that the TRIP effect took place.

In Figure 4.8a, the volume fraction of retained austenite is plotted against the total elongation for all steels. There is a positive correlation between the fraction of retained austenite and the total elongation, which is because of the TRIP effect, as indicated by the results from XRD. Steels that underwent the BAM heat treatment have a lower austenite fraction than TBF and Q&P, which is possibly

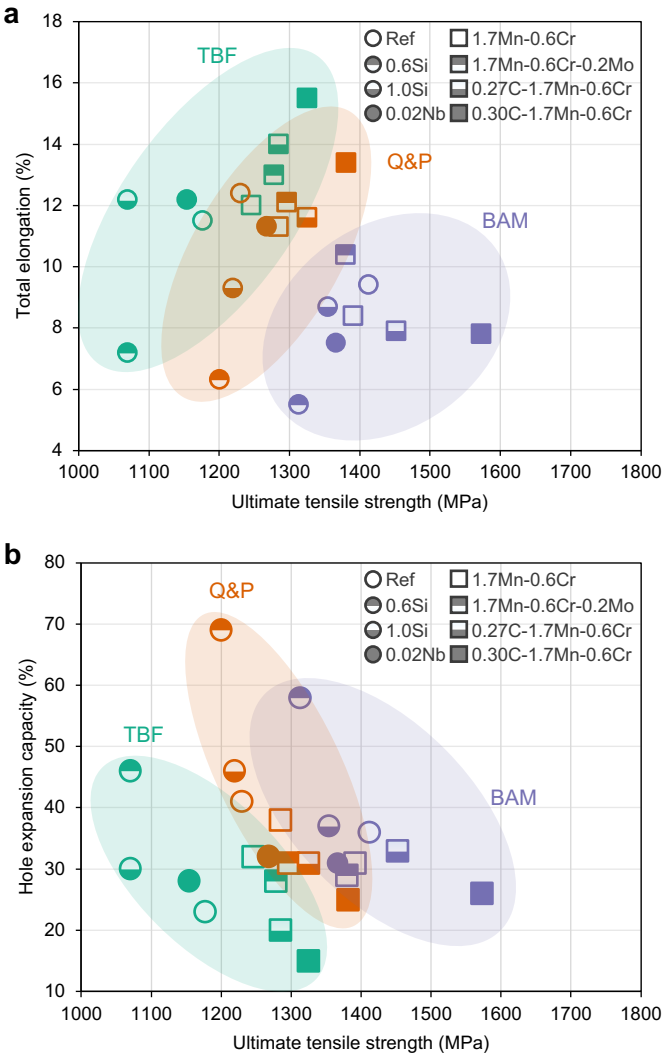

Figure 4.6. Ultimate tensile strength vs **a.** total elongation and **b.** hole expansion capacity of all steels treated in the CASim. Shape of the markers indicates the chemical composition, and the color indicates the heat treatment. The isothermal holding time for the BAM samples was 600 s.

the reason for their limited elongation. Figure 4.7 shows that, for all steels, the TBF heat treatment resulted in higher total elongation than the BAM treatment.

The transformation of austenite to martensite during deformation can have a positive effect on global formability, as deduced from the increase in total elongation. However, it can also have a negative impact on local formability, as indi-

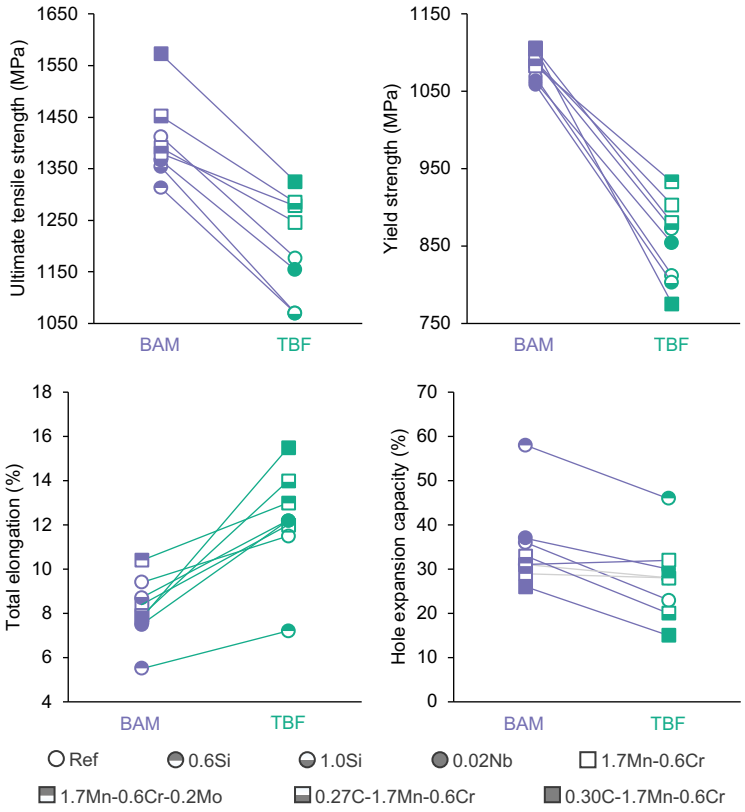

Figure 4.7. Mechanical properties of BAM steels with 600 s isothermal holding time compared to TBF steels.

cated by the lower hole expansion capacity. Martensite formed from the carbon-enriched retained austenite is much harder than other microstructure features because of its high carbon content; large differences in hardness between microstructure features are harmful to local formability [29]. Figure 4.8b shows that there is a negative correlation between the fraction of retained austenite and the hole expansion capacity.

Compared to TBF, BAM has a lower fraction of retained austenite and, in turn, presents slightly higher HEC (Figure 4.7). However, Q&P showed a higher HEC than BAM, despite the Q&P having more retained austenite. A possible reason for this result is the carbon heterogeneity in austenite. The partitioning step for Q&P took place at 400 °C, while bainite formation for BAM took place at temperatures ranging from 310 to 350 °C, and hence carbon distribution in austenite might be more homogeneous in Q&P than in BAM steels. Under strain, austenite with heterogenous carbon distribution will generate martensite with a gradient in hardness – which negatively impacts HEC [51]. Also, any region of retained

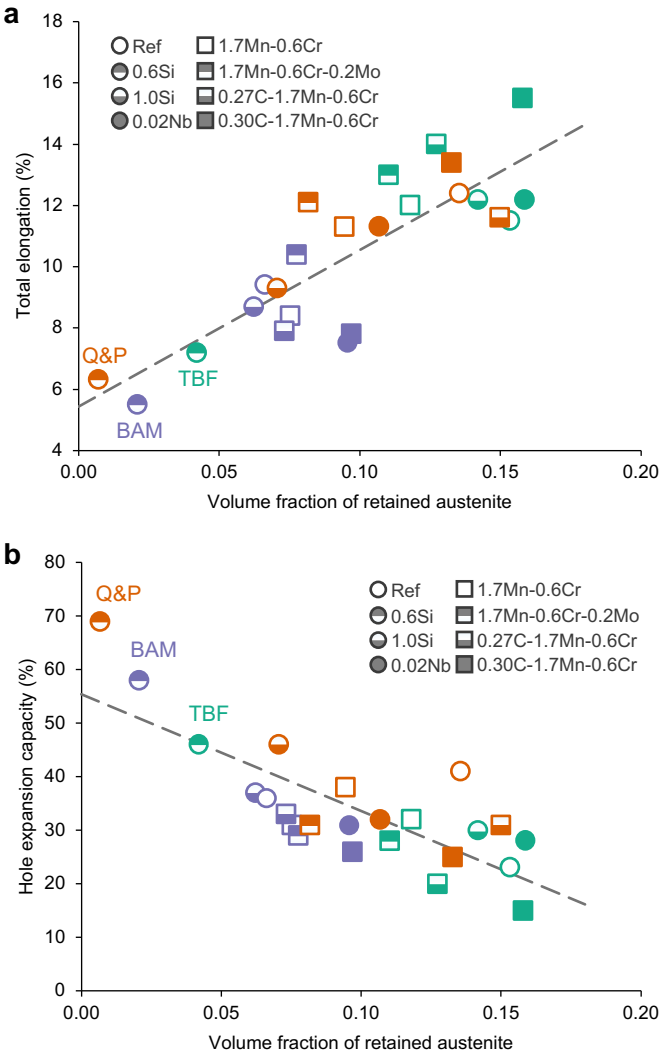

Figure 4.8. Volume fraction of retained austenite plotted against **a** total elongation and **b** hole expansion capacity. Shape of the markers indicates the chemical composition, color indicates the treatment, and dashed line is the linear trend. The isothermal holding time for the BAM samples was 600 s.

austenite that is relatively poor on carbon could readily transform to martensite even under low stress. A different origin for the higher HEC for Q&P steels could be the effect of martensite tempering. During partitioning, the martensite formed during the initial quench is tempered. If the mechanical properties of the strongly tempered martensite in Q&P steels are more homogeneous in compari-

son to the mixture of softly tempered martensite and carbide free bainite in the BAM samples, this leads to an improved HEC.

The ratio between the YS and UTS, called yield ratio (YR), has been shown to correlate with the HEC. Kim *et al.* [51] gathered data on the YR and HEC from different families of steels (DP, Q&P, TRIP, TWIP, martensitic, and medium manganese) and found a linear trend between YR and HEC. Figure 4.9 shows the YR plotted against HEC for the steels developed in the present study. Although Figure 4.9 also shows a linear trend between YR and HEC, as found Kim *et al.*, a single linear trend did not fit well all data points. Instead, grouping steels by heat treatment and calculating the linear trend separately for each group results in a more accurate trend. This result shows that even though YR correlates with HEC, this correlation is more accurate when used to compare steels with similar microstructures that underwent similar heat treatments.

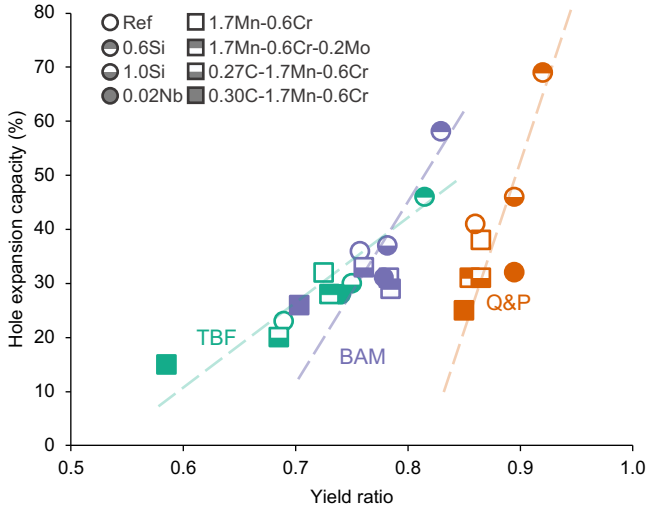

Figure 4.9. Yield ratio plotted against hole expansion capacity. Shape of the markers indicates the chemical composition, color indicates the treatment, and dashed lines are the linear trends calculated separately for each group of samples with the same heat treatment. The isothermal holding time for the BAM samples was 600 s.

4.4.2. Effect of chemical composition

In Figure 4.6, the mechanical properties for all chemical compositions and three different heat treatments were shown. The chemical compositions of the steels differ from each other in their content of silicon, carbon, manganese, chromium, molybdenum, and niobium – Table 4.1. Carbon and silicon were the elements that influenced the mechanical properties the most. Figure 4.10a,b show that both carbon and silicon increase the UTS while increasing (or maintaining) the total elongation. However, the trend is the opposite for the YS and the HEC, as

shown in Figure 4.10c,d. Both carbon and silicon decrease YS (or only slightly increase it, such as carbon in Q&P, Figure 4.10d) and HEC. No specific trend was found for the other alloying elements.

The pronounced effect of silicon and carbon on the mechanical properties could be related to their higher influence on the fraction and stability of retained austenite as compared to the other alloying elements investigated in the present work. As shown in Figure 4.8, the fraction of retained austenite is positively correlated with the total elongation, but negatively correlated with the HEC. Silicon increases the fraction of retained austenite (Figure 4.4) by inhibiting carbide formation [40], which in turn negatively affects the HEC. Retained austenite is less strong than bainite and martensite, and thus contributes little to the YS, which is possibly why increasing silicon content decreased YS. However, upon plastic deformation, the carbon-enriched retained austenite transforms into strong fresh martensite that increases the UTS. A similar mechanism might be operating for carbon. For instance, for TBF, increasing carbon also led to a higher fraction of retained austenite, UTS, and total elongation, and to a lower YS and HEC.

Despite the weak influence on the mechanical properties, substituting $0.6\,\mathrm{wt.\%}$ Mn by $0.6\,\mathrm{wt.\%}$ Cr refined the MA blocks (Figure 4.3) due to a higher kinetics of bainite formation (Figure 4.5). Even though bainite formation was faster in steel 1.7Mn-0.6Cr, no proeutectoid ferrite was found, neither in the microstructural characterization nor in the dilatometry curves, which indicates the steel has sufficient hardenability. The present finding that $0.6\,\mathrm{wt.\%}$ Mn has the same effect on the hardenability as $0.6\,\mathrm{wt.\%}$ Cr is consistent with the results presented by Grange [52].

The faster bainite kinetics while maintaining hardenability by the partial substitution of manganese for chromium can be explained in terms of driving force and diffusivity. In bainite formation, there is no diffusion of substitutional alloying elements [53]. Thus, substitutional alloying elements influence the kinetics of bainite formation mostly by their effect on the driving force. Figure 4.11a shows that the partial substitution of manganese for chromium increases the driving force for bainite nucleation, which in turn accelerates bainite formation [54, 55].

Conversely, there is significant diffusion of substitutional alloying elements during the formation of proeutectoid ferrite. Such elements can partition between austenite and ferrite and segregate to the interface. Hence, substitutional alloying elements influence the overall kinetics of ferrite formation by their effect not only on the driving force but on the average atomic mobility. Figure 4.11a shows that the partial substitution of manganese for chromium increases the driving force for ferrite nucleation, which is expected to accelerate the formation of ferrite. However, the diffusion coefficient of the solute atoms in austenite and ferrite also heavily influences the kinetics of ferrite formation [56]. Figure 4.11b shows that the diffusion coefficient of chromium is around one order of magnitude lower than that of manganese both in austenite and in ferrite. Thus, even though partially substituting manganese for chromium increases the driving force for ferrite formation, it decreases the rate at which solute atoms can be transferred across the moving ferrite/austenite interface. The overall effect of this substitution will

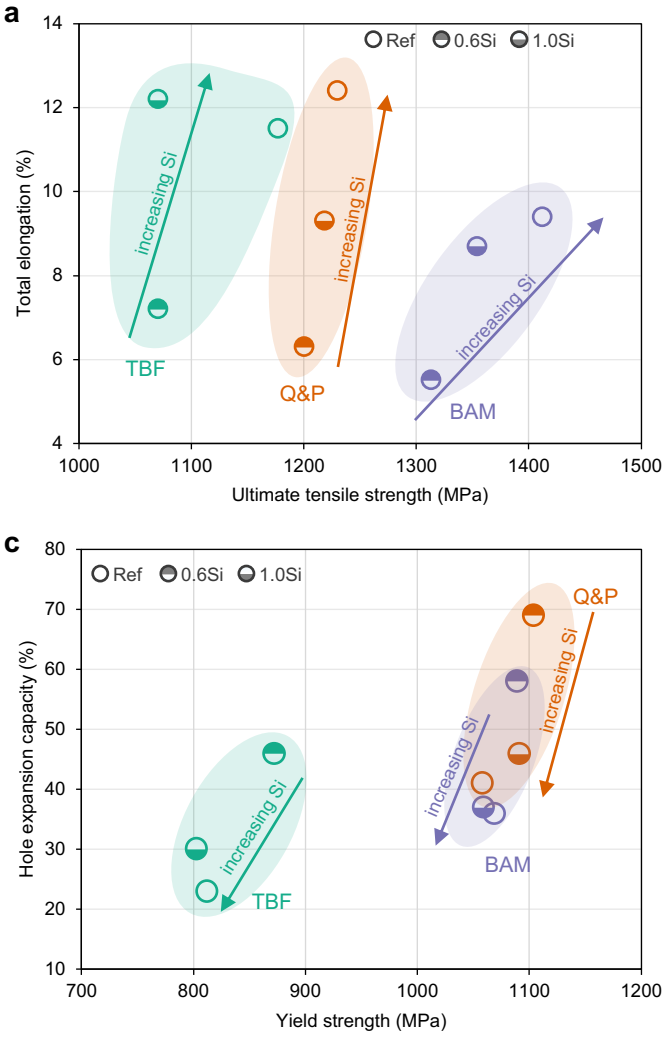

Figure 4.10. Effect of **a,c.** silicon and **b,d.** carbon on the balance between **a,b.** UTS and total elongation and **c,d.** YS and HEC. Shape of the markers indicates the chemical composition, and the color indicates the heat treatment. The isothermal holding time for the BAM samples was 600 s (continues on the next page).

depend on the balance between the effect of driving force and diffusion coefficient, as well as on the segregation of elements to the ferrite/austenite interface, which slows down the transformation because of the solute drag effect [57].

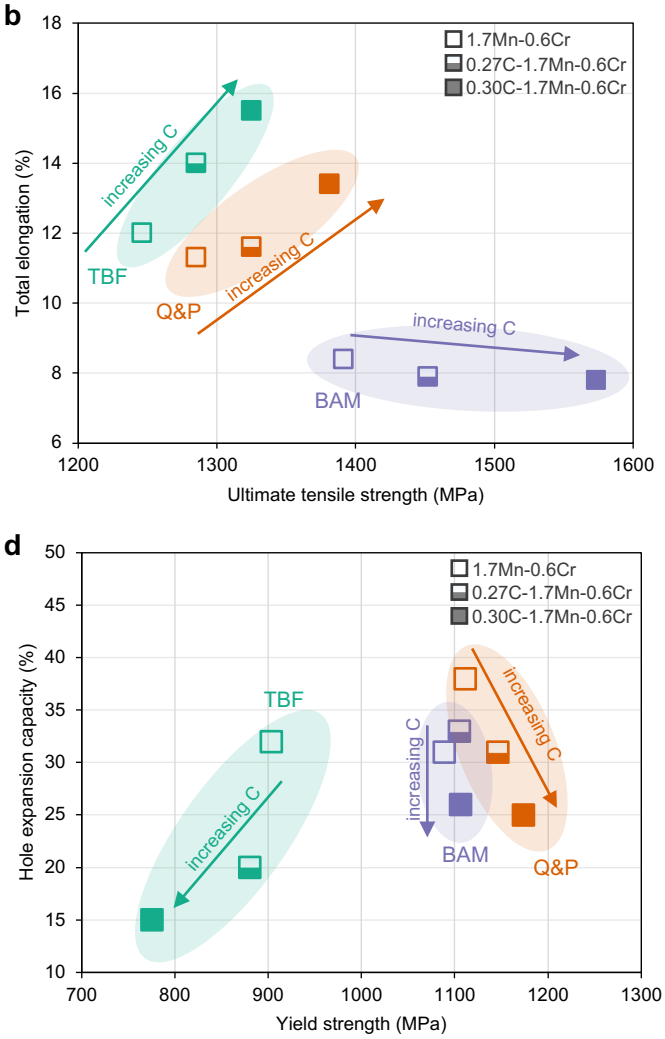

Figure 4.10. Part 2 of the Figure (continued).

4.5. Conclusion

This Chapter presented the design of a new 3rd gen AHSS that can be manufactured in existing continuous annealing lines for $1\,\mathrm{mm}$ thickness bare steel strips. Five different chemical compositions (Ref., 0.6Si, 1.0Si, 1.7Mn-0.6Cr, and 1.7Mn-0.6Cr-0.2Mo) met the requirements of steel grade CR1000Y1370UTS-CH – even delivering a surplus in total elongation – while showing a HEC value equal to or higher than $30\,\%$. This was achieved by balancing the chemical composition of steels to simultaneously have sufficient hardenability – meaning little to no

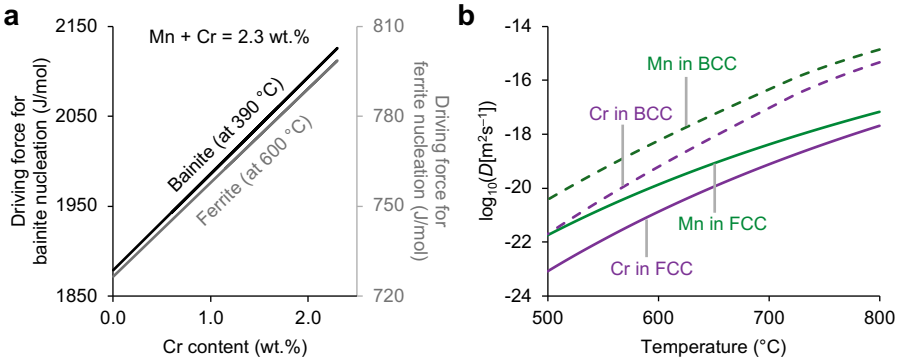

Figure 4.11. **a.** Driving force for bainite nucleation (values on left axis) at $390\,^{\circ}\mathrm{C}$ and ferrite nucleation (values on right axis) at $600\,^{\circ}\mathrm{C}$ as a function of the partial substitution of Mn for Cr in a Fe-0.24C-1.5Si-(2.3−x)Mn-xCr $\mathrm{wt.\%}$ steel. **b.** Log of the tracer diffusion coefficient, D, in $\mathrm{m^2\,s^{-1}}$ of Mn and Cr in ferrite (body-centered cubic, BCC) and austenite (face-centered cubic, FCC) as a function of temperature in a Fe-0.24C-1.5Si-1.7Mn-0.6Cr steel. All values were calculated using Thermo-Calc with databases TCFE12 and MOBFE7. The driving forces were calculated using the ferrite precipitation model within the steel model library of Thermo-Calc considering paraprecipitate for bainite and orthoprecipitate for ferrite.

formation of proeutectoid ferrite during cooling with rates typical of continuous annealing lines – and fast bainite kinetics. In the steels called BAM (bainite accelerated by martensite), the formation of a volume fraction of around 0.2 of prior martensite accelerated bainite formation and allowed an isothermal holding time of only $300\,\mathrm{s}$. The effect of varying the content of selected alloying elements (C, Mn, Si, Cr, Mo, and Nb) and varying the heat treatment (BAM, TBF, and Q&P) on the microstructure and mechanical properties of the steels were studied, and it was found that:

- Bainite formation is significantly accelerated by fractions of prior martensite as low as 0.05. This pronounced acceleration effect at low fractions of martensite can be used to shorten the heat treatment time of steels while maintaining a mostly bainitic microstructure.

- BAM heat treatment led to higher UTS but lower total elongation than TBF and Q&P because of its finer bainite laths and lower fraction of retained austenite. However, the lower fraction of retained austenite improved its local formability compared to TBF. This trend was verified for the steels and conditions tested here and might be different for different steel grades and ranges of temperature.

- Carbon and silicon are the elements that influence the mechanical properties the most because of their higher influence on the fraction and stability of retained austenite.

- The partial substitution of manganese for chromium accelerated bainite kinetics without any noticeable negative effect on hardenability. This partial substitution can be further investigated in future works to shorten even more the required time for bainite formation in 3rd gen AHSS.

References

[1] N. Fonstein. *Advanced High Strength Sheet Steels: Physical Metallurgy, Design, Processing, and Properties*. Springer International Publishing, 2015. doi: 10.1007/978-3-319-19165-2.

[2] *VDA 239-100 - Sheet Steel for Cold Forming (06/2016)*. Version 06/2016. 2016.

[3] C. Tasan, M. Diehl, D. Yan, M. Bechtold, F. Roters, L. Schemmann, C. Zheng, N. Peranio, D. Ponge, M. Koyama, K. Tsuzaki, and D. Raabe. "An Overview of Dual-Phase Steels: Advances in Microstructure-Oriented Processing and Micromechanically Guided Design". In: *Annual Review of Materials Research* 45 (2015), pp. 391–431. doi: 10.1146/annurev-matsci-070214-021103.

[4] B. C. De Cooman. "Structure–properties relationship in TRIP steels containing carbide-free bainite". In: *Current Opinion in Solid State and Materials Science* 8.3 (June 1, 2004), pp. 285–303. doi: 10.1016/j.cossms.2004.10.002.

[5] X. Li, A. Ramazani, U. Prahl, and W. Bleck. "Quantification of complex-phase steel microstructure by using combined EBSD and EPMA measurements". In: *Materials Characterization* 142 (Aug. 1, 2018), pp. 179–186. doi: 10.1016/j.matchar.2018.05.038.

[6] S. Allain, J. .-. Chateau, D. Dahmoun, and O. Bouaziz. "Modeling of mechanical twinning in a high manganese content austenitic steel". In: *Materials Science and Engineering: A*. 13th International Conference on the Strength of Materials 387-389 (Dec. 15, 2004), pp. 272–276. doi: 10.1016/j.msea.2004.05.038.

[7] K.-i. Sugimoto, T. Iida, J. Sakaguchi, and T. Kashima. "Retained Austenite Characteristics and Tensile Properties in a TRIP Type Bainitic Sheet Steel". In: *ISIJ International* 40.9 (2000), pp. 902–908. doi: 10.2355/isijinternational.40.902.

[8] J. Speer, D. K. Matlock, B. C. De Cooman, and J. G. Schroth. "Carbon partitioning into austenite after martensite transformation". In: *Acta Materialia* 51.9 (May 23, 2003), pp. 2611–2622. doi: 10.1016/S1359-6454(03)00059-4.

[9] Y.-K. Lee and J. Han. "Current opinion in medium manganese steel". In: *Materials Science and Technology* 31.7 (May 1, 2015). Publisher: Taylor & Francis _eprint: https://doi.org/10.1179/1743284714Y.0000000722, pp. 843–856. doi: 10.1179/1743284714Y.0000000722.

[10] K. Hickey. *Defining Steels*. AHSS Guidelines. Aug. 25, 2021. url: https://ahssinsights.org/metallurgy/defining-steels/ (visited on 07/16/2024).

[11] M. J. Santofimia, L. Zhao, R. Petrov, C. Kwakernaak, W. G. Sloof, and J. Sietsma. "Microstructural development during the quenching and partitioning process in a newly designed low-carbon steel". In: *Acta Materialia* 59.15 (Sept. 1, 2011), pp. 6059–6068. doi: 10.1016/j.actamat.2011.06.014.

[12] E. J. Seo, L. Cho, Y. Estrin, and B. C. De Cooman. "Microstructure-mechanical properties relationships for quenching and partitioning (Q&P) processed steel". In: *Acta Materialia* 113 (July 1, 2016), pp. 124–139. doi: 10.1016/j.actamat.2016.04.048.

[13] E. De Moor, S. Lacroix, A. Clarke, J. Penning, and J. Speer. "Effect of Retained Austenite Stabilized via Quench and Partitioning on the Strain Hardening of Martensitic Steels". In: *Metallurgical and Materials Transactions A* 39.11 (Nov. 1, 2008), pp. 2586–2595. doi: 10.1007/s11661-008-9609-z.

[14] X. Tan, Y. Xu, X. Yang, and D. Wu. "Microstructure–properties relationship in a one-step quenched and partitioned steel". In: *Materials Science and Engineering: A* 589 (Jan. 1, 2014), pp. 101–111. doi: 10.1016/j.msea.2013.09.063.

[15] D. Sun, H. Wang, X. An, G. Wang, S. Huang, and X. Huang. "Quantitative evaluation of the contribution of carbide-free bainite, lath martensite, and retained austenite on the mechanical properties of C-Mn-Si high-strength steels". In: *Materials Characterization* 199 (May 1, 2023), p. 112802. doi: 10.1016/j.matchar.2023.112802.

[16] A. Navarro-López, J. Hidalgo, J. Sietsma, and M. J. Santofimia. "Influence of the prior athermal martensite on the mechanical response of advanced bainitic steel". In: *Materials Science and Engineering: A* 735 (Sept. 26, 2018), pp. 343–353. doi: 10.1016/j.msea.2018.08.047.

[17] R. Hou, G. Xu, H. Hu, and M. Zhou. "Effects of Nb Addition on Transformation Kinetics and Microstructure Properties in Low-Carbon Bainitic Steels". In: *Metallography, Microstructure, and Analysis* 6.2 (Apr. 1, 2017), pp. 158–163. doi: 10.1007/s13632-017-0345-x.

[18] L. Zhao, L. Qian, J. Meng, Q. Zhou, and F. Zhang. "Below-*Ms* austempering to obtain refined bainitic structure and enhanced mechanical properties in low-C high-Si/Al steels". In: *Scripta Materialia* 112 (Feb. 1, 2016), pp. 96–100. doi: 10.1016/j.scriptamat.2015.09.022.

[19] H. Hu, G. Xu, L. Wang, Z. Xue, Y. Zhang, and G. Liu. "The effects of Nb and Mo addition on transformation and properties in low carbon bainitic steels". In: *Materials & Design* 84 (Nov. 5, 2015), pp. 95–99. doi: 10.1016/j.matdes.2015.06.133.

[20] E. P. Da Silva, D. De Knijf, W. Xu, C. Föjer, Y. Houbaert, J. Sietsma, and R. Petrov. “Isothermal transformations in advanced high strength steels below martensite start temperature”. In: *Materials Science and Technology* 31.7 (May 1, 2015). Publisher: SAGE Publications, pp. 808–816. doi: 10.1179/1743284714Y.0000000719.

[21] F. G. Caballero, S. Allain, J. Cornide, J. D. Puerta Velásquez, C. Garcia-Mateo, and M. K. Miller. “Design of cold rolled and continuous annealed carbide-free bainitic steels for automotive application”. In: *Materials & Design* 49 (Aug. 1, 2013), pp. 667–680. doi: 10.1016/j.matdes.2013.02.046.

[22] J.-C. Hell, M. Dehmas, S. Allain, J. M. Prado, A. Hazotte, and J.-P. Chateau. “Microstructure – Properties Relationships in Carbide-free Bainitic Steels”. In: *ISIJ International* 51.10 (2011), pp. 1724–1732. doi: 10.2355/isijinternational.51.1724.

[23] K.-i. Sugimoto, M. Murata, and S.-M. Song. “Formability of Al–Nb Bearing Ultra High-strength TRIP-aided Sheet Steels with Bainitic Ferrite and/or Martensite Matrix”. In: *ISIJ International* 50.1 (2010), pp. 162–168. doi: 10.2355/isijinternational.50.162.

[24] T. Hojo, K.-i. Sugimoto, Y. Mukai, and S. Ikeda. “Effects of Aluminum on Delayed Fracture Properties of Ultra High Strength Low Alloy TRIP-aided Steels”. In: *ISIJ International* 48.6 (2008), pp. 824–829. doi: 10.2355/isijinternational.48.824.

[25] K.-i. Sugimoto, M. Murata, T. Muramatsu, and Y. Mukai. “Formability of C–Si–Mn–Al–Nb–Mo Ultra High-strength TRIP-aided Sheet Steels”. In: *ISIJ International* 47.9 (2007), pp. 1357–1362. doi: 10.2355/isijinternational.47.1357.

[26] K.-I. Sugimoto, T. Muramatsu, S.-I. Hashimoto, and Y. Mukai. “Formability of Nb bearing ultra high-strength TRIP-aided sheet steels”. In: *Journal of Materials Processing Technology*. Proceedings of the 11th International Conference on Metal Forming 2006 177.1 (July 3, 2006), pp. 390–395. doi: 10.1016/j.jmatprotec.2006.03.186.

[27] K.-i. Sugimoto, J. Sakaguchi, T. Iida, and T. Kashima. “Stretch-flangeability of a High-strength TRIP Type Bainitic Sheet Steel”. In: *ISIJ International* 40.9 (2000), pp. 920–926. doi: 10.2355/isijinternational.40.920.

[28] S. Ebner, C. Suppan, R. Schnitzer, and C. Hofer. “Microstructure and mechanical properties of a low C steel subjected to bainitic or quenching and partitioning heat treatments”. In: *Materials Science and Engineering: A* 735 (Sept. 26, 2018), pp. 1–9. doi: 10.1016/j.msea.2018.08.026.

[29] S. K. Paul. “A critical review on hole expansion ratio”. In: *Materialia* 9 (Mar. 1, 2020), p. 100566. doi: 10.1016/j.mtla.2019.100566.

[30] S. Dhara, S. M. C. van Bohemen, and M. J. Santofimia. “Isothermal decomposition of austenite in presence of martensite in advanced high strength steels: A review”. In: *Materials Today Communications* 33 (Dec. 1, 2022), p. 104567. doi: 10.1016/j.mtcomm.2022.104567.

[31] *VDA 239-100 – Sheet Steel for Cold Forming (05/2024)*. 2024.

[32] S. M. C. van Bohemen and J. Sietsma. “Kinetics of martensite formation in plain carbon steels: critical assessment of possible influence of austenite grain boundaries and autocatalysis”. In: *Materials Science and Technology* 30.9 (July 1, 2014). Publisher: Taylor & Francis _eprint: https://doi.org/10.1179/1743284714Y.0000000532, pp. 1024–1033. doi: 10.1179/1743284714Y.0000000532.

[33] S. M. C. van Bohemen. “The nonlinear lattice expansion of iron alloys in the range 100–1600 K”. In: *Scripta Materialia* 69.4 (Aug. 1, 2013), pp. 315–318. doi: 10.1016/j.scriptamat.2013.05.009.

[34] A. Navarro-López, J. Sietsma, and M. J. Santofimia. “Effect of Prior Athermal Martensite on the Isothermal Transformation Kinetics Below Ms in a Low-C High-Si Steel”. In: *Metallurgical and Materials Transactions A* 47.3 (Mar. 1, 2016), pp. 1028–1039. doi: 10.1007/s11661-015-3285-6.

[35] C. F. Jatczak. “Retained Austenite and Its Measurement by X-Ray Diffraction”. In: *SAE Transactions* 89 (1980). Publisher: SAE International, pp. 1657–1676.

[36] P. Crowther and C. S. Daniel. “xrdfit: A Python package for fitting synchrotron X-ray diffraction spectra”. In: *Journal of Open Source Software* 5.52 (Aug. 31, 2020), p. 2381. doi: 10.21105/joss.02381.

[37] D. N. Hanlon, S. M. C. van Bohemen, and S. Celotto. “Critical Assessment 10: Tensile elongation of strong automotive steels as function of testpiece geometry”. In: *Materials Science and Technology* 31.4 (Mar. 1, 2015). Publisher: Taylor & Francis _eprint: https://doi.org/10.1179/1743284714Y.0000000707, pp. 385–388. doi: 10.1179/1743284714Y.0000000707.

[38] H. K. D. H. Bhadeshia. “A rationalisation of shear transformations in steels”. In: *Acta Metallurgica* 29.6 (June 1, 1981), pp. 1117–1130. doi: 10.1016/0001-6160(81)90063-8.

[39] L. Leach, P. Kolmskog, L. Höglund, M. Hillert, and A. Borgenstam. “Critical Driving Forces for Formation of Bainite”. In: *Metallurgical and Materials Transactions A* 49.10 (Oct. 1, 2018), pp. 4509–4520. doi: 10.1007/s11661-018-4819-5.

[40] S. Lin, A. Borgenstam, A. Stark, and P. Hedström. “Effect of Si on bainitic transformation kinetics in steels explained by carbon partitioning, carbide formation, dislocation densities, and thermodynamic conditions”. In: *Materials Characterization* 185 (Mar. 1, 2022), p. 111774. doi: 10.1016/j.matchar.2022.111774.

[41] J.-O. Andersson, T. Helander, L. Höglund, P. Shi, and B. Sundman. “Thermo-Calc & DICTRA, computational tools for materials science”. In: *Calphad* 26.2 (June 1, 2002), pp. 273–312. doi: 10.1016/S0364-5916(02)00037-8.

[42] A. Suhane, D. Scheiber, V. I. Razumovskiy, and M. Militzer. “Atomistically informed phase field study of austenite grain growth”. In: *Computational Materials Science* 228 (Sept. 1, 2023), p. 112300. doi: 10.1016/j.commatsci.2023.112300.

[43] A. Navarro-López, J. Hidalgo, J. Sietsma, and M. J. Santofimia. “Characterization of bainitic/martensitic structures formed in isothermal treatments below the Ms temperature”. In: *Materials Characterization* 128 (June 1, 2017), pp. 248–256. doi: 10.1016/j.matchar.2017.04.007.

[44] L. Morsdorf, C. C. Tasan, D. Ponge, and D. Raabe. “3D structural and atomic-scale analysis of lath martensite: Effect of the transformation sequence”. In: *Acta Materialia* 95 (Aug. 15, 2015), pp. 366–377. doi: 10.1016/j.actamat.2015.05.023.

[45] A. Creuziger, C. A. Calhoun, W. A. Poling, and T. Gnäupel-Herold. “Assessment of bias errors caused by texture and sampling methods in diffraction-based steel phase measurements”. In: *Journal of Applied Crystallography* 51.3 (June 1, 2018). Publisher: International Union of Crystallography, pp. 720–731. doi: 10.1107/S160057671800420X.

[46] P. J. Jacques, S. Allain, O. Bouaziz, A. De, A.-F. Gourgues, B. M. Hance, Y. Houbaert, J. Huang, A. Iza-Mendia, S. E. Kruger, M. Radu, L. Samek, J. Speer, L. Zhao, and S. van der Zwaag. “On measurement of retained austenite in multiphase TRIP steels — results of blind round robin test involving six different techniques”. In: *Materials Science and Technology* 25.5 (May 1, 2009). Publisher: Taylor & Francis _eprint: https://doi.org/10.1179/174328408X353723, pp. 567–574. doi: 10.1179/174328408X353723.

[47] S. Heibel, T. Dettinger, W. Nester, T. Clausmeyer, and A. E. Tekkaya. “Damage Mechanisms and Mechanical Properties of High-Strength Multiphase Steels”. In: *Materials* 11.5 (May 2018). Number: 5 Publisher: Multidisciplinary Digital Publishing Institute, p. 761. doi: 10.3390/ma11050761.

[48] K. Hickey. *3rd Generation Steels*. AHSS Guidelines. June 23, 2021. url: https://ahssinsights.org/metallurgy/steel-grades/3rd-generation-steels/ (visited on 10/23/2024).

[49] S. V. Parker. “Modelling of Phase Transformations in Hot-Rolled Steels”. PhD thesis. University of Cambridge, Jan. 27, 1998.

[50] c. H. Young and H. K. D. H. Bhadeshia. “Strength of mixtures of bainite and martensite”. In: *Materials Science and Technology* 10.3 (Mar. 1, 1994). Publisher: Taylor & Francis _eprint: https://doi.org/10.1179/mst.1994.10.3.209, pp. 209–214. doi: 10.1179/mst.1994.10.3.209.

[51] J. H. Kim, E. J. Seo, M.-H. Kwon, S. Kang, and B. C. De Cooman. “Effect of quenching temperature on stretch flangeability of a medium Mn steel processed by quenching and partitioning”. In: *Materials Science and Engineering: A* 729 (June 27, 2018), pp. 276–284. doi: 10.1016/j.msea.2018.05.083.

[52] R. A. Grange. “Estimating the hardenability of carbon steels”. In: *Metallurgical Transactions* 4.10 (Oct. 1, 1973), pp. 2231–2244. doi: 10.1007/BF02669363.

[53] H. K. D. H. Bhadeshia. *Bainite in Steels: Theory and Practice, Third Edition*. 3rd ed. London: CRC Press, Mar. 6, 2015. 616 pp. doi: 10.1201/9781315096674.

[54] D. d. S. Avila, S. E. Offerman, and M. J. Santofimia. “Modeling the effect of prior austenite grain size on bainite formation kinetics”. In: *Acta Materialia* 266 (Mar. 1, 2024), p. 119656. doi: 10.1016/j.actamat.2024.119656.

[55] L. Leach, J. Ågren, L. Höglund, and A. Borgenstam. “Diffusion-Controlled Lengthening Rates of Bainitic Ferrite a Part of the Steel Genome”. In: *Metallurgical and Materials Transactions A* 50.6 (June 1, 2019), pp. 2613–2618. doi: 10.1007/s11661-019-05208-x.

[56] H. S. Zurob, D. Panahi, C. R. Hutchinson, Y. Brechet, and G. R. Purdy. “Self-Consistent Model for Planar Ferrite Growth in Fe-C-X Alloys”. In: *Metallurgical and Materials Transactions A* 44.8 (Aug. 1, 2013), pp. 3456–3471. doi: 10.1007/s11661-012-1479-8.

[57] I. .-. Benrabah, H. P. Van Landeghem, F. Bonnet, B. Denand, G. Geandier, and A. Deschamps. “Solute drag modeling for ferrite growth kinetics during precipitation experiments”. In: *Acta Materialia* 221 (Dec. 1, 2021), p. 117364. doi: 10.1016/j.actamat.2021.117364.

5

Bainite formation observed by in situ transmission electron microscopy

The diffusional and diffusionless theories of bainite formation disagree on the growth mechanism of bainite plates (also called sub-units). While the diffusional theory argues for a constant lengthening rate controlled by carbon diffusion in the austenite, the diffusionless theory argues for a growth rate that could approach the speed of sound. Real-time observations of bainite growth by laser confocal microscopy could not confirm either theory because the theoretical size of bainite sub-units is smaller than the spatial resolution of the technique. In this Chapter, bainite formation is observed at a higher resolution by in situ transmission electron microscopy (TEM). The starting material is a steel with $1.24\,\mathrm{wt.\%C}$ *that retains from* 0.2 *to* 0.4 *volume fraction of austenite after quenching to room temperature. The quenched samples were heated to* $280\,^{\circ}\mathrm{C}$ *inside the TEM to observe the decomposition of retained austenite into bainite. Bainite plates were found to grow continuously at lengthening rates ranging from* 20 *to* $55\,\mathrm{nm\,s^{-1}}$ *and at a thickening rate of around* $1.6\,\mathrm{nm\,s^{-1}}$*. The observed growth behavior is in line with the diffusional theory of bainite formation. This Chapter also discusses the implications of the diffusional theory for the model developed in Chapters 2 and 3 and discusses ideas for future experiments using in situ TEM intended for further clarifying the role of carbon diffusion in the growth of bainite plates.*

To be submitted for publication.

5.1. Introduction

The role of carbon diffusion in bainitic transformation is still under debate [1]. While the diffusionless theory claims bainitic ferrite grows with the same carbon content as the parent austenite [2], the diffusional theory claims carbon diffusion takes place during the growth of bainitic ferrite and that carbon diffusion controls the growth rate [3]. The evidence for either theory is mainly indirect – surface relief [4], slight tetragonality and carbon supersaturation in bainitic ferrite [5], and lengthening rate of bainite sheaves predicted by carbon diffusion [3] – as there is no experimental technique that can track *in situ* the formation of bainite and carbon distribution at the required time and spatial resolution. Although the diffusional theory claims carbon diffusion takes place during the growth of bainite, many recent models based on the diffusional theory consider the transformation to be displacive – that is, the transformation involves a shear component that creates an energy barrier for bainite formation and causes the surface relief, and the substitutional elements across rearrange themselves across the moving interface by the movement of disconnections or dislocations [6].

The growth of individual bainite sheaves can be measured *in situ* by hot stage optical microscopy [7] and usually matches the order of magnitude of the expected lengthening rate for a process controlled by carbon diffusion [3]. This apparent good match is taken as evidence supporting the diffusional theory. However, the diffusionless theory proposes that bainite sheaves grow by the successive nucleation of bainite sub-units, which might not be resolved in most hot stage optical microscopy studies. Figure 5.1 illustrates the different proposed mechanisms for the growth of a bainitic sheaf.

The spatial resolution necessary to resolve individual sub-units depends on the length of those sub-units. Based on transmission electron microscopy (TEM) images, Bhadeshia proposed sub-units are $10\,\mu m$ long [2]. However, as discussed in Chapter 2, this might be an overestimation, and the length might be closer to $1\,\mu m$. In the hot stage laser confocal microscopy experiments of Hawkins and Barford [7] and Hu *et al.* [8], the growth of bainite sheaves was resolved up to $1\,\mu m$, and the growth still seemed to be continuous and at a constant rate. Their results indicate that the sheaves either grow continuously, as proposed by the diffusional theory, or that the length of sub-units is around $1\,\mu m$ or less, as proposed in Chapter 2.

Higher resolution observations using hot stage TEM were carried out by Zhao *et al.* [9] and by Nutter *et al.* [10]. The lengthening rate of bainite plates ranged from 0.01 to $30\,\mu m\,s^{-1}$ in their studies, which lies within the typical range of lengthening rates predicted by the diffusional theory. While Zhao *et al.* observed a somewhat constant lengthening rate of bainite plates, Nutter *et al.* observed a stepped growth with a succession of growth stages followed by stasis stages. Carbide formation was not detected in any of their works as they used steels alloyed with silicon. Additionally, the work of Nutter *et al.* discussed experimental challenges with the observation of bainite by hot stage TEM. The challenges were related to the high temperatures necessary for the austenitization step, such as the thickening of the thin foils by surface diffusion, evaporation of alloying ele-

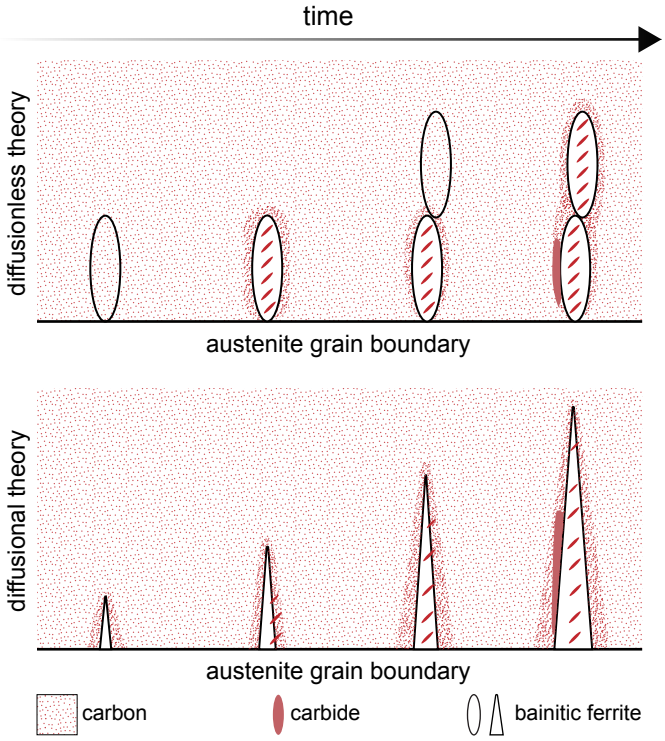

Figure 5.1. Mechanism of formation of lower bainite according to the diffusionless (upper) and diffusional (lower) theories of bainite formation.

ments (mainly manganese), and drift of the field of view during fast cooling.

This chapter presents the preliminary results of a new observation of bainite formation by hot stage TEM. The challenges involved with austenitizing inside the TEM are avoided by preparing the specimen from a steel with a low M_S (around $125\,^{\circ}\mathrm{C}$) that retains a 0.2 to 0.4 volume fraction of retained austenite at room temperature. Then, in the hot stage TEM, the specimen is heated up to only $280\,^{\circ}\mathrm{C}$, a temperature at which the retained austenite decomposes into lower bainite. The analysis of the results is still ongoing, and thus this chapter focuses on presenting the setup of the experiment, some preliminary results and images, possible paths to analyze the results, and suggestions for future experiments.

5.2. Choice of material

The first requirement for the desired experiment is that the M_S of the steel is such that after quenching to room temperature, the fraction of retained austenite is large enough to be easily observed in the TEM, and that the regions of retained austenite are large enough to allow bainite sheaves to grow. The M_S temperature of steels can be estimated using the empirical equation proposed by van

Bohemen [11],

$$M_S = 565 - 600\,[1 - \exp(-0.96 x_C)] - 31 x_{Mn} - 13 x_{Si} - 10 x_{Cr} - 18 x_{Ni} - 12 x_{Mo}, \quad (5.1)$$

where x_i is the content of element i (i = C, Mn, Si, Cr, Ni, or Mo) in weight percent.

From Equation (5.1), carbon is the most efficient element in decreasing the M_S. Manganese, silicon, chromium, nickel, and molybdenum also decrease M_S, but the addition of such elements is avoided here mostly because it slows down the kinetics of bainite formation. In the so-called nanobainitic steels, which have a high carbon content (around $1\,\mathrm{wt.\%}$) and are alloyed with manganese, silicon, and chromium, the formation of bainite can take up to a few days [12], which is impractical for *in situ* observation. Silicon is also avoided here because it hinders the formation of cementite, as discussed in Chapter 4, and the observation of carbide formation can help differentiate between the diffusional and the diffusionless theory. As Figure 5.1 shows, the diffusionless theory predicts that the carbides found inside the bainitic ferrite in lower bainite are nucleated inside the supersaturated plates of bainitic ferrite. On the other hand, the diffusional theory predicts that these carbides nucleate at the bainitic ferrite/austenite interface, and as the bainitic ferrite grows, these carbides get trapped inside the bainitic ferrite.

The selected material is a Fe-1.24C-0.2Mn-0.15Si-0.15Cr-0.015Al ($\mathrm{wt.\%}$) steel, with an M_S of around $125\,^\circ\mathrm{C}$, measured in the dilatometry experiments shown in Figure 5.2a,b. After quenching to room temperature, a volume fraction of retained austenite of around 0.2 is present, as measured by X-ray diffraction (XRD) and shown in Figure 5.2c. Figure 5.2d shows that after reheating to $280\,^\circ\mathrm{C}$ and holding for $120\,\mathrm{min}$, the retained austenite is almost fully decomposed (0.02 volume fraction remaining). The decomposition of retained austenite is also confirmed by analyzing the microstructure. Figure 5.2e shows the microstructure after quenching consists of fresh martensite and retained austenite. After isothermal holding at $280\,^\circ\mathrm{C}$, the microstructure consists mostly of regions with extensive carbide precipitation and only small and dispersed regions of retained austenite, as shown Figure 5.2f. The regions with extensive carbide precipitation can be either tempered martensite or lower bainite, as both microstructure constituents are virtually indistinguishable from each other.

Figure 5.2g,h show the electron backscatter diffraction (EBSD) maps of the steel after quenching and after the decomposition of retained austenite. In the EBSD map of the quenched sample, the volume fraction of austenite was 0.44. While it is common for EBSD to yield different values of retained austenite than XRD, the trend is usually the inverse, with XRD indicating a higher fraction of austenite [14], as EBSD is more sensitive to the formation of strain-induced martensite during sample preparation, and it might not capture small regions of retained austenite. After the isothermal holding at $280\,^\circ\mathrm{C}$, no austenite was detected in the EBSD.

Another important aspect is the temperature of bainite formation. It is important to choose a temperature in which bainite is expected to form according to both theories. The critical temperature of bainite formation according to the diffu-

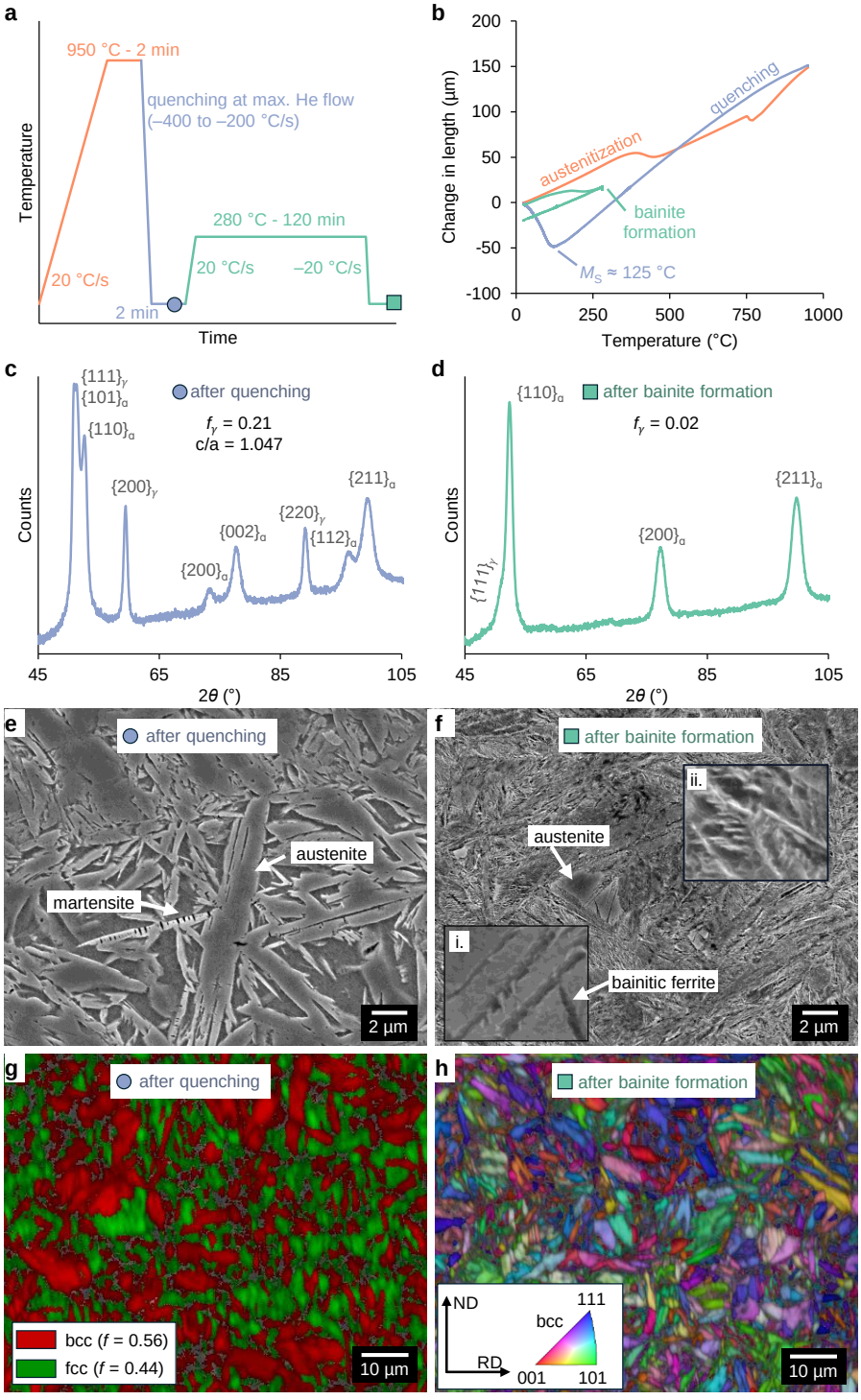
a
950 °C - 2 min
quenching at max. He flow
(–400 to –200 °C/s)
280 °C - 120 min
20 °C/s
20 °C/s
–20 °C/s
2 min
Temperature
Time
b
Change in length (µm)
Temperature (°C)
austenitization
quenching
bainite
formation
M_S ≈ 125 °C
c
after quenching
f_γ = 0.21
c/a = 1.047
Counts
2θ (°)
d
after bainite formation
f_γ = 0.02
Counts
2θ (°)
e
after quenching
austenite
martensite
2 µm
f
after bainite formation
austenite
ii.
i.
bainitic ferrite
2 µm
g
after quenching
bcc (f = 0.56)
fcc (f = 0.44)
10 µm
h
after bainite formation
ND
RD
111
bcc
001
101
10 µm

Figure 5.2. Analysis of phase transformations during quenching and reheating to $280\,^{\circ}\mathrm{C}$. **a.** time-temperature profile of the heat treatment performed in the dilatometer. **b.** relative change in length as a function of temperature as measured in the dilatometer, indicating the M_{S} temperature. No net expansion was detected during bainite formation possibly because of the counteracting contraction caused by martensite tempering and carbide formation. **c.** XRD results after quenching. c/a ratio of the tetragonal martensite lattice (I4/mmm) indicates a carbon content of $1.05\,\mathrm{wt.\%}$ [13]. **d.** XRD results after isothermal holding at $280\,^{\circ}\mathrm{C}$. **e.** SEM image after quenching, sample etched with Nital $2\,\%$. **f.** SEM image after isothermal holding at $280\,^{\circ}\mathrm{C}$, sample etched with Nital $2\,\%$. **g.** EBSD phase map after quenching. **h.** EBSD inverse pole figure of bcc phase after isothermal holding at $280\,^{\circ}\mathrm{C}$

sionless theory is given by T_{h}, T_0, and T_0', defined in Chapter 2. For the diffusional theory, this critical temperature is called WB_{S}, as the diffusional theory claims there is no difference between Widmanstätten ferrite and bainite [15]. Table 5.1 shows the critical temperatures calculated using Thermo-Calc, and all temperatures are below $280\,^{\circ}\mathrm{C}$. Therefore, the product of austenite decomposition is expected to be bainite according to both theories.

Table 5.1. Critical temperatures of bainite formation calculated using Thermo-Calc with database TCFE12.

WB_{S} (°C)	T_{h} (°C)	T_0 (°C)	T_0' (°C)
560	590	367	303

To investigate if bainite is the product of austenite decomposition of this steel at $280\,^{\circ}\mathrm{C}$, a specimen was heat treated in the dilatometer following a temperature profile similar to the one in Figure 5.2a, but instead of quenching to room temperature after austenitization, the sample was quenched to $280\,^{\circ}\mathrm{C}$ directly after austenitization and held isothermally for one hour. Figure 5.3a shows the relative change in length during isothermal holding at $280\,^{\circ}\mathrm{C}$. The sample expands following a sigmoidal-shaped curve and reaches stasis at a $0.22\,\%$ expansion after around $2000\,\mathrm{s}$, indicating austenite decomposition is finished after the one-hour holding. Figure 5.3b shows the microstructure of the steel after the heat treatment is lower bainite, as it consists of a fine dispersion of carbides inside a ferritic matrix.

5.3. Experimental procedure

Dilatometry samples ($10 \times 4 \times 1.5\,\mathrm{mm}^3$) were cut from a $1.5\,\mathrm{mm}$ thick cold rolled strip of a Fe-1.24C-0.2Mn-0.15Si-0.15Cr-0.015Al steel. Dilatometry and sample preparation followed the procedure described in Chapter 4. Data acquisition for XRD also followed the procedure from Chapter 4, but phase quantification was carried out using Rietveld refinement in the software MAUD [16]. EBSD maps

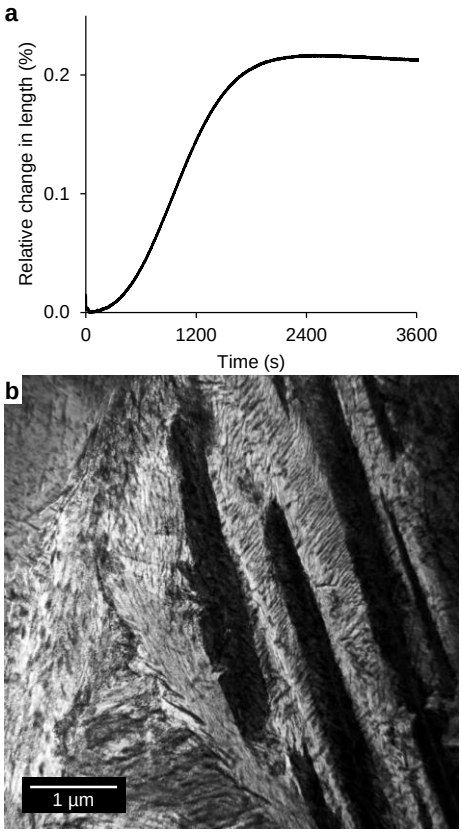

Figure 5.3. Sample heat treated isothermally at $280\,^{\circ}\mathrm{C}$ after austenitization, without prior quenching to room temperature. **a.** relative change in length during holding at $280\,^{\circ}\mathrm{C}$ measured by dilatometry. **b.** TEM image showing the microstructure of the material is lower bainite, as it consists of a fine dispersion of carbides (dark) in a plate-like ferritic matrix (light).

were collected in a Thermo Fisher Helios G4 UXe PFIB equipped with an EDAX EBSD detector, and the software OIM 8.0 was used for data analysis.

After heat treatment in the dilatometer, the samples for TEM were prepared by first manually grinding the dilatometry samples with a $320\,\mathrm{mesh}$ silicon carbide paper to a thickness of $0.1\,\mathrm{mm}$. Then, $3\,\mathrm{mm}$ diameter discs were cut from the ground samples. These discs were electropolished in a STRUERS Tenupol-5 unit cooled down by a Julabo FP-50 refrigerated circulator operating at $-15\,^{\circ}\mathrm{C}$ using a $5\,\%$ perchloric acid, $35\,\%$ 2-butoxyethanol, and $60\,\%$ methanol solution. TEM analysis was conducted in a JEOL JEM-F200 operating at $200\,\mathrm{kV}$ and equipped with a cold emission gun. The samples were mounted in GATAN 628 single tilt heating holder with a tantalum furnace and Hexring mechanism for sample securing. The images were collected using a GATAN Oneview IS camera at a collection rate of

25 frames per second. The equipment and procedure used for the hot stage TEM experiments (except sample preparation) were the same as those used by Nutter *et al.*, and more details can be found in their work [10].

5.4. Results

Figure 5.4 shows the typical microstructure as observed in the TEM before heating. The electropolishing etched more intensely the austenite than the martensite, and thus martensitic regions were usually thicker than austenitic regions and appeared darker. This effect was observed in all samples. A more uniform polishing could possibly have been obtained using the same electropolishing procedure as Nutter *et al.* [10], which involved cooling to $-40\,^{\circ}\mathrm{C}$. However, as cooling to such low temperatures could transform the retained austenite to martensite, it was discarded.

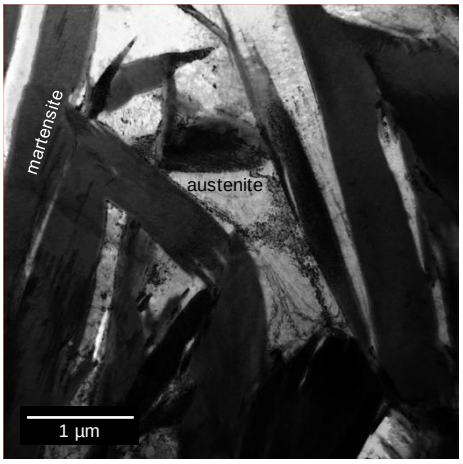

Figure 5.4. TEM image showing microstructure after quenching and before heating to $280\,^{\circ}\mathrm{C}$. Dark regions are fresh martensite, and bright regions are retained austenite.

Figure 5.5 shows the growth of a bainite sheaf at $280\,^{\circ}\mathrm{C}$. The nucleation of the first plate of the sheaf was not observed in real time, but it could be traced back to a martensite/austenite (M/A) interface to the left of the displayed images. In Figure 5.5, $t = 0\,\mathrm{s}$ is considered as the time at which the sheaf was first observed; at this time, the specimen had achieved $280\,^{\circ}\mathrm{C}$ for a few minutes. At $t = 0\,\mathrm{s}$, the thickness of the plate is around $10\,\mathrm{nm}$. The plate then thickens continuously, and at $t = 52\,\mathrm{s}$, its thickness is around $30\,\mathrm{nm}$. The lengthening of the sheaf is not continuous, but a two-stage process, as previously reported by Nutter *et al.* [10], in a repeating succession of growth and stasis stages. The average lengthening rate from $t = 0\,\mathrm{s}$ to $t = 52\,\mathrm{s}$, including the stasis stages, was $8\,\mathrm{nm\,s^{-1}}$. During the growth stages, the lengthening rate achieved velocities up to $20\,\mathrm{nm\,s^{-1}}$.

After a stasis stage, lengthening appeared to resume by the nucleation of a new plate of bainite at or close to the tip of the original plate, giving rise to the

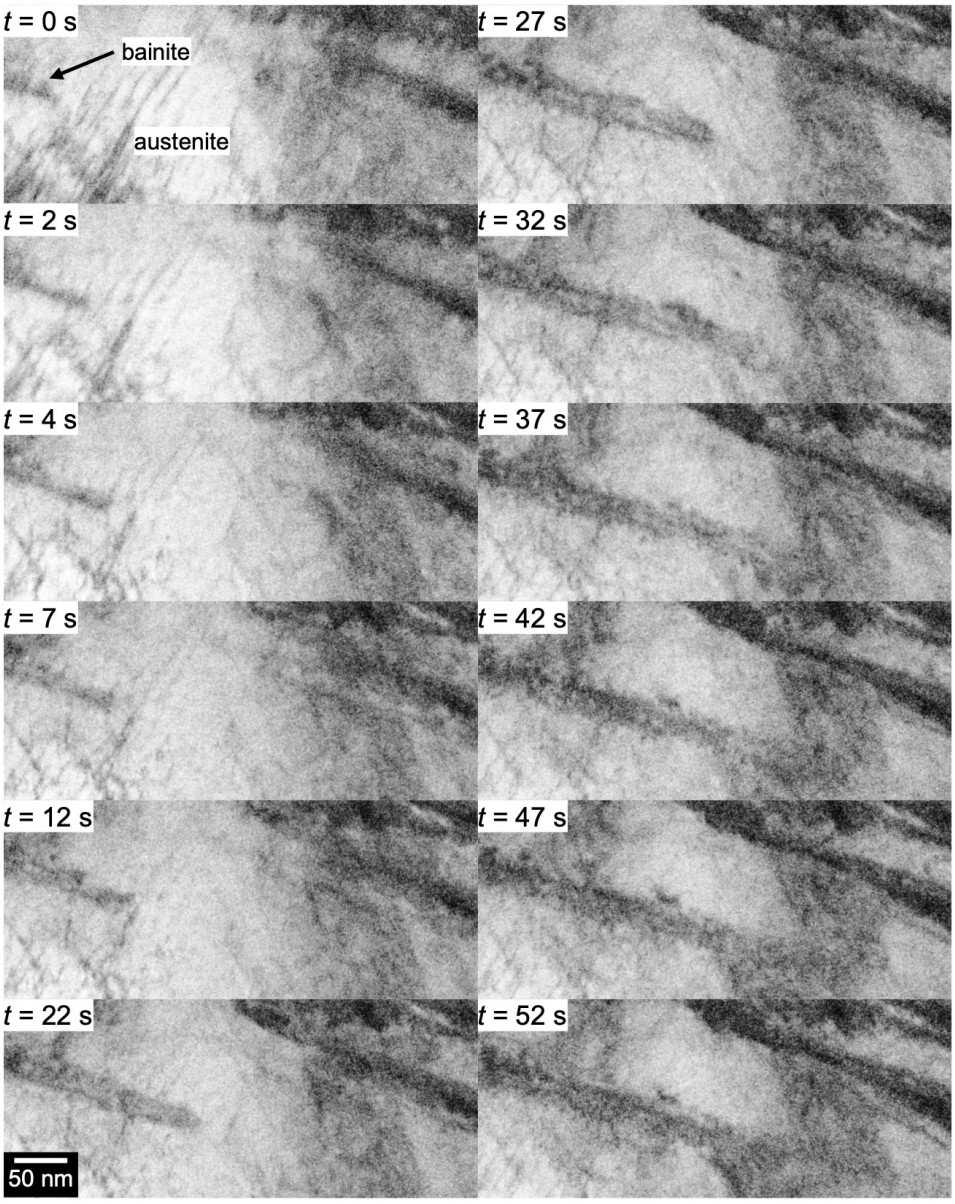

Figure 5.5. Growth of a bainite sheaf during isothermal holding in the hot stage TEM at $280\,^{\circ}\mathrm{C}$. All times are relative to the time at which the top left image was taken.

characteristic sheaf morphology of bainite. This nucleation of new plates is better visualized in the video available in Appendix C and in the observation shown in Figure 5.6. No carbides could be observed.

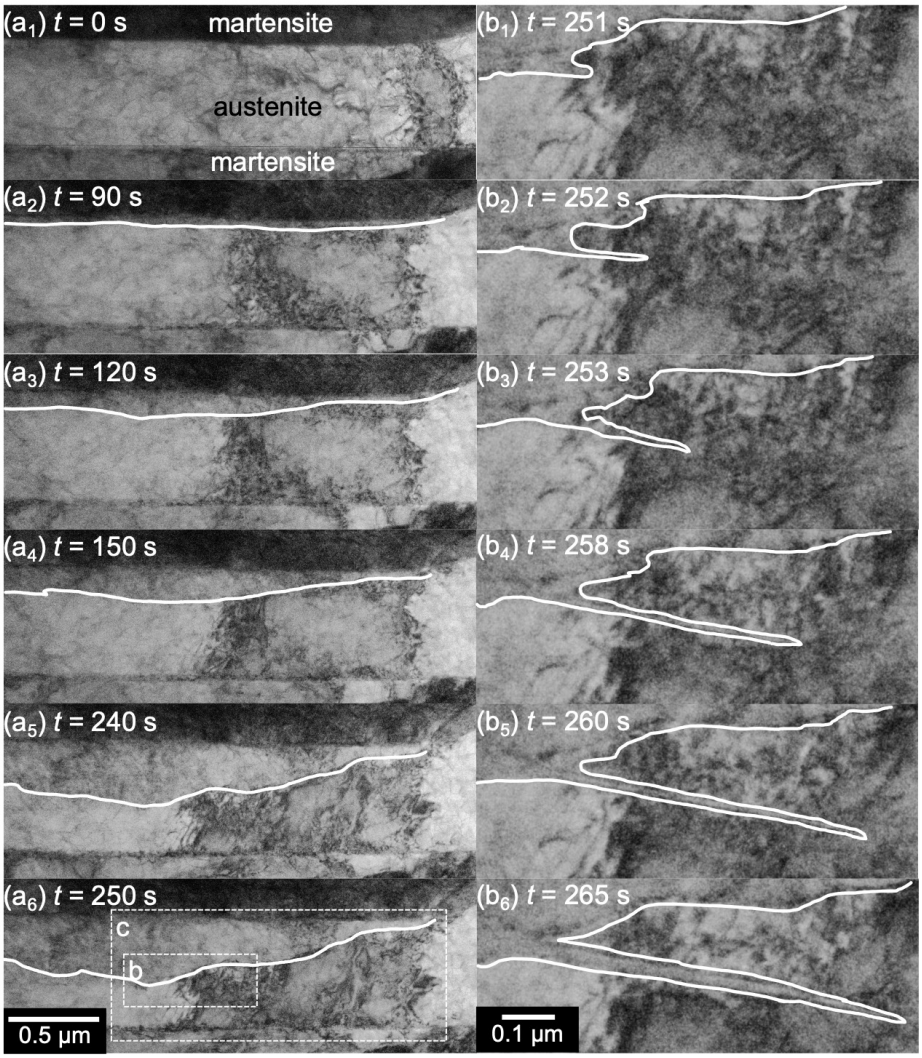

Figure 5.6. Growth of a bainite sheaf during isothermal holding in the hot stage TEM at 280 °C. The bainite/austenite interface is marked by a white line for better visualization. Images in **b$_{1–6}$.** and **c$_{1–6}$.** are from magnified regions of the area shown in images **a$_{1–6}$.**, with the approximate regions shown in **a$_6$**. All times are relative to the time at which image **a$_1$**) was taken. The images without the lines and annotations are shown in Figure C.1 (Appendix C) (continues on the next page)

The formation of bainite was observed in a second sample, and it was formed in a region of retained austenite sandwiched between two plates of martensite, as shown in Figure 5.6a$_1$. Bainite seemed to have nucleated at the upper M/A interface in Figure 5.6a$_1$ and lengthened sideways following the M/A interface.

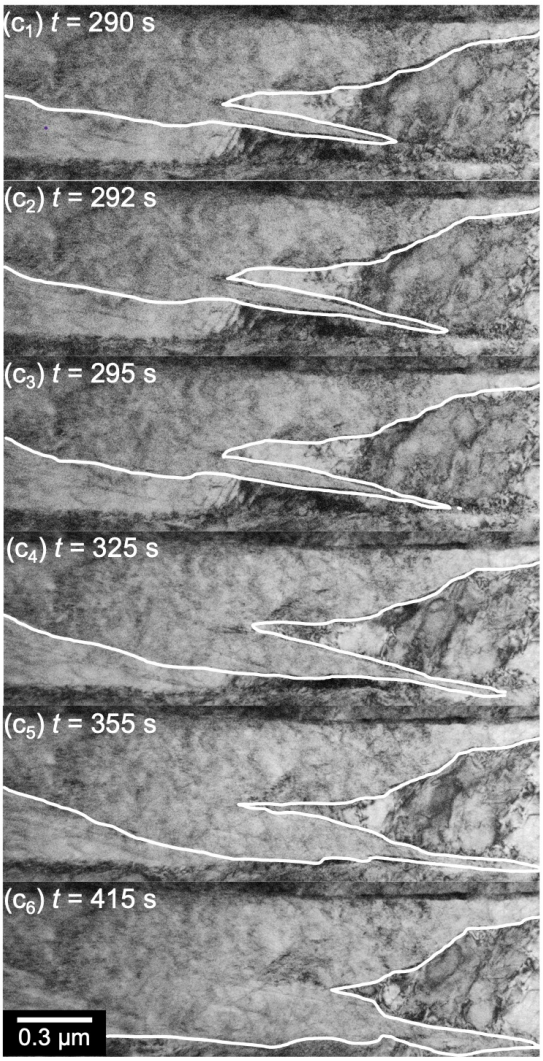

Figure 5.6. Part 2 of the Figure (continued).

At $t = 90\,\mathrm{s}$, bainite grew to consume the whole M/A interface, and the new bainite/austenite (B/A) interface is marked in Figure 5.6a$_2$. However, during this stage ($t = 0$ to $t = 90\,\mathrm{s}$), the bainite plate was still only a few nanometers thick, and the resolution of the images captured is not high enough to confirm that bainite indeed consumed the M/A interface by sideways lengthening. The bainite plate that nucleated at the M/A interface thickened continuously to a thickness of up to $400\,\mathrm{nm}$ at its largest section (Figure 5.6a$_{2\text{–}6}$). The average thickening rate from $t = 0$ to $t = 250\,\mathrm{s}$ was $1.6\,\mathrm{nm\,s^{-1}}$.

At $t = 251\,\mathrm{s}$, a new plate of bainite emerged at the B/A interface (Figure 5.6b$_1$). It was not possible to distinguish if it corresponds to a new plate nucleated at the B/A interface or to the growth of a protuberance from the B/A interface. This new plate started lengthening at an 8 to 9° of misorientation from the lengthening direction of the initial plate (considering that the initial plate grew parallel to the M/A interface), as shown in Figure 5.7a. From $t = 251\,\mathrm{s}$ to $t = 258\,\mathrm{s}$ (Figure 5.6b$_{1-4}$), the bainite plate lengthened continuously at an average velocity of $55\,\mathrm{nm\,s^{-1}}$. At around $t = 260\,\mathrm{s}$, a new plate of bainite nucleated close to or at the tip of a pre-existing plate. This new plate started lengthening almost parallel to the pre-existing plate, with a misorientation of around 4 to 5°, shown in Figure 5.7b. At $t = 290\,\mathrm{s}$, again, a new plate nucleated close to or at the tip of a previously formed plate. Figure 5.7c$_1$ shows the new plate at $t = 292\,\mathrm{s}$ at a 2° misorientation regarding the prior plate. The new plate then grows to merge with the preexisting plate. At $t = 350\,\mathrm{s}$, the two plates are completely merged, and a small dark line-shaped region that could be a carbide particle or a dislocation loop is at the merging point of the two plates (Figure 5.7c$_2$).

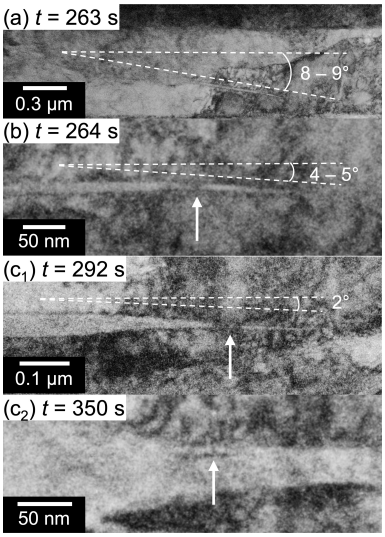

Figure 5.7. Creation of new plates of bainite, indicated by white arrows, close to or at the tip of pre-existing bainite plates. The direction of growth of the new plates is slightly misoriented in relation to the direction of growth of the pre-existing plates. **a.** plate shown in Figure 5.6b$_{1-4}$ growing at an 8 to 9° misorientation from the growth direction of the preexisting plate, which is the plate shown in Figure 5.6a$_{1\text{-}6}$ that grew along the M/A interface. **b.** formation of a new plate at a 4 to 5° misorientation. **$\mathbf{c_1}$.** formation of a new plate at a 2° misorientation and **$\mathbf{c_2}$.** trace left behind by the merging of the two plates. All images are from the same heating experiment shown in Figure 5.6, and all times are relative to the time at which the image in Figure 5.6a$_1$ was taken.

At around $t = 300\,\mathrm{s}$, a new plate of bainite, shown in Figure 5.8, nucleated close to or at the B/A interface. This new plate lengthened almost parallel to the plate

shown in Figure 5.6b. In addition to lengthening, the plate continuously thickened until it touched the preexisting plate of bainite shown in Figure 5.6b. When both plates touched, they seemed to merge. Figure 5.8 shows the merging process and the trace of the interface where the two plates merged.

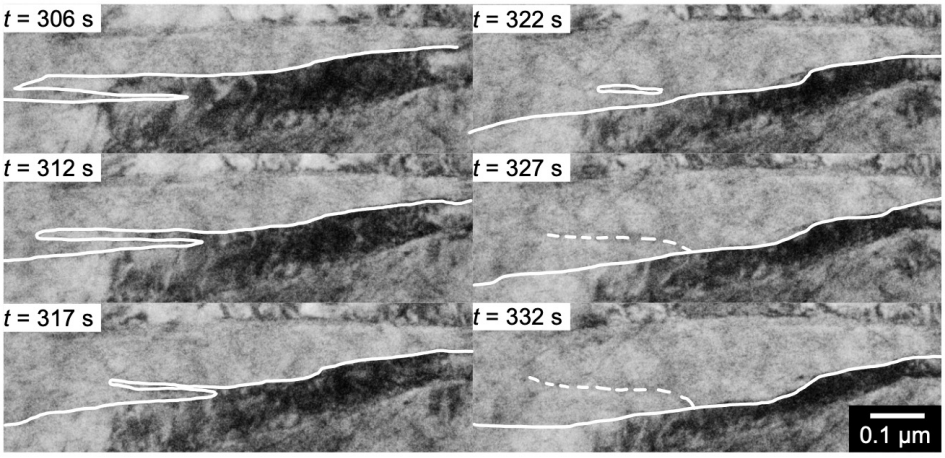

Figure 5.8. Formation of a new plate of bainite (lower plate) and its sideways merging with a preexisting plate of bainite. The upper plate of bainite is the plate shown in Figure 5.6b. The continuous white line marks the B/A interface, and the dotted white line marks the trace of where both plates merged. All times are relative to the time at which the image in Figure 5.6a$_1$ was taken. The images without the lines and annotations are shown in Figure C.2

5.5. Discussion

5.5.1. Nucleation

The formation of bainite could be observed in two different specimens. In both cases, the first plates of bainite nucleated at or close to the M/A interface. Given the spatial resolution, it was not possible to distinguish exactly where bainite nucleated: if at the interface or at dislocations near the interface. Another site at which plates of bainite nucleated is at or close to the B/A interface. This nucleation took place both at the tip of existing bainite plates (Figure 5.7b,c) or at the wavy B/A interface (Figure 5.6b and Figure 5.8). Such nucleation of new plates, often called autocatalysis or sympathetic nucleation, is an important aspect of the diffusionless theory of bainite formation. However, the formation of new plates (also called sub-units) is not necessarily an indication of a diffusionless theory. It rather implies that elastic stresses are accumulating at the interface and stopping the growth of the preexisting bainitic plate [17]. Therefore, the observation of autocatalytic – or sympathetic – nucleation is in line with the displacive component of both the diffusionless and the diffusional theory [18].

After nucleation at a B/A interface, the new plate of bainite started growing almost parallel to the growth direction of the preexisting plate at which it nucleated, with a misorientation varying from 2 to 9° (Figure 5.7). This is similar to an observation made by Olson, Bhadeshia, Edmonds, and Cohen [19, 20] shown in Figure 5.9, and therefore this misorientation is not an artifact of forming bainite in a thin film. The microstructure in Figure 5.9 consists of small bainite sub-units adjacent to a bainite sheaf in a partially transformed steel. Olson *et al.* [20] and Bhadeshia [2] argued that these plates, indicated by arrows in Figure 5.9, are below the operational nucleus size required for rapid, martensite-like, diffusionless growth. They also claimed that a piece of evidence for these sub-units being below the operational size for diffusionless growth is that no intermediate-sized sub-units were found, only large or small. Despite the relatively small size of the sub-units marked in Figure 5.9, it can be argued that they are already too large to be considered sub-operational. The plate marked by a white arrow in Figure 5.9 is around 120 nmin thickness and 700 nm in length, which corresponds to a few billions of atoms of iron. This is much larger than the typical tens or hundreds of atoms expected for the critical nucleus size of martensite or bainite (for instance, from ref. [21] and from the activation volume V^* calculated in Chapter 2).

Figure 5.8 shows a plate of bainite that nucleated and grew sideways and parallel to the direction in which another plate was already growing. After some time, this new plate and the preexisting plate merged. This observation might explain why Olson *et al.* and Bhadeshia [2, 20] did not observe intermediate-sized plates: After enough time, such small plates tend to merge into the main sheaf. Figure 5.7c$_2$ shows that a line of dislocations or carbides might be present at the intersection between two plates that merged together. In Figure 5.9, the white dotted arrows point to similar lines in the sheaf that could have a large density of dislocations and at which two plates might have merged. The separation between the regions indicated by the dotted arrows is around the same length as the small plate indicated by the white solid arrow. Regularly spaced lines in a bainite sheaf were also observed by Timokhina *et al.* [22]. Such lines were spaced in a few hundred nanometers, and the authors attributed them to the nucleation of new plates of bainite at the tip of the leading bainite plate. Timokhina *et al.* also found that these lines marked a slight change of orientation (1 to 2°) in the bainite sheafs, such that a misorientation of 8° was found between two points in the same bainitic sheaf at a 0.7 µm distance from each other.

5.5.2. Growth

In the experiments presented in this Chapter, the growth of bainite was observed with a resolution of a few nanometers and at a collection rate of 25 frames per second. Such spatial and temporal resolution should be enough to resolve individual sub-units, thus overcoming the limitation of confocal optical microscopes. Even so, the observed lengthening rate of bainite plates varied from 20 to 55 nm s^{-1}. This lengthening rate is much closer than that expected for the diffusional theory than for the diffusionless theory. The estimated lengthening rate based on carbon diffusion [3], calculated using Thermo-Calc 2023a coupled

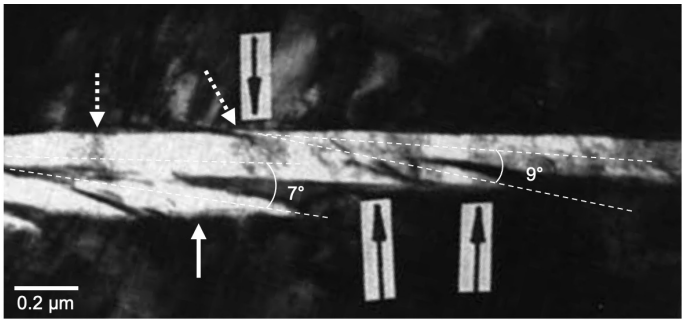

Figure 5.9. Small plates in a bainite sheaf in a partially transformed Fe-3.0Mn-2.1Si-0.43C steel isothermally treated at $286\,^{\circ}\mathrm{C}$. Dark regions are austenite, and bright regions are bainitic ferrite. The small plates are at an angle of 7 to 9° from the plate of bainite from which they nucleated. Reprinted from Acta Metallurgica, 37, G.B. Olson, H.K.D.H. Bhadeshia, M. Cohen, Coupled diffusional/displacive transformations, 381–390 (1989) [20] with permission from Elsevier. Angles between the bainite plates were manually added and are not part of the original image.

with the databases TCFE12 and MOBFE7, which uses the modified Zener-Hillert equation proposed by Leach *et al.* [3], was $34\,\mathrm{nm\,s^{-1}}$, while the lengthening rate expected for a martensitic-like diffusionless growth can be as high as $30\,\mathrm{m\,s^{-1}}$ [20].

The average thickening rate observed in the experiments shown in Figure 5.6a was $1.6\,\mathrm{nm\,s^{-1}}$, which is below the thickening rate expected for an interface movement controlled solely by carbon diffusion, as shown in Figure 5.10. However, it is faster than the expected thermally activated thickening rate for a semicoherent interface calculated according to the model from Santofimia *et al.* [23],

$$v = \frac{d^4 v_{\mathrm{D}}}{kT} \exp\left(-\frac{Q}{RT}\right)\Delta G, \tag{5.2}$$

where v is the interface velocity, d is the interatomic distance across the interface, estimated as $0.255\,\mathrm{nm}$, v_{D} is the Debye frequency, taken as $6.15\times10^{13}\,\mathrm{s^{-1}}$, k is Boltzmann's constant, T is the temperature in kelvin, Q is the migration activation energy, estimated as $165\,\mathrm{kJ\,mol^{-1}}$ for a semicoherent interface based on the measurement of de Knijf *et al.* [24] for an M/A interface or $140\,\mathrm{kJ\,mol^{-1}}$ for an incoherent interface [25], R is the universal gas constant, and ΔG is the driving force.

The simulations in Figure 5.10 consider that thickening is controlled only by either carbon diffusion or interface mobility. However, carbide precipitation might affect the thickening of bainite plates by locally decreasing the carbon content of austenite. At $280\,^{\circ}\mathrm{C}$, the carbon content in austenite in paraequilibrium with cementite for the steel used here is $0.05\,\mathrm{wt.\%}$. At this carbon content, the M_{S} of the austenite is estimated from Equation (5.1) to be $527\,^{\circ}\mathrm{C}$. Therefore, if cementite nucleates at the B/A interface and locally depletes austenite of its carbon, it is

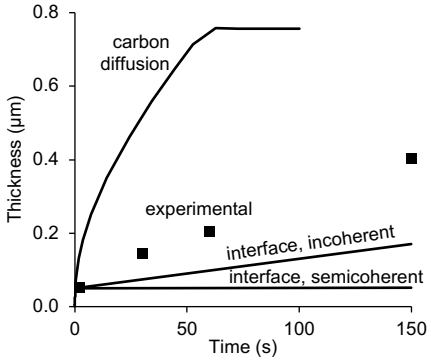

Figure 5.10. Simulated (solid lines) and experimentally measured (markers) thickening of a bainite plate. The carbon diffusion controlled simulation was performed using the diffusion module of Thermo-Calc 2023a with databases TCFE12 and MOBFE7, considering a flat bcc region of $1\,\mathrm{nm}$, with $0.02\,\mathrm{wt.\%}$ C, adjacent to a $1\,\mu\mathrm{m}$ fcc region, with $1.24\,\mathrm{wt.\%}$ C, being isothermally held at $280\,^{\circ}\mathrm{C}$. The interface mobility controlled simulation was performed using Equation (5.2), with $Q = 140\,\mathrm{kJ\,mol^{-1}}$ for the incoherent interface and $Q = 165\,\mathrm{kJ\,mol^{-1}}$ for the semicoherent interface. The experimental thickness was measured from the images shown in Figure 5.6a.

possible to have fast, martensite-like growth of bainite at such depleted regions. The presence of carbides at the bainite/austenite interface was observed in the micrograph in the inset of Figure 5.2f$_{(i)}$. A higher magnification image is shown in Figure C.3.

Spanos *et al.* [26] already proposed that the thickening of bainite plates in lower bainite is aided by cementite nucleation at the B/A interface, as illustrated in a reprint of their sketch in Figure 5.11. They proposed that bainitic ferrite first forms as a thin, elongated plate, free from carbides, and then cementite forms at the B/A interface as regularly spaced discs, and that the bainite plate proceeds to thicken in the space between the cementite particles. Although the formation of carbides could not be detected in the experiments presented here, the growth of bainitic ferrite shown in Figures 5.5 and 5.6 is similar to the sketch proposed by Spanos *et al.* First, thin and elongated bainite plates were formed, and then the plates gradually thickened.

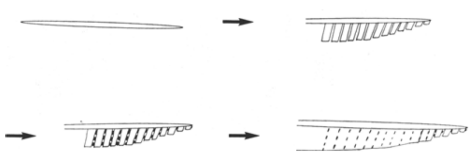

Figure 5.11. Mechanism of lower bainite formation proposed by Spanos *et al.* [26]. Reproduced with permission from Springer Nature.

The thickening assisted by carbide precipitation at the B/A interface might help to explain the fine structure of low temperature carbide free bainitic steels [12]. By alloying the steel with silicon, carbide precipitation at the B/A interface is delayed or even suppressed. Therefore, the thickening of bainite plates might rely on the thermally assisted interface movement of a semicoherent bcc/fcc interface, which has very low mobility – especially at low temperatures –, as shown in Figure 5.10. Additionally, carbon partitioning to the austenite gradually decreases the driving force for interface movement and consequently the velocity of the interface.

Although the lengthening rate measured here agrees with the Thermo-Calc simulations, the ones also measured in a hot stage TEM by Zhao *et al.* [9] and Nutter *et al.* [10] do not. Zhao *et al.* measured a lengthening rate of $0.14\,\mu m\,s^{-1}$ for a Fe-0.43C-1.1Mn-1.4Si-0.9Cr-0.5Ni-0.1Mo steel at $305\,^{\circ}C$, while Thermo-Calc predicts only a $0.004\,\mu m\,s^{-1}$ lengthening rate. Nutter *et al.* found rates mostly between 0.01 to $1\,\mu m\,s^{-1}$, with the highest measured rate at $30\,\mu m\,s^{-1}$ (which is the detection limit in their experiment), while Thermo-Calc predicts a rate of $0.03\,\mu m\,s^{-1}$ nm/s for a Fe-0.3C-0.5Mn-1.5Si-0.1Mo steel at $300\,^{\circ}C$.

A lengthening rate faster than permitted by carbon diffusion could possibly be explained by growth with carbon supersaturation, such as in the model proposed by Olson *et al.* [20] and the model proposed by Hillert [17, 27]. Both models, although based on different assumptions, propose a smoother transition from a diffusional process to a diffusionless process. According to both models, at lower driving forces, a diffusional process close to local equilibrium is favored. As the driving force increases, the bcc product (Widmanstätten ferrite or bainite) deviates from local equilibrium and is formed with higher carbon supersaturation. At some point, when the driving force is high enough, a complete diffusionless transformation is possible. Because of carbon supersaturation, the lengthening rate can be higher than that predicted by considering local equilibrium at the B/A interface. Dai *et al.* recently proposed a diffusion controlled growth model that includes carbon supersaturation, but their model predicts that supersaturation originates from a solute drag effect of carbon at the B/A interface, and thus supersaturation leads to a lower growth rate than predicted by local equilibrium [28].

In the experiments presented here, the driving force for a diffusionless transformation, calculated using Thermo-Calc, is $550\,J\,mol^{-1}$. For Zhao *et al.*, the driving force is $1859\,J\,mol^{-1}$; and for Nutter *et al.*, it is between 1865 and $2297\,J\,mol^{-1}$ (range given by the possible Mn evaporation). Therefore, in the present work, the driving force is lower, and the lengthening rate is closer than that predicted by local equilibrium. For Zhao *et al.* and Nutter *et al.*, the driving force for diffusionless transformation is higher, and bainite might have formed with carbon supersaturation, and thus at a lengthening rate faster than predicted by local equilibrium.

5.6. Implications for the diffusionless-based model

In Chapters 2 and 3 of this dissertation, a model based on the diffusionless theory of bainite formation was developed. In the present chapter, observation of bainite growth by *in situ* TEM indicates that the growth of bainite is much closer to the one predicted by carbon diffusion than to the fast, martensitic-like growth predicted by the diffusionless theory. Therefore, it is important to discuss the implications of the TEM observations for the model proposed in this thesis.

First, a few of the assumptions made when developing the model were confirmed by the TEM observations. All initial nucleation sites of bainite sheaves could be traced to a martensite/austenite interface. In the absence of martensite, the model considers that the sheaves of bainite grow by the successive nucleation of sub-units, rather than the constant growth of a single plate. Nucleation of sub-units at the B/A interface was observed in the experiments of this Chapter, and it could be an important aspect controlling the kinetics of bainite formation.

The main point of disagreement between the model and the experiments presented here is the growth rate of the bainite sub-units. From a fundamental point of view, the assumption made when developing the model was that the growth of sub-units approaches that of martensite, which in turn may approach the speed of sound. From a mathematical point of view, the assumption is that the growth of sub-units to their final size is much faster than the time required for the nucleation of new sub-units at the B/A interface, and thus, nucleation is the rate-limiting factor in bainite formation. Both assumptions are contradicted by the experiments presented here and by the ones from Zhao *et al.* and Nutter et al, as all observations indicate that both the nucleation and the growth of bainite sub-units happen at a similar time scale and are thus important to the overall kinetics.

Based on the model's outcome and validation, two main hypotheses were formulated. The first hypothesis is that the difference in activation energy for bainite nucleation at austenite grain boundaries and at bainite/austenite interfaces controls the effect of prior austenite grain size on bainite formation kinetics. The second hypothesis is that enough potential nucleation sites are created at the martensite/austenite interface to account for most of the bainite nucleation events. These two hypotheses do not rely on a diffusionless growth mechanism and can still hold true even if the growth of sub-units is controlled by carbon diffusion.

The model proposed in this thesis could be further improved by considering the overall kinetics to depend on both the nucleation and the growth of bainite sub-units. While the treatment of nucleation can be maintained as it is, a new expression for the growth of sub-units is needed. The growth should include not only lengthening but thickening. The lengthening rate of sub-units can be estimated using diffusional models that include carbon supersaturation in the bainitic ferrite, such as the models of Olson *et al.* [20] and Hillert [17, 27]. A model for the thickening rate needs to include carbon diffusion in the austenite, interface mobility, and possible carbide precipitation at the B/A interface. It is

also important to consider the accumulation of stress and strain surrounding the sub-units, which limits their size. Considering both the nucleation and growth of bainite sub-units might make the problem too complex to be reduced into an analytical model. Therefore, models that represent the microstructure evolution in 2D or 3D, such as cellular automata and phase-field, might be more suitable.

5.7. Future experiments

The experiments in this Chapter were facilitated by choosing a steel with low M_S that retains a large fraction of retained austenite after quenching to room temperature. Using this approach, bainite formation could be observed in the hot stage TEM by heating only to $280\,^{\circ}\mathrm{C}$. This avoids complications of heating the sample at high temperatures inside the TEM, such as evaporation of high vapor pressure elements, thickening of the specimen, and sample drift during cooling. A high carbon steel was chosen, as carbon is the element that mostly influences M_S without having such a pronounced effect on the kinetics of bainite formation. However, different compositions can be tested for different purposes.

Carbon, in addition to its effect on M_S, increases the driving force for carbide formation while decreasing the driving force for bcc formation, as Figure 5.12 shows. Therefore, by increasing the carbon content, the more carbide formation might influence and change the morphology of bainite, such as by the formation of inverse bainite [29].

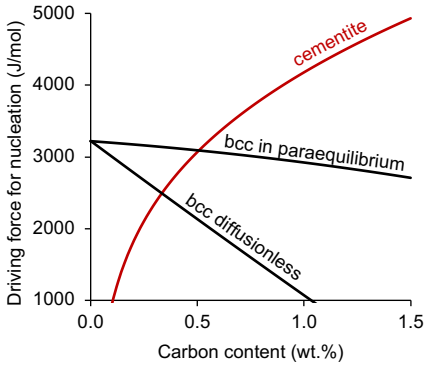

Figure 5.12. Driving force for cementite and bcc nucleation from austenite for the Fe-C system at $280\,^{\circ}\mathrm{C}$ calculated using Thermo-Calc.

To avoid carbide formation, the steel can be alloyed with silicon. A suitable composition might be similar to that of nanobainitic carbide free steels, such as the Fe-0.98C-1.46Si-1.89Mn-0.26Mo-1.26Cr steel studied by Garcia-Mateo *et al.* [12], which has an M_S of $120\,^{\circ}\mathrm{C}$. However, bainite formation in this steel is extremely sluggish, and *in situ* experiments might become unpractical. The composition might be adjusted by slightly increasing carbon content, to ensure a low M_S, and decreasing the content of manganese. Another suitable composition

could be the Fe-1.07C-2.2Si-2.9Mn ($MS = 41\,^{\circ}\mathrm{C}$) steel that Toji *et al.* used to analyze the effect of prior martensite on the formation of bainite [30].

Alloying the steel with silicon is an interesting strategy to study the effect of carbide precipitation at the B/A interface on the thickening of bainite plates. If carbide formation at the B/A interface assists plate thickening, as Spanos *et al.* [26] proposed, then bainite plates in Si alloyed steels should thicken more slowly, possibly at a rate controlled by the thermally activated interface migration from Equation (5.2).

The experiments discussed so far involve quenching the steel to room temperature outside the TEM (in the dilatometer, for instance) to start with a microstructure containing retained austenite and analyzing the decomposition of retained austenite to bainite. However, it is also possible to austenitize the steel in the hot stage TEM, as done by Nutter *et al.* [10]. To avoid the complications associated with high temperatures, a few strategies can be used.

The first issue faced by Nutter was manganese evaporation. The bulk Mn concentration in the steel was $3\,\%$, but after the high temperature experiments, it was only $0.5\,\%$. Manganese was added to the steel to ensure sufficient hardenability, as the cooling rate inside the TEM is limited ($\approx 20\,^{\circ}\mathrm{C\,min^{-1}}$). Better results can be achieved by substituting manganese with other elements that also increase the steel's hardenability but that have a lower vapor pressure. Figure 5.13 shows that at $1000\,^{\circ}\mathrm{C}$, manganese has a vapor pressure five orders of magnitude higher than that of iron and thus is more prone to evaporation. Chromium and nickel have a similar vapor pressure as that of iron, and molybdenum has a much lower vapor pressure than iron. Therefore, alloying the steel with Cr, Ni, and Mo to ensure sufficient hardenability might be a better choice than alloying with Mn, and might avoid problems related to evaporation at high temperatures. Both carbon and silicon have a lower vapor pressure than iron [31, 32].

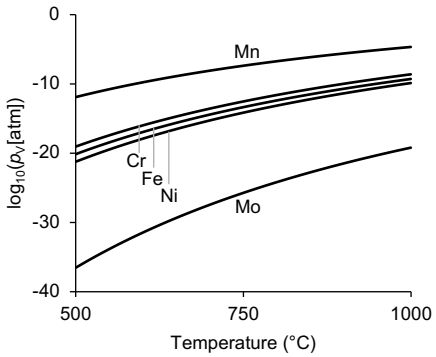

Figure 5.13. Vapor pressure of manganese, chromium, iron, nickel, and molybdenum. Data from reference [33].

A second issue encountered by Nutter was the thickening of the thin foil by surface diffusion of atoms from the thicker regions of the sample to the thinner re-

gions of the sample. This thickening can be reduced by using a steel with a lower austenitization temperature, which can be achieved by adjusting the carbon content to match the eutectoid point and by alloying with austenite-stabilizing elements such as nickel. Nutter *et al.* used an austenitization temperature of $1000\,^{\circ}\mathrm{C}$ in their experiments. If, instead, an austenitization temperature of $800\,^{\circ}\mathrm{C}$ were to be used, then the surface self-diffusion coefficient of iron would decrease by 50 to 70 times for austenite and ferrite, respectively [34], which would greatly slow down the thickening of the thin regions of the TEM specimen.

The third issue related to high temperature austenitization in the TEM is sample drift. Unfortunately, this issue cannot be solved by changing the chemical composition of the specimen. However, if the steel has sufficient hardenability and bainite formation is slow enough, there should be enough time to correct for sample drift during cooling without missing the beginning of bainite formation. Another important aspect that might improve the robustness of the results is to use a double-tilt holder. In the present experiments, only a single-tilt holder was available, and it was not possible to tilt the specimen to reveal microstructure features (such as dislocations) or to study the orientation relationship between bainite and austenite. Also, with a double tilt, it is possible to start the experiment with the austenite at a strong diffracting angle to the beam, such that it appears dark in the bright field image. Then, when bainite forms, there'll be a sharper contrast between bainite and austenite, which will allow a more accurate measurement of the lengthening and thickening rates.

A double tilt can also help in observing the presence of carbides. In the experiments presented here, no carbide formation could be detected. However, this does not mean that carbides were not formed. The difficulty in detecting the presence of carbides lies mostly in their small size and in analyzing the imaging contrast inside the bainite plates. The holding time at $280\,^{\circ}\mathrm{C}$ inside the TEM was only about $10\,\mathrm{min}$, and thus carbides are expected to be much smaller than the ones shown in Figure 5.3b for a sample isothermally treated in the dilatometer at $280\,^{\circ}\mathrm{C}$ for one hour. Also, a clear contrast in the image is to be expected only if the radius of the disc-shaped carbides spans along the thickness of the sample. Even so, with a double tilt holder, it might be possible to take better diffraction patterns to investigate the presence of cementite particles inside bainite plates and at the B/A interface.

A final aspect that needs to be mentioned is sample preparation. The best results are achieved by electropolishing at $-40\,^{\circ}\mathrm{C}$. However, at this temperature, the retained austenite might decompose into martensite. By electropolishing at $-15\,^{\circ}\mathrm{C}$, austenitic regions of the sample got thinner than martensitic regions of the sample. A second possibility, which was not tested here, is to prepare the samples by focused ion beam (FIB). This technique avoids cooling down the sample and allows preparing the TEM sample from a selected region of the microstructure.

5.8. Preliminary conclusions and future analysis

The experiments performed in this Chapter showed the decomposition of austenite at $280\,^{\circ}\mathrm{C}$ by *in situ* hot stage TEM. Based on the thermodynamic limits of both diffusionless and diffusional theory, the product of this decomposition is expected to be bainite, and the morphology of the product formed is similar to that of bainite. The bainitic reaction proceeded by the successive nucleation of plates (also called sub-units), and the lengthening rate of such plates ranged from 20 to $55\,\mathrm{nm\,s^{-1}}$, which is consistent with the modified Zener-Hillert equation developed by Leach *et al.* [3] for a carbon diffusion controlled lengthening of bainite plates. The plates thickened continuously – at least until reaching an obstacle such as another plate –, and the measured thickening rate was $1.6\,\mathrm{nm\,s^{-1}}$ for the plate shown in Figure 5.6a. The observations are in line with the displacive-diffusional theory of bainite formation.

A few more analyses can still be carried out with the data presented here. For instance, in Figure 5.10, only purely diffusion controlled and interface controlled thickening rates were calculated. However, a mixed mode can also be calculated. The lengthening rate calculated using Thermo-Calc, which assumes local equilibrium at the B/A interfaces, matched the rates observed in the present experiments. However, it is interesting to also apply models that allow the supersaturation of carbon in bainitic ferrite, such as the ones from Hillert [27] and from Olson *et al.* [20], especially to analyze if they match the observations presented here and also the lengthening rates measured by Zhao *et al.* and Nutter *et al.*, which were faster than predicted by local equilibrium.

In the past 94 years, since the classical work of Davenport and Bain in 1930 [35], bainite has been widely discussed in the literature, and many models were proposed to represent the morphology [36], crystallography [37], and kinetics [3, 38] of bainite formation. It is worthwhile to revisit this literature and compare the proposed mechanisms to the recent high-resolution observations of bainite formation, such as the one presented here. Finally, it is also important to analyze the differences between displacive transformations – such as bainite and martensite – when they happen in the bulk and when they happen in thin films.

References

[1] L. C. D. Fielding. “The Bainite Controversy”. In: *Materials Science and Technology* 29.4 (Apr. 1, 2013), pp. 383–399. doi: 10.1179/1743284712Y.0000000157.

[2] H. K. D. H. Bhadeshia. *Bainite in Steels: Theory and Practice, Third Edition*. 3rd ed. London: CRC Press, Mar. 6, 2015. 616 pp. doi: 10.1201/9781315096674.

[3] L. Leach, J. Ågren, L. Höglund, and A. Borgenstam. “Diffusion-Controlled Lengthening Rates of Bainitic Ferrite a Part of the Steel Genome”. In: *Metallurgical and Materials Transactions A* 50.6 (June 1, 2019), pp. 2613–2618. doi: 10.1007/s11661-019-05208-x.

[4] E. Swallow and H. K. D. H. Bhadeshia. “High resolution observations of displacements caused by bainitic transformation”. In: *Materials Science and Technology* 12.2 (Feb. 1, 1996). Publisher: Taylor & Francis _eprint: https://doi.org/10.1179/mst.1996.12.2.121, pp. 121–125. doi: 10.1179/mst.1996.12.2.121.

[5] C. Garcia-Mateo, J. A. Jimenez, H. .-. Yen, M. K. Miller, L. Morales-Rivas, M. Kuntz, S. P. Ringer, J. .-. Yang, and F. G. Caballero. “Low temperature bainitic ferrite: Evidence of carbon super-saturation and tetragonality”. In: *Acta Materialia* 91 (June 1, 2015), pp. 162–173. doi: 10.1016/j.actamat.2015.03.018.

[6] I.-E. Benrabah, Y. Brechet, G. Purdy, C. Hutchinson, and H. Zurob. “On the origin of the barrier in the bainite phase transformation”. In: *Scripta Materialia* 223 (Jan. 15, 2023), p. 115076. doi: 10.1016/j.scriptamat.2022.115076.

[7] M. J. Hawkins and J. Barford. “A rapid quenching optical hot-stage microscope”. In: *Journal of Physics E: Scientific Instruments* 3.11 (Nov. 1970), p. 892. doi: 10.1088/0022-3735/3/11/314.

[8] Z.-w. Hu, G. Xu, H.-j. Hu, L. Wang, and Z.-l. Xue. “In situ measured growth rates of bainite plates in an Fe-C-Mn-Si superbainitic steel”. In: *International Journal of Minerals, Metallurgy, and Materials* 21.4 (Apr. 1, 2014), pp. 371–378. doi: 10.1007/s12613-014-0918-5.

[9] X. Zhao, Z. Yang, C. Zheng, F. Zhang, and X. Long. “In situ observation of bainitic transformation behavior in medium carbon bainitic steel”. In: *Journal of Materials Research and Technology* 21 (Nov. 1, 2022), pp. 330–338. doi: 10.1016/j.jmrt.2022.09.057.

[10] J. Nutter, J. Qi, H. Farahani, W. M. Rainforth, and S. van der Zwaag. “In situ TEM observations of the growth of bainitic ferrite in an Fe-0.3C-3Mn-1.5Si-0.15Mo steel”. In: *Acta Materialia* 252.118924 (2023). doi: 10.1016/j.actamat.2023.118924.

[11] S. M. C. van Bohemen. “Bainite and martensite start temperature calculated with exponential carbon dependence”. In: *Materials Science and Technology* 28.4 (Apr. 1, 2012). Publisher: Taylor & Francis _eprint: https://doi.org/10.1179/1743284711Y.0000000097, pp. 487–495. doi: 10.1179/1743284711Y.0000000097.

[12] C. Garcia-Mateo, F. G. Caballero, and H. K. D. H. Bhadeshia. “Development of Hard Bainite”. In: *ISIJ International* 43.8 (2003), pp. 1238–1243. doi: 10.2355/isijinternational.43.1238.

[13] L. Cheng, A. Böttger, T. H. de Keijser, and E. J. Mittemeijer. “Lattice parameters of iron-carbon and iron-nitrogen martensites and austenites”. In: *Scripta Metallurgica et Materialia* 24.3 (Mar. 1, 1990), pp. 509–514. doi: 10.1016/0956-716X(90)90192-J.

[14] P. J. Jacques, S. Allain, O. Bouaziz, A. De, A.-F. Gourgues, B. M. Hance, Y. Houbaert, J. Huang, A. Iza-Mendia, S. E. Kruger, M. Radu, L. Samek, J. Speer, L. Zhao, and S. van der Zwaag. “On measurement of retained austenite in multiphase TRIP steels — results of blind round robin test involving six different techniques”. In: *Materials Science and Technology* 25.5 (May 1, 2009). Publisher: Taylor & Francis _eprint: https://doi.org/10.1179/174328408X353723, pp. 567–574. doi: 10.1179/174328408X353723.

[15] L. Leach, P. Kolmskog, L. Höglund, M. Hillert, and A. Borgenstam. “Critical Driving Forces for Formation of Bainite”. In: *Metallurgical and Materials Transactions A* 49.10 (Oct. 1, 2018), pp. 4509–4520. doi: 10.1007/s11661-018-4819-5.

[16] L. Lutterotti and P. Scardi. “Simultaneous structure and size–strain refinement by the Rietveld method”. In: *Journal of Applied Crystallography* 23.4 (Aug. 1, 1990). Publisher: International Union of Crystallography, pp. 246–252. doi: 10.1107/S0021889890002382.

[17] G. R. Purdy and M. Hillert. “Overview no. 38: On the nature of the bainite transformation in steels”. In: *Acta Metallurgica* 32.6 (June 1, 1984), pp. 823–828. doi: 10.1016/0001-6160(84)90018-X.

[18] A. Borgenstam, M. Hillert, and J. Ågren. “Metallographic evidence of carbon diffusion in the growth of bainite”. In: *Acta Materialia* 57.11 (June 1, 2009), pp. 3242–3252. doi: 10.1016/j.actamat.2009.03.026.

[19] H. K. D. H. Bhadeshia and D. V. Edmonds. “The mechanism of bainite formation in steels”. In: *Acta Metallurgica* 28.9 (Sept. 1, 1980), pp. 1265–1273. doi: 10.1016/0001-6160(80)90082-6.

[20] G. B. Olson, H. K. D. H. Bhadeshia, and M. Cohen. “Coupled diffusional/displacive transformations”. In: *Acta Metallurgica* 37.2 (Feb. 1, 1989), pp. 381–390. doi: 10.1016/0001-6160(89)90222-8.

[21] G. B. Olson and M. Cohen. “A general mechanism of martensitic nucleation: Part III. Kinetics of martensitic nucleation”. In: *Metallurgical Transactions A* 7.12 (Dec. 1, 1976), pp. 1915–1923. doi: 10.1007/BF02659824.

[22] I. B. Timokhina, K. D. Liss, D. Raabe, K. Rakha, H. Beladi, X. Y. Xiong, and P. D. Hodgson. “Growth of bainitic ferrite and carbon partitioning during the early stages of bainite transformation in a 2 mass% silicon steel studied by in situ neutron diffraction, TEM and APT”. In: *Journal of Applied Crystallography* 49.2 (Apr. 1, 2016). Publisher: International Union of Crystallography, pp. 399–414. doi: 10.1107/S1600576716000418.

[23] M. J. Santofimia, L. Zhao, and J. Sietsma. “Model for the interaction between interface migration and carbon diffusion during annealing of martensite–austenite microstructures in steels”. In: *Scripta Materialia* 59.2 (July 1, 2008), pp. 159–162. doi: 10.1016/j.scriptamat.2008.02.045.

[24] D. De Knijf, M. J. Santofimia, H. Shi, V. Bliznuk, C. Föjer, R. Petrov, and W. Xu. “In situ austenite–martensite interface mobility study during annealing”. In: *Acta Materialia* 90 (May 15, 2015), pp. 161–168. doi: 10.1016/j.actamat.2015.02.040.

[25] G. P. Krielaart and S. van der Zwaag. “Kinetics of $\gamma \rightarrow \alpha$ phase transformation in Fe-Mn alloys containing low manganese”. In: *Materials Science and Technology* 14.1 (Jan. 1, 1998). Publisher: SAGE Publications, pp. 10–18. doi: 10.1179/mst.1998.14.1.10.

[26] G. Spanos, H. S. Fang, and H. I. Aaronson. “A mechanism for the formation of lower bainite”. In: *Metallurgical Transactions A* 21.6 (June 1, 1990), pp. 1381–1390. doi: 10.1007/BF02672558.

[27] M. Hillert. “Diffusion and interface control of reactions in alloys”. In: *Metallurgical Transactions A* 6.1 (Jan. 1, 1975), pp. 5–19. doi: 10.1007/BF02673664.

[28] Z. Dai, H. Chen, J. Sun, S. van der Zwaag, and J. Sun. “Carbon solute drag effect on the growth of carbon supersaturated bainitic ferrite: Modeling and experimental validations”. In: *Acta Materialia* 268 (Apr. 15, 2024), p. 119791. doi: 10.1016/j.actamat.2024.119791.

[29] A. Borgenstam, P. Hedström, M. Hillert, P. Kolmskog, A. Stormvinter, and J. Ågren. “On the Symmetry Among the Diffusional Transformation Products of Austenite”. In: *Metallurgical and Materials Transactions A* 42.6 (June 1, 2011), pp. 1558–1574. doi: 10.1007/s11661-010-0539-1.

[30] Y. Toji, H. Matsuda, and D. Raabe. “Effect of Si on the acceleration of bainite transformation by pre-existing martensite”. In: *Acta Materialia* 116 (Sept. 1, 2016), pp. 250–262. doi: 10.1016/j.actamat.2016.06.044.

[31] A. L. Marshall and F. J. Norton. “Carbon Vapor Pressure and Heat of Vaporization”. In: *Journal of the American Chemical Society* 72.5 (May 1, 1950). Publisher: American Chemical Society, pp. 2166–2171. doi: 10.1021/ja01161a081.

[32] P. D. Desai. “Thermodynamic Properties of Iron and Silicon”. In: *Journal of Physical and Chemical Reference Data* 15.3 (July 1, 1986), pp. 967–983. doi: 10.1063/1.555761.

[33] C. B. Alcock, V. P. Itkin, and M. K. Horrigan. “Vapour Pressure Equations for the Metallic Elements: 298–2500K”. In: *Canadian Metallurgical Quarterly* 23.3 (July 1, 1984). Publisher: Taylor & Francis _eprint: https://doi.org/10.1179/cmq.1984.23.3.309, pp. 309–313. doi: 10.1179/cmq.1984.23.3.309.

[34] G. Matsumura. “Sintering of iron wires”. In: *Acta Metallurgica* 19.8 (Aug. 1, 1971), pp. 851–855. doi: 10.1016/0001-6160(71)90141-6.

[35] E. S. Davenport and E. C. Bain. “Transformation of austenite at constant subcritical temperatures”. In: *Metallurgical Transactions* 1.12 (Dec. 1, 1970), pp. 3503–3530. doi: 10.1007/BF03037892.

[36] J. Yin, M. Hillert, and A. Borgenstam. “Morphology of Upper and Lower Bainite with 0.7 Mass Pct C”. In: *Metallurgical and Materials Transactions A* 48.9 (Sept. 1, 2017), pp. 4006–4024. doi: 10.1007/s11661-017-4208-5.

[37] N. Takayama, G. Miyamoto, and T. Furuhara. “Effects of transformation temperature on variant pairing of bainitic ferrite in low carbon steel”. In: *Acta Materialia* 60.5 (Mar. 1, 2012), pp. 2387–2396. doi: 10.1016/j.actamat.2011.12.018.

[38] M. J. Santofimia, F. G. Caballero, C. Capdevila, C. García-Mateo, and C. G. d. Andrés. “Evaluation of Displacive Models for Bainite Transformation Kinetics in Steels”. In: *Materials Transactions* 47.6 (2006), pp. 1492–1500. doi: 10.2320/matertrans.47.1492.

6

Conclusion

This dissertation presented an extensive analysis of different aspects of bainite formation in steels. The first part of the thesis, which includes Chapters 2 and 3, presents a new kinetic model of bainite formation. The second part (Chapter 4) presents the design of a third generation advanced high strength steel that can be manufactured in existing continuous annealing lines. The last part (Chapter 5) presents high resolution observations of bainite formation by *in situ* transmission electron microscopy. The contributions of each part will be summarized below and will be followed by recommendations for future work.

6.1. Modeling the kinetics of bainite formation

A new kinetic model of bainite formation was developed by independently calculating site saturation for each type of nucleation site. Chapter 2 studied the cases in which the possible nucleation sites are the austenite grain boundaries (AGBs) and the bainite/austenite (B/A) interface. When the austenite grain size is refined, it can either accelerate or decelerate the formation of bainite, depending on the chemical composition of the steel and the temperature of bainite formation. The model was able to reproduce both effects, and it showed that the opposing effects might be controlled by the difference in activation energies at the AGBs and B/A interfaces. In Chapter 3, the model was extended to the case in which prior martensite is present, and it was possible to show, aided by the model, that the accelerating effect of martensite is caused by the large number of potential nucleation sites that are created at the martensite/austenite (M/A) interface.

The main contribution, in terms of kinetic modeling, was introducing a maximum fraction of the transformation product that each type of nucleation site can give rise to. Thus, the model developed here can be extended to cases in which other types of potential nucleation sites for bainite are present, such as ferrite/austenite interfaces and carbide/austenite interfaces. Also, the model is not limited to bainite formation in steels. It can be applied to any type of transformation in which different types of potential nucleation sites are present, and after a nucleation event, the product of transformation can only grow to a limited size, and thus each type of nucleation site has a limited fraction of the product phase that it can give rise to.

One of the most important discoveries was that martensite/austenite interfaces are the main site of bainite nucleation – given that enough martensite is present. Thus, the hardenability of steels can be increased by segregation of elements (such as boron) to the austenite grain boundaries without slowing down bainite formation in the presence of martensite, as the new martensite/austenite interfaces created during quenching are free from segregation. By partially substituting elements added for hardenability – such as manganese, chromium, or nickel – with boron, which is the most effective element for hardenability, the emission of equivalent CO_2 could be reduced by up to $200\,\mathrm{kg}$ per ton of steel [1], while also reducing the costs of production and shortening the time for the formation of bainite in the presence of martensite. This strategy – which can be called

selective segregation, as austenite grain boundaries are enriched in boron, but the new martensite/austenite interfaces are free from segregation – can possibly be extended to other materials that undergo martensitic transformation, such as titanium alloys.

6.2. Design of novel third generation advanced high strength steels

Chapter 4 presented the design of a new family of third generation advanced high strength steels. By careful alloy design to balance the hardenability and kinetics of bainite formation and by taking advantage of the accelerating effect of prior martensite on the kinetics of bainite formation, the steels developed can be manufactured in existing modern continuous annealing lines, with bainite formation realized under $300\,\mathrm{s}$.

Five compositions, including the reference composition Fe-0.24C-2.3Mn-1.5Si ($\mathrm{wt.\%}$), achieved an ultimate tensile strength higher than $1370\,\mathrm{MPa}$ and tensile elongation higher than $5\,\%$, which meets the requirements of steel grade CR1000Y1370UTS-CH of VDA's (German Association of the Automotive Industry) most recent standard for high strength sheet steels [2]. The isothermal bainite formation, designed for the overaging section of continuous annealing lines, was carried out at approximately $20\,^{\circ}\mathrm{C}$ below the martensite start temperature (M_{S}) of the steels for $300\,\mathrm{s}$. This proposed heat treatment, called BAM (bainite accelerated by martensite), yields higher ultimate tensile strength than conventional bainite formation above M_{S}, as bainite laths are finer when formed at lower temperatures.

6.3. In situ high resolution observation of bainite formation

In Chapter 5, bainite formation was observed by *in situ* transmission electron microscopy (TEM). To avoid the difficulties associated with heating the sample to high temperatures in the TEM – such as foil thickening, evaporation of elements, and sample drift during cooling [3] –, a steel with low M_{S} ($\approx 125\,^{\circ}\mathrm{C}$) was used, so that some austenite is retained at room temperature after quenching. The only step performed inside the TEM was heating the quenched steel, which consisted of a martensitic-austenitic microstructure, to $280\,^{\circ}\mathrm{C}$ for the retained austenite to decompose into bainite, thus circumventing the difficulties associated with heating to high temperatures inside the TEM.

The formation and growth of individual bainite plates could be observed in high resolution. The lengthening rates closely matched the expected rate, according to the modified Zener-Hillert model [4], for a process controlled by carbon diffusion. Therefore, the results presented in Chapter 5 directly contradict one of the assumptions made when developing the model in Chapters 2 and 3, which is that plates of bainite grow much faster than is allowed by carbon diffusion and

are thus initially supersaturated in carbon. While this may have major implications in the model, and the growth rate of individual bainite plates might need to be included in the model to better capture the kinetics of bainite formation, it does not contradict the most important insights drawn from the model, which were related to the nucleation sites of bainite and not to the growth of individual plates.

In addition to showing that the highest resolution *in situ* observations of bainite formation match the diffusional theory better than the diffusionless one, Chapter 5 also discusses ideas and setups for new *in situ* TEM experiments. The comparison between such proposed experiments and the diffusional and diffusionless theories of bainite formation might yield key contributions to unraveling the widely discussed mechanism of bainite formation.

6.4. Recommendation for future works

Segregation of alloying elements to austenite grain boundaries and the effect of prior austenite grain size

In Chapter 2, it was proposed that the difference in activation energy for bainite nucleation at AGBs and B/A interfaces is one of the key factors controlling the effect of prior austenite grain size (PAGS) on bainite formation kinetics. This proposition can be tested using steels that contain alloying elements that strongly segregate to AGBs, such as boron. The results in Figure 3.10 indicate that boron influences the kinetics of bainite formation by changing the activation energy of bainite nucleation at AGBs. Therefore, steels that differ in chemical composition only by their boron content (such as steels 3B and 17B in Chapter 3) can be used to directly study the influence of the activation energy for bainite nucleation at AGBs on the effect of PAGS on bainite formation kinetics.

Since the boron content is usually in the range of a few ppm, it is not expected that boron will affect the average driving force for bainite nucleation and the yield strength of austenite, and therefore it is also interesting to study how the bainite plate thickness varies as a function of PAGS in steels with different boron content. This study might help to correlate the plate thickness with the kinetics of bainite formation and to clarify if, for instance, faster bainite formation results in more impingement events that limit the thickening of bainite plates.

The austenitization step in such experiments need extra consideration. PAGS is usually controlled by the austenitization temperature. However, the austenitization temperature also controls the equilibrium content of alloying elements at AGBs [5]. It might be a good practice to, after austenitization at any given temperature, have an isothermal holding step slightly above A_{e3} to ensure the same content of alloying elements segregated to AGBs in all samples.

Autocatalysis in martensite formation

Figure 3.12 showed that the rate of martensite formation per fraction of austenite available is not constant throughout martensite formation, as assumed by

Koistinen-Marburger's (KM) equation [6] and as proposed by Magee in the derivation of KM's equation [7]. It has been proposed that the increase in martensite formation rate could be because of chemical inhomogeneities in the material [8]. It could also be proposed that is an artifact of measurement because of the thermal gradients present in dilatometry samples (Figure 3.8). However, we also analyzed martensite formation *in situ* by synchrotron X-ray diffraction (XRD) – experiments which were not included in this dissertaion – in samples that were homogenized at $1250\,^{\circ}\mathrm{C}$ for $48\,\mathrm{h}$. The size of the X-ray beam was $1 \times 1\,\mathrm{mm}^2$ and directed at the center of the specimen, which avoids the thermal gradient, while the homogenization treatment avoids (or at least minimizes) the chemical inhomogeneity. Even so, a similar curve to that of Figure 3.12 was observed. Therefore, this phenomenon is intrinsic to martensite formation, and not an artifact of measurement.

Models that consider autocatalysis in martensite have been proposed, such as the one by Khan *et al.* [9] and Huyan *et al.* [10]. Both models introduce a term proportional to the fraction of martensite when calculating the rate of transformation to account for autocatalysis. Consequently, both models predict that the rate of martensite formation per available fraction of austenite increases linearly as a function of martensite fraction until the end of the transformation. However, as Figure 3.12 shows, the rate first increases, reaches a maximum at a fraction of 0.2 to 0.3, and then decreases. In Chapter 3 it is proposed that autocatalysis is controlled by the area of M/A interface rather than the fraction of martensite – Equation (3.24) –, which would explain the shape of the curve in Figure 3.12.

It would be valuable to our understanding of martensite formation to develop new kinetic models based on the assumption of autocatalysis dominated by the area of M/A interfaces, as proposed on Equation (3.24). To make sure such a model correctly captures autocatalysis, this new model should be validated against curves of the rate of martensite formation per available fraction of austenite rather than simply curves of martensite fraction as a function of temperature. It is also important to verify if there are any pronounced competing phenomena happening, such as bainite formation or carbon partitioning to the austenite. For instance, in Figure 3.12, since bainite formation is fast ($0.02\,\mathrm{s}^{-1}$) and natural cooling in the dilatometer is used ($< 20\,^{\circ}\mathrm{C}\,\mathrm{s}^{-1}$ when below M_S), it is possible that bainite formation has affected the results. This could be further investigated by using different cooling rates – however, at the cost of introducing larger thermal gradients in the samples.

The most difficult aspect in developing such a model might be choosing a function to represent the evolution of the area of M/A interface as a function of martensite fraction. Such a function could be derived from experiments, geometrical analysis, or 2D and 3D simulations of microstructure evolution.

Analyzing the autocatalysis in martensite, as proposed here, could lead to the development of more physically accurate models of martensite formation, with possibly better predictive capabilities. It could also help to explain the effect of alloying elements on the kinetics of martensite formation, which are usually taken

into account in the empirical alpha parameter of the KM equation [11]. Also, since autocatalysis in martensite formation might be linked to the accelerating of bainite formation, a better understanding of autocatalysis in martensite could help to better understand this accelerating effect. In turn, this might aid the design of even shorter and more energy efficient heat treatments for bainite formation.

In situ observation of bainite by TEM

A few ideas for future work using *in situ* TEM were discussed in Section 5.7. However, given the potential of these experiments to clarify the role of carbon diffusion during the growth of bainite laths (diffusional and diffusionless theory of bainite formation, Figure 5.1), a few ideas are given here:

- Observe bainite formation in steels alloyed with silicon, preferentially with a chemical composition close to that of nanobainitic steels [12], in which fine laths of bainite ($< 0.1\,\mu m$) are separated by films of retained austenite. If the same fine microstructure is observed forming *in situ* in the TEM, it is a piece of evidence that the mechanism of bainite transformation in the thin foil is similar to that of bulk, and it will help to elucidate the effect of carbides on the thickening of bainite laths.

- Observe martensite formation *in situ* in the TEM. This will require using a steel alloyed with elements that increase the hardenability and that have a low vapor pressure. Comparing the temperature of martensite formation to that of bulk samples can clarify what is the effect of using a thin foil on the energy barrier for a displacive transformation.

- Using a double tilt holder to better observe dislocations, carbides, and orientation relationships. If a double tilt holder is not available, it is possible to interrupt bainite formation by turning off the heating stage when a lath of bainite is growing. Then, the sample can be transported to a double tilt holder. This type of experiment with interrupted bainite formation also allows to analyze a snapshot of the transformation. Then, it is possible to analyze the presence of carbides at the interfaces, the character of the interface, and possibly the carbon distribution around and within the bainite lath. However, the interrupted treatment requires that no transformation or interface movement happens during cooling.

Combining nucleation-based models with diffusional growth

In Chapters 2 and 3, a kinetic model of bainite formation based on the nucleation rate was proposed. The assumption that nucleation of bainite laths is the rate-controlling factor in bainite formation comes from the diffusionless theory. However, considering the diffusional theory, both the nucleation and growth of laths could control the overall kinetics. Therefore, it is interesting to modify the model proposed in Chapters 2 and 3 to include the growth of individual laths. If

the nucleation of the laths is considered to take place by the dissociation of dislocations, then the equations for the nucleation rate in the model proposed here do not need to be modified.

Nucleation of bainite

The model proposed in Chapters 2 and 3 considers that bainite nucleates by a mechanism similar to that of martensite, with the main difference being that carbon diffusion takes place during bainite nucleation and that the dissociation of dislocations is aided by thermal activation in the case of bainite. This assumption is shared by other kinetic models that adopt the diffusionless theory of bainite formation [13–16] – even though the diffusionless growth and the nucleation by dissociation of dislocations are not necessarily linked. However, as discussed in Chapter 2, the direct correspondence of martensite and bainite nucleation raises a few questions.

First, bainite sheaves are often observed to nucleate at austenite grain boundaries. Conversely, there is evidence that martensite nucleates inside austenite grains. This evidence is mainly from works, such as the one of Magee [17], using small Fe-Ni particles. In these experiments, micrometric and submicrometric particles that were fully austenitic at room temperature were cooled down to below room temperature to form isothermal martensite. By correlating number of particles in which any fraction of martensite was formed to the size of such particles, it is possible to estimate the density of initially present potential nucleation sites. As this number scales with the volume of the particle, it was concluded that nucleation sites are present in the volume – that is, inside the austenite grains – rather than at austenite grain boundaries or at the surface of the particles. A similar experiment with bainite would be interesting and might allow to better compare the nucleation of bainite to that of martensite. It would be necessary to use a steel that is still austenitic at room temperature and can transform to bainite upon heating.

A second question that can be raised is how the mechanism of nucleation by dissociation of dislocations leads to the observation that bainite sheafs mostly nucleate at austenite grain boundaries. It is not clear if this is because the density of dislocations is higher close to austenite grain boundaries, or if bainite nucleates from dislocations or disconnections at the grain boundaries. As it is extremely difficult to observe nucleation experimentally, this question might be better tackled by theoretical analysis, atomistic simulations, or carefully designed experiments to control the distribution of dislocations within the austenite grains.

References

[1] A. Gramlich, C. Helbig, M. Schmidt, and W. Hagedorn. “A comprehensive design approach to increase the performance of steels under minimal costs and environmental impacts”. In: *Sustainable Materials and Technologies* 41 (Sept. 1, 2024), e01040. doi: 10.1016/j.susmat.2024.e01040.

[2] *VDA 239-100 – Sheet Steel for Cold Forming (05/2024)*. 2024.

[3] J. Nutter, J. Qi, H. Farahani, W. M. Rainforth, and S. van der Zwaag. “In situ TEM observations of the growth of bainitic ferrite in an Fe-0.3C-3Mn-1.5Si-0.15Mo steel”. In: *Acta Materialia* 252.118924 (2023). doi: 10.1016/j.actamat.2023.118924.

[4] L. Leach, J. Ågren, L. Höglund, and A. Borgenstam. “Diffusion-Controlled Lengthening Rates of Bainitic Ferrite a Part of the Steel Genome”. In: *Metallurgical and Materials Transactions A* 50.6 (June 1, 2019), pp. 2613–2618. doi: 10.1007/s11661-019-05208-x.

[5] G. Da Rosa, P. Maugis, A. Portavoce, S. Lartigue-Korinek, N. Valle, E. Lentzen, J. Drillet, and K. Hoummada. “Boron segregation at austenite grain boundaries: An equilibrium phenomenon”. In: *Acta Materialia* 255 (Aug. 15, 2023), p. 119098. doi: 10.1016/j.actamat.2023.119098.

[6] D. P. Koistinen and R. E. Marburger. “A general equation prescribing the extent of the austenite-martensite transformation in pure iron-carbon alloys and plain carbon steels”. In: *Acta Metallurgica* 7.1 (Jan. 1, 1959), pp. 59–60. doi: 10.1016/0001-6160(59)90170-1.

[7] C. L. Magee. “The nucleation of martensite”. In: *Phase Transformations*. ASM, 1970, pp. 115–156.

[8] T. Sourmail and V. Smanio. “Determination of Ms temperature: methods, meaning and influence of ‘slow start’ phenomenon”. In: *Materials Science and Technology* 29.7 (July 1, 2013). Publisher: SAGE Publications, pp. 883–888. doi: 10.1179/1743284713Y.0000000209.

[9] S. Khan and H. Bhadeshia. “Kinetics of Martensitic transformation in partially bainitic 300M steel”. In: *Materials Science and Engineering: A* 129.2 (Nov. 1990), pp. 257–272. doi: 10.1016/0921-5093(90)90273-6.

[10] F. Huyan, P. Hedström, L. Höglund, and A. Borgenstam. “A Thermodynamic-Based Model to Predict the Fraction of Martensite in Steels”. In: *Metallurgical and Materials Transactions A* 47.9 (Sept. 1, 2016), pp. 4404–4410. doi: 10.1007/s11661-016-3604-6.

[11] S. M. C. van Bohemen. “Bainite and martensite start temperature calculated with exponential carbon dependence”. In: *Materials Science and Technology* 28.4 (Apr. 1, 2012). Publisher: Taylor & Francis _eprint: https://doi.org/10.1179/1743284711Y.0000000097, pp. 487–495. doi: 10.1179/1743284711Y.0000000097.

[12] F. G. Caballero, H. K. D. H. Bhadeshia, K. J. A. Mawella, D. G. Jones, and P. Brown. “Very strong low temperature bainite”. In: *Materials Science and Technology* 18.3 (Mar. 2002), pp. 279–284. doi: 10.1179/026708301225000725.

[13] S. van Bohemen and J. Sietsma. “Modeling of isothermal bainite formation based on the nucleation kinetics.” In: *International Journal of Materials Research* 99 (2008), pp. 739–747. doi: 10.3139/146.101695.

[14] H. Matsuda and H. K. D. H. Bhadeshia. “Kinetics of the Bainite Transformation”. In: *Proceedings: Mathematical, Physical and Engineering Sciences* 460.2046 (2004). Publisher: The Royal Society, pp. 1707–1722. doi: 10.1098/rspa.2003.1225.

[15] A. Ravi, J. Sietsma, and M. Santofimia. “Exploring bainite formation kinetics distinguishing grain-boundary and autocatalytic nucleation in high and low-Si steels”. In: *Acta Materialia* 105 (2016), pp. 155–164. doi: 10.1016/j.actamat.2015.11.044.

[16] M. J. Santofimia, F. G. Caballero, C. Capdevila, C. García-Mateo, and C. G. d. Andrés. “Evaluation of Displacive Models for Bainite Transformation Kinetics in Steels”. In: *Materials Transactions* 47.6 (2006), pp. 1492–1500. doi: 10.2320/matertrans.47.1492.

[17] C. L. Magee. “The kinetics of martensite formation in small particles”. In: *Metallurgical Transactions* 2.9 (Sept. 1, 1971), pp. 2419–2430. doi: 10.1007/BF02814879.

A

Appendix to Chapter 2

A.1. Effect of carbon enrichment

The theoretical analysis in Sections 2.3.1 and 2.3.2 considered that no carbon enrichment of the austenite took place ($X_b = \overline{X}$). To study the influence of carbon enrichment on the effect of the prior austenite grain size, we repeated the simulations shown in Figures 2.2 to 2.4 but considered different levels of carbon enrichment of the austenite. The results are shown in Figures A.1 to A.3 and indicate that the carbon enrichment of austenite has no noticeable influence on the effect of the prior austenite grain size on bainite formation kinetics.

A.2. Ratio f_{BA}/f_{AGB} at the end of the transformation

Figure 2.4e and Figure A.3e show that according to the model developed in the present work, the ratio of autocatalytically nucleated bainite to grain boundary nucleated bainite at the end of the transformation (f_{BA}/f_{AGB}) is a linear function of the prior austenite grain size. Such a relationship can be derived from the following reasoning.

First, we consider that the total fraction of bainite nucleated at prior austenite grain boundaries at the end of the transformation is proportional to the interface area of those boundaries, S_{AGB}. Since the interface area S_{AGB} is inversely proportional to the prior austenite grain size, d_γ [1], we arrive at the proportionality in Equation (A.1).

$$f_{AGB,final} \propto S_{AGB} \propto \frac{1}{d_\gamma}, \tag{A.1}$$

where $f_{AGB,final}$ refers to the fraction of bainite nucleated at prior austenite grain boundaries at the end of the transformation. Because of the proportionality, $f_{AGB,final}$ can be written as

$$f_{AGB,final} = \frac{k}{d_\gamma}, \tag{A.2}$$

where k is a proportionality constant.

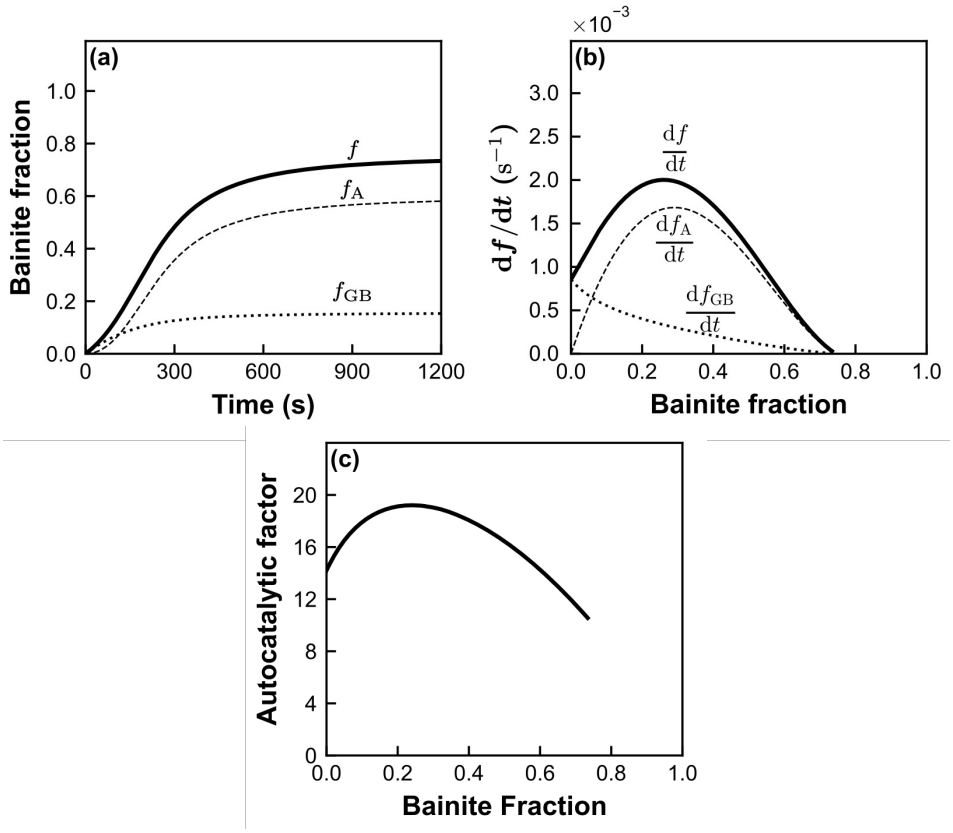

Figure A.1. Simulated kinetics of bainite formation considering the same parameters used in Figure 2.2, but $\overline{X} = 0.02283$ (equivalent to 0.5 wt.%), $X_b = 0.8\overline{X}$, $T_0' = 400\,^{\circ}\mathrm{C}$, and $C_2 = 7500\,\mathrm{K/at.fr.}$

The ratio f_{BA}/f_{AGB} at the end of the transformation can be written as

$$\frac{f_{BA,final}}{f_{AGB,final}} = \frac{f_{final} - f_{AGB,final}}{f_{AGB,final}}, \tag{A.3}$$

where f_{final} is the total fraction of bainite at the end of the transformation and $f_{BA,final}$ is the fraction of autocatalytically nucleated bainite at the end of the transformation. Substituting Equation (A.2) in Equation (A.3),

$$\frac{f_{BA,final}}{f_{AGB,final}} = \frac{f_{final}}{k} d_\gamma - 1, \tag{A.4}$$

which is the linear relationship seen in Figure 2.4e and Figure A.3e.

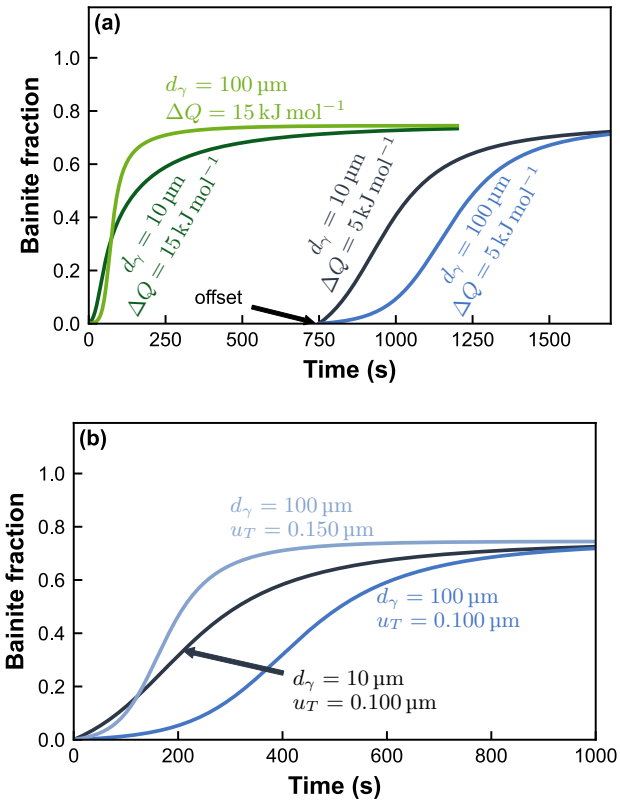

Figure A.2. Simulated kinetics of bainite formation considering the same parameters used in Figure 2.3, but $\overline{X} = 0.02283$ (equivalent to 0.5 wt.%), $X_b = 0.8\overline{X}$, $T_0' = 400\,^\circ C$, and $C_2 = 7500\,K/at.fr.$

A.3. Uncertainty in estimating the activation energies for bainite nucleation

The uncertainty in the estimated values of the activation energies is calculated by taking into account the uncertainty associated with the fitting procedure itself, $\sigma_{Q,\text{fit}}$, and with the uncertainty in the input parameters of the model, $\sigma_{Q,\text{input}}$. The uncertainty $\sigma_{Q,\text{fit}}$ is calculated automatically by Lmfit [2] and was, in all cases, smaller than $0.1\,kJ\,mol^{-1}$.

To calculate the uncertainty related to the input parameters, we considered a 10 % uncertainty in the values of the prior austenite grain size, d_γ, 10 % uncertainty in the bainite plate thickness, u_T, and 50 % uncertainty in the bainite plate aspect ratio, u_{AR}. Then, we varied d_γ, u_T, and u_{AR} within their uncertainty range and refitted the model to the experimental data to get new values of $Q_{AGB\overline{X}}$ and $Q_{BA\overline{X}}$.

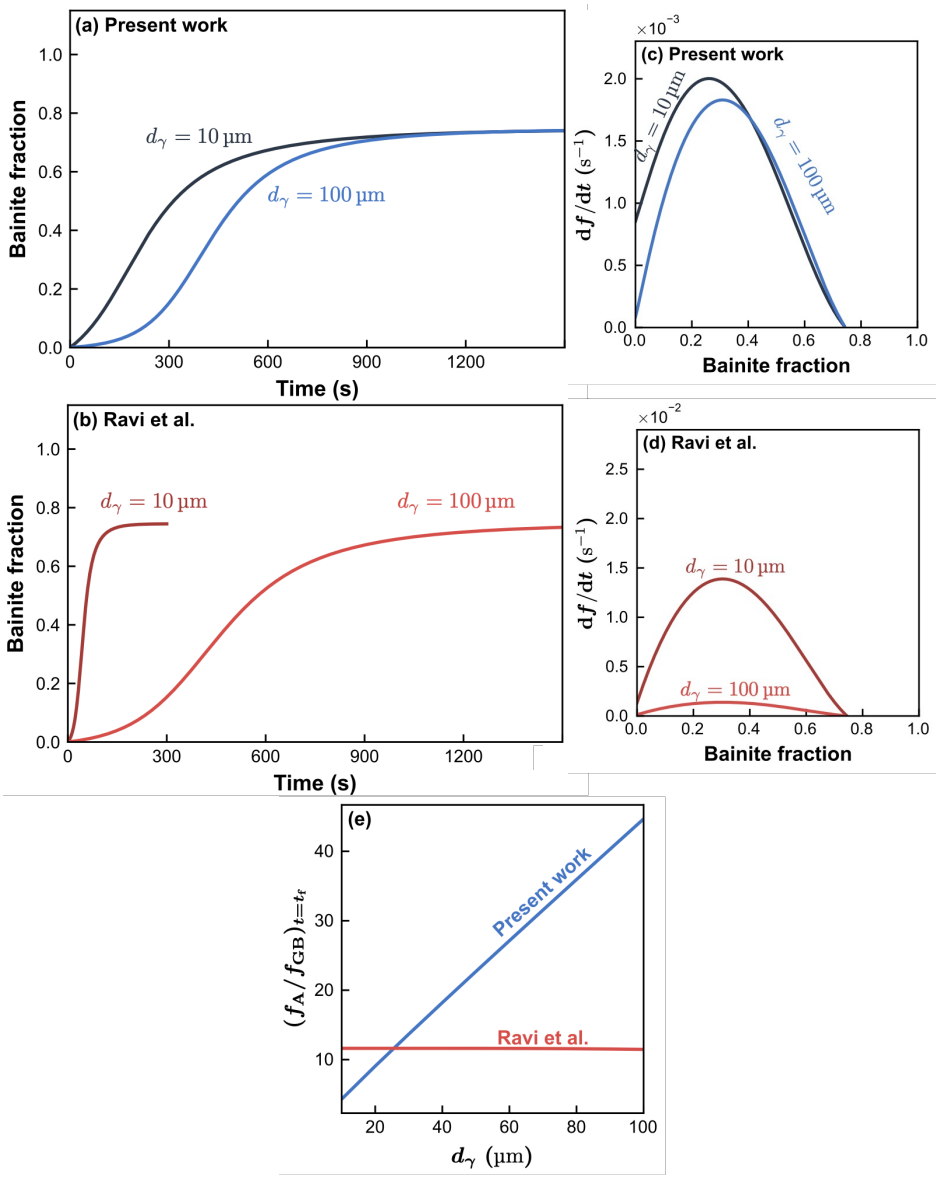

Figure A.3. Simulated kinetics of bainite formation considering the same parameters used in Figure 2.4, but $\overline{X} = 0.02283$ (equivalent to 0.5 wt.%), $X_b = 0.8\overline{X}$, $T_0' = 400\,°C$, and $C_2 = 7500\,K/at.fr.$

Figure A.4 shows such a procedure and the range of values of activation energies found for steel B isothermally treated at 370 °C. The estimated activation energy, $\widehat{Q}$, depends on the estimated value of the input parameters ($\widehat{Q}$ =

$\widehat{Q}\left(\widehat{d_\gamma}, \widehat{u_\mathrm{T}}, \widehat{u_\mathrm{AR}}\right)$, where ^ denotes the estimated value of the given input parameter).

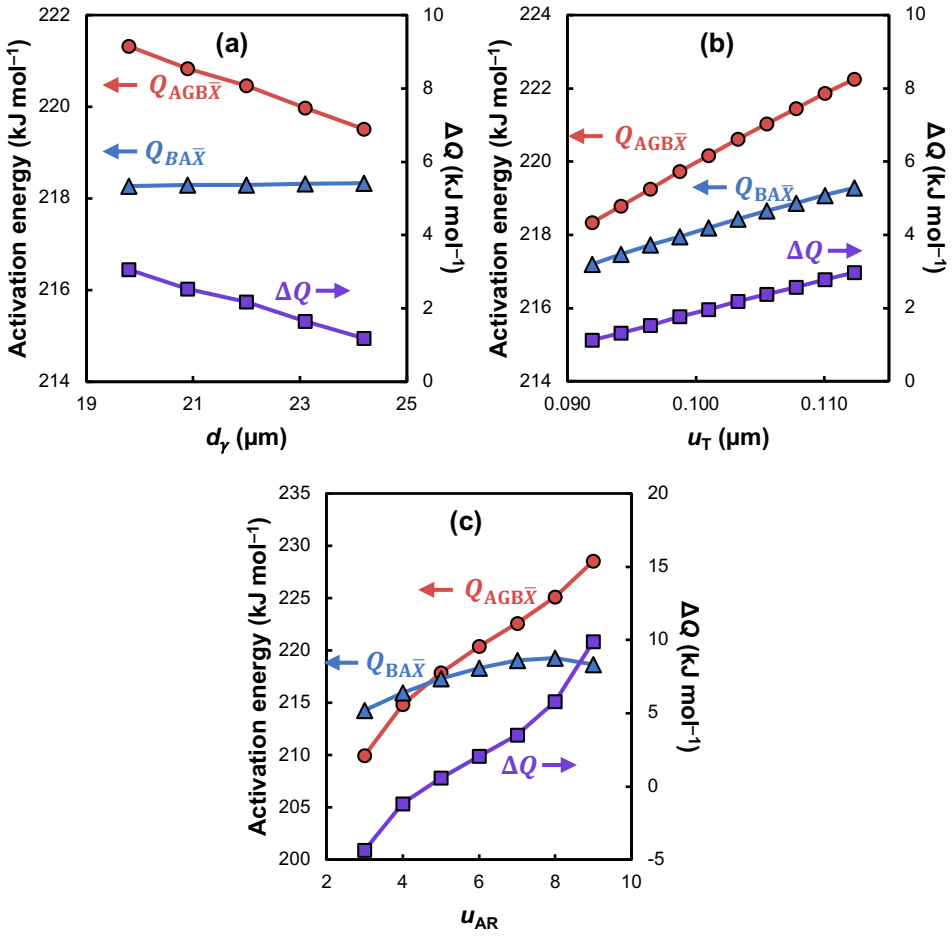

Figure A.4. Activation energies for bainite nucleation extracted from fitting as a function of the assumed values of **a.** prior austenite grain size, d_γ, **b.** thickness of the bainite sub-unit, u_T, and **c.** aspect ratio of the bainite sub-unit, u_AR, for isothermal bainite formation in steel B treated at $370\,^\circ\mathrm{C}$.

The uncertainties in Q induced by the uncertainty in each input parameter are calculated as

$$\sigma_{Q,i} = \frac{\max\left\{Q_{(i)}\right\} - \min\left\{Q_{(i)}\right\}}{2} \tag{A.5}$$

where i can be d_γ, u_T, or u_AR and Q can be $Q_{\mathrm{AGB}\overline{X}}$, $Q_{\mathrm{BA}\overline{X}}$, or ΔQ. Finally, the

total uncertainty $\widehat{Q}$ is given by the Pythagorean sum of all uncertainties, that is

$$\sigma_Q = \sqrt{{\sigma_{Q,\mathrm{fit}}}^2 + {\sigma_{Q,d_\gamma}}^2 + {\sigma_{Q,u_\mathrm{T}}}^2 + {\sigma_{Q,u_\mathrm{AR}}}^2}. \tag{A.6}$$

The uncertainties calculated from Equations (A.5) and (A.6) are displayed in Table A.1. The largest source of uncertainty in the estimation of activation energies is the uncertainty in the aspect ratio of the bainite sub-unit, u_AR.

Table A.1. Uncertainty in the activation energies for bainite nucleation in steel B treated at 370 °C.

	$\sigma_{Q,\mathrm{fit}}$ kJ mol^{-1}	σ_{Q,d_γ} kJ mol^{-1}	σ_{Q,u_T} kJ mol^{-1}	σ_{Q,u_AR} kJ mol^{-1}	σ_Q kJ mol^{-1}
$Q_{\mathrm{AGB}\overline{X}}$	0.1	0.9	2.0	9.3	9.6
$Q_{\mathrm{BA}\overline{X}}$	0.1	0.0	1.0	2.5	2.7
ΔQ	0.1	0.9	0.9	7.1	7.2

References

[1] J. W. Cahn. “The kinetics of grain boundary nucleated reactions”. In: *Acta Metallurgica* 4.5 (Sept. 1, 1956), pp. 449–459. doi: 10.1016/0001-6160(56)90041-4.

[2] M. Newville, R. Otten, A. Nelson, T. Stensitzki, A. Ingargiola, D. Allan, A. Fox, F. Carter, Michał, R. Osborn, D. Pustakhod, S. Weigand, Ineuhaus, A. Aristov, Glenn, Mark, mgunyho, C. Deil, A. L. R. Hansen, G. Pasquevich, L. Foks, N. Zobrist, O. Frost, Stuermer, J.-C. Jaskula, S. Caldwell, P. Eendebak, M. Pompili, J. H. Nielsen, and A. Persaud. *lmfit/lmfit-py: 1.3.2*. Version 1.3.2. July 19, 2024. doi: 10.5281/zenodo.12785036.

B

Appendix to Chapter 4

Table B.1. Mechanical properties of the steels heat treated in the CASim. The value presented is the mean of two tests, and the error is the average absolute deviation from the mean.

Heat treatment	Steel	YS (MPa)	UTS (MPa)	TE (%)	HEC (%)
BAM (600 s)	Ref	1069 ± 11	1413 ± 5	9.5 ± 1.0	36 ± 4
	0.6Si	1089 ± 8	1314 ± 15	5.5 ± 0.1	58 ± 2
	1.0Si	1059 ± 4	1355 ± 20	8.7 ± 0.5	37 ± 1
	0.02Nb	1063 ± 8	1366 ± 12	7.5 ± 0.2	31 ± 4
	1.7Mn-0.6Cr	1089 ± 2	1391 ± 2	8.5 ± 1.0	31 ± 1
	1.7Mn-0.6Cr-0.2Mo	1083 ± 6	1380 ± 2	10.4 ± 0.5	29 ± 4
	0.27C-1.7Mn-0.6Cr	1105 ± 15	1452 ± 17	7.9 ± 0.3	33 ± 4
	0.30C-1.7Mn-0.6Cr	1106 ± 9	1573 ± 15	7.8 ± 0.6	26 ± 3
BAM (300 s)	Ref	1026	1427	9.0	32
	0.6Si	1077	1390	8.1	40
	1.0Si	1018	1414	8.0	37
	0.02Nb	933	1394	9.6	25
	1.7Mn-0.6Cr	1039	1396	9.2	33
	1.7Mn-0.6Cr-0.2Mo	1018	1382	9.9	33
	0.27C-1.7Mn-0.6Cr	1103	1541	9.2	19
	0.30C-1.7Mn-0.6Cr	966	1669	8.5	19
TBF	Ref	813 ± 58	1177 ± 26	11.6 ± 1.8	24 ± 1

Continued on next page

B

Table B.1. (Continued)

Heat treatment	Steel	YS (MPa)	UTS (MPa)	TE (%)	HEC (%)
	0.6Si	870 ± 23	1069 ± 31	7.2 ± 1.3	46 ± 1
	1.0Si	803 ± 4	1071 ± 3	12.3 ± 0.3	30 ± 5
	0.02Nb	853 ± 8	1154 ± 1	12.2 ± 0.9	28 ± 3
	1.7Mn-0.6Cr	903 ± 13	1246 ± 2	12.1 ± 0.5	33 ± 10
	1.7Mn-0.6Cr-0.2Mo	938 ± 7	1278 ± 8	13.0 ± 0.7	28 ± 5
	0.27C-1.7Mn-0.6Cr	879 ± 20	1285 ± 2	14.0 ± 0.4	20 ± 1
	0.30C-1.7Mn-0.6Cr	778 ± 15	1325 ± 4	15.5 ± 0.3	16 ± 1
Q&P	Ref	1061 ± 20	1231 ± 9	12.4 ± 1.2	42 ± 10
	0.6Si	1108 ± 4	1205 ± 5	6.4 ± 0.7	70 ± 3
	1.0Si	1091 ± 22	1218 ± 13	9.3 ± 0.7	46 ± 2
	0.02Nb	1134 ± 15	1269 ± 9	11.3 ± 1.3	32 ± 1
	1.7Mn-0.6Cr	1112 ± 16	1286 ± 8	11.3 ± 0.1	38 ± 2
	1.7Mn-0.6Cr-0.2Mo	1107 ± 15	1297 ± 12	12.1 ± 0.2	31 ± 4
	0.27C-1.7Mn-0.6Cr	1145 ± 2	1326 ± 5	11.6 ± 0.1	31 ± 3
	0.30C-1.7Mn-0.6Cr	1167 ± 27	1371 ± 15	13.4 ± 0.5	26 ± 4

C

Appendix to Chapter 5

The full videos can be downloaded from:
https://doi.org/10.4121/6f40147a-d36f-4ef2-9b5e-950f35fba57a

Figure C.1. Same as Figure 5.6, but without the lines and annotations (continues on the next page)

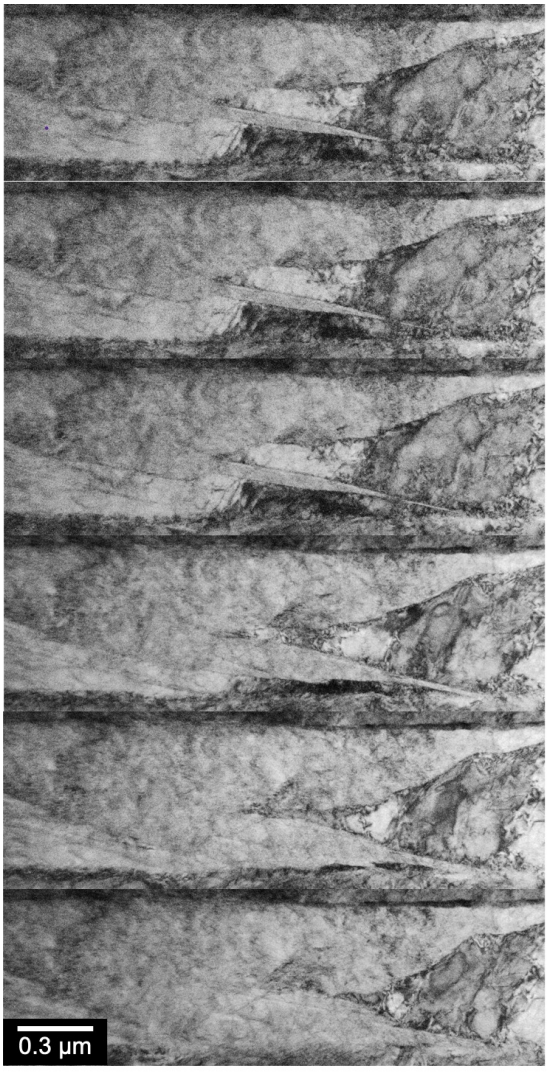

Figure C.1. Part 2 of the Figure (continued).

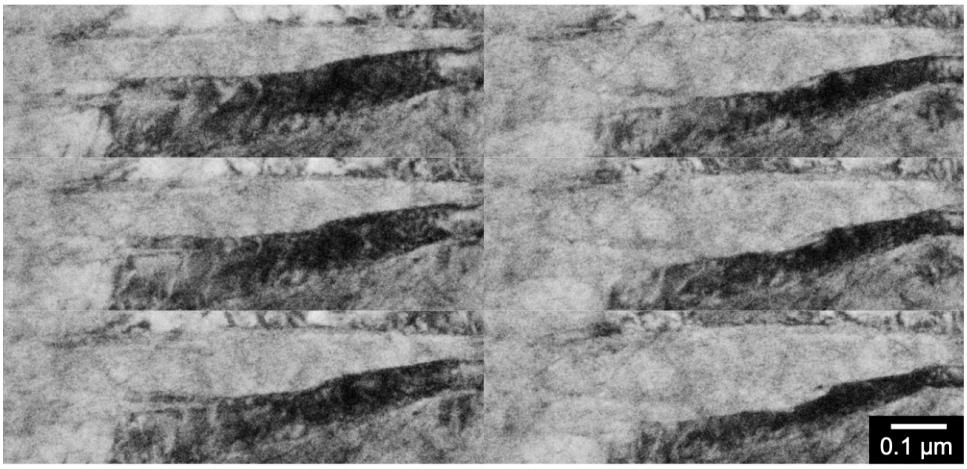

Figure C.2. Same as Figure 5.8, but without the lines and annotations

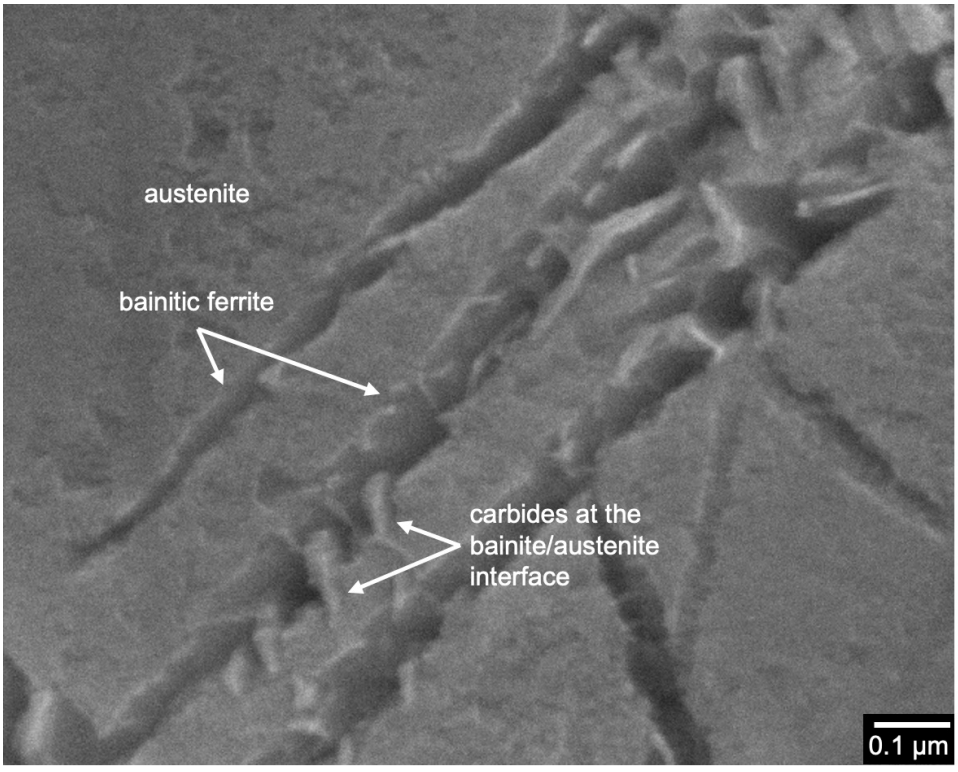

Figure C.3. Magnified image of Figure 5.2f$_{(i)}$.

Ultra aequinoxialem non peccari.

Caspar Barlaeus, 1647

Não existe pecado do lado de baixo do equador
Vamos fazer um pecado rasgado, suado, a todo vapor

Chico Buarque and Ruy Guerra, 1973

Acknowledgments

Maria, I could not start this section in any other way than by thanking you. You are an amazing supervisor in more ways than I can describe in this limited space. You were present at all times. You always knew in detail what I was doing and planning and were always available to have deep discussions about my research. Whenever I brought up a new idea to you, you always listened carefully and were open to discussing it as many times as I wanted. You always helped me to keep track of what I should prioritize to finish my thesis on time – and that's definitely one of the reasons I finished on time. You pushed me but always made sure not to push beyond my limit. You always trusted me. You always cared about how I was feeling. Your door was always open to discuss matters of the department, labs, and the PhD program, no matter if our opinions were similar or opposite. You are understanding to a level that still surprises me. During the last year of my PhD, every week I would come to your office with a new idea of what to do after finishing the PhD, and you always encouraged me to do whatever would make me the happiest. The PhD years are not easy, but I'm sure mine were made a lot easier by having you as my supervisor. Thank you!

Erik, I would like to thank you next. You were always very supportive of me and always had some kind words ready to be said. We had many long talks about so many different aspects of nucleation – activation energies, density of potential nucleation sites, measurements of nucleation rates, composition and size of the critical nucleus, driving forces, and much more. Thanks for all of those moments.

I also want to thank the technical staff of the MSE department. I especially want to thank Kees for all the help with the SEM, Richard for all the discussions and XRD measurements, and Durga for all the work in maintaining the metallography lab.

This PhD received funding from the Research Fund for Coal and Steel, whom I want to thank. And I want to thank not only for the funding, but for the opportunity to work in the MARTBAIN consortium. Working with all of you was among the best experiences of the PhD. You were always engaged and genuinely interested in my PhD work. Thank you, Thomas, Amandine, and Fanny, from Ascometal; Johannes, Markus, and Sophie, from Schaeffler; Carlos, from CENIM; and Stefan, from Tata Steel. I want to especially thank Stefan. You were always willing to meet up to discuss results, share your opinion on the modeling work, perform extra experiments, share literature, and ask difficult questions that would leave me thinking about them for days.

I want to thank John, from the University of Sheffield, for your openness when I approached you wanting to run the *in situ* TEM experiments.

I also want to thank all the friends I made along the way. Moving to a new country during a lockdown is usually not great for making new friends. However, I was

lucky to have met great people from day one. Vitória, you were the first friend I made in Delft. You brought me food on my first day when I was quarantined in my apartment and I could not order it online because I didn't have internet (you later also brought me the internet router!). Then I met Marco, Jithin, Raquel, John, Ana, Soroush, and Eszter. Thank you all for the dinners, drinks, games, nonsense talks and jokes, and for all the good and bad moments we shared!

I met many more amazing people at the MSE department. Philipp (triple colleague: MSE, marsenite, and kinetics group), Alfonso (thanks for not letting me go homeless!), Viviam, Arthur, Giovani, Konstantina, Javier, Sudhindra, Vibhor, Gaojie, Pablo Saint-Martin, Sharmistha, Farnaz, Naveena, Alice, Anniken, Tim, José, Luis, Arjun, Aravind, Gautham, Camila, Devi, Elsa, Fabian, Joep, Amir, Mohammed, Can, Jasper, and anyone else I might have forgotten (making sure I wrote down the name of everyone I want to thank is harder than I imagined!)

To all of my friends back home: thank you, and I miss you! Being away from you was definitely one of the hardest parts of my PhD journey. But I was always so happy to go back home and see you all. Thanks for all your support during these years, and for all the great memories we have together. I'm lucky to have had a few of you visiting me (Ariely, Jordan, Natalie, André, and Julia). I'm even luckier to have one of you actually moving to Delft to work at MSE: Julia Siedschlag. I'm so happy to have you here during these last months. Thanks for all the coffee, beers, and talks!

Finally, I want to thank my family: my parents, grandparents, brother, niece, uncles, aunt, and cousins. I want to thank especially the three people with whom I spent the first six months of lockdown: my mother, Regina, my grandmother Seni, and my late grandfather Manoel. When I was applying for the PhD position at TU Delft, I kept it a secret. Before telling anyone, I wanted to wait and see if I would get approved. Then, on a random morning in 2020, I told you three I had gotten an offer from TU Delft and that in two months I would move to the Netherlands, in the middle of a pandemic. Despite the initial shock, you all supported me. You helped me with everything I needed. Thank you for everything!

Curriculum Vitæ

Daniel dos Santos Avila

29-10-1994 Born in Pelotas, Brasil.

Education

2020–2024 PhD
Materials Science and Engineering
Delft University of Technology, Netherlands

2018–2020 Masters
Materials Science and Engineering
Universidade Federal de Santa Catarina, Brazil

2012–2017 Bachelors
Materials Engineering
Universidade Federal de Santa Catarina, Brazil

Awards

2021 Three-minute thesis video competition of TU Delft's 3mE Faculty
https://www.youtube.com/watch?v=wS8lKpMyz8w

List of Publications

7. **D. dos S. Avila**, J. Nutter, W.M. Rainforth, S.E. Offerman, M.J. Santofimia, Bainite formation observed by in situ transmission electron microscopy, *to be submitted for publication*

6. **D. dos S. Avila**, S.M.C. van Bohemen, C. Garcia-Mateo, T. Sourmail, S.E. Offerman, M.J. Santofimia, Modeling the effect of prior martensite on bainite formation kinetics, *to be submitted for publication*

5. J. Li, Y. Xu, X. Hou, **D. dos S. Avila**, A. Banis, J. Sietsma, R.H. Petrov, L.A.I. Kestens, New insights into the influence of Al and Si on the austenitization and element partitioning of medium-Mn steel, *submitted for publication*.

4. **D. dos S. Avila**, R.M. Huizenga, S.M.C. van Bohemen, S.E. Offerman, M.J. Santofimia, Shortening the heat treatment of third generation advanced high strength steels by forming carbide free bainite in the presence of martensite, *submitted for publication*.

3. **D. dos S. Avila**, S.E. Offerman, M.J. Santofimia, Modeling the effect of prior austenite grain size on bainite formation kinetics, Acta Materialia 266 (2024) 119656. https://doi.org/10.1016/j.actamat.2024.119656.

2. I.S. Deschamps, **D. dos S. Avila**, E. Vanzuita Piazera, R.C. Dudley Cruz, C. Aguilar, A.N. Klein, Design of in situ metal matrix composites produced by powder metallurgy—A critical review, Metals 12.12 (2023), 2073. https://doi.org/10.3390/met12122073.

1. L.L. Evangelista, **D. dos S. Avila**, M.A. Carvalho, H.D. Lopes, P.A.P. Wendhausen, Mechanical strength and energy losses optimization of somaloy 3P 700-based components, IEEE Transactions on Magnetics 52.5 (2016) 1-4. 10.1109/TMAG.2016.2516964.